THÈSE

En vue de l'obtention du

DOCTORAT DE L'UNIVERSITÉ DE TOULOUSE

Délivré par :

Université Toulouse 3 Paul Sabatier (UT3 Paul Sabatier)

Présentée et soutenue par :
Renjie WANG
le mercredi 12 octobre 2016

Titre :

Quantitative analysis of chromatin dynamics and nuclear geometry in living yeast cells

---

École doctorale et discipline ou spécialité :
ED BSB : Biologie structurale et fonctionnelle

Unité de recherche :
Laboratoire de Biologie Moléculaire Eucaryote (LBME) - UMR 5099 CNRS

Directeur/trice(s) de Thèse :

Olivier GADAL and Aurélien BANCAUD

Jury :

Kerstin BYSTRICKY	Professeur des Universités, Toulouse , France	Président
Gilles CHARVIN	Chargé de recherche, IGBMC, Illkirch	Rapporteur
Isabelle SAGOT	Directeur de recherche, IBGC, Bordeaux	Rapporteur
Sylvie TOURNIER	Directeur de recherche, LBCMCP, Toulouse	Examinateur
Karine DUBRANA	Directeur de recherche, CEA, Fontenay	Examinateur
Julien MOZZICONACCI	Maître de conférences ,LPTMC, Paris	Examinateur
Olivier GADAL	Directeur de recherche, LBME, Toulouse	Co-directeur de thèse
Aurélien BANCAUD	Chargé de recherche, LAAS, Toulouse	Co-directeur de thèse

Acknowledgements

First and foremost, I would like to give my sincere respects to my supervisors **Olivier Gadal** and **Aurélien Bancaud**. It is exactly them who brought me here three years ago, and helped me initiate my PhD projects. They allow me to knock their office door at any time when I encountered problems in biology and mathematics, and every time they could offer me an appropriate solution. I highly appreciate their guidance, discussion, patience, and encouragement during my PhD study. I also thank them for providing me opportunities to go for the international conferences.

I am appreciative of the help from **Christophe Normand**. I feel very lucky to be in the same group as him. Christophe is such a skilled person who trained me much about the biology technologies. In addition he is also an easy-going person who helped me much of my life in France, such as accommodations and entertainment.

Isabelle Léger, I am deeply indebted to her. She has a broad knowledge of biology. I benefited much from the discussion with her. Every time when I was confused by problems (either cell biology or biophysics), she always proposed me to make cross-checks on imperceptible points. She also taught me much about the culture in France. I also need thank her help in the modification of my PhD thesis. Without her help, I cannot easily arrive at the end for sure.

I particularly thank **Alain Kamgoue**, who taught me how to use Matlab. He is such a talented mathematician. Each time he can help me to find a best way to resolve the problem I met in mathematic (especially in Matlab and R language field). I cannot forget his intelligent forever.

I thank **Sylvain Cantaloube**, who trained me much how to use the confocal microscope. In addition, he also helped me much in the analysis of the microscope images.

Many thanks to my collegues **Christophe Dez, Frédéric Beckouët, Marta Kwapisz, Lise Dauban and Tommy Darrière**. They are so kind to me and always help me much in my life. I feel so pleasure to be in the same group with them. Frédéric Beckouët taught me many things in molecular biology; Marta Kwapisz helped me to prepare the mutant strains I need in my project; Lise Dauban and Tommy Darrière also helped me many in the basic biology experiments. You guys made me a confortable environment for learning and discussing. I will memorize great time spent with you all for life.

I must thank the members of my thesis committee: **Sylvie Tournier and Julien Mozziconacci**. Each year I would present my work of the previous year to them, and each time they gave me many interesting suggestions from their own field.

I also must thank our ‘mother’ in the lab **Catherine Rousseau**. She is so kind to help me to arrange all the travel tickets and the restaurant for my international conference. Without her, I cannot participate these international conferences so easy and happy.

I am grateful to the jury members of my PhD defense. I thank **Isabelle Sagot** and **Gilles Charvin** for their acceptance being my referees, and reading my manuscript carefully. The remarks from them are also appreciated. I also must thank **Karine Dubrana** as the examiner of my defense, the talk about chromatin dynamics with her also helped me understand my project much more.

I thank **Prof. Kerstin Bystricky** as the president to host my PhD defense. I also thank her and **Silvia Kocanova**’s care during the “Advanced workshop on interdisciplinary views on chromosome structure and function” in Italy.

Also, all friends are appreciated for their hospitality and kindness.

I cannot forget all activities (travelling, party, chatting……) with my friends, **Faqiang Leng, Weikai Zong, Diandian Ke, Zhouye Chen, Yu Chen, Congzhang Gao**. I like to play games with these guys and I enjoy our party time. I will remember these days all my life.

Finally, I would like to thank my father **Fujian Wang**, my mother **Erqin Wang** and my brother **Junjie Wang** for their continuous supports and their family love. My parents as farmers have been working very hard to afford all costs of my education sinc the first day I stepped into the school. I now reward them with a doctorate son. My girfriend, **Tingting Bi**, she is always standing by my side and giving me endless love. It is much difficult to keep a long-distance relation spanning six to seven time zones. We have together passed through the hard time. Without her supports, I would not be the person who I am today. Thank you, my darling.

A special thanks to **China Scholarship Council (CSC)** as the main financial support during 09/2013-09/2016.

王仁杰

Toulouse, August 2016

SUMMARY

Chromosome high-order architecture has been increasingly studied over the last decade thanks to technological breakthroughs in imaging and in molecular biology. It is now established that structural organization of the genome is a key determinant in all aspects of genomic transactions. Although several models have been proposed to describe the folding of chromosomes, the physical principles governing their organization are still largely debated. Nucleus is the cell's compartment in which chromosomal DNA is confined. Geometrical constrains imposed by nuclear confinement are expected to affect high-order chromatin structure. However, the quantitative measurement of the influence of the nuclear structure on the genome organization is unknown, mostly because accurate nuclear shape and size determination is technically challenging.

This thesis was organized along two axes: the first aim of my project was to study the dynamics and physical properties of chromatin in the *S. cerevisiae* yeast nucleus. The second objective I had was to develop techniques to detect and analyze the nuclear 3D geomtry with high accuracy.

Ribosomal DNA (rDNA) is the repetitive sequences which clustered in the nucleolus in budding yeast cells. First, I studied the dynamics of non-rDNA and rDNA in exponentially growing yeast cells. The motion of the non-rDNA could be modeled as a two-regime Rouse model. The dynamics of rDNA was very different and could be fitted well with a power law of scaling exponent ~0.7. Furthermore, we compared the dynamics change of non-rDNA in WT strains and temperature sensitive (TS) strains before and after global transcription was actived. The fluctuations of non-rDNA genes after transcriptional inactivation were much higher than in the control strain. The motion of the chromatin was still consistent with the Rouse model. We propose that the chromatin in living cells is best modeled using an alternative Rouse model: the "branched Rouse polymer".

Second, we developed "NucQuant", an automated fluorescent localization method which accurately interpolates the nuclear envelope (NE) position in a large cell population. This algorithm includes a post-acquisition correction of the measurement bias due to spherical aberration along Z-axis. "NucQuant" can be used to determine the nuclear geometry under different conditions. Combined with microfluidic technology, I could accurately estimate the shape and size of the nuclei in 3D along entire cell cycle. "NucQuant" was also utilized to detect the distribution of nuclear pore complexes (NPCs) clusters under different conditions, and revealed their non-homogeneous distribution. Upon reduction of the nucleolar volume, NPCs are concentrated in the NE flanking the nucleolus, suggesting a physical link between NPCs and the nucleolar content.

In conclusion, we have further explored the biophysical properties of the chromatin, and proposed that chromatin in the nucleoplasm can be modeled as "branched Rouse polymers". Moreover, we have developed “NucQuant”, a set of computational tools to facilitate the study of the nuclear shape and size. Further analysis will be required to reveal the links between the nucleus geometry and the chromatin dynamics.

RESUME

L'analyse de l'organisation à grande échelle des chromosomes, par des approches d'imagerie et de biologie moléculaire, constitue un enjeu important de la biologie. Il est maintenant établi que l'organisation structurelle du génome est un facteur déterminant dans tous les aspects des « transactions » génomiques: transcription, recombinaison, réplication et réparation de l'ADN. Bien que plusieurs modèles aient été proposés pour décrire l'arrangement spatial des chromosomes, les principes physiques qui sous-tendent l'organisation et la dynamique de la chromatine dans le noyau sont encore largement débattus. Le noyau est le compartiment de la cellule dans lequel l'ADN chromosomique est confiné. Cependant, la mesure quantitative de l'influence de la structure nucléaire sur l'organisation du génome est délicate, principalement du fait d'un manque d'outils pour déterminer précisément la taille et la forme du noyau.

Cette thèse est organisée en deux parties: le premier axe de mon projet était d'étudier la dynamique et les propriétés physiques de la chromatine dans le noyau de la levure *S. cerevisiae*. Le deuxième axe visait à développer des techniques pour détecter et quantifier la forme et la taille du noyau avec une grande précision.

Dans les cellules de levure en croissance exponentielle, j'ai étudié la dynamique et les propriétés physiques de la chromatine de deux régions génomiques distinctes: les régions codant les ARN ribosomiques regroupés au sein d'un domaine nucléaire, le nucléole, et la chromatine du nucléoplasme. Le mouvement de la chromatine nucléoplasmique peut être modélisé par une dynamique dite de « Rouse ». La dynamique de la chromatine nucléolaire est très différente et son déplacement caractérisé par une loi de puissance d'exposant ~ 0,7. En outre, nous avons comparé le changement de la dynamique de la chromatine nucléoplasmique dans une souche sauvage et une souche porteuse d'un allèle sensible à la température (ts) permettant une inactivation conditionnelle de la transcription par l'ARN polymérase II. Les mouvements chromatiniens sont beaucoup plus importants après inactivation transcriptionnelle que dans la souche témoin. Cependant, les mouvements de la chromatine restent caractérisés par une dynamique dite de « Rouse ». Nous proposons donc un modèle biophysique prenant en compte ces résultats : le modèle de polymère dit "branched-Rouse".

Dans la deuxième partie, j'ai développé "NucQuant", une méthode d'analyse d'image permettant la localisation automatique de la position de l'enveloppe nucléaire du noyau de levures. Cet algorithme comprend une correction post-acquisition de l'erreur de mesure due à l'aberration sphérique le long de l'axe Z. "NucQuant" peut être utilisée pour déterminer la géométrie nucléaire dans de grandes populations cellulaires. En combinant « NucQuant » à la technologie microfluidique, nous avons pu estimer avec précision la forme et la taille des noyaux en trois dimensions (3D) au cours du cycle cellulaire. "NucQuant" a également été utilisé pour détecter la distribution des regroupements locaux de complexes de pore nucléaire (NPCs) dans des conditions différentes, et a révélé leur répartition non homogène le long de l'enveloppe nucléaire. En particulier, nous avons pu montrer une distribution particulière sur la région de l'enveloppe en contact avec le nucléole.

En conclusion, nous avons étudié les propriétés biophysiques de la chromatine, et proposé un modèle dit "branched Rouse-polymer" pour rendre compte de ces propriétés. De plus, nous avons développé "NucQuant", un algorithme d'analyse d'image permettant de faciliter l'étude de la forme et la taille nucléaire. Ces deux travaux combinés vont permettre l'étude des liens entre la géométrie du noyau et la dynamique de la chromatine.

Table of Contents

Figure list

ABBREVIATIONS

DNA	Deoxyribonucleic acid
RNA	ribonucleic acid
mRNA	messenger RNA
A	adenine
T	thymine
C	cytosine
G	guanine
U	uracil
NMR	nuclear magnetic resonance
bp	base pair
Å	Ångstrom
TEM	transmission electron microscopy
NRL	nucleosome repeat lengths
CEMOVIS	cryo-EM of vitreous sections
SAXS	small-angle X-ray scattering
CTs	chromosome territories
FISH	fluorescent in situ hybridization
IC	interchromatin compartment
CT-IC	chromosome territory-interchromatin compartment
3C	chromosome conformation capture
4C	3C-on chip or circular 3C
5C	3C carbon copy
rDNA	ribosomal DNA
NE	nuclear envelope
SPB	spindle pole body
CEN	centromeres
TEL	telomeres
NPC	nuclear pore complex
tRNA	transfer RNA
FROS	fluorescent repressor-operator system
MSD	mean square displacement

SNR	signal to noise ratio
DH-PSF	Double-Helix Point Spread Function
fBm	fractional Brownian motion
MTs	microtubules
MTOC	microtubule-organizing center
EM	electron microscopy
INM	inner nuclear membrane
SUN	Sad1p and UNC-84
KASH	Klarsicht, ANC-1 and Syne homology
LINC	Linker of Nucleoskeleton and Cytoskeleton
FCs	fibrillar centers
DFC	dense fibrillar component
GC	granular component
IGS	intergenic spacers
RENT	regulator of nucleolar silencing and telophase exit
RFB	replication fork barrier
Nups	nucleoporins
DIC	differential interference contrast
SBF-SEM	serial block-face scanning electron microscopy
ET	electron tomography
HVEM	high-voltage electron microscope
STEM	scanning transmission electron microscopy
PSF	point spread function
µm	micrometer
nm	nanometer
TS	temperature sensitive
PVP	poly-vinylpyrrolidone
SDF	step distribution function

Chapter I

Introduction

1. The chromosome organization in space

Chromosome spatial organization plays a key role in transcriptional regulation, DNA repair and replication. How do chromosomes organize in the eukaryotic nucleus is still an open question. In the following chapter of the introduction, I will present a general overview of the chromatin structure, chromosome spatial organization in the eukaryotic nucleus and the techniques used to study the chromosome structure and organization.

1.1 Chromatin structure

1.1.1 The DNA molecule

Deoxyribonucleic acid (DNA) is the molecule which carries the genetic instructions used for the formation of all compounds within the cells, such as proteins and Ribonucleic acid (RNA). Most genomic DNA consists of two biopolymer strands, coiled around a common axis; these two strands are composed of nucleotides. The genetic information is stored in the nucleotides sequence. Each nucleotide is composed of a deoxyribose, a phosphate group and a kind of nitrogenous base, either adenine (A), thymine (T), cytosine (C) or guanine (G). The nucleotides are linked together by a specific hydrogen-bond, to form a double helix (Watson and Crick, 1953b) (Figure 1A). Genetic information is expressed in two steps: first the genomic information coded in DNA is transmitted to a messenger known as messenger RNA (mRNA). RNA is a polymer of ribonucleotides in which thiamine (T) is replaced by a different nucleotide, uracil (U). The information in mRNA is then translated by an RNA based ribozyme, the ribosome, into a sequence of amino acids that forms a protein (Figure 1B). Results from X-ray diffraction, nuclear magnetic resonance (NMR) or other spectroscopic studies have shown that the DNA molecule adapts its structure according to the environment. This leads to polymorphism of the DNA structure. The three billion base pairs in the human genome exhibit a variety of structural polymorphisms which is important for the biological packaging as well as functions of DNA. B-DNA is the most commonly found structure *in vivo* by far. However, DNA repeat-sequences can also form several non-B DNA structures such as the G-quadruplex, the i-motif and Z-DNA (Choi and Majima, 2011; Doluca et al., 2013). Various DNA structures have been characterized as A, B, C, etc. (Bansal, 2003; Ghosh and Bansal, 2003). The currently accepted three major DNA configurations include the A-DNA, the B-DNA and the Z-DNA (Ghosh and Bansal, 2003) (Figure 1C). A-DNA and B-DNA are all right-handed double helix. A-DNA was observed under conditions of low hydration; it has 11 nucleotides per turn and the projected displacement along the overall helical axis can be as low as 2.4 Å. B-DNA is the closest to the original Watson-Crick model with a near-perfect 10 units per turn and the projected displacement is ~3.4 Å; it was observed under the conditions of relative high hydration (Ghosh and Bansal, 2003; Lu et al., 2000). Unlike the A- and B-DNA, Z-DNA is a left-handed duplex structure with 12 nucleotides per turn and helix pitch is ~3 Å (Bernal et al., 2015).

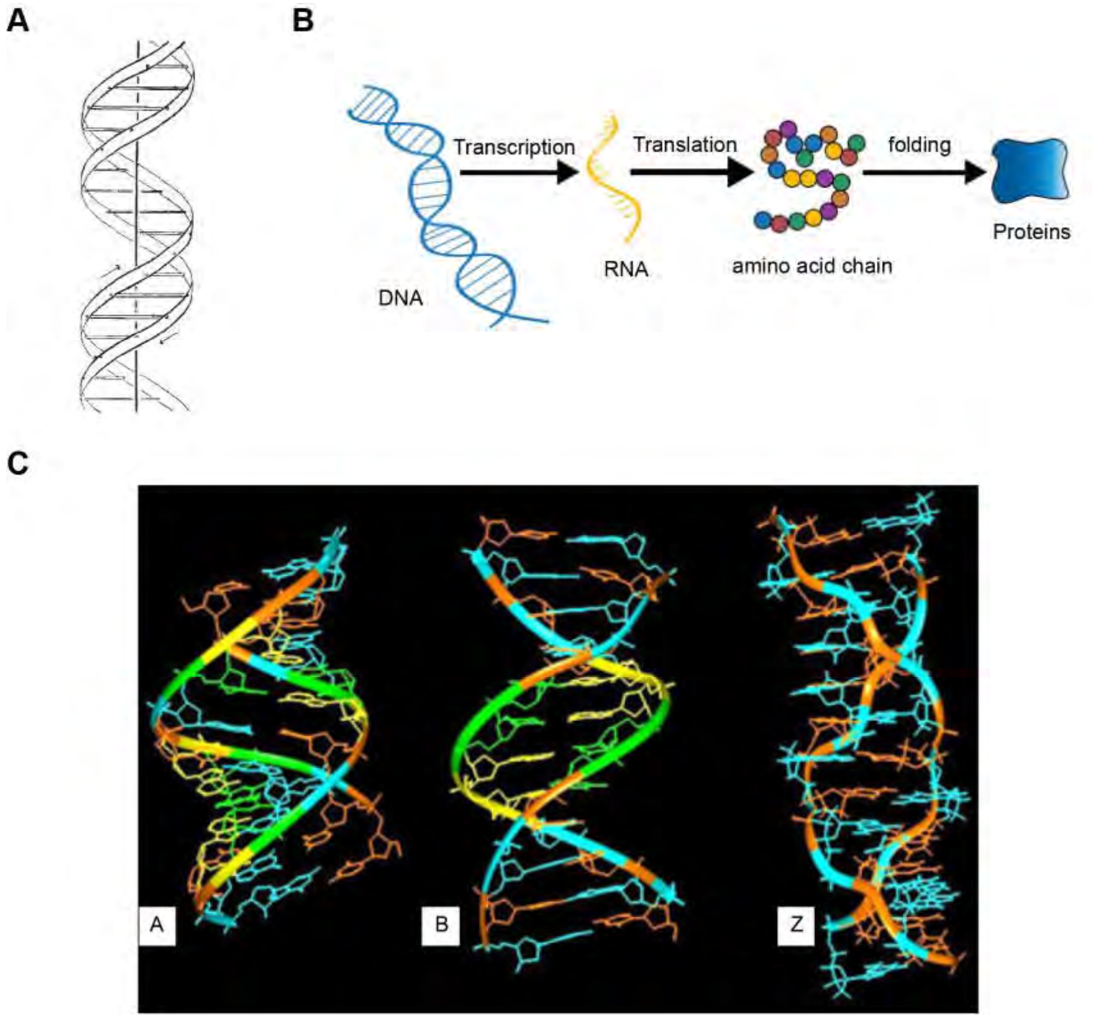

Figure 1. DNA structure and gene expression

A. The double helix structure of the DNA proposed by Watson and Crick in 1953. From (Watson and Crick, 1953b).

B. Schema of the gene expression process.

C. Three possible helix structures: from left to right, the structures of A, B and Z DNA. From (Bansal, 2003).

X-ray diffraction, NMR or other spectroscopic techniques are used to characterize DNA conformation *in vitro* but, *in vivo* configuration of DNA molecule is still challenging. The human nucleus of 10 µm in diameter contains ~2 m of linear DNA (Watson and Crick, 1953). Nucleus in budding yeast is often described as a sphere of radius ~1 µm (Berger et al., 2008). Electron microscopic analysis indicates that the yeast nuclear DNA can be isolated as linear molecules ranging in size from 50 µm (1.2×10^8 daltons) to 355 µm (8.4×10^8 daltons) (Petes et al., 1973). To duplicate and segregate the genomic DNA, the long DNA sequence is organized in a condensed structure made of DNA and proteins to fit into the cell nucleus: the chromatin in eukaryotic cells.

1.1.2 Nucleosomes

The nucleosome is the fundamental unit of chromatin. It is formed by a pool of 8 polypeptides (histones) around which 145 DNA base pairs (bp) are wrapped in 1.65 turns (Absolom and Van Regenmortel, 1977; Fischle et al., 2003; Thomas and Furber, 1976). The histone octamer is composed of eight proteins, two of each core histones H2A, H2B, H3 and H4 (Hansen, 2002). The histone octamer is assembled with one H3/H4 tetramer and two H2A/H2B dimers (Figure 2A). Each histone has both an N-terminal tail and a C-terminal histone-fold. X-ray crystallography of the structural details of the nucleosome core indicates that the histone N-terminal tails can extend from one nucleosome and contact with adjacent nucleosomes (Davey et al., 2002; Luger et al., 1997). Modifications of these tails affect the inter-nucleosomal interactions and allow recruitment of specific protein complexes therefore affecting the overall chromatin structure (Dorigo et al., 2003; Shogren-Knaak et al., 2006). The modification of the histone tails is regulating accessibility of chromatin to transcription and many other DNA processes, are defined as the "histone code" (Strahl and Allis, 2000).

1.1.3 10 nm chromatin fibers

The so-called 10 nm fiber corresponds to nucleosome core particles more or less regularly spaced on the genome that form a string of beads, with short stretches of bare DNA- the linker DNA- connecting adjacent nucleosomes (Figure 2B).

Since the linker DNA should be phased with respect to the histones core, the precise orientation of a nucleosome relative to the previous one is largely determined by the linker DNA length and by the torsional constraint of the fiber (Barbi et al., 2012). The short size of the linker DNA is hardly compatible with its bending, so one can assume the linkers as straight. This assumption helps researchers to describe the chromatin structure by the entry-exit angle α, the rotational angle β and the linker length (Woodcock et al., 1993) (Figure 2C). A change in α and β modifies the fiber architecture and consequently induces a rotation of one strand end with respect to the other. However, *in vivo*, the linker DNA length is variable depending on organisms, tissues and genomic regions and is usually associated with the H1 class of linker histone. The alternative nucleosomes spacing has significant influence on the chromatin fiber plasticity (Recouvreux et al., 2011).

In addition, the linker DNA crossing state has also significant impact on the chromatin fiber structure. According to their position at the exit of a nucleosome, the linker DNA can adopt three main states. The negatively crossed state corresponds to the standard crystallographic structure; in the positively crossed state, the two linkers DNA cross instead in the opposite, positive way; and in the open state, the DNA is partially unwrapped from the nucleosome core histones and linkers DNA do not cross anymore (De Lucia et al., 1999; Sivolob et al., 2003) (Figure 2D).

All these variations can result in the formation of irregular fibers *in vivo*.

The physical properties of the chromatin fibers may govern the structural changes necessary for the functioning and dynamics of chromatin. So it is important to understand the higher-order organization of the chromatin.

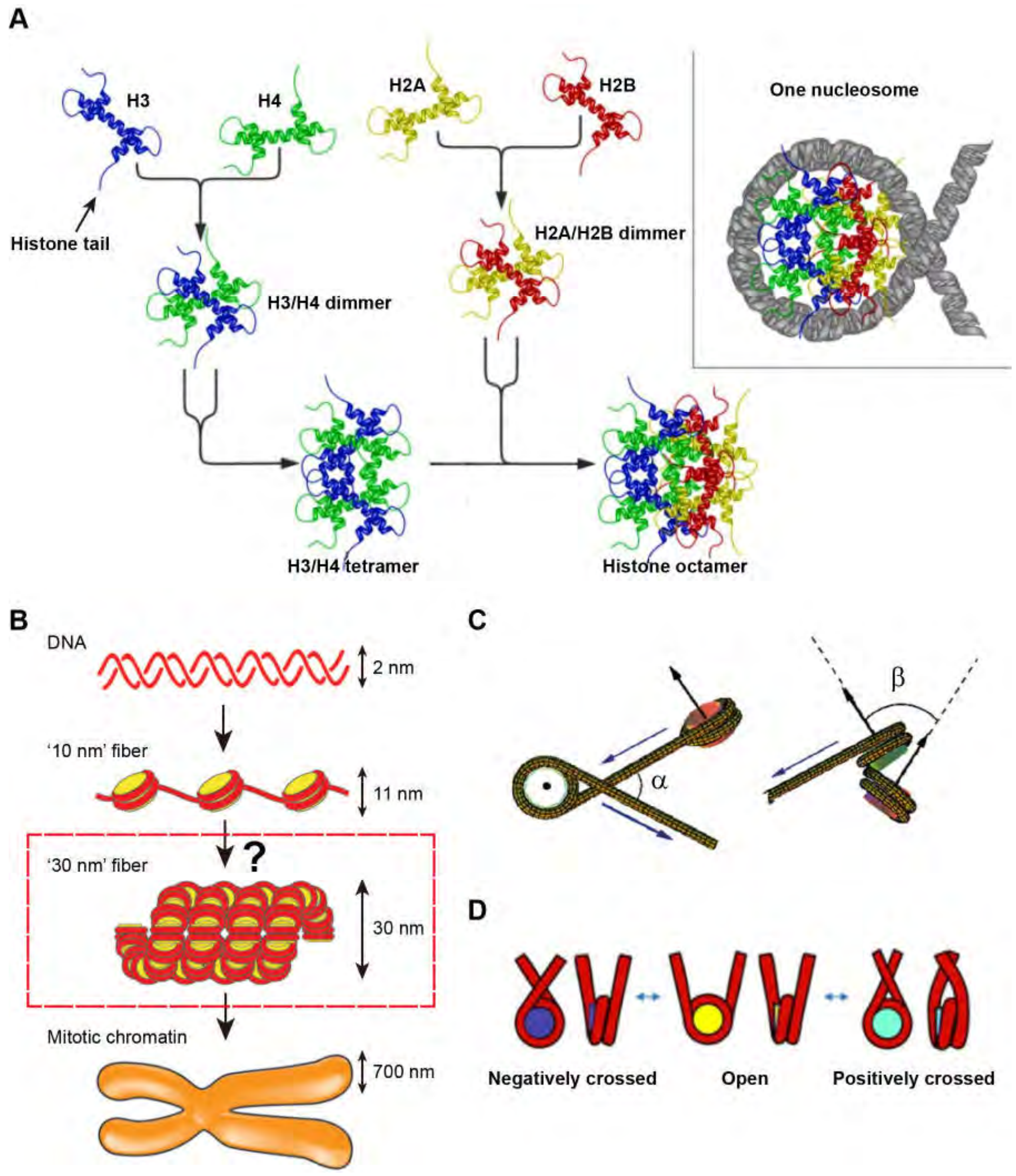

Figure 2. The nucleosome and chromosome structures.

A. Schematic representation of the assembly of the core histones wrapped by the DNA to form one nucleosome. Each histone octamer contains one H3/H4 tetramer and two H2A/H2B dimers. From Wikipedia, author Richard Wheeler (Zephyris).

B. The nucleosome arrays form the "10 nm" chromatin fiber. The "10 nm" fibers compact to form the "30 nm" chromatin fibers which was for long time considered to represent a higher order chromatin organization *in vivo*. From (Maeshima et al., 2010).

C. Schematic of the DNA winding pattern along two neighbouring nucleosomes. From (Recouvreux et al., 2011).

D. The states of the Linker DNA. From (Recouvreux et al., 2011).

1.1.4 The controversial “30 nm” chromatin fiber

The nucleosome has long been assumed to compact into irregular fibers with ~30 nm diameter (Bednar et al., 1998; Robinson et al., 2006). Although “30 nm” fibers have been observed *in vitro* (Finch and Klug, 1976), their existence *in vivo* remains an open and highly debated question since most attempts to visualize these fibers *in vivo* have failed so far (Joti et al., 2012; Maeshima et al., 2010).

Two main “30 nm” structures have been described: one-start helix with interdigitated nucleosomes, called ‘solenoid’ model, and ‘two-start helix’ model (Robinson and Rhodes, 2006). Solenoid fibers in which consecutive nucleosomes are located close to one another in the fiber and compacting into a simple one-start helix have been observed by conventional transmission electron microscopy (TEM) (Thomas and Furber, 1976). The ‘two-start helix’ model has been extrapolated from the crystal structure of a four-nucleosomes core array lacking the linker histone. In this model, the nucleosomes are arranged in a zigzag manner: a nucleosome in the fiber is bound to the second neighbor but not to the closest (Schalch et al., 2005) (Figure 3). Grigoryev’s team found that under certain conditions *in vitro* these two models can be simultaneously present in a 30 nm chromatin fiber (Grigoryev et al., 2009).

In vivo, the length of the linkers DNA is not identical which will result in many various folding. Routh’s group found that the nucleosome repeat length (NRL) and the linker histone can influence the chromatin higher-order structure. Only the 197-bp NRL array with the linker histone H1 variant, H5, can form 30 nm fibers. The 167-bp NRL array displays a thinner fiber (~20 nm) (Routh et al., 2008). Rhodes's lab found two different fiber structures which were determined by the linker DNA length: when the linker DNA length is 10-40 bp the produced fibers have a diameter of 33 nm, and the fibers have a diameter of 44 nm when the linker DNA length is from 50 to 70 bp (Robinson et al., 2006).

We should note that, all these studies were all led *in vitro* or on purified fibers. Any small variations in experimental conditions will impact the regulation of the nucleosomes arrays. *In vivo*, the length of the linkers DNA is varied, the flexibility of each nucleosome also. If the “30 nm” chromatin fiber exists *in vivo* is still controversial. More recently, cryo-EM of vitreous sections (CEMOVIS) or small-angle X-ray scattering (SAXS) techniques were used to study the nucleosomes organization of HeLa cells: the results showed that no matter in interphase or in mitotic chromatins, there was no “30 nm” chromatin structure formation. *In vivo*, nucleosomes concentration is high. Therefore, nucleosome fibers are forced to interdigitate with others, which can interfere with the formation and maintenance of the static 30-nm chromatin fiber and lead to the “polymer melt” behaviour (Joti et al., 2012; Maeshima et al., 2010).

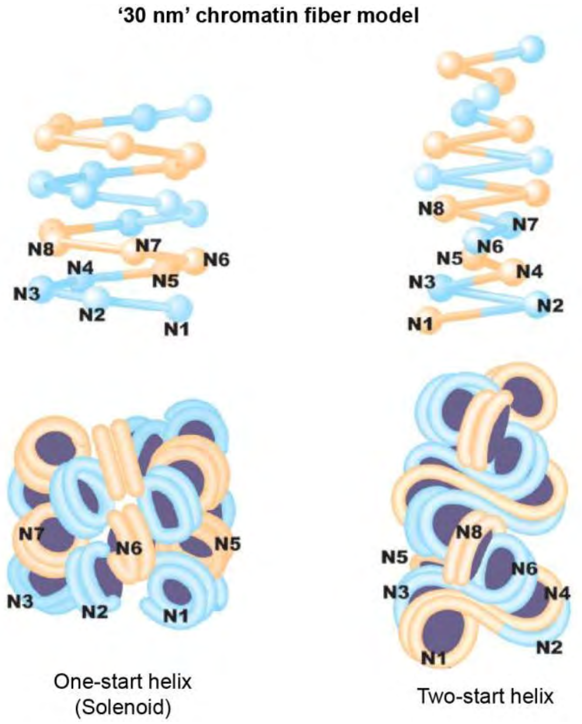

Figure 3. The two main models of the “30 nm” chromatin fibers. The one-start helix is an interdigitated solenoid. The first nucleosome (N1) in the fiber contacts with its fifth (N5) and sixth (N6) neighbors. In the two-start model, nucleosomes are arranged in a zigzag manner. The first nucleosome (N1) in the fiber binds to the second-neighbor nucleosome (N3). Blue and orange represent the alternate nucleosome pairs. From (Maeshima et al., 2010).

1.2 The chromosome spatial organization

The linear array of nucleosomes that comprises the primary structure of chromatin is folded and condensed to different degrees in nuclei and chromosomes forming “higher order structures”. The chromosomes in mitosis are highly condensed and moved independently by the mitotic spindle apparatus. After cell division, the compacted chromatin is decondensed in interphase phases (Antonin and Neumann, 2016). In this part, I will introduce the spatial organization of the chromosomes in mitosis and interphase.

1.2.1 Condensed mitotic chromosomes

Mitosis is a part of the cell cycle in which chromosomes are separated into two identical sets. The mitotic chromosome structure in metazoan cells has been observed by light microscopy (Rieder and Palazzo, 1992). To avoid the truncation of chromosome arms during cell division and to facilitate proper separation and segregation of sister chromatids, the mitotic chromosomes are highly condensed with an iconic structure of X-shaped (Figure 4A). How mitotic chromosomes organize is still controversial. Solid evidence suggests that the topoisomerase II and condensin complexes contribute to this condensation (Hudson et al., 2009; Lau and Csankovszki, 2014; Maeshima and Laemmli, 2003; Moser and Swedlow, 2011). There are two main models to explain the mitotic chromosome organization: hierarchical folding model and radial loop model (Antonin and Neumann, 2016) (Figure 4B). Crick and co-workers proposed hierarchical folding model, which proposes that the mitosis chromosomes are formed by a hierarchical helical folding of ‘30 nm’ chromatin fibers (Bak et al., 1977). The radial loop model suggests that the mitotic chromosomes are folded with radial loop model, in which mitotic chromatin forms series of chromatin loops which are attached to a central chromosome scaffold axis (Maeshima and Eltsov, 2008). Immunofluorescence of the isolated human chromosome topoisomerase IIα and the condensin I component indicates that the chromosome scaffold components have axial distributions at the center of each chromatid in the mitotic chromosome (Maeshima and Laemmli, 2003). Recent Hi-C data also proved the mitotic chromosome organized with radial loop model (See section 1.2.4). However, if the ’30 nm’ chromatin fibers exist in the living cells is still controversial.

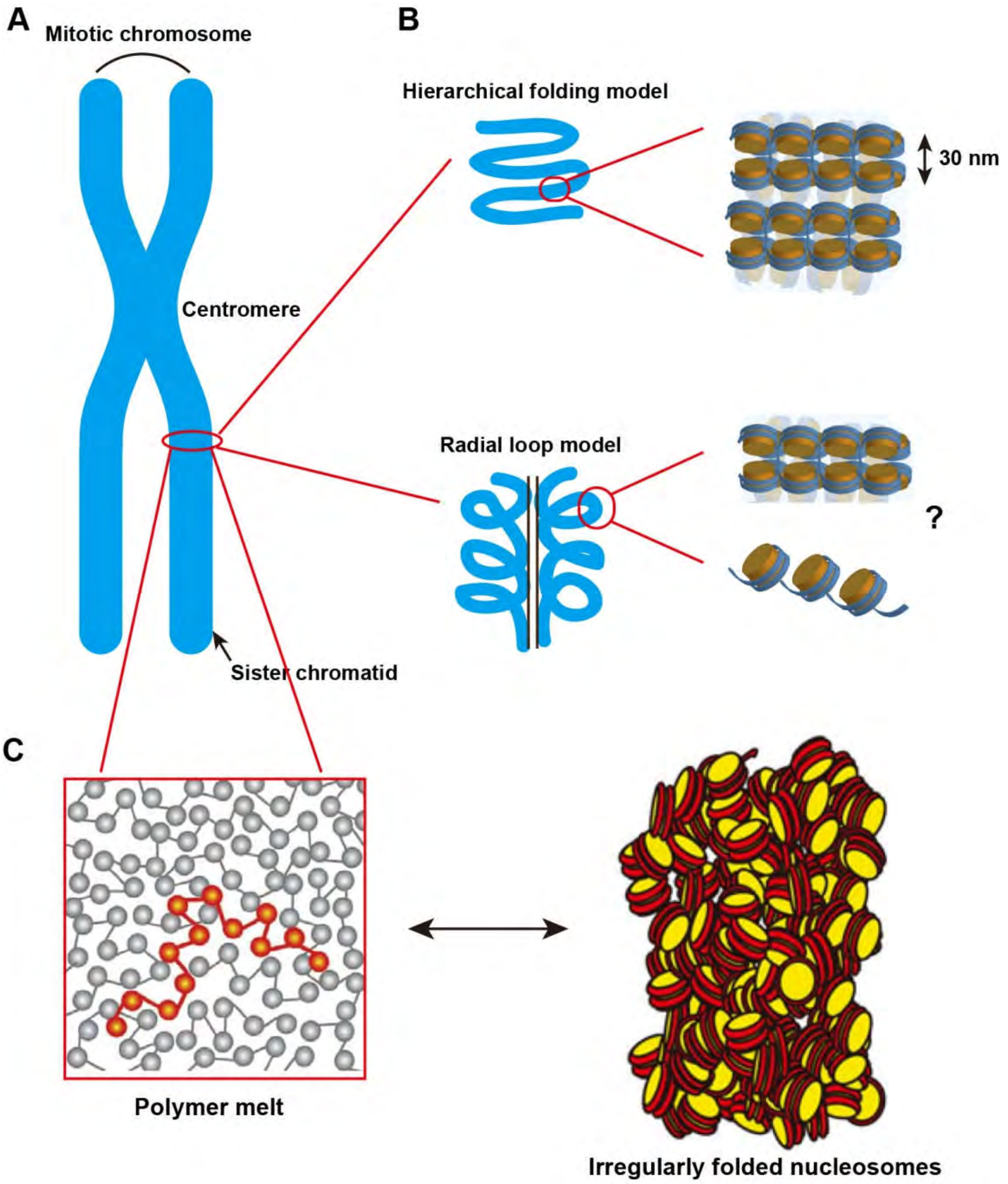

Figure 4. The organization of condensed mitotic chromosomes.

A. The structure of a mitotic chromosome: two sister chromatids are anchored each other through centromere. Adapted from (Antonin and Neumann, 2016).

B. Two main models of the mitotic chromatin organization. Adapted from (Antonin and Neumann, 2016).

C. In mitotic chromosomes, the nucleosome fibers exist in a highly disordered, interdigitated state like a ‘polymer melt’ that undergoes dynamic movement. Adapted from (Maeshima et al., 2010).

To study the chromosome organization in living cells, the highest resolution microscopic technics is achieved using cryo-EM of vitreous sections (CEMOVIS), but with the cost of low contrast. Cells are collected and frozen by high-pressure freezing, then they are sectioned and the ultrathin sections are observed directly under a cryo-EM with no chemical fixation or staining which guarantees the cellular structures in a close-to-native state (Maeshima et al., 2010). Maeshima *et al.* observed the human mitotic chromosomes by using this technique and they did not find any higher-order structures including “30 nm” chromatin fibers formation; their results suggest that the nucleosomes fiber exists in a highly disordered 10 nm fiber, in an interdigitated state like a ‘polymer melt’ that undergoes dynamic movement (Maeshima et al., 2010) (Figure 4C). Since the thickness of the cryo-EM section is only ~70 nm, this prevents the observation of a whole chromosome organization. Joti and colleagues utilized small-angle X-ray scattering (SAXS), which can detect periodic structures in noncrystalline materials in solutions, to observe the chromatin structures of HeLa cells in mitosis and interphase. They found that, no matter in interphase or mitosis, there was no ‘30 nm’ chromatin structure formation in cells (Joti et al., 2012). Nishino *et al.* also found that, in human mitotic HeLa chromatin, there was no regular structure >11 nm detected (Nishino et al., 2012).

Actually, the “10 nm” fiber is high dynamic because the nucleosomes are dynamic (~50 nm/30 ms). So, we think that the chromatin consists of dynamic and disordered “10 nm” fibers. The chromosome can be seen as one polymer chain and the dynamic folding can offer a driving force for chromosome condensation and segregation (Maeshima et al., 2014; Nozaki et al., 2013).

In mitosis, the chromosomes are highly compacted to facilitate the segregation of their chromatids. After cell division, the compacted chromatin is decondensed to re-establish its interphase states (Antonin and Neumann, 2016). Interphase is the phase in which cells spend most of its life, the DNA replication, transcription and most of the genome transactions take place during interphase. In next sections, I will focus on the interphase chromosome organization in space.

1.2.2 Euchromatin and heterochromatin

Electron microscopy has shown that in metazoan nucleus, there are at least two structurally distinct chromatins in the nucleus in interphase, one is euchromatin and the other is heterchromatin (Albert et al., 2012; Tooze and Davies, 1967). Euchromatin is more dynamic and uncondensed. Euchromatin is often associated with transcriptionally active regions (Adkins et al., 2004). Unlike euchromatin, heterochromatin is condensed around functional chromosome structures such as centromeres and telomeres, it is genes poor and can silence the expression of the genes embedded in it (Grewal and Moazed, 2003). Heterochromatin is largely transcriptionally inert. However, it plays key roles in chromosome inheritance, genome stability, dosage compensation (X-inactivation) in mammals (Lam et al., 2005). Solid evidence show that heterochromatin is required for the cohesion of the sister chromatids at centromeres and proper chromosome segregation (Bernard et al., 2001; Hall et al., 2003). Grewal's team also found that the formation of the heterochromatin structures at telomeres can maintain their stability (Hall et al., 2003). As for localization close to the nuclear envelope, nucleoli are often surrounded by a shell of heterochromatin which is realted to the establishment and maintenance of silencing of non-rDNA-related genomec regions (McStay and Grummt, 2008).

The chromatin state are not static (Grewal and Jia, 2007). There are many factors that can influence the chromatin structure, including chromatin associated proteins, histones, linker DNA and DNA methylation. Although many studies over the past few decades have established the basic properties of the heterochromatin and euchromatin, it is still not clear how chromatin participate the cellular processes.

1.2.3 Chromosome territory

Although the "10 nm" chromatin fibers are highly dynamic (see 1.2.1), the chromosomes are not randomly organized in the nucleus. The chromosomes "prefer" to occupy specific regions in the nucleus named "chromosome territories" (CTs). The concept of CTs was first suggested for animal cell nuclei by Carl Rabl in 1885 and the name was first introduced by Theodor Boveri in 1909 (Cremer and Cremer, 2010). The fluorescent *in situ* hybridization (FISH) techniques enabled the generation of chromosome specific painting probes used for the direct visualization of chromosomes in many species (Bolzer et al., 2005; Manuelidis, 1985; Schardin et al., 1985) (Figure 5A). Bolzer *et al.* utilized FISH to mape simultaneously all chromosomes in human interphase nuclei. The map showed that the small chromosomes were organized closer to the nuclear center and the larger chromosomes located closer to the nuclear periphery (Bolzer et al., 2005). Cremer's group combining FISH techniques and 3D-microscopy, could reconstruct the spatial arrangement of targeted DNA sequences in the nucleus. The new generation confocal microscopes allowed the distinct observation of at least five different targets at the same time (Cremer et al., 2008).

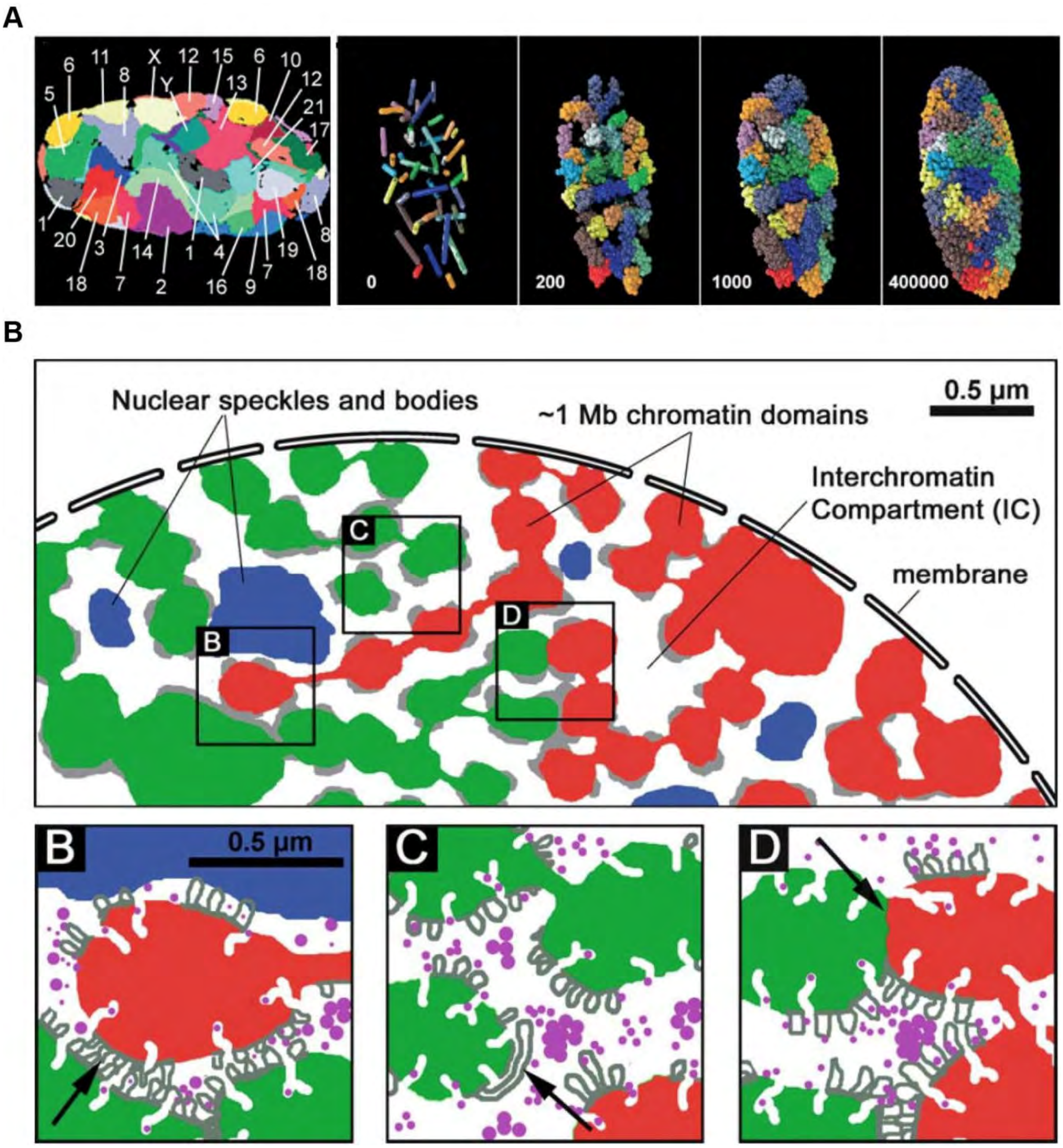

Figure 5. The chromosome territories and the chromosome territory-interchromatin compartment model.

A. 24-Color 3D FISH technologies allowed the visualization of the 46 human chromosomes in the nucleus. From (Bolzer et al., 2005).

B. Illustration of a partial interphase nucleus with differentially colored higher-ordered CTs (red and green) from neighboring CTs separated by the interchromatin compartment (IC) (white). Blue regions represent integrated IC channel network with nuclear speckles and bodies which expand between CTs. Gray regions represent perichromatin regions which locate at the periphery of the CTs. Narrow IC channels allow for the direct contact of loops from neighboring CTs (arrow, B). For the broad IC channel, the larger loop (arrow, C) expands along the perichromatin region. The arrow in D represents the direct contact between neighboring CTs. From (Albiez et al., 2006).

3D-FISH technique used to analyze the chromosome organization in different cell types, these studies indicated that the nuclear geometrical constrains influence CTs; CTs distribution also correlated with the genes density on the chromosome (Neusser et al., 2007). However, FISH cannot reveal the internal structure of the CTs and their interactions with neighboring CTs. Peter Lichter and colleagues defined the interchromatin compartment (IC) as the network-like space expanding mainly around CTs with little penetration into the CT interior (Zirbel et al., 1993). The chromosome territory-interchromatin compartment (CT-IC) model assumes that IC expands between chromatin domains both in the interior and the periphery of CT (Albiez et al., 2006) (Figure 5B).

These methods and models clearly show the arrangement of the CTs in the nucleus. However, we should note that FISH cannot be used for living cells, since cells must be fixed before hybridization with the probe (Rodriguez and Bjerling, 2013). In addition, limited by resolution, microscopy lacks the ability to highlight the sub-organization of the chromosomes inside the CTs. This limitation is addressed by the emergence of very different experimental approaches based on chromosome conformation capture (3C).

1.2.4 Chromosome conformation

1.2.4.1 The technical breakthrough of chromosome conformation capture: 3C-technologies

Over the last decade, the newly developed technique of chromosome conformation capture (3C) mapping the interactions between chromosomes, has significantly improved the observational resolution on the chromosomes organization (Dekker et al., 2002). For classical 3C techniques, cells are first treated with formaldehyde to covalently link the chromatin segments that are in close spatial proximity. Then, crosslinked chromatin is digested by a restriction enzyme and the restriction fragments are ligated together to form unique hybrid DNA molecules. Finally, the DNA is purified by standard phenol/chloroform extraction and analyzed (Dekker et al., 2002) (Figure 6A). The 3C products represent the chromatin fragments that may be separated by large genomic distances or located on different chromosomes, but are close in 3D. Classical 3C techniques measure the contact frequency of the genomic loci in close proximity within the nucleus (Dekker et al., 2013; Montavon and Duboule, 2012). Most 3C analysis typically cover only ten to several hundreds Kb (Naumova et al., 2012). Several techniques have been developed based on 3C to increase the throughput.

3C-on-Chip or circular 3C (4C) techniques allows the detection of the genome-wide interactions of one selected locus after selective amplification of this region by inverse PCR performed on the 3C products (Simonis et al., 2006; van Steensel and Dekker, 2010). 3C carbon copy (5C) techniques can identify all interactions among multiple selected loci. The specific mixture of 5C oligonucleotides is used to anneal and ligate the 3C library; this step is used to generate the 5C library. Then the 5C library is amplified by PCR for analysis (Dostie et al., 2006). Hi-C techniques, collectively named 3C-technologies provide a view of chromatin interactions map through whole genome (Belton et al., 2012; Lieberman-Aiden et al., 2009).

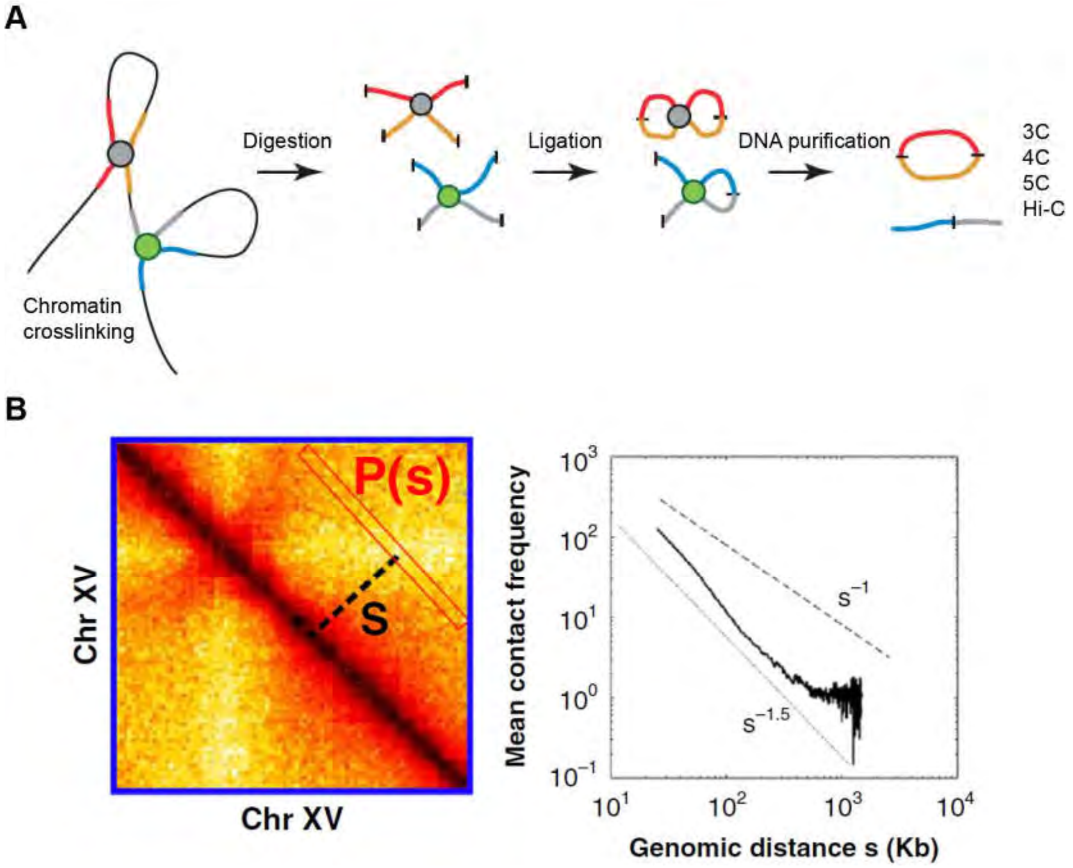

Figure 6. The outline of the chromosome conformation capture (3C) and 3C-based techniques.

A. Overview of 3C and 3C-derived techniques strategy. Crosslinked chromatin is digested with a restriction enzyme and the restriction fragments are ligated together to form unique hybrid DNA molecules. Finally the ligated DNA is purified and analyzed. From (Montavon and Duboule, 2012).

B. The analysis of the ligated DNA content produces the contact density map (left) and based on this, it is easy to correlate contact frequecy and the genomic distance (right). From (Wang et al., 2015).

3C and 3C-derived techniques allow to detect and quantify physical contacts between DNA segments (Figure 6B), yielding massive quantitative data about genome architecture at the level of large cell populations.

1.2.4.2 Chromosome conformation according chromosome conformation capture methods

These techniques can be applied to the spatial organization of entire genomes in organisms from bacteria to human (Lieberman-Aiden et al., 2009; Umbarger et al., 2011). In 2009, Lieberman-Aiden and colleagues used Hi-C to construct the contact maps of the human genome in interphase. The contact maps immediately showed some interesting features. Firstly, the contact probability between loci on one chromosome was always larger than the contact probability between loci on different chromosomes: this result confirms the existence of chromosome territories. Also, the small genes-rich chromosomes localized preferentially in the nuclear center by FISH studies, were found to interact preferentially with each other. Based on the contact frequencies, the authors suggested a ‘fractal globule’ model, a knot-free conformation that enables maximally dense packing while preserving the ability to easily fold and unfold any genomic region. This highly compact state would be formed by an unentangled polymer that would crumple into a series of small globules in a ‘beads-on-a-string’ configuration (Lieberman-Aiden et al., 2009) (Figure 7).

Further, study of the human cells chromosomes also show that long-range interactions are highly nonrandom and the same DNA fragments often interacting together (Botta et al., 2010). The longer range interactions drive the formation of compact globules along chromosomes (Sanyal et al., 2011). 5C and Hi-C maps also indicate that the mitotic chromosomes adopt a linearly-organized longitudinally compressed array of consecutive chromatin loops, these loops are irregular and would form a uniform density “melt” which is consistent with the EM and SAXS studies (Joti et al., 2012; Maeshima et al., 2010; Naumova et al., 2013).

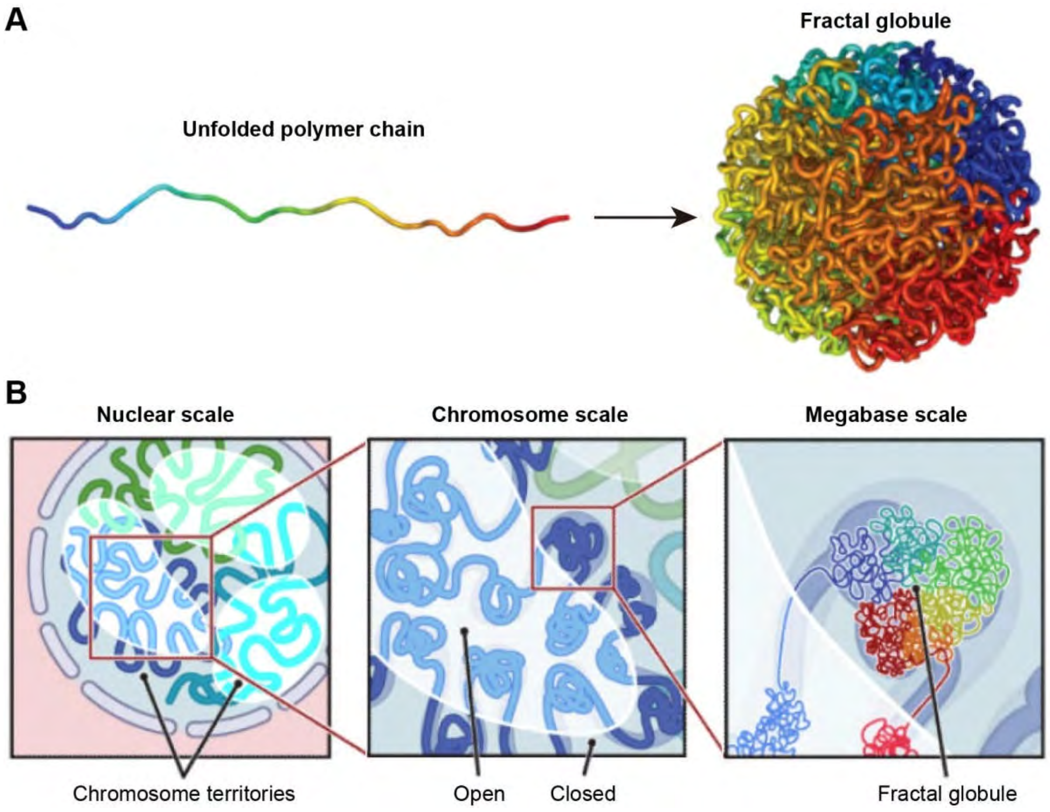

Figure 7. The "fractal globule" model of the human chromosomes. Adapted from (Lieberman-Aiden et al., 2009).

A. A fractal globule. The polymer chains are unknotted. Genomically close loci tend to remain close in 3D, leading to monochromatic blocks both on the surface and in cross-section (not shown).

B. The genome architecture of the "fractal globule" model at three scales. At nuclear scale, chromosomes (blue, cyan, green) occupy distinct territories (chromosome territories). At chromosome scale, individual chromosomes weave back-and-forth between the open and closed chromatin compartments. At the megabase scale, the chromosome consists of a series of fractal globules.

In general, the size of the genomic DNA, and the frequency of repeated DNA sequences, will impact the density of the contacts. Due to unambiguous assembly, repeated DNA sequences are excluded from the 3C analysis or should be studied independently (Cournac et al., 2016). For a similar amount of "reads", the larger the genomic DNA, the lower resolution of the contact map (Lieberman-Aiden et al., 2009). Therefore, highest resolution using 3C-technologies is achieved with small genomes and limited repeated DNA, such as the bacteria *C. Caulobacter* or the budding yeast *S. Cerevisiae* (Dekker et al., 2002; Umbarger et al., 2011). Exploration of budding yeast genome dataset might help us to understand local, specific interactions with higher resolution than data collected on the complex, repeated diploid genome of metazoan cells.

1.2.4.3 Yeast genome to explore chromosome conformation

The budding yeast *Saccharomyces cerevisiae* is an unicellular organism that can be grown in very well controlled chemical and physical conditions. *S. cerevisiae* is the first eukaryote with its entire genome sequenced (Goffeau et al., 1996). Within eucaryotic phylum, yeast belongs to the same supergroup than metazoan, the opisthokonts (Wainright et al., 1993). This classification is based on the existence of a common ancestor of fungi and animals. Note that the denomination "higher eukaryots", including two distantly related groups, multicellular plantae and metazoan, opposed to "lower eukaryots" as yeast, will not be used here. Each *S. cerevisiae* nucleus contains 16 relatively small chromosomes, comprising between 230 and 1500 kb DNA, plus ~100-200 copies of ribosomal genes (rDNA) encompassing 1-2 Mb on the chromosome XII (Figure 8). The budding yeast has played a major role in understanding the eukaryotic chromosome organization in interphase (Taddei and Gasser, 2012). Despite its small size, budding yeast has become a unique model that recaptitulates some of the main features of metazoan chromosome, and ultimately help to understand the human biology (Ostergaard et al., 2000).

In all eukaryots, chromosomes are separated from the cytoplasm by the nuclear envelope (NE). In budding yeast, NE remains closed during the entire life cycle, including mitosis. Past researches have uncovered few structural features characterizing the budding yeast nucleus in interphase: the spindle pole body (SPB), centromeres (CEN), telomeres (TEL), and the nucleolus. In interphase, the nucleolus is organized in a crescent-shaped structure adjacent to the nuclear envelope (NE) and contains quasi-exclusively genes coding ribosomal RNA (rDNA) present on the right arm of the chromosome XII. Diametrically opposed to the nucleolus, the SPB tethers the CEN during the entire cell cycle via microtubules to centromere-bound kinetochore complex (Bystricky et al., 2005a; Duan et al., 2010; Yang et al., 1989; Zimmer and Fabre, 2011). TEL are localized in clusters at the NE (Gotta et al., 1996; Klein et al., 1992). These contraints result in chromosome arms extending from CEN toward the nucleolus and periphery, defining a Rabl-like conformation (Figure 8).

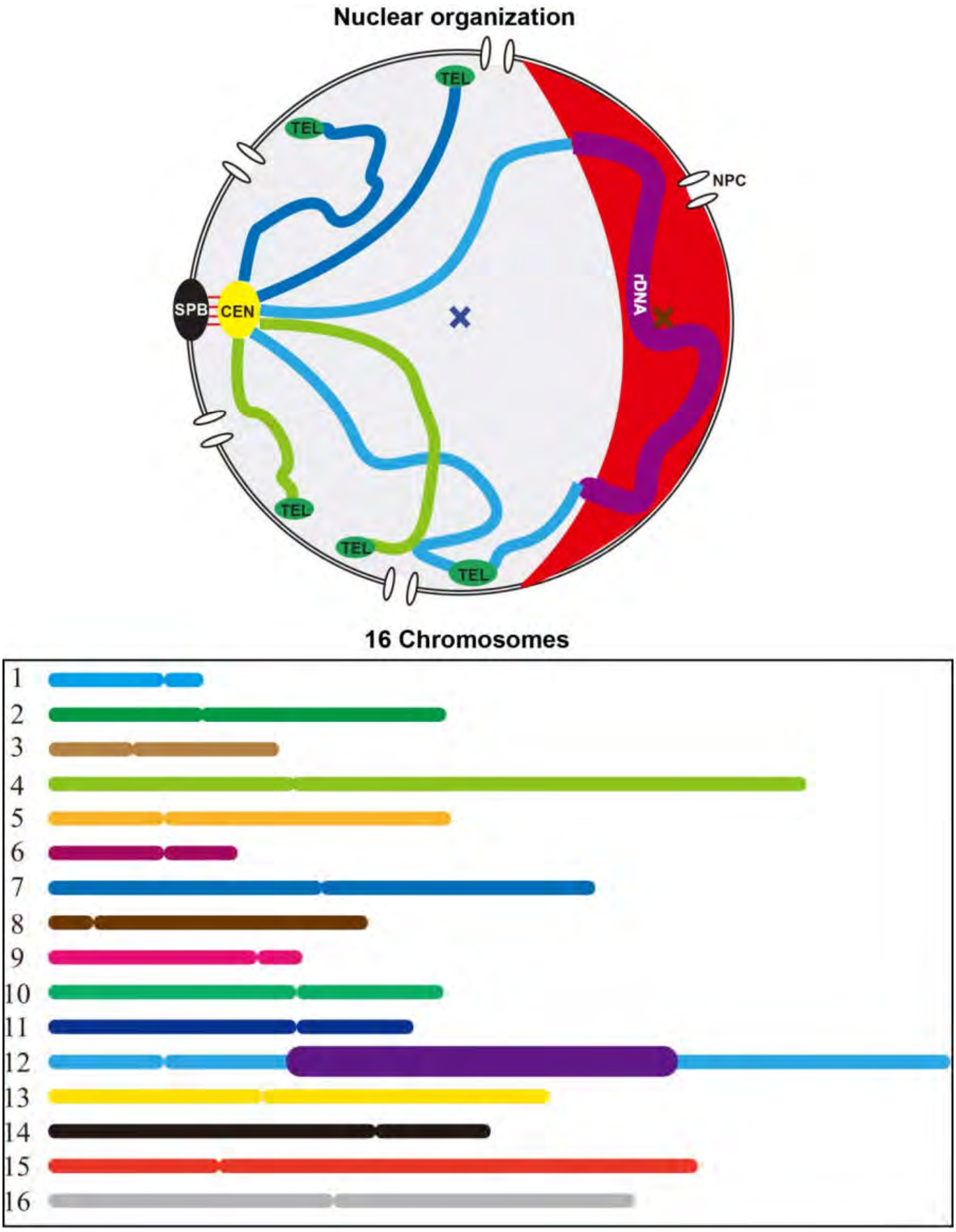

Figure 8. **Schematic representation of the yeast nucleus.** Chromosome arms are depicted in color lines and their centromeres (CEN) (yellow circle) are anchored to spindle pole body (SPB) (black circle) by microtubules (red lines). All of the telomeres (TEL) (green circle) are distributed near the nuclear envelope (NE) (double-black-line circle). The nucleolus (red crescent part) is organized around the rDNA (bold purple line). Nuclear pore complexes (NPCs) are embedded in the envelope to control the nucleo-cytoplasmic transport of molecules.

High resolution 5C contact map of budding yeast genome was obtained in 2010 by the Noble lab (Duan et al., 2010). A computational challenge raised by 3C-technology is to reconstruct spatial distances from observed contacts between genomic loci. To achieve this goal, it is required to plot the average measured contact frequencies as function of genomic distances (Figure 6B). Then the genomic distances were transformed into spatial distances by assuming a DNA compaction in chromatin of 130 bp/nm (based on 110-150 bp/nm range estimated previously) and implicitly assuming a straight fiber geometry (Bystricky et al., 2004; Duan et al., 2010). Duan *et al.* identified the intra- and inter-chromosomal interactions in yeast nucleus by combining 4C and largely parallel sequencing. The genome-wide contact frequencies were then used to reconstruct a 3D model of all 16 chromosomes in the nucleus (Figure 9A). This model reproduces the features of yeast chromosome organization (Rabl-like). In addition, this model is compatible with preferential clustering of tranfer RNA (tRNA) coding genes in the nucleus (Duan et al., 2010).

Julien Mozziconacci and co-workers also created one computationally effective algorithm to reconstruct the yeast genome organization in 3D based on the Hi-C data (the genome-wide contact map) (Lesne et al., 2014). Based on this algorithm, we could reconstruct the 3D structure of chromosomes in yeast which recapitulates known features of yeast genome organization such as strong CEN clustering, weaker TEL colocalization and the spatial segregation of long and short chromosomal arms (Figure 9B). In addition, the finding that contact frequency $P(s)$ follows a power law decrease with genomic distance s characterized by an exponent close to -1 ($P(s) \sim s^{-1.08}$) is in agreement with the crumple globule model (Wang et al., 2015).

The advances of the C-technologies can help to reconstruct the chromosome organization based on the contact frequency between chromosome segments. However, because the contact frequency is an averaged frequency of a large cell population, a single structural model is not sufficient to reflect all the spatial features of the genome. It is increasingly clear that computational model of chromatin polymer is an indispendable complement for a better understanding of chromosome organization.

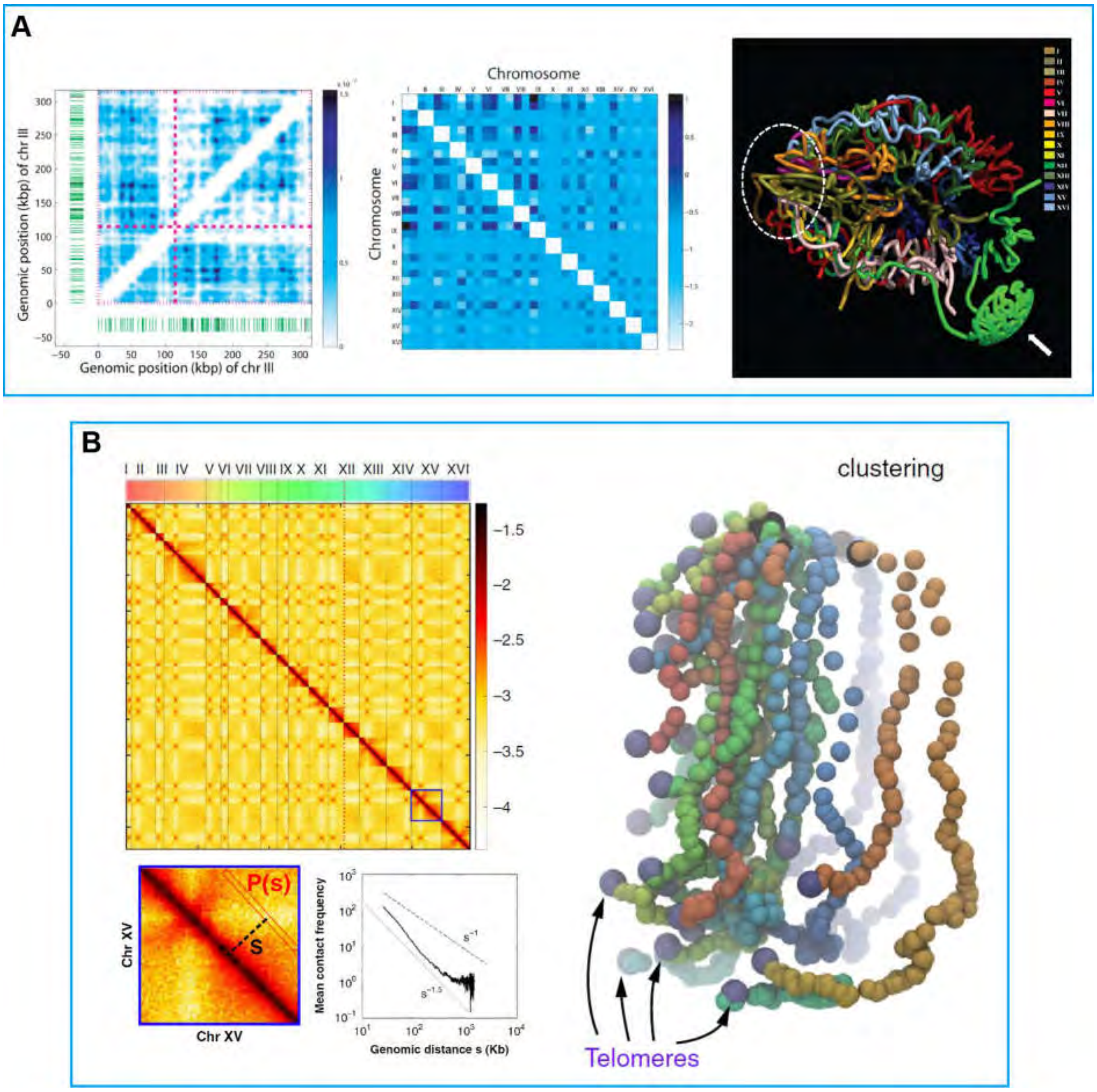

Figure 9. The chromosomes conformation in the *S. cerevisiae.*

A. Based on 5C techniques to detect the intra- (left, Chromosome III) and inter-chromosomal (middle) interactions in the yeast one can calculate the three-dimensional conformation of the yeast genome (right). From (Duan et al., 2010).

B. Hi-C insights on the structure of the *S. cerevisiae* chromosomes. Contacts map of the 16 chromosomes as obtained by Hi-C, individual chromosomes are labeled with roman numbering. Direct 3D modeling is derived from the contacts map. From (Wang et al., 2015).

1.2.5 Computational model of yeast chromosome

Since the chromosomes can be seen as long polymers, the study of chromosomes can capitalize on a large body of preexisting theoretical and computational works in statistical physics of polymers. Models based on these theories have the unique potential to offer predictive mechanistic insights into the architecture of chromosomes at a quantitative level. Several groups have recently developed independent computational models of budding yeast chromosome organization.

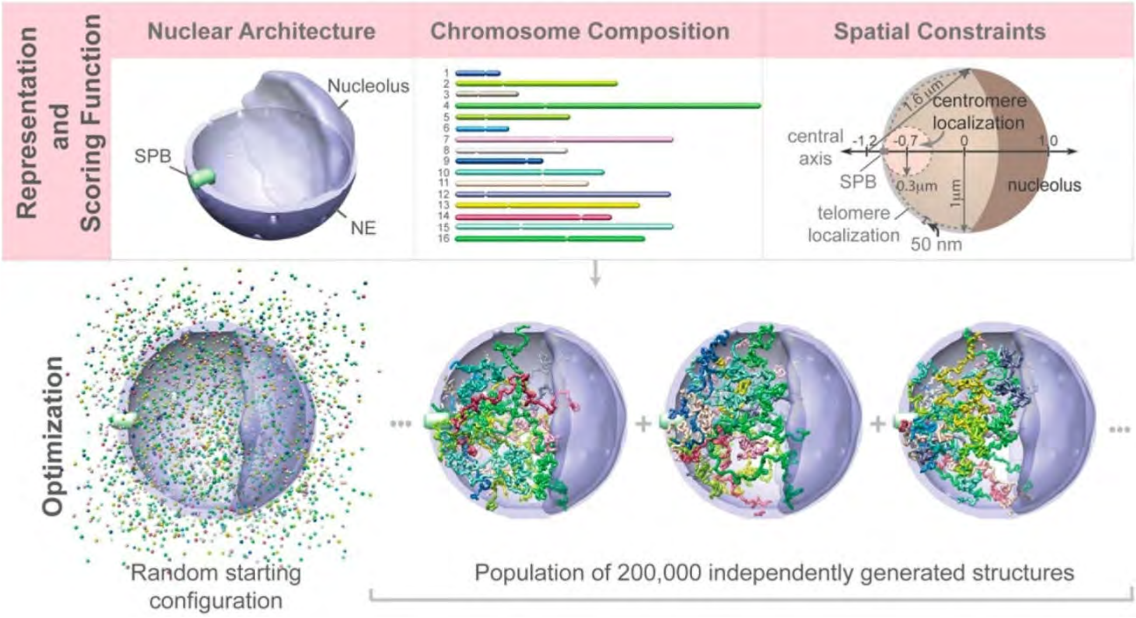

Figure 10. The statistical constrained random encounter model. From (Tjong et al., 2012).

Considering the physical tethering elements and volume exclusion effect of the genome, Tjong *et al.* introduced a constrained random encounter model (Figure 10) (Tjong et al., 2012). In this model, all chromosomes are modeled as random configurations and confined in the nucleus, all the centromeres (CEN) are attached to the spindle pole body (SPB) through microtubules, and all the telomeres (TEL) are located near the periphery. In addition, the nucleolus is inaccessible to chromosomes except for the region containing rDNA repeats. When the simulated chromatin excluded volume restraint is limited at 30 nm this model can recapitulate the contact frequency of the entire genome. Such modelisation favors the possibility of 30 nm chromatin fibers. This model simulates that the chromosome chains behave like random polymers with a persistence length between 47 and 72 nm which is consistent with experiments. Note that because of the repeated nature of rDNA genes, this model does not explore the organization of the rDNA within the nucleolus.

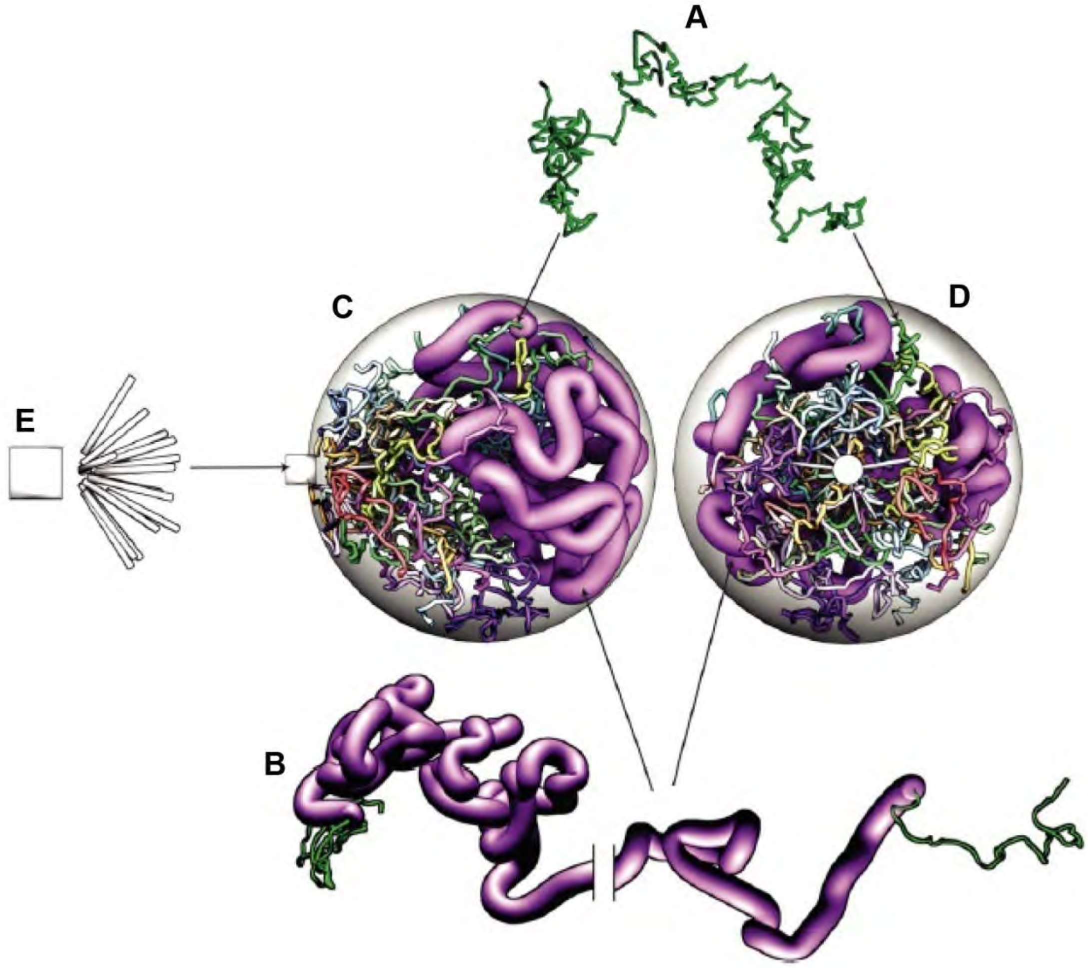

Figure 11. Computational model of the dynamic interphase yeast nucleus. From (Wong et al., 2012).

A. Each chromosome is modeled as a self-avoiding polymer with jointed rigid segments.

B. The rDNA segment on chromosome XII is modeled by thicker segments (pink) than the non-rDNA (other colors).

C, D. A snapshot of the full model from different angle of views.

E. The SPB and the 16 microtubules.

To statistically predict the positioning of any locus in the nuclear space, Wong *et al.* presented a computational model of the dynamic chromosome organization in the interphase yeast nucleus. In this model, the 16 chromosomes of haploid yeast were modeled as self-avoiding chains consisting of jointed rigid segments with a persistence length of 60 nm and a 20 nm diameter (Figure 11A). All of the chromosomes were enclosed by a 1 µm radius sphere representing the nuclear envelope (Figure 11C, D) and their motion was simulated with Brownian dynamics, while respecting topological constraints within and between chains. This model also added constraints for three specific DNA sequences: CEN, TEL and the rDNA. Each CEN was tethered by a single microtubule to the SPB (Figure 11E). All the 32 TEL were anchored to the nuclear envelope. Considering the intense transcriptional activity of the rDNA, which leads to a strong accumulation of RNA and proteins at this locus, the diameter of the rDNA segments was considered larger than the 20 nm diameter assumed elsewhere (Figure 11B). Chromosome XII which contains the rDNA segments was therefore modeled as a copolymer.

This simple model accounted for most of the differences in average contact frequencies within and between individual chromosomes. It also performed well in predicting contact features at smaller genomic scales, down to roughly 50 kbp.

To determine which forces drive the positioning and clustering of functionally related loci in yeast, Gehlen *et al.* developed a coarse grained computational model (Gehlen et al., 2012). In this model, the chromosomes were modeled as coarse grained polymer chains and numerous constraints were implemented by users. Assuming that chromatin may exists at different compacted states (euchromatin and heterochromatin), at different locations within the genome of an individual cell, this model employs two different models to represent compact (30 nm diameter) and open (10 nm diameter) chromatin fibers. Compact chromatin was modeled as 30 nm fibers with a persistence length of 200 nm. Open chromatin was modeled as 10 nm fibers with a persistence length of 30 nm. Both types of chromatin fiber were used alternatively as part of the modeling of polymer chains in which 70% of the genome was compacted. This model allows to explore putative external constraints (nuclear envelope, tethering effects, and chromosome interactions).

Contact maps generated by 3C-technologies provide without any doubt the highest resolution dataset to constrain possible simulation of genome organization *in vivo*. Computational models allow to explore forces and constraints driving the folding of the genome in interphase nucleus. However, contact maps are mostly based on population analysis of asynchronous cell culture. Moreover, the impossibility to visualize the chromatin in individual cell nuclei and the difficulties to convert contact frequency to physical distances should not be ignored. Microscope-based techniques, combined with labeling methods to detect loci position and motion offer important new perspectives for imaging genome structure. In the next part, I will present microscope-based techniques to study the spatial organization of chromosomes.

1.2.6 Gene position and gene territory

Fluorescence microscopy can fast acquire data and target molecules of interest with specific labeling strategies; therefore it has become an essential tool for biological research *in vivo* (Han et al., 2013). Thanks to the fluorescent labeling of chromosome loci in living cells, advanced imaging techniques can also provide considerable amount of data describing the spatial organization of single gene loci on chromosomes (Marshall et al., 1997). Fluorescent labeling of DNA sequences in living cells is mostly performed using fluorescent repressor-operator system (FROS) which combines the expression of a bacterial repressor fused to a fluorescent protein and the integration of an operator sequence as tandem arrays at a specific locus. A unique FROS tagged locus appears as a bright fluorescent spot in the nucleus (Loiodice et al., 2014; Meister et al., 2010) (Figure 12A).

The spatial resolution in fluorescence microscopy, 200 nm in X-Y and about 500 nm in Z-axis, is a barrier for high-resolution simultaneous detection of a large number of single molecules (Nelson and Hess, 2014). However, when single fluorescent molecules are spatially separated by more than the resolution limit of fluorescent microscopy, localization of their mass centers is only limited by signal-to-noise ratio. Such high precision of localization can be achieved by fitting pixel intensities spatially with the characteristic Gaussian distribution of fluorescence around local maxima. Therefore detection of the centroid of individual fluorescent molecules allows tracking the target with a resolution not limited by the diffraction of light (Thompson et al., 2002).

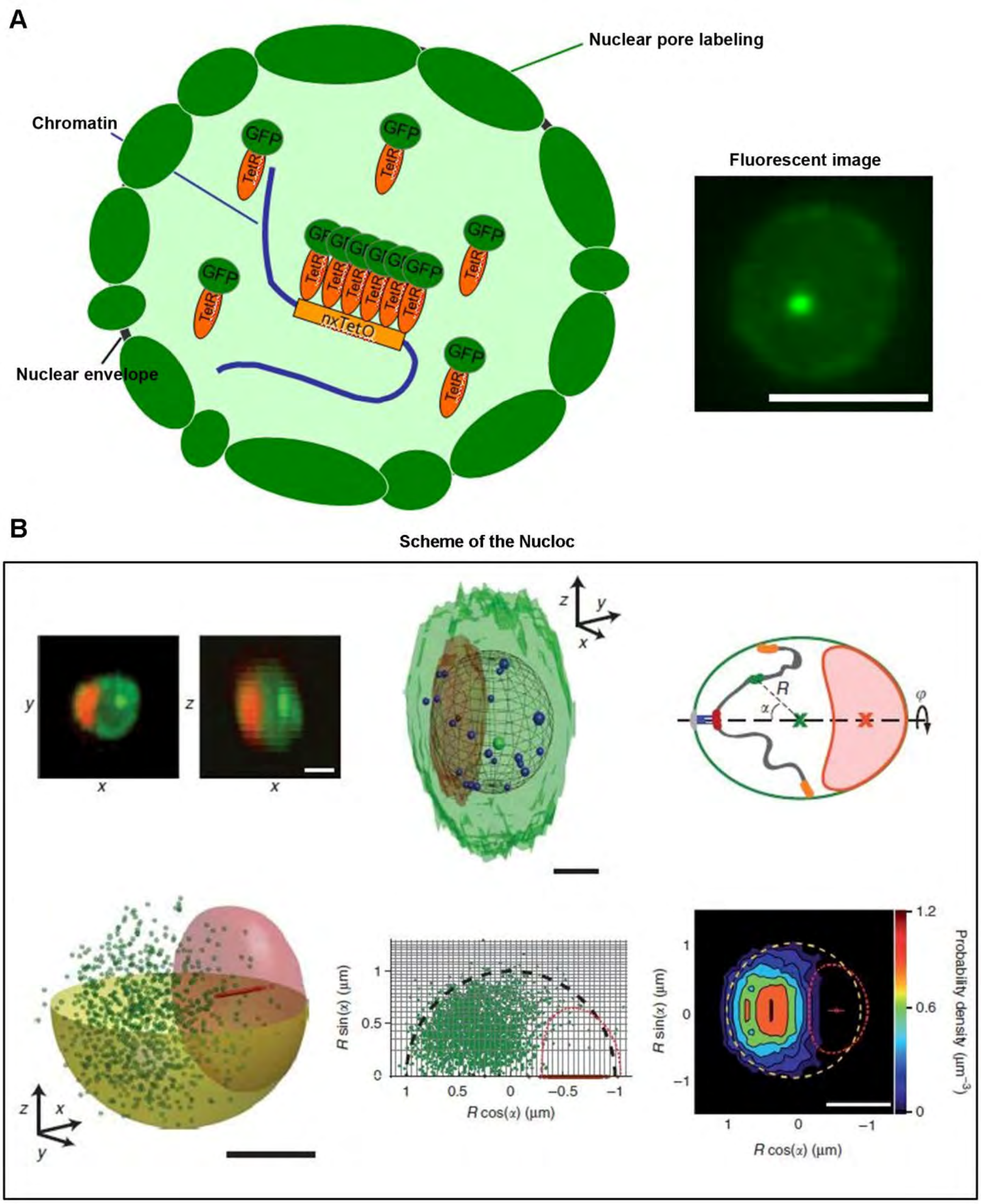

Figure 12. Nucloc to study the gene position.

A. The fluorescent repressor-operator system (FROS). Scale bar, 2 µm.

B. The yeast locus and the nuclear pores labeled in green and the nucleolus labeled in red. Nucloc can automatically detect the locations of a locus (green sphere), nuclear pores (blue spheres), nucleolar centroid (red sphere) and an estimated nuclear envelope. It enables to define a cylindrical coordinates system with an oriented axis in which we describe the position of the locus by its distance from the nuclear center (R) and the angle from the axis nuclear-nucleolar centroid (α). The angle φ is defined by the angle around this axis, and is independent of the distances between the locus and the nuclear or nucleolar centroids. Nucloc uses nuclear center as the first landmark and translates all nuclear centers to the origin, and then rotated them around the origin so that nucleolar centroids (secondary landmark) became aligned on the X-axis. Then in these coordinates, the locus positions were rotated around the central axis and into a single plane ($\varphi=0$; cylindrical projection) without loss of information. From this 2D distribution of points, we could estimate the probability densities that are color coded on a genemap. Scale bars, 1 μm. Adapted from (Berger et al., 2008).

To analyze the spatial localization of a given locus in the yeast nucleus, Berger and colleagues created 'Nucloc' algorithm in which each cell nucleus of a population, determines the three dimensional position of a locus relative to the nuclear envelope, and the nuclear and nucleolar centers as landmarks (Berger et al., 2008). Automated detection allows high-throughput analysis of a large number of cells (>1000) automatically. The 'Nucloc' algorithm can create a high-resolution (30 nm) probability density map of subnuclear domains occupied by individual loci in a population of cells, thereby defining the domain in the nucleus in which a locus is confined: the 'gene territory' (Figure 12B) (Berger et al., 2008).

The genemap of specific loci, as well as 3C-techniques, can recover yeast chromosome organization in space compatible with their known features. The chromosome XII in budding yeast carries the ribosomal DNA (rDNA) confined in the nucleolus. Our group's previous work analyzed 15 loci (12 non-rDNA loci and 3 rDNA loci) along chromosome XII by 'Nucloc'. By comparing the maps, we could observe that loci around the CEN are attached to the SPB, at an opposite position of the nucleolus, the rDNA genes are clustered in the nucleolus, the TEL, are anchored to the NE. All these features are in agreement with the Rabl-like configuration and the recent computational models (Figure 13) (Albert et al., 2013; Duan et al., 2010; Tjong et al., 2012; Wong et al., 2012). We also assessed whether chromosome XII folding could be predicted by nuclear models based on polymer physics (Wong et al., 2012). The results showed that the measured median distance of loci on chromosome XII to the nuclear and nucleolar centers are compatible well with the model predictions (Figure 14 A,B) (Wong et al., 2012). However, we also should note that the fit to the model prediction was poorer for genomic positions 450-1050 kb, from the nucleolus to the right TEL (Figure 14 A, B).

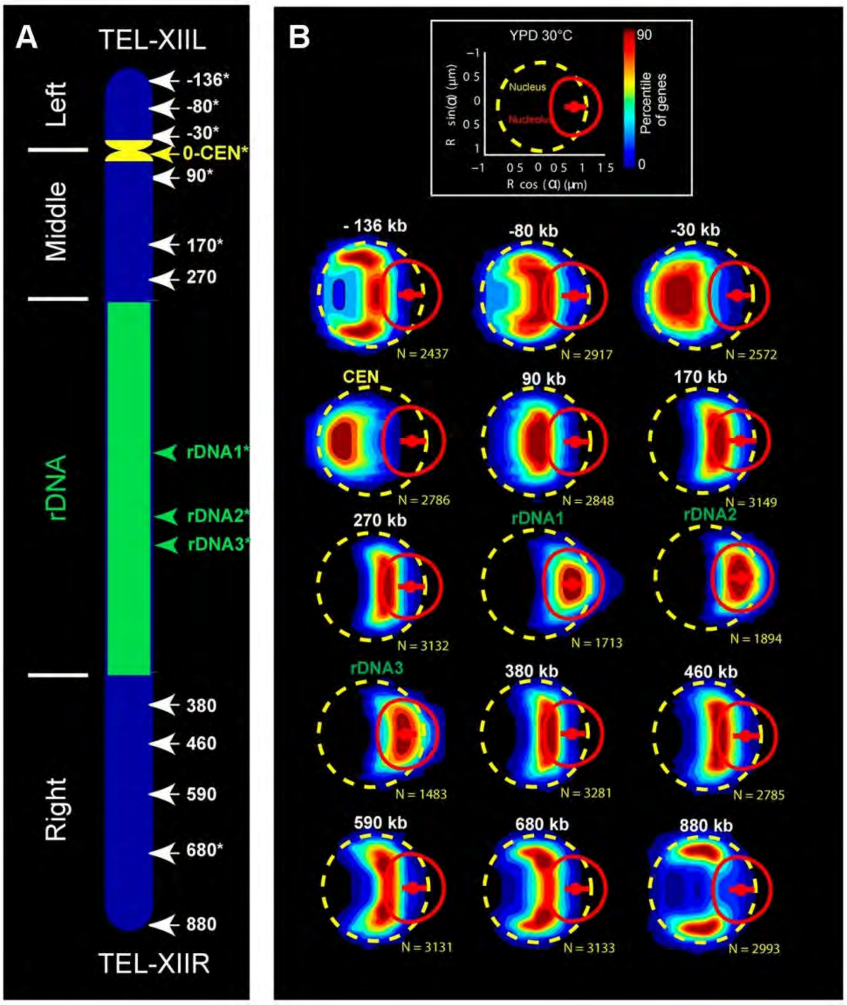

Figure 13. The gene territories of 15 loci along chromosome XII.

A. 15 FROS labeled loci along the chromosome XII.

B. Spatial distributions of each locus. The dashed yellow circle, the red circle, and the small red dot depict the median NE, the median nucleolus and the median location of the nucleolar center, respectively. From (Albert et al., 2013).

The gene territories can be remodeled during transcriptional activation. Based on this, we could study the gene motion during transcriptional activation. In glucose, the *GAL1* gene is repressed and the gene positions indicate that the *GAL1* gene concentrates in an intranuclear domain close to the nuclear center, whereas in galactose, *GAL1* is actively transcribed and frequently re-localized to the nuclear periphery. This is consistent with the model where the on/off states of transcription correspond to two locations (Berger et al., 2008; Cabal et al., 2006). Recently, imaging entire chromosome II revealed global shift to nuclear periphery in different physiological conditions modifying the yeast transcriptome (Dultz et al., 2016). Peripheral recruitment of chromosome arms strongly argues for transcription-dependent anchoring point along a chromosome (Tjong et al., 2012). Therefore, tethering sites organizing chromosomes locally remain to be identified (Dultz et al., 2016).

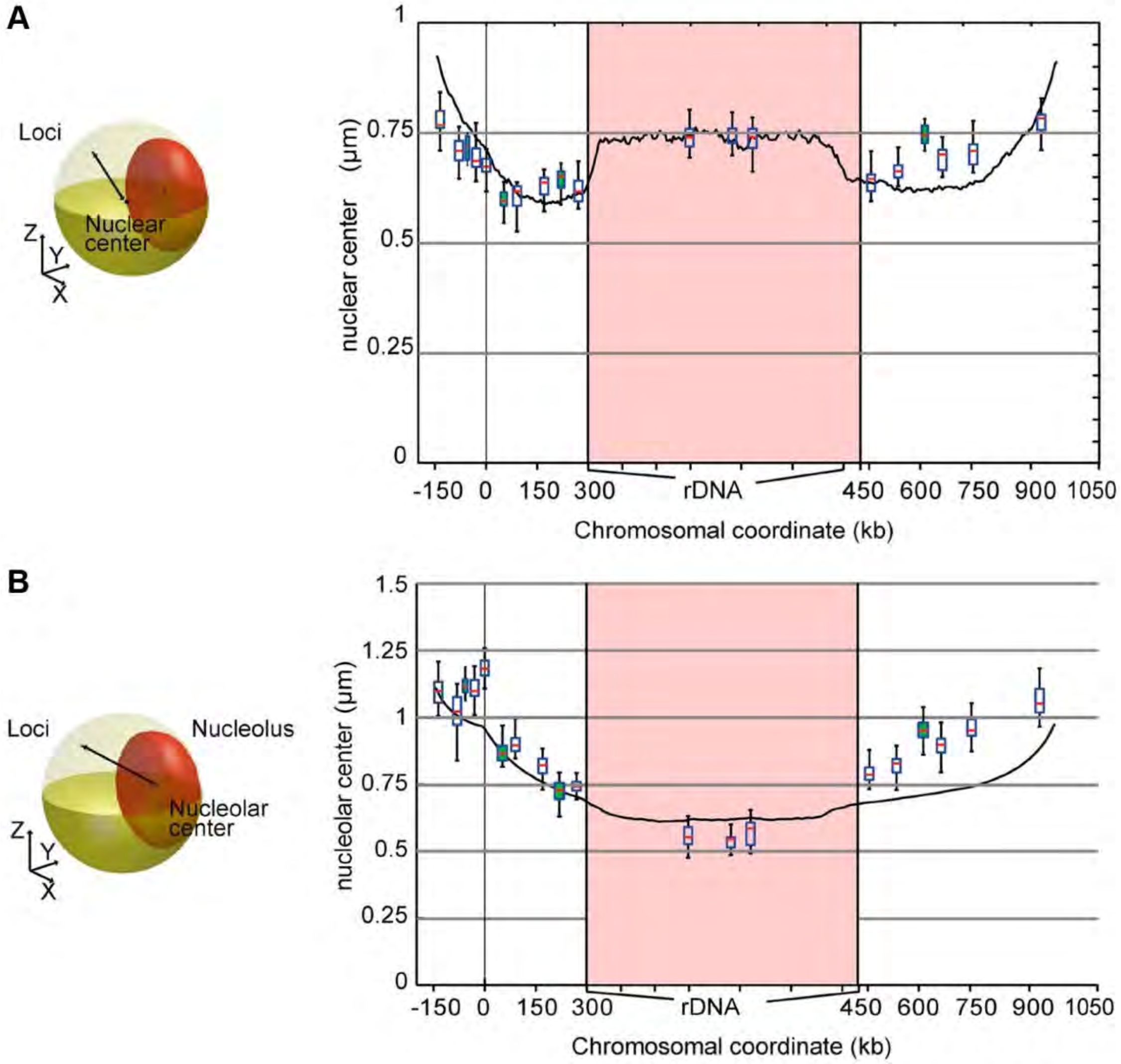

Figure 14. Positions of loci along the chromosome XII relative to the nuclear and nucleolar centers determined experimentally and predicted by computational modeling. From (Albert et al., 2013).

A, B. The distance of the locus to the nuclear center (**A**) and to the nucleolar center (**B**) is plotted versus its genomic position. Yellow and red ellipsoids represent the nuclear envelope and the nucleolus, respectively. The median distance experimentally measured is shown with box plots. The median distance of chromosome XII loci to the nuclear center and to the centroid of the rDNA segments from a computational model of chromosome XII is shown with solid black lines.

Existing computational models are not sufficient to reveal all the features of the chromosome organization. Visualization by microscopy of the genomic loci positioning can be compared with prediction of computational model. However, our goal is not a description, but a physical understanding of the genomic folding process. We now need to understand the physical properties of the chromosome, which can be more directly using tracking of chromatin dynamics.

1.2.7 Chromatin dynamics

The chromatin can be seen as a complex polymer, consisting of a DNA chain and associated proteins. However, because of the complicated nuclear organization, study of chromatin dynamics is still a major biological challenge (Amitai and Holcman, 2013). The gene motion reflects the local biophysical properties of the chromatin. In this part, I will introduce the study of chromatin motion in living cells.

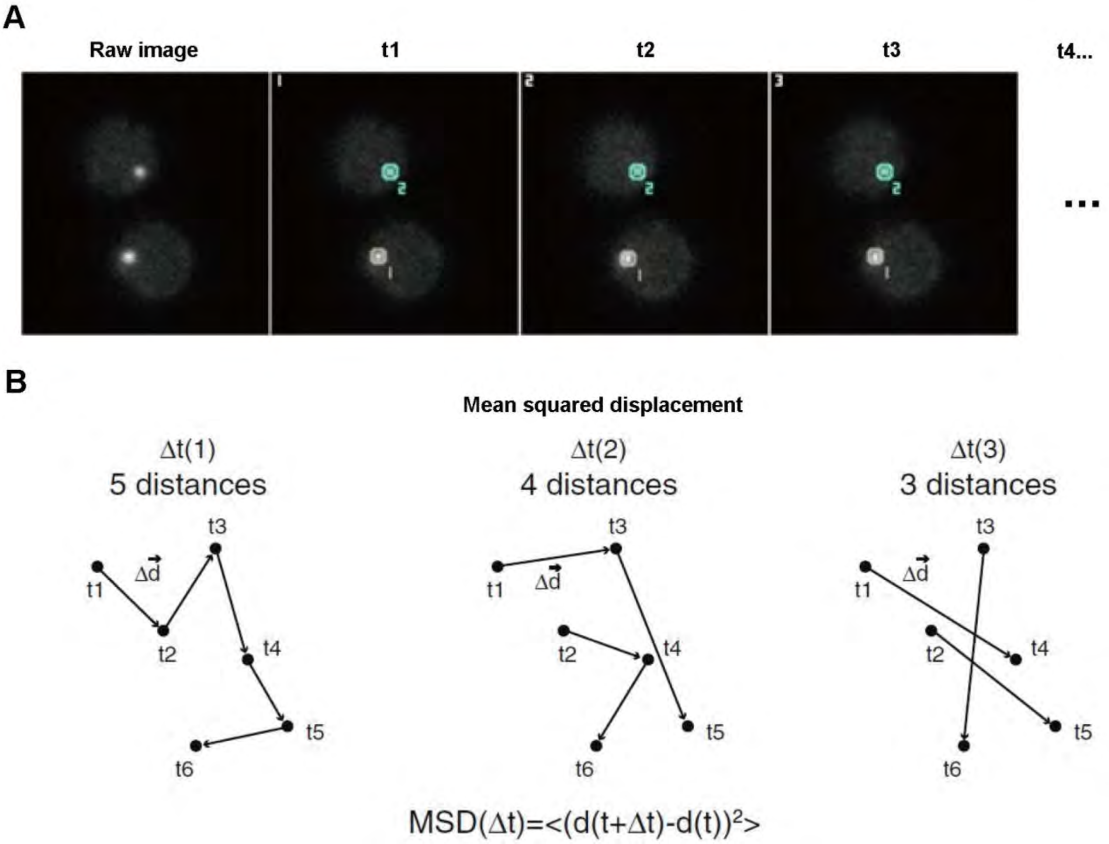

Figure 15. Tracking the gene motion in living cells.

A. Based on the time-lapse fluorescent microscopy and advanced image analysis the position of the labeled loci can be detected (t1, t2, t3…).

B. Mean square displacement (MSD) calculation and interpretation. From (Albert et al., 2012).

In a previous section (see section 1.2.6), we introduced the use of the FROS to track the position of single loci. By combining time-lapse fluorescent microscopy and advanced image analysis the motion of genes labeled by FROS can be quantified (Hajjoul et al., 2013) (Figure 15A). The mean squared displacement (MSD) (Figure 15B) is the most common readout to analyze the motion of a fluorescent locus. The MSD is the average distance traveled by a locus after a given time lag. It provides a statistical response for trajectories driven by Brownian noise. .

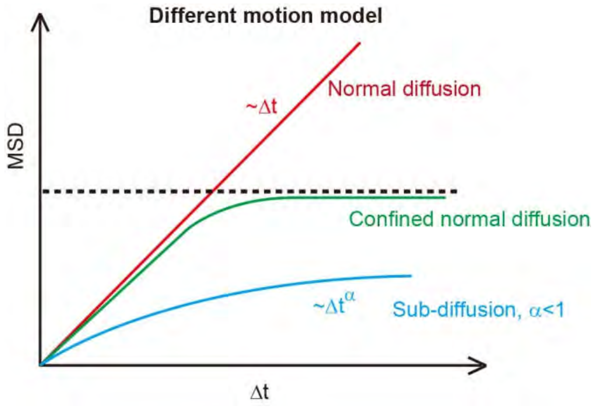

Figure 16. The MSD of three different diffusion models.

The motion of one target can be recapitulated with three models: normal diffusion, sub-diffusion and super-diffusion depending on the temporal power law dependence of the MSD response. Here, I will focus on two main models: normal diffusion model and sub-diffusion model, meaning that power-law of MSD is characterized by an exponent of 1 or lower than 1, respectively (Figure 16) (Gal et al., 2013).

1.2.7.1 Normal diffusion and confined normal diffusion

Ideally, isolated objects, influenced only by thermal fluctuations, can follow the normal diffusion principle. However, there is increasing evidence that the motion of chromatin in interphase nucleus is not approximated accurately using normal diffusion model because the chromosomes are confined in the nucleus by nucleus envelope (NE). When combining fluorescent microscopy and single-particle tracking techniques to analyze the motion of the chromatin in interphase with large time scale (~ 10 min), the researchers suggested that the chromatin segments can move freely within limited subregions of the nucleus (Marshall et al., 1997).

Heun *et al.* used the same method to analyze the chromatin dynamics in yeast interphase nucleus at different cell cycle stages. In G1 phase, the chromatin can move fast in an energy-dependent fashion. In S phase, its rapid movement is constrained through a mechanism dependent on active DNA replication. In addition, the telomeres and centromeres also confine the movement of the labeled loci in both G1 and S phases (Heun et al., 2001).

1.2.7.2 Sub-diffusion motion

With the improvement of the microscope and detection techniques, the limitation due to poor signal to noise ratio (SNR) is overcome, so accurate tracking of the position of fluorescent labeled loci is achieved. In 2006, Cabal and co-worker found a different behaviour than random movement at short time scale (< 90 s). The anomalous diffusion of the *GAL1* fitted well with a sub-diffusion model with a power $\alpha \approx 0.4$-0.5. This kind of motion was observed in medium with glucose or galactose. In galactose, *GAL genes* are activated, no matter the locus in the center or at the periphery of the nucleus; they both follow the same motion model (Cabal et al., 2006). In 2009, Hajjoul *et al.* utilized a novel Lab-on-Chip technology to track the 3D motion of *HM* and *MAT* loci. The motion of *HM* locus confirmed the sub-diffusion model. Although the *MAT* locus moved with sub-diffusion in the nuclear center region, it moved with normal diffusion after 200 ms at the nuclear periphery (Hajjoul et al., 2009).

Weber *et al.* analyzed the chromosome loci motion in live bacterial cells: the chromatin moved sub-diffusively with exponent ~0.4. The authors proposed that this model arises from relaxation of the Rouse model and the motion of the chromosomal loci are most consistent with fractional Langevin motion which rules out the random diffusion model (Weber et al., 2010).

1.2.7.3 Rouse polymer model

Numerous properties can account for sub-diffusion motion. We propose one suitable model in order to allow a quantitative understanding of how chromosomes organize in space.

The chromatin can be seen as a sequence of generic monomers. In the case of polymer loci, elastic interactions between neighboring monomers and long-range hydrodynamic interactions associated to solvent flux must be considered when the surrounding environment is diluted polymers solution (Teraoka and Cifra, 2002). Actually, in budding yeast, all of the 16 chromosomes are space filling in the nucleus, but in addition, many substances are dissolved in the nucleoplasm. So the nucleus can be seen as a highly concentration environment. Therefore the long-range hydrodynamic interactions associated to solvent flux can be neglected. As the ideal simple polymer model, Rouse model, assumes that the polymer chain is composed of beads connected by harmonic springs (Figure 17A). We could use Rouse model to study the chromosome organization. We will present novel experimental data fully compatible with this polymer model.

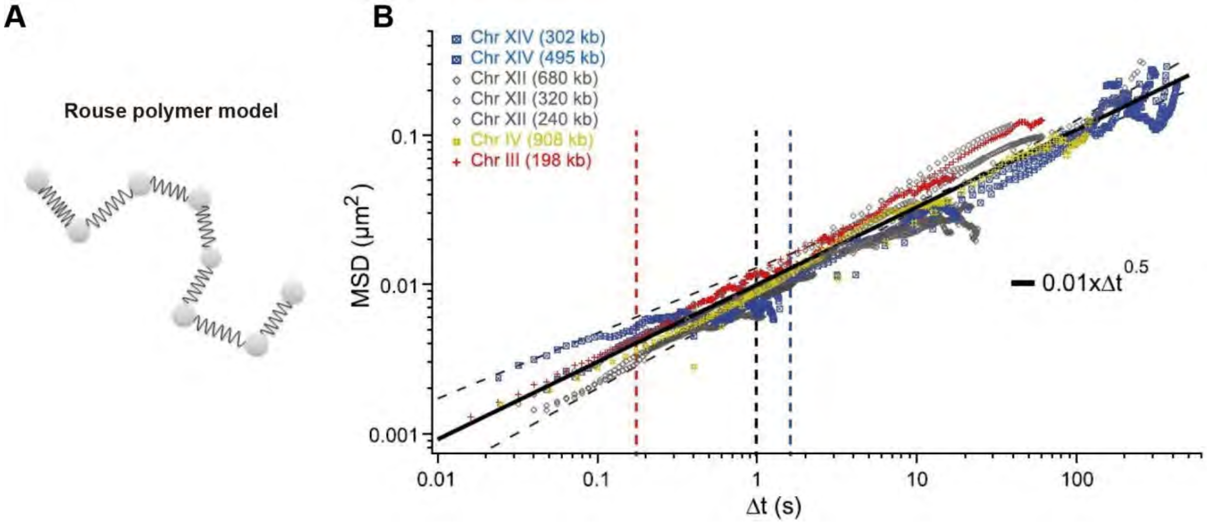

Figure 17. The Rouse polymer model.

A. The Rouse polymer model assumes that the polymer behaves as homogeneous series of beads connected by elastic springs. There is no volume exclusion in ideal Rouse polymer.

B. The budding yeast chromatin dynamics can be well fitted by Rouse model with exponent ~0.5. From (Hajjoul et al., 2013).

Hajjoul *et al.* analyzed the motion of nine fluorescently labeled chromosome loci on chromosome III, IV, XII and XIV in budding yeast cell nuclei over an extended temporal range spanning more than four orders of magnitude (10^{-2}-10^{3} s). The results showed that the motion is characterized by sub-diffusive behavior and in agreement with the Rouse polymer model, the exponent of the power-law is ~0.5, which assumes that chromatin fiber behaves as homogeneous series of beads connected by elastic springs (Figure 17B). The Rouse regime is characteristic of polymers in crowded environments and is associated with compact exploration, implying that chromosome loci efficiently search for the nearby targets, which is consistent with the contact frequency results. The analysis of the amplitude of fluctuations by the Rouse model shows that the persistence length of chromatin in living yeast is ~5 nm which is very short compared to the dimensions of a single nucleosome. If taking volume exclusion between monomers into account, the correct persistence length of chromatin is ~3 nm which is comparable to the DNA diameter. All of these data indicate that the chromatin in yeast is highly flexible (Hajjoul et al., 2013). However, the very low persistence length measured, inconsistent with known features of chromatin, motivated an improved modelisation of chromatin *in vivo* (see the "Results" section).

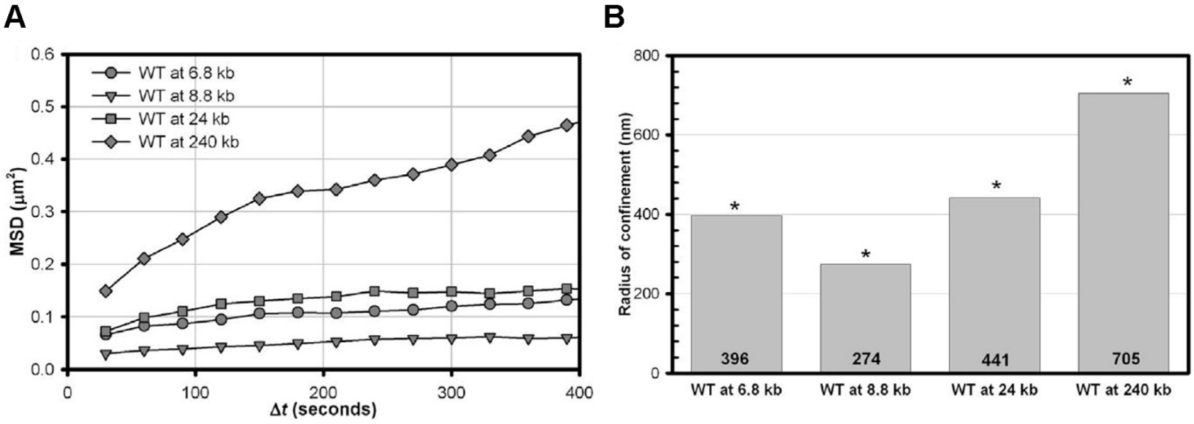

Figure 18. The chromatin dynamics and confinements vary along the length of the chromosome. From (Verdaasdonk et al., 2013).

A. The motion of WT chromatin loci at different distances from the CEN.

B. The confinement radius of WT chromatin loci at different distance from the CEN.

CEN are clustered and attached to the SPB via microtubules, TEL are localized near the NE. Known attachment to the NE of TEL, and microtubules dependent anchoring of CEN modify their local properties. We know that the CEN and TEL are at the opposite poles of the chromosome arms. These physical tethering will also influence the chromatin dynamics and organization (Bystricky et al., 2005; Duan et al., 2010; Tjong et al., 2012). Kerry Bloom's lab quantified the motion and confinement of the loci along the length of the chromosomes. They found that because of the tethering of the CEN, loci motion varies along the length of the chromosome (Figure 18). Detachment of loci from the tethering elements (CEN or TEL) increased the chromatin dynamics. They proposed a confined bead-spring chain tethered at both ends model: the chromosome can be seen as one confined Rouse chain tethered by CEN and TEL. Based on this model, reducing the nucleosomes density by depleting H3 would result in reduced persistence length (from 50 nm to 25 nm), which is consistent with the one experimentally observed (Kim et al., 2013; Verdaasdonk et al., 2013).

Albert and colleagues provided a detailed analysis of the dynamics of the budding yeast's chromosome XII. They detected the motion of 15 loci along the entire Chr XII: 12 were non-rDNA loci and 3 were rDNA sequences. They tracked the loci motion at different time intervals, 0.19s, 0.36s, 1s, 1.5s and 10s. The data indicated that the non-rDNA loci motions well fitted with the Rouse model with exponent of 0.5±0.07 even for the loci around the CEN and TEL. The movements of rDNA were slow compared with the non-rDNA loci and its motion did not fit with the Rouse model, maybe because it is constrained in the nucleolus. (Albert et al., 2013).

A recent publication however challenged the relevance of the Rouse model by monitoring the motion in 3D of the *GAL* gene and control loci in the 0.5-5 s time domain (Backlund et al., 2014). The authors employed the dual-color 3D Double-Helix Point Spread Function (DH-PSF) microscopy to study the *GAL* locus dynamics. They indeed showed that the exponent of sub-diffusion was ~ 0.7, which is apparently not compatible with the Rouse regime. They suggested that this discrepancy was caused by the time scale they used, which was too short for the loci to sense their subnuclear confinement. The authors suggested that fractional Brownian motion (fBm) could account for this scaling exponent, though the underlying physics accounting for this behavior remains unclear. Another possibility is that the Rouse model remains valid and that the initial unexpected exponent is explained by the size of the labeled DNA detected by microscopy (see "Results" 1.2) (Wang et al., 2015).

Furthermore, Judith Miné-Hattab and co-workers used ultra-fast microscopy and improved the analysis of chromatin dynamics in living *S. cerevisiae*. They found that the chromatin dynamics followed the sub-diffusion regime (the time scales range from 10 ms to few mins), and based on the MSD analysis of their results, we could easily found that the motion chromatin dynamics consitent with the Rouse model (Mine-Hattab et al., 2016).

In summary, motion addresses the local biophysical properties of the chromatin, while position gives information about confinement and long-range nuclear organization (Huet et al., 2014). Proper polymer model can help us to understand the chromosome organization. The Rouse polymer model has been proposed to be useful to explore biophysical properties of budding yeast chromosome (Albert et al., 2013; Hajjoul et al., 2013). However, the predictive value of this model in living cells remains to be fully explored.

1.3 Summary

With development of techniques, it is possible to study chromosome organization with high-resolution and high accuracy. 3C and 3C-derived techniques collectively called 3C-technologies, can map the contacts between chromosome loci at different resolution scales allowing the exploration of the conformation of chromosomes (Duan et al., 2010; Lesne et al., 2014). Computational models accurately recapitulating contact matrix data are also consistent with chromosome organization. However, most 3C-technologies are intrinsically averaging methods and cannot assess individual cell nuclei. Individual contact maps are now starting to be developed (Nagano et al., 2013). Further, the difficulties to convert contact frequencies to physical distances should not be ignored. FROS and fluorescent microscopy allow to detect and visualize the position of specific loci on the chromosome (Berger et al., 2008). FROS combines fast time-lapse imaging techniques allowes to track the motion of specific loci, and appears a reliable method to explore the physical properties of the chromosome (Hajjoul et al., 2013; Marshall et al., 1997; Saxton, 1994). Suitable polymer models can help to understand the physical properties of the chromosome. The past two decades research on the chromatin dynamics have revealed the Rouse model as the best simple model to recapitulate the physical properties of the chromosome (Table 1). So, in the first part of this my PhD project, I studied the chromatin dynamics with the Rouse model. We should also note that chromosomes are all space-filling in the nucleus and the nuclear organization and nuclear shape has significant impact on the chromosome organization; therefore I was also interested in the study of the nuclear shape and size. (see part 2).

Table 1. The study of chromatin dynamics.

Study	MSD response	Interpretation
Marshall et al. 1997	1	Confined random motion
Cabal et al. 2006	0.4-0.5	Sub-diffusion
Hajjoul et al. 2009	0.52	Sub- diffusion
Weber et al. 2010	0.4	Fractional Langevin motion
Hajjoul et al. 2013	~0.5	Rouse model
Verdaasdonk et al. 2013		Double-tethered Rouse model
Albert et al. 2013	0.5±0.07	Rouse model
Backlund et al. 2014	0.7	Fractional Brownian motion
Wang et al. 2015	0.7 and 0.5	Two regimes of Rouse model

2. Nuclear shape and size

In budding yeast, the chromosomes are ‘space filling polymers’. The chromosome organization in space has significant links with the nuclear shape and organization. The nuclear shape and size vary along cell cycle and are different in different cell types; they are likely to have an important impact on nuclear and chromosome organization. Therefore, it is important to be able to determine the nuclear shape and size accurately to further explore the relations between the nuclear geometry and the chromosomes organization. In this section, I will focus on the study of the nuclear shape and size in budding yeast.

2.1 The nuclear organization

As described before (see section 1.2.4.3), there are few structural features characterizing the budding yeast nucleus in interphase: the spindle pole body (SPB), centromeres (CEN), telomeres (TEL), and the nucleolus. In addition, unlike mammalian cells nucleus, there is no nuclear lamina on the interior of the NE. Nuclear pore complexes (NPCs) are embedded in the nuclear envelope to form channels that regulate the transport of macromolecules (Grandi et al., 1995). The alteration of the nuclear organization will impact the chromosome organization.

2.1.1 The spindle pole body

Microtubules (MTs) are tubular polymers composed of two proteins, α- and β-tubulin, which are very important in a great number of cellular processes. The number, length, distribution and polarity of MTs are largely controlled by microtubule-organizing centers (MTOCs). Electron microscopy (EM) visualized two structures as important MTOCs, the centrosome in human cells and the SPB in yeast. Studies have shown that in both centrosome and SPB, γ-tubulin was considered to be the main microtubule “nucleator” (Luders and Stearns, 2007).

In budding yeast, SPB as the MTOC anchors the nuclear and the cytoplasmic MTs (Winey and Byers, 1993) (Figure 19A). The SPB is a cylindrical organelle that contains three plaques: an outer plaque that faces the cytoplasm and is associated with cytoplasmic MTs, an inner plaque that faces the nucleoplasm and is associated with nuclear MTs and a central plaque that spans the nuclear envelope (Jaspersen and Winey, 2004). The cytoplasmic MTs are important for the nuclear positioning in the cell. The nuclear MTs are essential for SPB and chromosomes segregation (Knop et al., 1999).

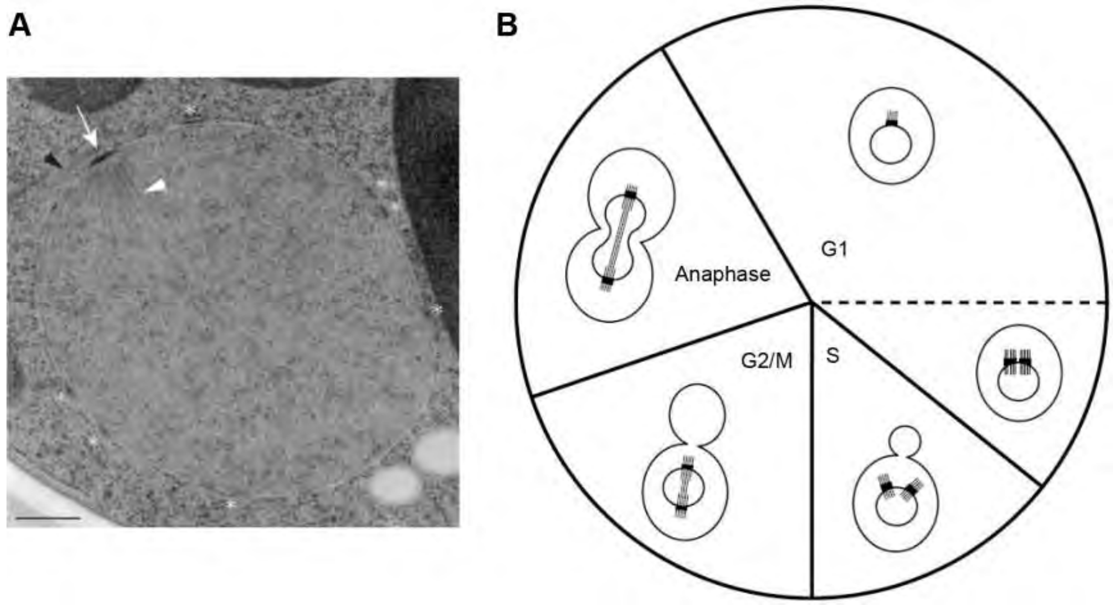

Figure 19. The structure and organization of the spindle pole body (SPB).

A. Electron micrography of a budding yeast nucleus. SPB is embedded in the nuclear envelope (white arrow) and NPCs are represented by asterisks. The white and black arrowheads represent the nuclear and cytoplasmic microtubules respectively. Scale bar, 0.2 µm. From (Jaspersen and Ghosh, 2012).

B. The organization of the SPB along the cell cycle. Adapted from (Winey and O'Toole, 2001).

The SPB is dynamic and plays a key role in the cell division. In G1 phase, there is a single SPB with nuclear and cytoplasmic MTs and the SPB positioned opposite to the nucleolus (Figure 19A). The attachement of the CEN to the SPB contributes to the Rabl-like configuration of chromosomes. At the end of G1 phase, the SPB starts to duplicate. After the bud formation, the nucleus enters S phase, SPBs separate and the old SPB is segregated to the bud and the new SPB stays in the mother’s nucleus; the microtubules between the two separated SPBs form a bipolar mitotic spindle (Yoder et al., 2003). During mitosis, the spindle elongates with the nucleus and enters the bud. At anaphase, the task of the spindle is to ensure that the chromatids correctly distribute into the mother’s and daughter’s nuclei after division (McIntosh and O'Toole, 1999; Osborne et al., 1994) (Figure 19B). SPB duplication must be controled because reduplication of SPB can result in the formation of a multipolar spindle and lead to chromosomes mis-segregation (Simmons Kovacs et al., 2008). Segregation of the replicated genome during cell division requires the chromosomes CEN to link with the SPB through MTs. This process is critical, because incorrect attachments lead to mitotic errors that result in genomic instabilities (Bertalan et al., 2014; Cheeseman and Desai, 2008).

As the two complexes directly embedded into the NE throughout the cell cycle, SPB and NPCs, also have some links. Niepel *et al.* found that Mlp2p, a nuclear pore-associated protein, binds directly to the core components of the SPB and its deletion will directly impact the cell division (Niepel et al., 2005). SPB structure is not static and it is remodeled in two ways: by growth, in which new components are added, and by exchange, in which old components are replaced by new components. Greenland and co-workers found that the nucleoporine Nup60 is required for SPB growth during cell cycle (Greenland et al., 2010). In addition, our results also show that the NPCs are concentrated around SPB (see "Results" part).

2.1.2 Telomeres are distributed at the nuclear periphery

The chromosomes in *S. cerevisiae* are tethered by CEN and TEL. TEL are portion of the DNA that localized at the chromosomes ends and maintain the genome stability (Louis, 1995; Zakian, 1996). The distribution of the TEL will also impact the chromosomes organization in the nuclear compartment.

There is evidence that TEL cluster at the nuclear periphery; the 32 telomeres of the 16 yeast chromosomes are detected in fluorescent microscopy as 3 to 6 foci (Gotta et al., 1996). Proteins at the nuclear periphery and on the inner nuclear membrane (INM) contribute to this tethering. The anchoring of the TEL to the nuclear periphery requires at least two nuclear envelope proteins, Mps3 and Esc1 (Kupiec, 2014). Mps3 localized on the INM and is necessary for TEL association to the nuclear pheriphery during S phase (Bupp et al., 2007). Mps3 is a SUN-domains protein (Jaspersen et al., 2006). An emerging theme shows that SUN-domain proteins, which are integral membrane proteins of the inner nuclear membrane, bind to the KASH-domain proteins located at the outer nuclear membrane. Outer nuclear membrane KASH domain proteins and inner nuclear membrane SUN domain proteins interact to form the core of the LINC complex and connect nucleus to the cytoskeleton (Sosa et al., 2012). Esc1, localized on the INM, binds to Sir4 and Yku80 which are two components required for the TEL association with nuclear perphery (Gotta et al., 1996; Taddei et al., 2004). Researchers also found that the deletion of the genes encoding yKu70p or its partner yKu80p altered the positioning of telomeric DNA in the yeast nucleus (Laroche et al., 1998).

INM proteins are organizing interactions between chromatin and NE. The change of the nuclear shape and size will influence the structure of the nuclear periphery which impacts the localization of the TEL.

2.1.3 Nucleolus-the "ribosomes factory"

The nucleoli are specific nuclear domains present in all eukaryotic cells. In budding yeast, the nucleolus, a membraneless nuclear subdomain where rDNA clusters, is confined in one domain occupying about one-third of the nuclear volume as a crescent-shaped structure (Melese and Xue, 1995; Thiry and Lafontaine, 2005) (Figure 20A). The nucleolus consists of three sub-structures defined on the basis of their ultrastructural morphology: the fibrillar centers (FCs), the dense fibrillar component (DFC) and the granular component (GC). The FCs are roundish structures composed by thin and loosely distributed fibrils, the DFC is constitued of tightly packed fibrils which surround and are associated to the FCs and extend as a network in the nucleolar volume, the GC is composed of granules with a diameter of 15-20 nm and fill the rest of the nucleolar volume (Figure 20A). FCs and DFC altogether are so embedded in the GC. The position where the rDNA transcription occurs is still debated: some experiments indicate that rDNA transcription occurs in the FC and some researchers found that it likely occurs at the border between the FCs and DFC (Raska et al., 2004; Thiry et al., 2000; Trumtel et al., 2000). In the DFC, the pre-rRNA accumulate and their maturation leads to the formation of 18S, 5.8S and 28S rRNA, components of the mature ribosomes (Raska et al., 2004). Late processing of pre-rRNA occurs in GC where preribosomal subunits assemble (Grob and McStay, 2014; Wang et al., 2013).

The three nucleolar subdomains in human cells were also described in the yeast nucleus (Albert et al., 2012; Leger-Silvestre et al., 1999). However, another model of the budding yeast nucleolus containing only two compartments, a network of fibrillar strands (F) and granules (G), was proposed (Thiry and Lafontaine, 2005) (Figure 20B). As there is only one fibrillar component in which rRNA synthesis takes place, the F compartment has features of both FCs and DFC. According to this model, the F compartment specialized into FCs and DFC during the evolution. In bipartite nucleoli, the size of the rDNA transcription unit is larger or similar compared to the size of the intergenic spacers. In species containing tripartite nucleoli, the intergenic regions are always much larger than the transcription units (Hernandez-Verdun et al., 2010; Thiry and Lafontaine, 2005).

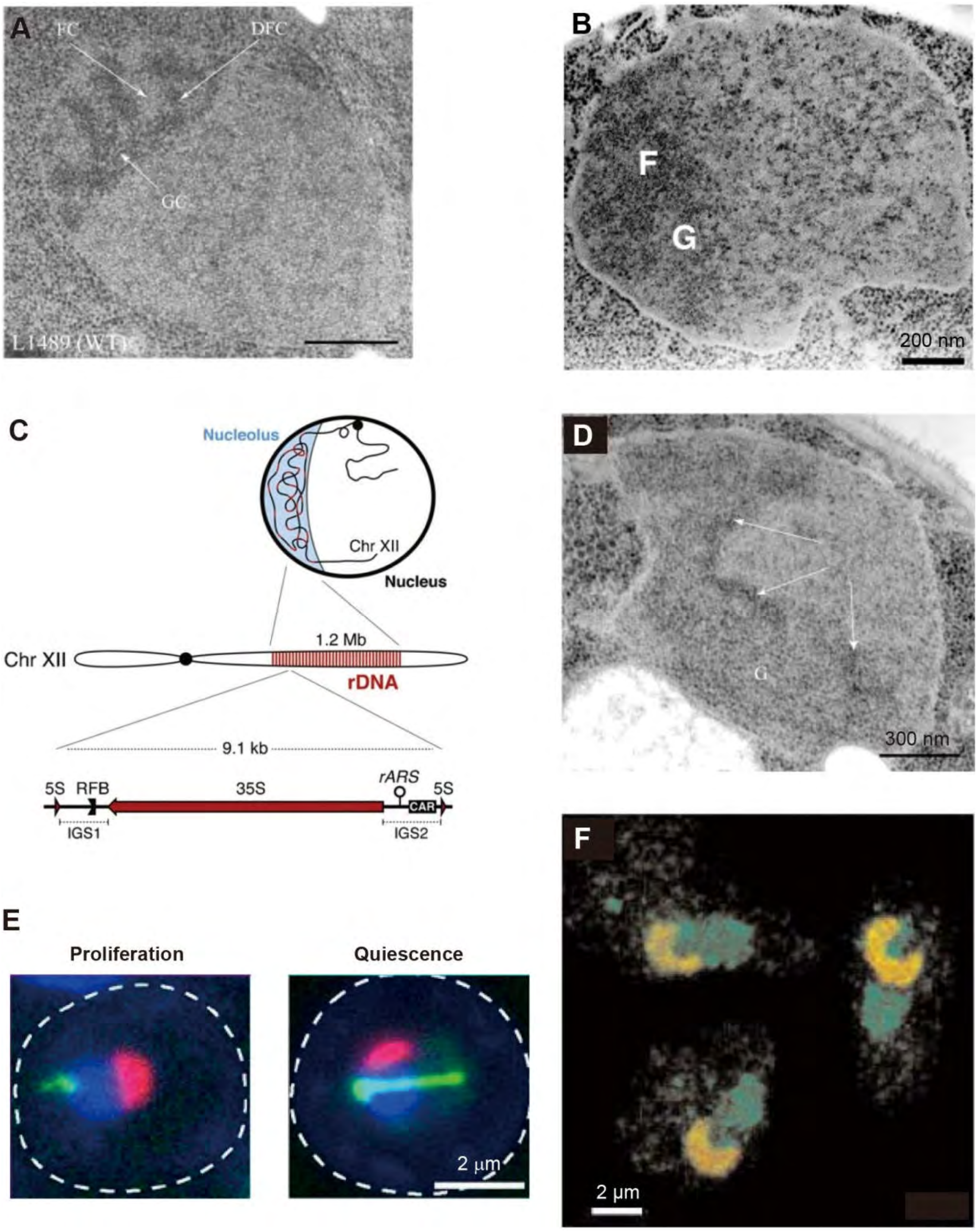

Figure 20. The nucleolar organization.

A. Transmission electron micrography of the yeast nucleus. The nucleolus is tripartite. From (Albert et al., 2012).

B. A wild-type yeast nucleolus with fibrillar strands and granules. From (Hernandez-Verdun et al., 2010).

C. The organization of the rDNA in the nucleolus. From (Eckert-Boulet and Lisby, 2009).

D. The mutant L1494 (rdnΔ, pRDN-wt) nuclear structure. From (Trumtel et al., 2000).

E. The nucleolar structure in proliferation and quiescent cells. The nucleololus was labeled with red color, the microtubules array was labeled with green color. From (Laporte et al., 2013).

F. The nucleolar structure of MATa cells (LPY2686) after treatment with α factor. Cells are stained with affinity purified antibodies against Sir3p (green) to identify the telomeres and against Nop1p (red) to identify the nucleolus. From (Stone et al., 2000).

Growing cells require continuous rRNA synthesis to ensure that subsequent generations contain the ribosome supply necessary for protein synthesis. Historically, the nucleolus was considered as a "ribosome factory": ribosomes biogenesis is a process that includes transcribing the rDNA, processing the pre-rRNA transcripts and assembling the pre-rRNA with ribosomal proteins (McStay and Grummt, 2008; Melese and Xue, 1995). The budding yeast has 100-200 rDNA units tandemly located on chromosome XII, each unit of rDNA contains two rRNA genes, 35S and 5S, and two intergenic spacers (IGS1 and IGS2) that promote repeats integrity (Eckert-Boulet and Lisby, 2009; Mekhail et al., 2008) (Figure 21C). Only half of the rDNA copies are actively transcribed in *S. cerevisiae* (Dammann et al., 1993). It has been proved that the nucleolar protein complex RENT (regulator of nucleolar silencing and telophase exit), composed of Cdc14, Net1, Sir2 and Nan1, is linked to the ability to induce rDNA silencing (Cockell and Gasser, 1999). In addition, Fob1 gene is located on the chromosome IV. Fob1p can associate with the replication fork barrier (RFB), thereby inhibiting the replication (Kobayashi, 2003; Kobayashi and Horiuchi, 1996).

The efficiency of rDNA transcription plays an important role in the nucleolar morphology. The wild type yeast strains in interphase display a unique crescent shaped nucleolus close to the nuclear envelope and occupying one-third of the nucleus (Figure 20A). Trumtel and co-workers deleted most of the rDNA repeats and replaced them by an equivalent number of plasmids bearing a single rDNA repeat: the efficiency of rDNA transcription in this strain is lower than in wild type. In this mutant, the nucleolar morphology is significantly changed and the nucleolus almost occupies half of the nucleus and spread along the NE (R. et al., 1997; Trumtel et al., 2000) (Figure 20D).

Stress conditions also can influence the nucleolar structure. In quiescent cells, the structure and the position of the nucleolus are changed (Laporte et al., 2013) (Figure 20E). α factor, a mating pheromone, also triggers major changes in gene expression and cellular architecture that are necessary for the mating process. Stone and colleagues found that, when one uses α factor to block the MATa strains into G1 phase, the nucleolus lost its crescent shape and became bigger (Stone et al., 2000) (Figure 20F). Note that for different cell types, cell cycle stages and culture conditions, the nucleolus also has different shape and size (Dundr et al., 2000; Leung and Lamond, 2003).

The nucleolus plays a key role in the genome organization. The nucleolus excludes other genetic loci from the region it occupies. Decrease of the nucleolar volume results in the decrease of the confinement of the nucleoplasm (Therizols et al., 2010). Therefore, genome structure and the nucleolar organization are intimately connected, and we are just starting to explore those relationships.

2.1.4 Nuclear pore complexes

In metazoan cells, the NE consists of a double membrane, nuclear pore complexes (NPCs) and the lamina. The nuclear lamina is a proteinaceous layer found at the interface between chromatin and the inner nuclear membrane (INM). Nuclear lamins from the group of the intermediate filaments of cytoskeleton were initially identified as the exclusively components of the lamina. However, experimental evidence indicates that the nuclear lamins are also found in the nucleoplasm. The nuclear lamina plays a key role in the NE assembly, including the membranes and NPCs. In addition, the lamins and lamin-associated proteins are also involved in DNA replication, transcription and apoptosis (Goldman et al., 2002; Lopez-Soler et al., 2001; Stuurman et al., 1998).

There is no nuclear lamina in the budding yeast nuclei, and the large multiprotein structures known as the NPCs penetrate the NE (D'Angelo and Hetzer, 2008). The NPCs are embedded in the NE along entire cell cycle, and in budding yeast, each nucleus contains 65~182 NPCs distributed over the whole NE. So NPCs are good landmarks to determine the yeast nuclear shape and size (Berger et al., 2008). NPCs are the central complex that controls the “communication” between the nucleoplasm and the cytoplasm. Small molecules, such as water, ions and sugars, can freely diffuse through the NPCs. However, proteins and RNAs are highly selective to transport (Corbett and Silver, 1997; Wente and Rout, 2010). The NPC is an eightfold-symmetrical structure comprising a NE-embedded scaffold that surrounds a central transport channel and two rings – the cytoplasmic and nuclear rings – to which eight filaments are attached. Whereas the cytoplasmic filaments have loose ends, the nuclear filaments are joined in a distal ring, forming a structure known as the “nuclear basket” (D'Angelo and Hetzer, 2008; Ryan and Wente, 2000) (Figure 21A).

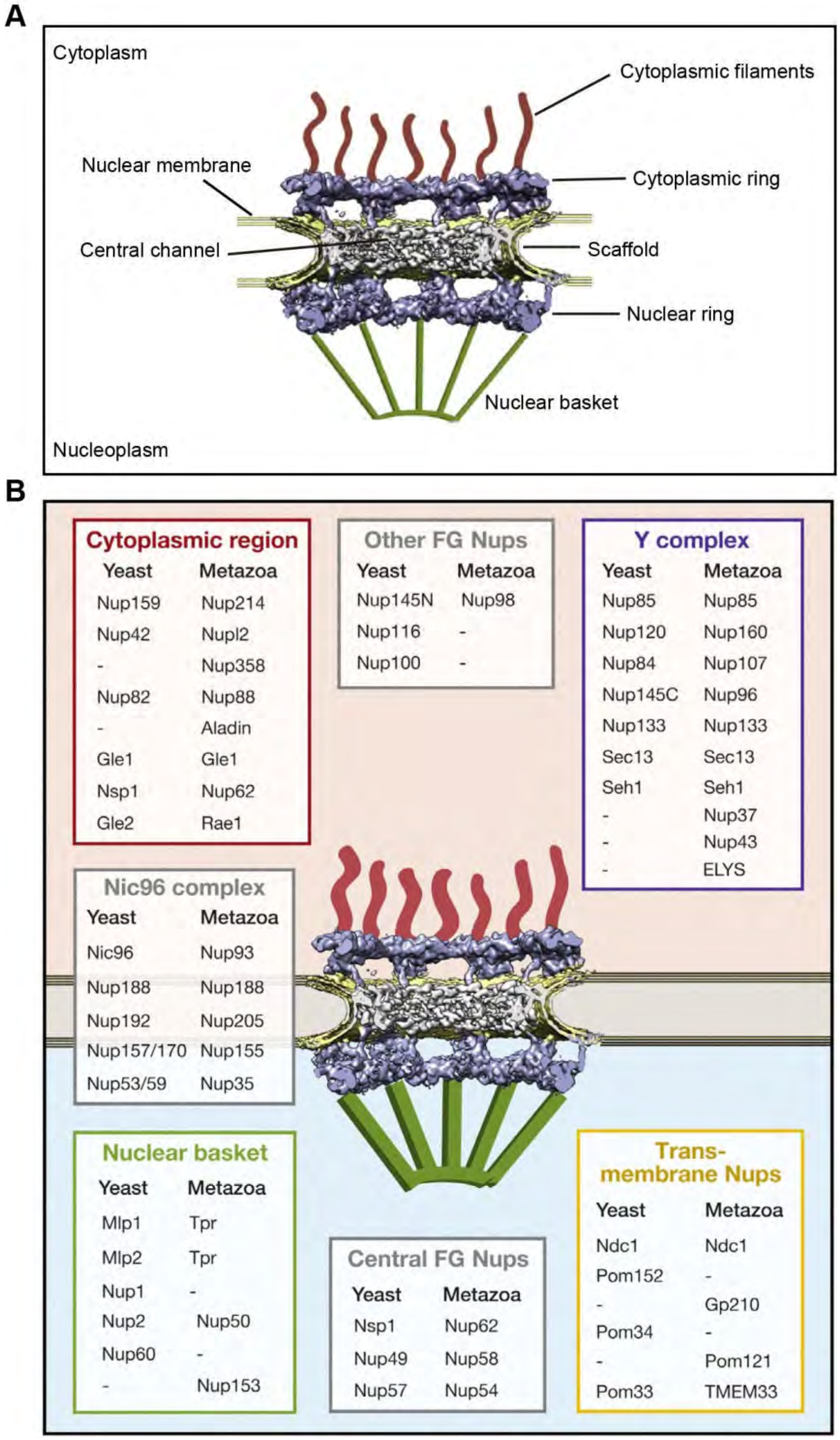

Cytoplasmic region

Yeast	Metazoa
Nup159	Nup214
Nup42	Nupl2
-	Nup358
Nup82	Nup88
-	Aladin
Gle1	Gle1
Nsp1	Nup62
Gle2	Rae1

Other FG Nups

Yeast	Metazoa
Nup145N	Nup98
Nup116	-
Nup100	-

Y complex

Yeast	Metazoa
Nup85	Nup85
Nup120	Nup160
Nup84	Nup107
Nup145C	Nup96
Nup133	Nup133
Sec13	Sec13
Seh1	Seh1
-	Nup37
-	Nup43
-	ELYS

Nic96 complex

Yeast	Metazoa
Nic96	Nup93
Nup188	Nup188
Nup192	Nup205
Nup157/170	Nup155
Nup53/59	Nup35

Nuclear basket

Yeast	Metazoa
Mlp1	Tpr
Mlp2	Tpr
Nup1	-
Nup2	Nup50
Nup60	-
-	Nup153

Central FG Nups

Yeast	Metazoa
Nsp1	Nup62
Nup49	Nup58
Nup57	Nup54

Trans-membrane Nups

Yeast	Metazoa
Ndc1	Ndc1
Pom152	-
-	Gp210
Pom34	-
-	Pom121
Pom33	TMEM33

Figure 21. Overall structure of Nuclear Pore Complex (NPC).

A. Overview of a NPC. The NPC embedded in the double membrane surrounding the nucleus of eukaryotic cells. Adapted from (Schwartz, 2016).

B. The position of the nucleoporins in the NPC. Nucleoporins from yeast and metazoan are listed and color-matched according to their approximate positions within the NPC. From (Knockenhauer and Schwartz, 2016).

The substructures of NPC are comprised of ~30 subunits, termed as nucleoporins (Nups) (Figure 21B). Most Nups are symmetrically distributed on the nuclear and cytoplasmic faces. However, a small number of Nups appear to be biased to one side of the NPCs rather than present on both faces. Nup1p, Nup2p and Nup60p localize only to the distal nucleoplasmic face of the NPC and likely form the nuclear basket. Nup159p, Nup42p and Nup82p are found only on the cytoplasmic face (Dilworth et al., 2001; Rout et al., 2000). With the improvement of the technology, the study of Nups organization in the budding yeast is facilitated, and the measurement of radial distance of two Nups in the NPC is possible; typically, distance between Nup159p and Nup1p is ~45 nm (Alber et al., 2007).

The yeast *S. cerevisiae* lacks lamins, but NPCs and INM proteins have been proposed to play a role in chromatin organization (Taddei and Gasser, 2006). Actually, the NPCs components, Nups, are connected to the chromosomes and regulate the expression of certain genes (Ishii et al., 2002; Takagi and Imamoto, 2014). Casolari's research revealed that most Nups preferentially associate with a subset of highly transcribed genes. They also showed that transcriptional activation of *GAL* genes results in their association with the Nups (Casolari et al., 2004). The research of Cabal *et al.* also showed that after their activation, the *GAL* genes relocated to the nuclear periphery (Cabal et al., 2006). Recent researches also proved that the release of *Ulp1*, a peripheral NPC protein, increases the kinetics of *GAL1* de-repression; the *Ulp1* modulates the sumoylation state of *Tup1* and *Ssn6*, two regulators of glucose-repressed genes (Bonnet et al., 2015; Jani et al., 2014; Texari et al., 2013). Some other genes, such as *HXK1*, *INO1*, *TSA2*, *HSP104*, *SUC2* and *MFA2*, also were proved recruited to the nuclear periphery from the nucleoplasm upon their transcriptional activation (Brickner and Walter, 2004; Burns and Wente, 2014; Taddei et al., 2006).

Therefore, the NPC is not only the gate to control the transport of the molecules between nucleoplasm and cytoplasm, but also participates in regulation of genes expression.

2.2 Plasticity of nuclear envelope and nuclear size

In budding yeast, alterations of the nuclear shape and size have important impact on the nuclear and chromosome organizations. In fact, the nuclear shape and size *in vivo* are dynamic.

Along the cell cycle, the nucleus adopts different morphologies and sizes. In G1/S phase, the nucleus is often described as a sphere; this structure is clearly established when yeast are growing in rich medium containing glucose (Figure 22A). Yeh *et al.* examined the nucleus with high-resolution using differential interference contrast (DIC) microscopy. The results indicate that the nucleus is more or less spherical (Yeh et al., 1995).After sample-preserving fixation, such as high-pressure cryo-fixation followed by cryo-substitution, Transmission Electron Microscopy (TEM) analysis of ultra-thin (60-80 nm) sections of entire cells showed a smooth double membrane envelope with circular or ellipsoidal contours. When performed on ultra-thin serial sections of an entire nucleus, TEM became directly informative of the nuclear shape and size in 3D. This technique also showed that the yeast nucleus in interphase undergoes a two-fold increase in volume from G1 to S phase (Winey et al., 1997). Jorgensen *et al.* confirmed this initial measurement and they also found that the size of the nucleus increases with the cells growth: the nuclear volume is proportional with the cell volume, with the nuclear size ~7% of the cell size (Jorgensen et al., 2007). The "Nucloc" program created by Berger *et al.* to analyze the "genes territories" in the nucleus can fit the NE based on the detection of labeled NPC (see part 1.2.6); the results of this approach showed that the median budding yeast nucleus in interphase can be approximated as a sphere of ~1µm radius.The budding yeast undergoes "closed mitosis", where the nuclear envelope remains intact throughout the cell cycle. Due to a closed mitosis and the bud-neck constriction, the nucleus adopts a characteristic hourglass shape in G2/M phase. Koning and Wright also observed heart-shaped nucleus in mitosis (Koning et al., 1993). The division process is asymmetric: the division results in the mother cell's nucleus being one half larger than the daughter cell's nucleus (Heun et al., 2001) (Figure 22A). After cell division, the nucleus resumed its usually spherical shape.

The carbon source has significant impact on the nuclear growth and size (Jorgensen et al., 2007). Electron microsocpy (EM) revealed that there is a significant decrease (~17%) in the nuclear size when cells were cultured from glucose to raffinose. Galactose just decreases the nuclear size a little compare with glucose. When the carbon source was replaced by ethanol, cell growth was strongly impaired and the nucleus appeared much smaller; so the researchers also use ethanol to arrest the nucleus into G1 (Jorgensen et al., 2007). After carbon source exhaustion, the cells enter quiescence. It was shown that for short time starvation, the nucleus just became smaller; for long time starvation, the nucleus lost its sphericity (Laporte et al., 2013).

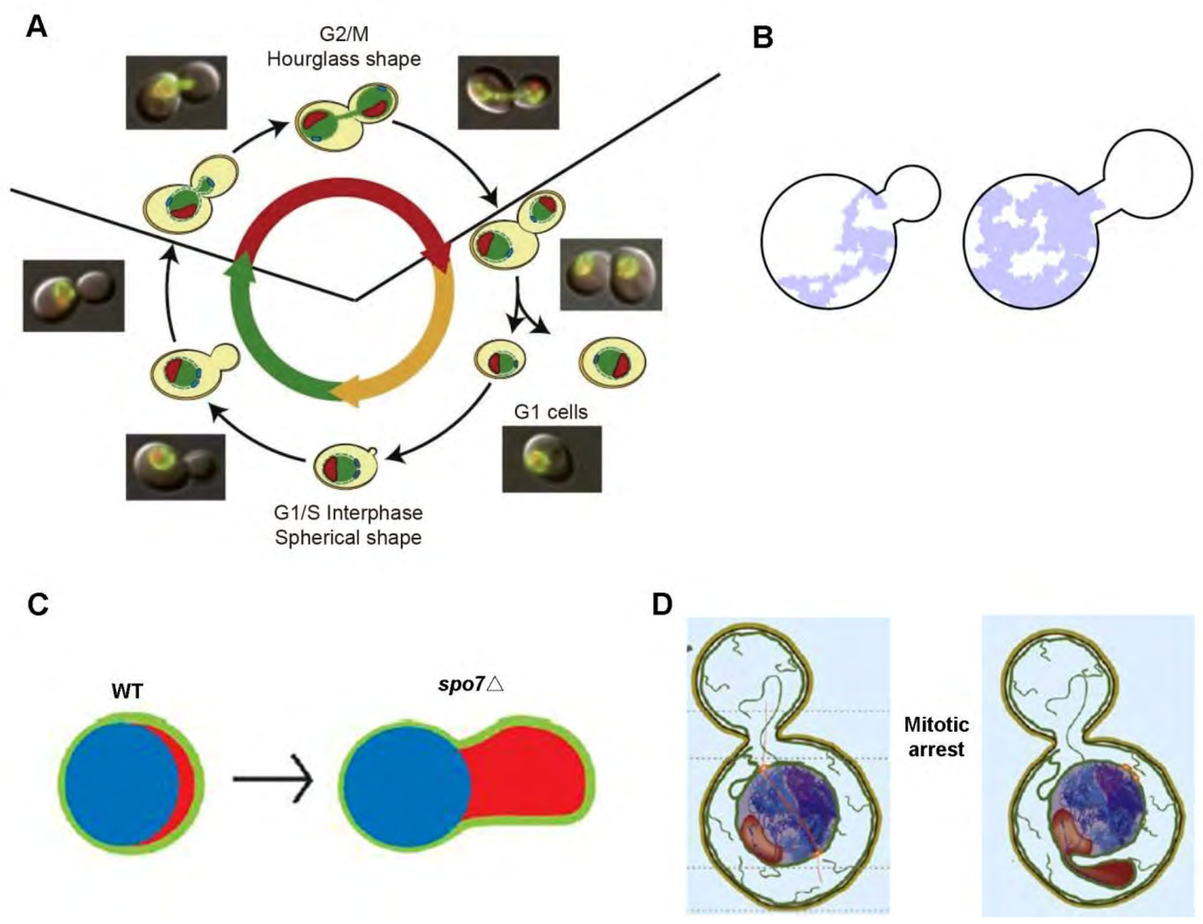

Figure 22. Nuclear shape is dynamic.

A. The nuclear shape and organization along the cell cycle. Adapted from (Albert et al., 2012).

B. The nuclear morphology constrains the diffusion of the nucleoplasmic components. From (Gehlen et al., 2011).

C. The nucleus of *spo7*Δ mutant prefers to extend along the nucleolus direction. From (Webster et al., 2010).

D. In mitotic arrested cells, the nuclear envelope forms a large flare juxtaposed to the nucleolus. From (Vjestica and Oliferenko, 2012).

There is evidence that the NE geometry during the mitotic division in budding yeast constrains the diffusion of the nucleoplasmic components into the daughter nucleus. Ace2 is a transcription factor that activates the daughter-specific transcriptional program. In anaphase, before cytokinesis, the nucleus adopts an asymmetric dumbbell shape which leads to the asymmetrical segregation of the Ace2, and only a restricted exchange of Ace2 was observed for the nucleoplasmic proteins between the mother and the daughter nuclei (Boettcher et al., 2012). Gehlen's work also suggested that the dividing yeast nuclear morphology and the length of mitosis significantly restrict the diffusion of episomes into the daughter nuclei (Gehlen et al., 2011) (Figure 22B).

The NE shape can influence the distribution of the proteins at the nuclear periphery, and in turn, some proteins at nuclear periphery also can modify the shape of the yeast nucleus. The Esc1p localized to the periphery of the nucleoplasm, can anchor chromatin and affect genes transcription. Overexpression of Esc1 leads to NE extension into the cytoplasm. This extension does not happen in the daughter nucleus because of the septin filaments at the bud neck that restrict transfer of proteins from the mother's nucleus to the daughter's one. The increase of the Mlp1 protein localized to the nuclear periphery, is toxic for the cells. However, the deletion of Esc1p or Mlp1p does not seem to influence nuclear shape (Hattier et al., 2007).

There are more and more evidences indicating that in most mutants altering nuclear shape, the NE preferentially elongates at the nucleolar side. The arrest of cells in G1 leads to a dumbbell shape nucleus in which the nucleolus lost its crescent shape and localizes at one lobe of the dumbbell (Stone et al., 2000). Polo kinase Cdc5 is known to be required for NE expansion at mitotic onset. The inactivation of the Cdc5 delays the mitotis, and the NE expansion preferentially takes place at the nucleolar side (Arnone et al., 2013; Walters et al., 2014). Deletion of the phospholipid biosynthesis inhibitor Spo7 also leads to a single nuclear envelope 'flare' that elongate the NE adjacent to the nucleolus (Figure 22C) (Webster et al., 2010). The delay or arrest of the mitotic process also provokes nuclear extension around the nucleolus which possibly can avoid the disruption of intranuclear organization (Vjestica and Oliferenko, 2012; Witkin et al., 2012) (Figure 22D).

In summary, the nuclear shape and size have a high plasticity. To explore possible link between genome and nuclear shape and size, accurate determination of the 3D nuclear morphology is instrumental.

2.3 The techniques used to analyze the nuclear shape and size

By far, there are many different techniques that have been developed to determine the nuclear geometry and size: the electron microscopy (EM) derived techniques, the tomography-based techniques and the fluorescent microscopy techniques.

2.3.1 EM and EM-based techniques

Electron microscopy (EM) is the most common used technique to observe the nuclear structure. Electron microscope uses a beam of accelerated electrons as a source of illumination providing a high resolution, such as conventional transmission electron microscopy (TEM) with ~1 nm resolution. Since long, using TEM, one can observe thin sections of nuclei from chemically fixed or cryofixed cells. For conventional fixation methods, the cells are fixed by chemicals which can alter the nuclear morphology (Figure 23A). Cryo-fixation is a physical fixation technique that reduces fixation artifact and therefore preserve the nuclear ultrastructure (Figure 23B) (Trumtel et al., 2000). After cryo-fixation, following cryo-substitution and resin embedding to prepare the ultra-thin sections are also source of artifacts. Morover, the analysis of the ultrathin sections (50-100 nm) only allows the measurement of nuclear shape and size in 2D. To estimate the nuclear size in 3D from the 2D results, one has to do statistical analysis of many sections which is technical challenging. In addition, this method is generally biased due to the random sectioning orientation.

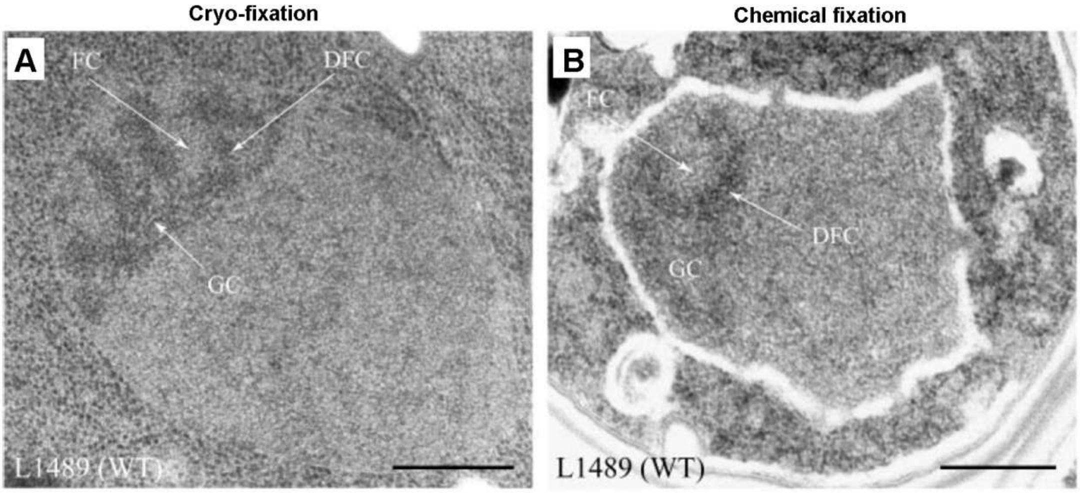

Figure 23. Nuclear morphology of yeast L1489 prepared by cryo-fixation and chemical fixation techniques, respectively. From (Trumtel et al., 2000).

A. Cryo-fixation better preserves the nuclear structure, even the sub-structures of the nucleus (the nucleolar structure).

B. Chemical fixation alters the nuclear structure. While the sub-structures of the nucleolus, FC, DFC and GC, still can be observed, the nuclear envelope appears clearly "broken" and the general shape of the nuclear section is modified. Scale bars, 300 nm.

One way to detect the nuclear shape and size in 3D based on the EM technique is to analyze serial sections of an entire nucleus (Winey et al., 1997; Yamaguchi et al., 2011). Ultra-thin serial sections (60 nm thick) of cryofixed cells are harvested and analysed in order. For each section, the NE position is registred in order to reconstruct the 3D NE (Figure 24) (Winey et al., 1997). Winey *et al.* used this method to detect the nuclear shape and size in different cell cycle phases of budding yeast cells. In G1 and S phase, the nucleus is spherical and the average size increases ~21%. In early mitosis, the nuclear size is almost twice bigger than in G1 phase. In mitosis, the nucleus adopts an hour-glass shape. Although the resolution of EM is very high, however, for each single nucleus, there is no guarantee that all the serial sections are intact; this technique is complex and time-consuming. For each cell cycle stage, Winey *et al.* just acquired ~10 nuclei, and it is difficult to acquire the nucleus in mitosis because of the random sectioning orientation.

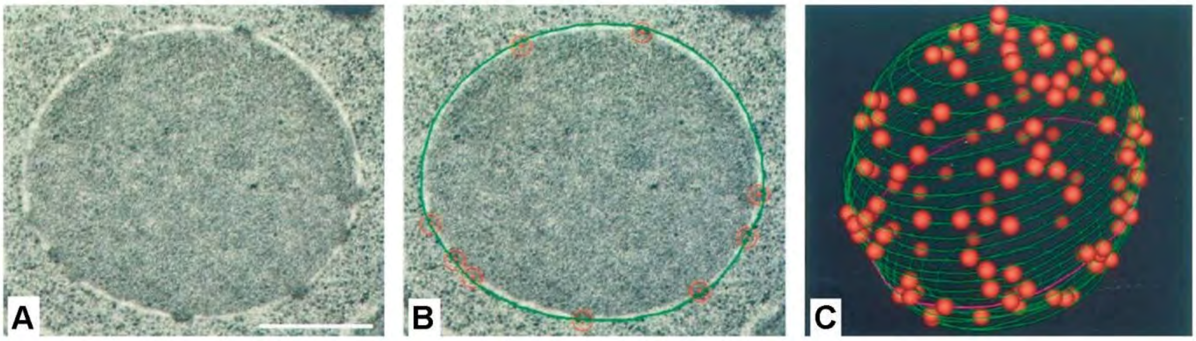

Figure 24. 3D reconstruction of the *S. cerevisiae* nuclear envelope analyzed by TEM. From (Winey et al., 1997).

A. Micrography of an ultra-thin section (from a serie) of a yeast nucleus analyzed by TEM.. Scale bar, 0.5 µm.

B. Detection of the positions of NPC and NE in each section, red circles represent the NPCs, green curve represents the NE.

C. Combination of all the NE contours and NPCs positions from serial sections to reconstruct the 3D NE.

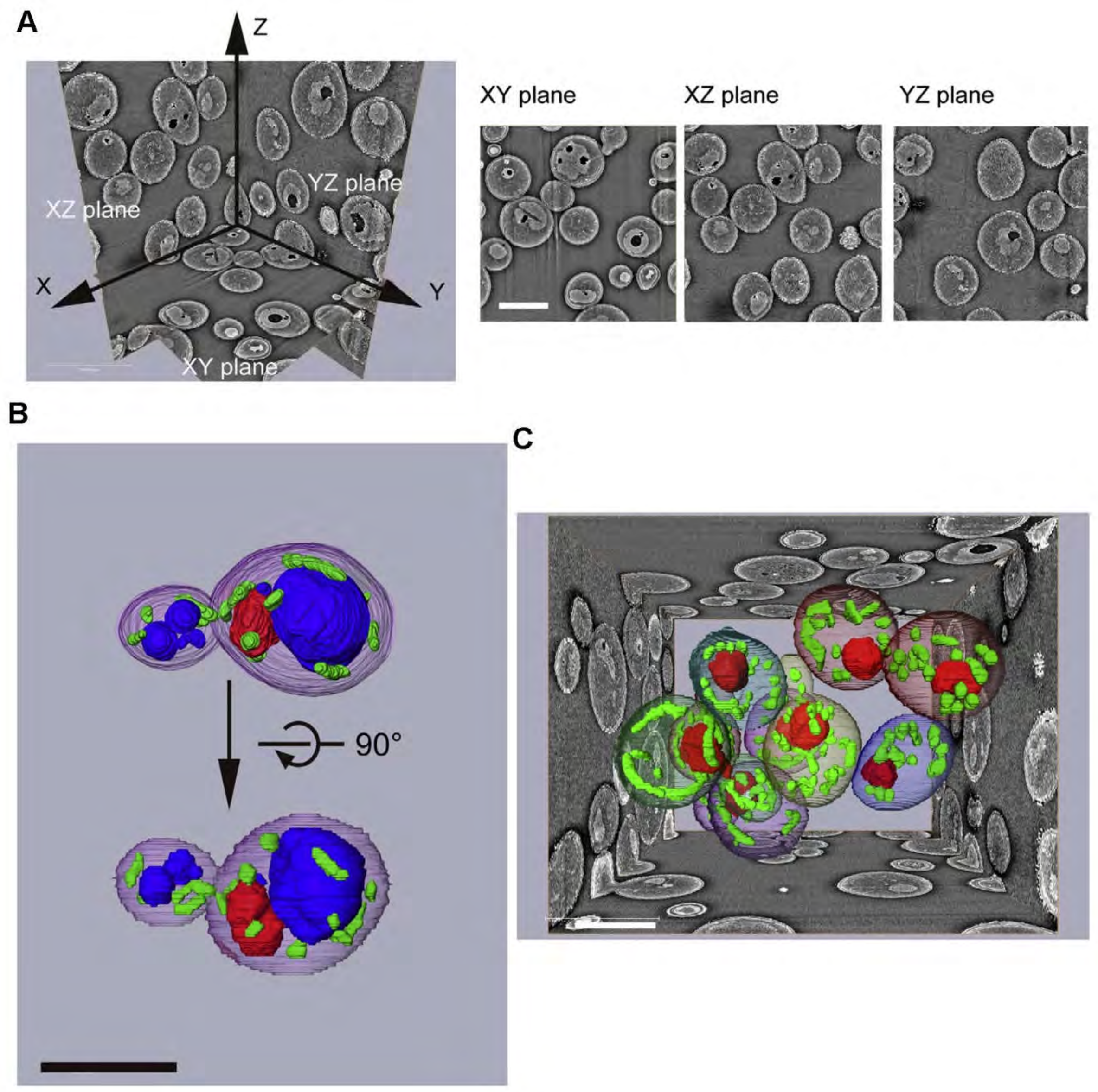

Figure 25. 3D reconstruction of the yeast cells by SBF-SEM technology. From (Miyazaki et al., 2014).

A. Acquisition of the images of the serial block-faces (XY plane, XZ plane and YZ plane). Scale bar, 5 µm.

B. Reconstruction of the 3D morphology of the yeast cell based on these block-face images. The outer semitransparent surface is the cell surface. The red volume represents the nucleus. The blue volume represents the vacuoles. The mitochondria are colored green. Scale bar, 5 µm.

C. Reconstruction of the 3D morphology of several yeast cells simultaneously. Scale bar, 5 µm.

Miyazaki *et al.* proposed one technique, serial block-face scanning electron microscopy (SBF-SEM), to study the fine structures and morphological changes at nanometer scales in yeast cells. The sample is typically fixed with aldehyde, staining with heavy metals and then embedding in a resin. The surface of the block of resin-embedded sample was imaged by detection of back-scattered electrons. Following acquisition, the ultramicrotome which was mounted inside the vacuum chamber of a SEM was used to cut thin sections (typically less than 30 nm) from the face of the block. After the section was cut, the sample block was raised back to the focal plane and imaged again (Figure 25A). These serial block-face images allow to reconstruct the 3D morphology of the cells (Figure 25B) (Miyazaki et al., 2014). This technique also allows to visualize the organelle structures in cells, such as mitochondria, vacuoles, the ER and the nucleus, which can help us to study the cell processes.

SBF-SEM is a promising tool to detect several cells simultaneously. This is because SBF-SEM allows the examination of large volumes, such as 21×21×50 μm^3, so one can segment several cells from a single reconstructed volume (Figure 25C). However, the sample number is still not enough to get robust statistical data. Furthermore, the preparation of the samples is still based on the fixation and section techniques, which maybe altere geometry of the cells compared to living yeast cells.

In conclusion, EM and EM-based techniques require fixation and sectioning steps of the samples which may influence the nuclear shape. The integrity of the serial sections which is essential for reconstruction of the 3D morphology of a nucleus is not guaranteed. Moreoevr, these approaches are extremely long, tedious and time-consuming which prevent to acquire enough data to perform robust statistical analysis. Finally, these techniques are not compatible with *in vivo* acquirement.

2.3.2 Tomography techniques

To eliminate the influence of the section on the nuclear morphology, X-ray tomography and high-voltage scanning transmission electron tomography are two promising techniques that can be used to reconstruct the 3D geometry of yeast cells.

Tomography is a familiar tool for obtaining 3D information in diagnostic medical imaging. A. Larabell and A. Le Gros used the similar technique, X-ray tomography, to reconstruct the 3D information of the cells (Larabell and Le Gros, 2004). Before imaging, the cells are loaded into a 10-µm-diameter capillary from the beveled tip end of the capillary. The cells are rapidly frozen with a blast of liquid-nitrogen-cooled Helium gas, placed in the X-ray microscope and maintained at cryogenic temperature throughout the data collection process. Then transmission X-ray microscope is used to collect 45 projection images at 4° intervals through 180° of rotation. All these 45 images are then aligned to a common axis of rotation. The X-ray microscope images are collected at X-ray energy of 514 eV which produces a quantifiable natural contrast of biological material to visualize the cellular structures. Then based on these images, one can reconstruct the whole cells with a resolution of ~60 nm. By using different volume analysis algorithms, one can extract the different information of the cells (Figure 26A). Using several processing algorithms after reconstruction, one can also extract the structure of the internal organelles, such as the nucleus, the vacuole and so on (Figure 26B) (Larabell and Le Gros, 2004).

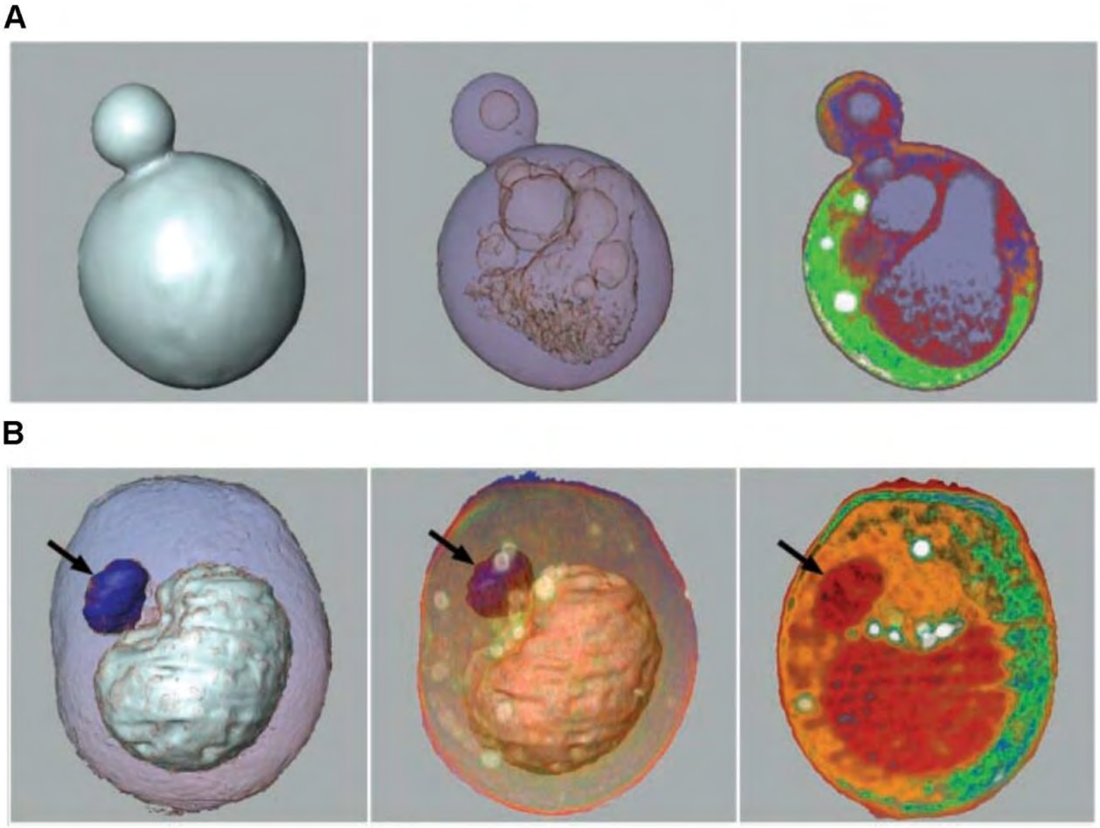

Figure 26. Reconstruction of the yeast cells by X-ray tomography. From (Larabell and Le Gros, 2004).

A. Reconstruction of one yeast cell by using different volume analysis algorithms. (Left) The cell surface. (Middle) Transparent surface and the internal organelles. (Right) Different colors render the different organelles, the white represents the lipid droplets, gray represents the vacuoles.

B. The yeast cell 3D structure is showed by using different processing algorithms after reconstruction. (Left) The transparent outer surface represents the plasma membrane. The opaque blue volume represents the nucleus (arrow). The white surface represents a big vacuole. (Middle) The surface from left is combined with volume rendering. (Right) According to the amount of X-ray absorption to render the cell, lipid droplets are white, the nucleus and the vacuole are red, other colors represent other cytoplasmic structures.

This technique avoids sectioning step than the EM approaches, but the acquisition of each cell lasts 3 minutes. Moreover, the resolution of this method, ~60 nm, is not as good as the EM. Finally, technology and apparatus are complex and time-consuming.

Budding yeast *S. cerevisiae* is a single-cell organism, typically egg-shaped and ~5 μm long and ~3 μm wide. Electron tomography (ET) using a high-voltage electron microscope (HVEM) can provide 3D information of cellular components in sections thicker than 1 μm (Murata et al., 2014). Murate *et al.* applied scanning transmission electron microscopy (STEM) with 1 MeV high-voltage to extend the useful specimen thickness for ET, and they found that high-voltage STEM tomography can be used to reconstruct the 3D structure of cellular structures in sections of 3-4 μm thickness. After harvesting serial sections of 3-4 μm, for each section, the serial images at 2° angular interval from -60° to +64° were collected. Based on these serial images, they could reconstruct the 3D morphology of the yeast cell. Similar with X-ray tomography, this method also can provide the organelle structures in the yeast cells (Murata et al., 2014).

Tomography techniques can provide whole-cell information in 3D, including the nucleus. Moreover, there is no need to cut the samples therefore avoiding the influence of the sectionning step on the nuclear geometry. However, for all these techniques, including the EM techniques, the cells are not living; the samples need to be fixed by chemical or high-pressure fast freezing which also have impact on the nuclear shape and size. In biology, it is essential to study the nuclear shape and size *in vivo*.

2.3.3 Fluorescent microscopy

Accurate determination of the NE position using fluorescent microscopy is technically challenging because of the resolution barrier in fluorescent microscopy: 200 nm in X-Y and about 500 nm in Z-axis (Nelson and Hess, 2014). In section 1.2.6, we have shown that the "localization microscopy" can measure the position of isolated objects with a resolution of a few tens of nanometers (Thomann et al., 2002). Moreover, fluorescent microscopy is presently the only way to observe the structure of the nucleus in living cells. In budding yeast, the NPCs were found in large clusters over the entire NE which can be used to reconstruct the NE structure in 3D (Winey et al., 1997). Fluorescent labeled NPCs appear as typical punctate rings staining the NE perfectly adapted for acquisition by "localization microscopy". In recent years, the researchers always used fluorescently labeled NPC to observe the NE geometry (Berger et al., 2008; Dultz et al., 2016).

Berger *et al.* created an algorithm, 'Nucloc', to determine the 3D position of loci relative to the NE (Berger et al., 2008) (See 1.2.6). They used fluorescent repressor-operator system (FROS) to fluorescently tag single loci and express, in the same cells, the nuclear pores by fusing fluorescence proteins to the Nup49 nucleoporin. For each nucleus, based on the detected NPC positions, the NE was approximated with an ellipsoid. This technique can collect thousands of cells images automatically which guarantee the robustness of statistical results. The results showed that the yeast nucleus in interphase is approximately a sphere of median radius ~1 μm. However, the approximation of the yeast nucleus as a sphere is an over-simplificated, the nuclear shape being dynamic along the cell cycle and in different conditions. Ellipsoid approximation is not suitable for the nucleus with non-spherical geometry and it is also not accurate for individual nucleus along its life.

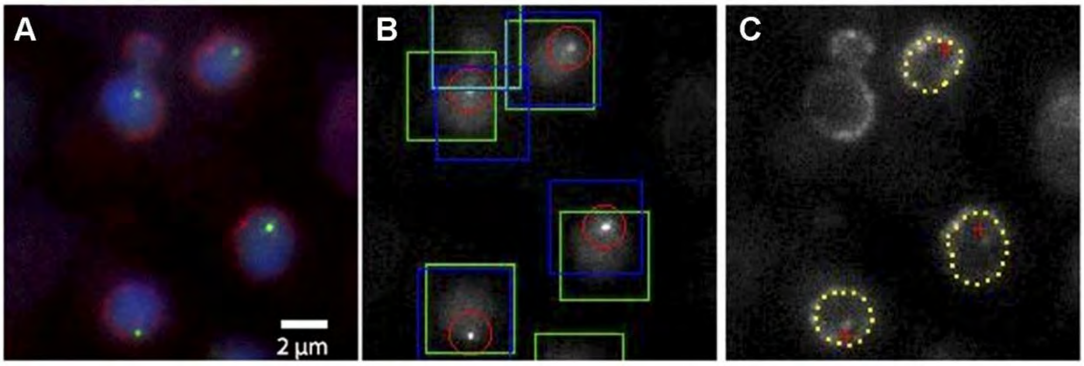

Figure 27. Reconstruction of the nuclear envelope by fluorescent microscopy in 2D. From (Dultz et al., 2016).

A. Use of different fluorescent proteins to label the nucleoplasm (NLS of Rpl25 tagged with CFP), NPC (nucleoporin Ndc1 tagged with tdTomato) and the interested locus (LacI-GFP).

B. The software can detect the locus (red circle), the cell nucleus (green box) and the NPC signal (blue box) automatically.

C. Based on the positions of detected NPCs (yellow dots), the "spline method" can reconstruct the NE.

Using ‘Nucloc’ to analyze the yeast nucleus, the fitted NE along Z-axis was always longer than along X-Y which is caused by the point spread function (PSF) along Z-axis. The accuracy of localization microscopy along Z-axis is much lower than in X-Y plane (Kirshner et al., 2013). Therefore, determination of the NE using fluorescent microscopy is mostly performed in two dimensions (2D). Dultz and colleagues used the “spline method” to accurately reconstruct the NE position in 2D and to study the global reorganization of the chromosomes relative to the NE in budding yeast (Dultz et al., 2016). First, they used GFP to label a specific locus to track its position. The NLS of RPL25 was tagged with CFP to label the nucleoplasm(Figure 27A, B) and the nucleoporin Ndc1 was tagged with tdTomato for the detection of the NPC in the NE (Figure 27A, C). Thanks to use of “localization microscopy” technique, the NPC positions in 2D were highly accurate. The method created by Dultz *et al.* can automatically fit the NE of numerous cells. Although the “spline method” is an accurate method to fit the NE based on NPC positions, this approach was just tested on interphase nucleus. It is still difficult to reconstruct the NE in mitosis. In addition, to study the nuclear organization, we need the 3D information.

2.4 Summary

In budding yeast, the chromosomes are segregated away from the cytoplasm by the NE. The nuclear organization ensures the proper expression, duplication, repair of the genome and correct segregation of chromosomes (Taddei and Gasser, 2012). Changes in nuclear shape and size might change the nuclear organization and the chromosomes organization. The nuclear shape and size are highly dynamic. EM approaches provide high resolution to observe the nuclear structure in 2D. When performed on ultra-thin serial sections of an entire nucleus, EM becomes directly informative of the nuclear shape and size. However, the sectionning process may influence the NE geometry. Tomography techniques eliminate this influence, but because these methods also need fixation step, they are not compatible with *in vivo* imaging. Fluorescent microscopy is a technique often used *in vivo* in biology. Accurate determination of the NE geometry using fluorescent microscopy is technically challenging and is mostly performed in 2D. In addition, the current fluorescent microscopy techniques always focused on the interphase nucleus. However, the nucleus geometry in mitosis also plays a significant role in cellular processes. In summary, it was urgent to create an accurate technique, which can reconstruct the NE along cell cycle and in different conditions, to detect the 3D nuclear shape and size *in vivo*.

3. Overview

After this introduction, I hope that I have convinced you that the study of chromatin motion of individual loci in genomic DNA is critical to understand the chromosome organization. Rouse model was suggested to explore physical properties of chromatin. However, estimated persistence length of chromatin appears inconsistent.

In addition, nuclear shape and size could have significant links with the nuclear organization and chromosome organization. EM techniques and tomography techniques are not compatible with *in vivo* imaging and it is difficult to acquire numerous data. Accurate determination of the NE geometry using fluorescent microscopy is technically challenging and is mostly performed in 2D.

So, my PhD project was organized along two axis: The first aim of my project was to study the chromatin dynamics in the S. cerevisiae nucleus. The second objetcive I had was to develop techniques to detect and analyze in 3D the yeast nuclear shape and size with a high accuracy. By using this approach, we could describe the nuclear shape and size, along the cell cycle and in different physiological conditions. We also could detect the organization of the basic features of the nuclear, inlcuding the SPB, NPC and the nucleolus, under different conditions by using this method.

Chapter II

Results

1. The dynamics of the chromatin in nucleoplasm and nucleolus

1.1 Objective and summary

Past two decades research on the chromatin dynamics have confirmed that the Rouse model is the best fitted polymer model to study the chromatin dynamics (see "Introduction" 1.2.7). Our group's previous work also confirmed the Rouse dynamics of the yeast chromosomes in nucleoplasm. However, movements of rDNA in the nucleolus are different (Albert et al., 2013). Recent research from Backlund *et al.* showed that the exponent of sub-diffusion of the chromosomes in the nucleoplasm was ~ 0.7, which is not compatible with the Rouse regime (Backlund et al., 2014). So, during my PhD project, I firstly focused on quantitative assessment of chromatin's dynamics of the chromatin in both nucleoplasm and nucleolus.

Thanks to the fluorescent repressor-operator system (FROS), which combines the expression of a bacterial repressor fused to a fluorescent protein and the integration of an operator sequence as tandem arrays at a specific locus, we can track the dynamics of the labeled loci. However, because of the limitation of the signal to noise ratio (SNR) and the photobleaching of the fluorescence, it is difficult to track the motions of the labeled loci accurately and for long-time. In this project, we selected fluorescently tagged loci with very high signal. With such labelling, we could track longer trajectories of the labeled loci (~1000 frames). Longer trajectories could guarantee the accuracy of the mean square displacement (MSD) which was used to analyze the chromatin dynamics.

In this study, I will present our analysis of the motion of the non-rDNA loci on chromosome XII (Wang et al., 2015) (Figure 2) and rDNA (unpublished data presented in the extended discussion). The analysis of the nucleoplasmic chromatin trajectories revealed a two-regime Rouse model which is more accurate than previous studies (Albert et al., 2013; Hajjoul et al., 2013). The investigation of the rDNA motility showed that its motion is actually slower than non-rDNA and can be fitted very well with a power law with the exponent ~0.7 ; this result is different with the two-regime model (for $t < 5$s, the exponent ~0.25 and after 5s, the exponent ~0.7) Albert *et al.* reported before (Albert et al., 2013).

1.2 Review: “Principles of chromatin organization in yeast: relevance of polymer models to describe nuclear organization and dynamics"

Principles of chromatin organization in yeast: relevance of polymer models to describe nuclear organization and dynamics

Renjie Wang, Julien Mozziconacci, Aurélien Bancaud, Olivier Gadal

(Published)

Available online at www.sciencedirect.com
ScienceDirect
ELSEVIER
Current Opinion in Cell Biology

Principles of chromatin organization in yeast: relevance of polymer models to describe nuclear organization and dynamics

Renjie Wang[1,2], Julien Mozziconacci[3,4], Aurélien Bancaud[4,5,6] and Olivier Gadal[1,2,4]

Nuclear organization can impact on all aspects of the genome life cycle. This organization is thoroughly investigated by advanced imaging and chromosome conformation capture techniques, providing considerable amount of datasets describing the spatial organization of chromosomes. In this review, we will focus on polymer models to describe chromosome statics and dynamics in the yeast *Saccharomyces cerevisiae*. We suggest that the equilibrium configuration of a polymer chain tethered at both ends and placed in a confined volume is consistent with the current literature, implying that local chromatin interactions play a secondary role in yeast nuclear organization. Future challenges are to reach an integrated multi-scale description of yeast chromosome organization, which is crucially needed to improve our understanding of the regulation of genomic transaction.

Addresses
[1] LBME du CNRS, France
[2] Laboratoire de Biologie Moleculaire Eucaryote, Université de Toulouse, 118 route de Narbonne, F-31000 Toulouse, France
[3] Laboratory for Theoretical Physics of Condensed Matter UMR7600, Sorbonne University, UPMC, 75005 Paris, France
[4] Groupement de recherche Architecture et Dynamique Nucléaire (GDR ADN), France
[5] CNRS, LAAS, 7 avenue du colonel Roche, F-31400 Toulouse, France
[6] Univ de Toulouse, LAAS, F-31400 Toulouse, France

Corresponding author: Gadal, Olivier (gadal@biotoul.fr)

Current Opinion in Cell Biology 2015, **34**:54–60
This review comes from a themed issue on **Cell nucleus**
Edited by **Katherine L Wilson** and **Karsten Weis**
For a complete overview see the Issue and the Editorial
Available online 15th May 2015
http://dx.doi.org/10.1016/j.ceb.2015.04.004

Introduction: the necessary jump toward an integrative view of chromatin organization

The driving forces responsible for the establishment and maintenance of high-order chromatin structure remain the subject of intense research. Our understanding of genome organization has always been intimately linked to technical progresses, which fed new insights that confirmed or contradicted working hypotheses [1,2••]. From the seminal use of dyes by Flemmings to identify chromatin, microscopy was, and still is, a central tool to study nuclear organization [3]. Carl Rabl suggested that interphase chromosome organization was guided by the tethering of centromeres and telomeres in opposite directions, a folding latter named 'Rabl-organisation' [4]. Rabl-like configuration of budding yeast chromosomes was established more than 100 years later [5–8]. At smaller length scales, the heterogenous distribution of chromatin in the nucleus was observed in 1928 by Emil Heitz [9] using optical microscopy of Giemsa stained chromosomes. This heterogeneous organization was confirmed by Transmitted Electron Microscopy (TEM) with a considerable gain in resolution [10]. After extraction of the soluble nuclear material, TEM also led to the observation of the 'nuclear matrix' as a nucleo-skeleton onto which chromatin was attached [11]. Live cell imaging of fluorescently labeled nuclear components were later developed, collectively called F-techniques, and showed that a large fraction of nuclear proteins, some of which present in the nuclear matrix fraction, were highly dynamic [12]. Techniques aiming at labeling chromosome loci based on fluorescent operator–repressor system (FROS), which involve LacI-GFP or TetR-GFP binding to array of 256 *lacO* or 112 *tetO*, equivalently $\sim$10 kb of DNA, have then been developed, and time-lapse analysis of chromosome motion revealed the mobility of chromosomal loci *in vivo* [13–15]. Over the last decade we witnessed the advent of genomic methods to sense nuclear architecture, such as Chromatin immunoprecipitation (ChIP), DNA adenine methyltransferase identification (DamID), and the now widely used intra-molecular ligation of cross-linked DNA, named chromosome conformation capture (3C), and its genome wide derivatives including Hi-C [16,17]. This booming field calls for new models to integrate datasets of different nature (microscopic distance measurements, ChIP, DamID, contact frequency map from 3C. Coarse-grained polymer physics models met some success in the recapitulation of heterogeneous data with a single and unified representation [18]. Some improvements are nonetheless still needed to recapitulate the folding principles of DNA, chromatin and chromosomes. Here we wish to discuss the successes of these models in the context of *S. cerevisiae* nuclear architecture, as well as the clarifications that are needed to reach a better understanding of chromosome organization *in vivo*.

Models of nuclear architecture: direct *versus* indirect modeling

In the last 25 years, essentially two classes of models have been proposed to describe genome organization: direct (or data driven) modeling or inverse (or physics driven) modeling (for review, see [19**]). In direct modeling, experimental datasets are used as inputs, and modeling is built by minimizing the discrepancy of the model to the data. Therefore, such models are tailored to recapitulate input data but by construction, they have little or no predictive value, and new datasets must be obtained before generating a modified model. They can be however very useful since they recapitulate complex data in a frame which is usually amenable to be visually interpreted directly. The other approach consists in building a model with a set of assumptions involving, among others, the mechanics of chromosomes (rigidity and friction) and the geometry of the nucleus. The output of the model can be compared with experiments [20*,21**,22**], and its predictive value can be challenged with novel datasets or whenever the set of microscopic parameters that are used to fit the experiments appears to be inconsistent with the literature. In most cases, however, genome modeling is not sufficiently explored to evaluate the consistency of a model based on its fitting accuracy, because the key molecular parameters to describe nuclear architecture are still debated. At this step we propose to highlight some of the main conclusions inferred from modeling of eukaryotic organization with polymer physics.

What do we learn from chromosome conformation capture?

The genome wide implementation of the 3C technique (Hi-C) enables the mapping of the self contacts resulting from the DNA molecules being folded in chromosomes within the live nucleus and is therefore reflecting this architecture (see Figure 1a a contact map for the yeast genome, [23]). Direct 3D modeling [24] applied on this contact map leads to a 3D structure which recapitulates known features of yeast chromosomes organization such as strong centromere clustering, weaker telomere colocalization and the spatial segregation of long and short chromosomal arms (Figure 1b). A pending question is whether or not this organization is quantitatively compatible with polymer physics. In the seminal Hi-C paper, the authors compared their data with two polymer models describing chromosomes as crumple or equilibrium globules [25]. These models differ in their predictions on the decrease of the contact probability P between two loci on the same chromosomes as a function of their genomic distance s (see Figure 1c). The finding that $P(s)$ followed a power law decrease with s characterized by an exponent close to -1 ($P(s) \sim s^{-1.08}$) appeared to be in agreement with the crumple globule model. Other results were later published on different organisms, including the yeast *S. cerevisiae* [26]. They seemed to indicate that metazoan genomes shared common folding principles with a similar exponent of -1 whereas the yeast genome, which has shorter chromosomes are organized as an equilibrium globule in agreement with physical models (see Figure 1d) [21**,22**]. This simple view has been challenged as additional Hi-C data obtained with standardized protocols became available [27*]. It was for instance found that the exponent of $P(s)$ somewhat varied in the range of -1.5 to -1 for different human cell lines [28]. The general relevance of the crumpled globule model has therefore been called into question, because $P(s) \sim s^{-1.5}$ is expected to be detected in equilibrium globules. Concerning the yeast *S. cerevisiae*, only two genome-wide datasets are available [23,29], and more data and analysis are needed to confirm or invalidate the actual folding scheme. Notably, GC content biais, possible fixation artifacts (some of which can be normalized) in 3C techniques, and the difficulties to convert contact frequency to physical distances should not be ignored [24,30**,31,32,33*]. One way around these technical limitations is to combine 3C methods with microscopy observations [17,25]. In conclusion, the folding principles of chromosomes at the *entire* genome level remain controversial, but the number of contributions in this booming field should rapidly clarify these central questions. Conversely the motion of a chromosome locus is associated to the *local* properties of chromatin, and the main results obtained by physical modeling of spatial fluctuations will be described in the following paragraph.

What do we learn from chromosome motion analysis?

Chromatin loci are in constant random motion within some finite volume of confinement detectable with long time-lapse acquisitions [13,14,34,35]. When the locus is released from chromosome (i.e. through inducible excision of tagged chromatin rings), chromatin is diffusing in the nucleoplasm, and boundaries are defined by the nuclear envelope [34,36]. Chromosomal loci instead seem to be confined in a ‘gene territory’, as defined by the region of preferential steady-state localization [37]. For shorter time scales, the displacement of chromosome loci was mainly analyzed based on the mean square displacement (MSD). The MSD was adjusted with models of diffusion or sub-diffusion, meaning that power-law scaling describing its temporal dependence was characterized by an exponent of 1 or lower than 1, respectively. Notably normal diffusion is expected to occur for isolated objects, that is, influenced by thermal fluctuations and viscous friction only. In the case of polymer loci, elastic interactions between neighboring monomers and long-range hydrodynamic interactions associated to solvent flux have to be considered [38]. The nucleus is a concentrated environment composed of DNA, diffusing and bound

Figure 1

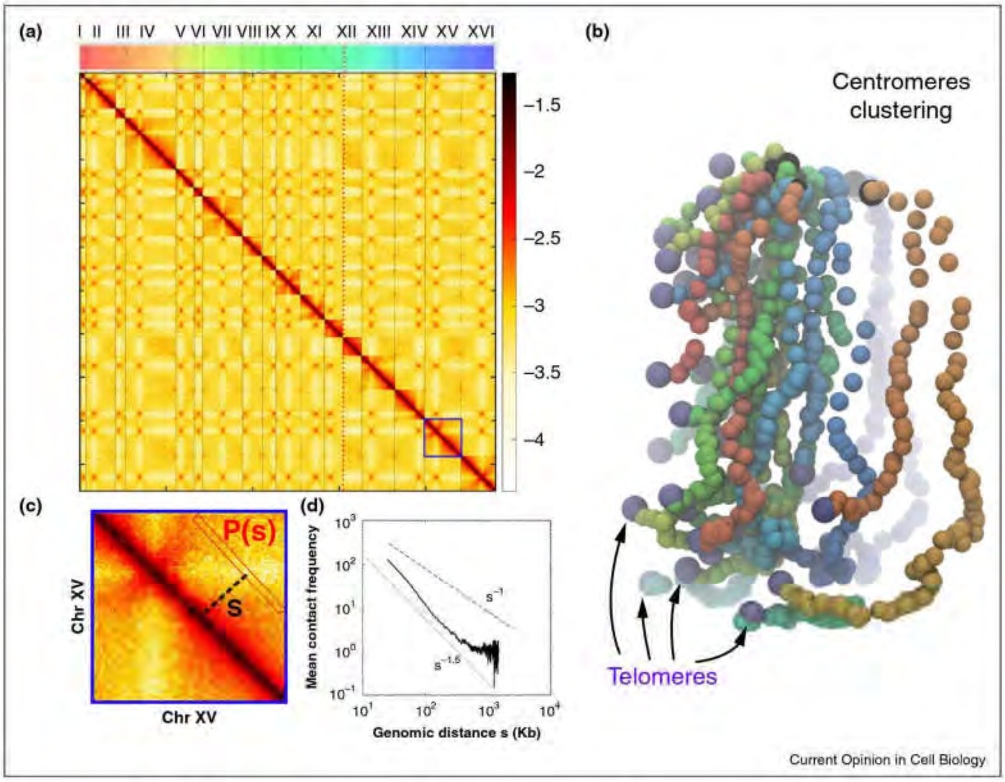

3C insights on the structure of the *S. cerevisiae* chromosomes. **(a)** Contact map of the 16 chromosomes as obtained by genome-wide 3C ([23], individual chromosomes are labeled with roman numbering). The map has been normalized so that the sum over each line and column is equal to one [32]. Note that the colorscale is in log arithmic scale. **(b)** Direct 3D modeling from this map [24]. The color-code for each chromosome on the structure is indicated in (a). Telomeres and centromeres are labeled with purple and black beads, respectively. **(c)** Zoom on the intra chromosomal contact map of chromosome XV, corresponding to the blue box in (a). The value *P*(s) is obtained by averaging the signal in the red box. **(d)** Plot (adapted from [22**]) of the mean number of contacts obtained in the experiment with varying distances (s). Note that these number of contacts were not normalized.

proteins, as well as RNA, which are expected to screen out hydrodynamic interactions. As was described for the bacterial chromosome [39], the dynamics of chromosomes in yeast was proposed to follow the Rouse model, which assumes that chromatin fiber behaves as a homogeneous series of beads connected by elastic springs, with the notable exception of ribosomal DNA (rDNA) in the nucleolus [40**,41*]. For an isolated chain and disregarding volume exclusion, the motion of a locus in chain composed of N monomers, of known stiffness characterized by the Kuhn length (Lk) is described by three consecutive regimes (Figure 2). For very short time intervals, elastic interactions between neighboring monomers do not restrain motion. This is only valid for small displacements ($MSD < < Lk$; $< \sim 30$ nm for chromatin), which are difficult to access experimentally (see below). For long displacements, that is, larger than the polymer diameter ($\mathrm{MSD} \gg Lk \cdot \sqrt{N}$), the entire polymer chain diffuses freely in solvent. In the yeast nucleus, this behavior is not relevant because chromosomes are confined in the nucleus and tethered at their centromeres [7,42,43] and telomeres [44,45]. Notably this tethering also induces topological constraints that do not allow for reptation, that is, longitudinal diffusion of a monomer along the contour path of the chain. In between those two regimes (for $\mathrm{Lk} \ll \mathrm{MSD} \ll Lk \cdot \sqrt{N}$), Rouse regime is characterized by $MSD(\tau) = \Gamma\tau^{\alpha}$, with scaling exponent α of 0.5, which increases to 0.54 whenever volume exclusion is considered. Although this simplistic model overlooks local variations in chromatin structure, it appeared to be consistent with the motion of loci located on chromosome XII, XIV and IV in *S. cerevisiae* [40**,41*]. These results are further supported by molecular simulations using a polymer model of the entire yeast genome [40**,41*]. A recent publication however challenged the relevance of the Rouse model by monitoring the motion

Figure 2

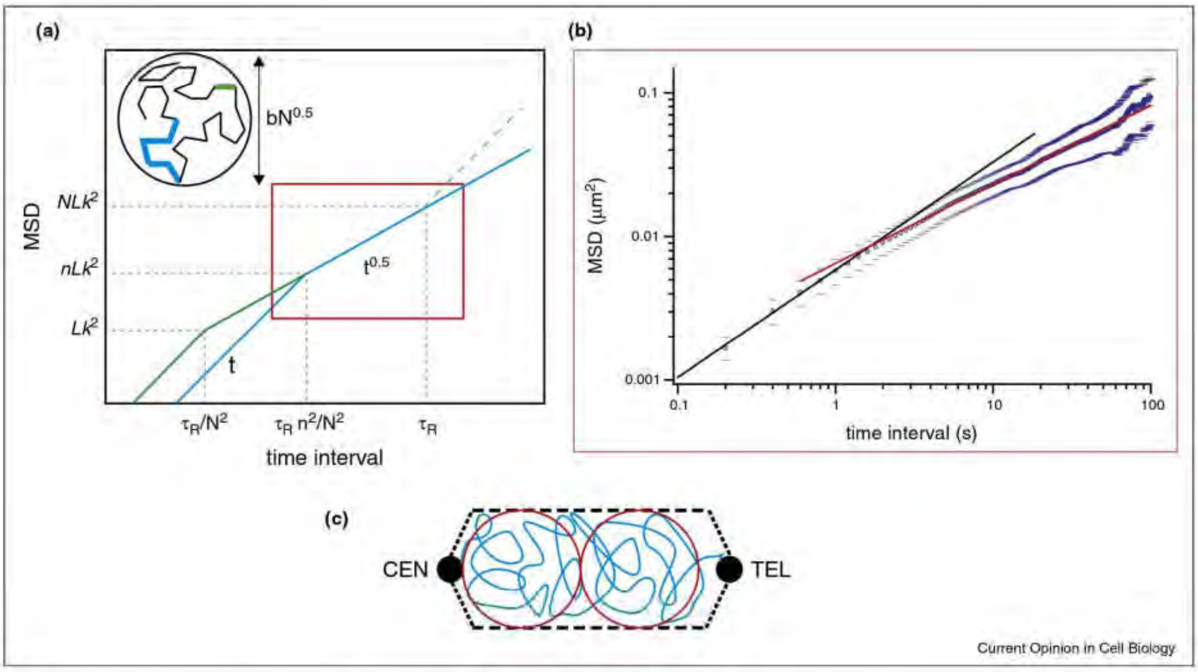

Rouse model of polymer dynamics. **(a)** This figure describes the difference in segmental dynamics of one monomer or a fragment with *n* monomers (color-coded in green or blue, respectively). In the short time limit, the motion of the locus is not restricted by elastic interactions with its neighboring polymer segments, leading to a regime of free diffusion. The larger dimension of a fragment with n monomers is associated to a slow down in diffusion (the blue curve is below the green one). The second regime corresponds to Rouse model of polymer dynamics, in which the MSD increases with time with a power-law scaling of 0.54. The red rectangle represents the observation window in a real experiment with finite temporal and spatial resolutions. **(b)** The blue dataset represents the average MSD over 45 trajectories for a selected bright locus located at position 380 kb on chromosome XII (the experiment has been carried out at room temperature). Note that standard errors are indicated as vertical caps. Two regimes can be distinguished with a sharp increase of the MSD at short time scales (scaling exponent of 0.75) followed by a behavior consistent with the Rouse regime (scaling exponent of 0.54). Respective trend lines are shown in black and red. **(c)** Schematic representation of a yeast chromosome arm attached by its extremities at its centromere and telomere. Confinement driven by volume exclusion direct the folding in a tube-like configuration composed of a series of blobs.

in 3D of *GAL* genes and control loci in the 0.5–5 s time domain [46**]. These authors indeed showed that the exponent of subdiffusion was $\alpha \sim 0.7$, which is apparently not compatible with Rouse regime. The authors suggested that fractional Brownian motion (fBm) could account for this scaling exponent, though the underlying physics accounting for this behavior remains unclear. Another possibility is that the Rouse model remains valid despite the unexpected exponent. High precision 3D microscopy is achieved with strains in which chromosome loci are characterized by high signal-to-noise ratio. These imaging conditions are obtained by increasing the number of bacterial operator binding sites from 56 to 224 *tetO* sequences, equivalently 2.5–11 kb of DNA, in order to enhance brightness of the locus. However, due to the increased length of the labeled DNA, the initial free diffusive motion is expected to be slower than for a single monomer (Figure 2). The transition to the Rouse regime should hence be delayed, leading to an 'intermediate' exponent lower than 1 but greater than 0.54 in the short time regime, as was for instance discussed for particle migration in a dense meshwork [47]. In fact we recently observed the same behavior in clones with long FROS labels (Figure 2). The dynamics of a locus on chromosome XII showed a smooth transition to the Rouse regime after ~5 s. Note that this two-phase response was not detected in our previous report using clones with shorter FROS labels [40**,45]. Consequently, the Rouse polymer model does not seem to be invalidated by analyzing the MSD over a limited temporal domain comprised between 0.5 and 5 s. Nevertheless we suggest that further validations of the Rouse model require additional analyses, including among others step distribution functions, velocity autocorrelation function of locus trajectories [48*], or probability of backward motion.

Conclusion: toward an integrated view of nuclear organization and dynamics

This overview suggests that the implementation of a physics model providing an integrated picture of yeast

Figure 3

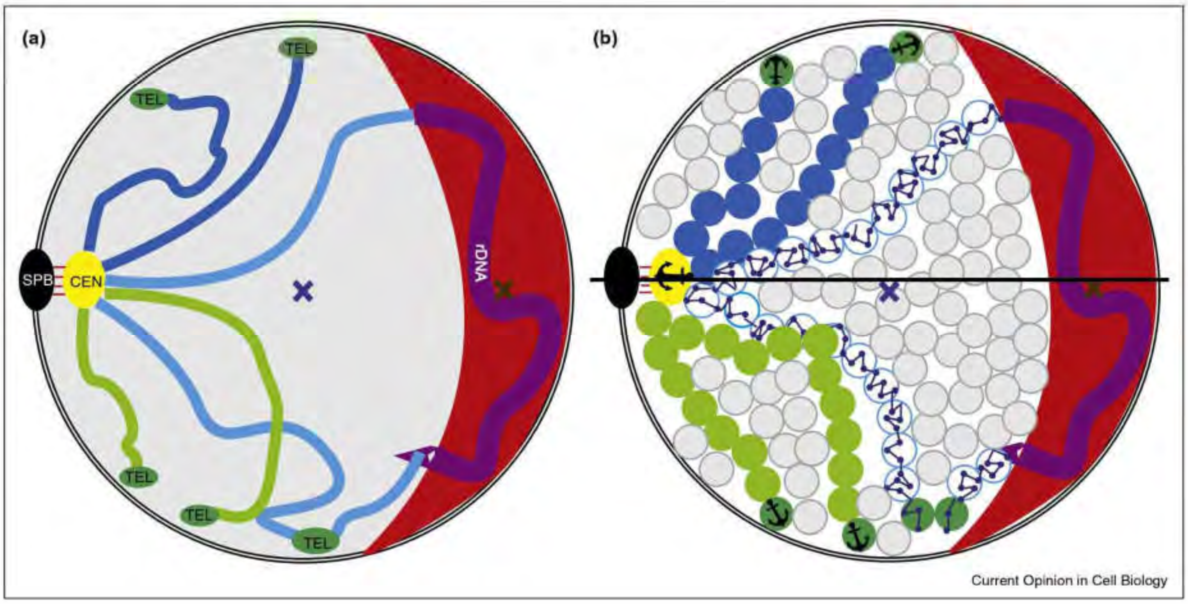

Current Opinion in Cell Biology

Two schematic representations of the yeast nucleus. **(a)** Yeast nucleus from a biologist's perspective. Chromosome arms are depicted with color lines. Centromeres (CEN; yellow circle) are attached to the spindle pole body (SPB; black circle) by microtubules (red lines). Telomeres (TEL; green circles) are distributed near the nuclear envelope (NE) (double-black-line). Nucleolus (red crescent abutting NE) contains rDNA (bold purple line). Blue and brown crosses depict the nuclear and nucleolar center, respectively. **(b)** Yeast nucleus from a polymer physicist's perspective. The color circles represent polymer blobs, which are arranged in linear arrays. Each chain represents one chromosome arm anchored at both ends. Blobs are filling the nucleoplasm. Nuclear and nucleolar centers define a central axis around which chromosomes are organized. Note that rDNA in the nucleolus has distinct dynamic properties from bulk chromatin.

nuclear organization is under rapid and constant improvement. Based on the current literature, it becomes increasingly clear that each chromosome arm extends in the nucleus from its centromere, behaving as a space-filling polymer in a preferential path dictated by the centromere to nucleolus axis (Figure 3). Volume exclusion defines a characteristic tube in which chromosome can be described as a series of polymer beads, called blobs, in which the chain behaves as an ideal constraint-free polymer. In this description, the Rabl-like organization of yeast chromosomes is marginally dictated by specific polymer–polymer interactions, rather chromosomes behave as extended polymer chains organized by volume exclusion. This description covers the length spectrum from the Kuhn length to the nucleus size, and disregards the folding of the chromatin fiber. We argue that the next challenge is to build multi-scale models with improved description at every spatial dimension to explore gene specific properties: gene relocalization documented in yeast during gene expression such as tRNA gene preferential interaction with NPC or nucleolus [49,50], peripheral recruitment of SAGA-regulated genes [51–53], the formation of replication factory [54•] or increased motility toward DNA damage [55–57]. The benefits of this effort are expected to clarify how the cell organizes its genome for gene expression regulation or efficient repair. Finally, the recently determined globular organization of chromosome arms in fission yeast mediated by local cohesin association at specific sites demonstrate that combination of biophysical properties of chromatin and mapping chromatin bound factors will allow tremendous progress in our understanding of chromatin architecture *in vivo* [58••].

Acknowledgements

O.G. was supported by an ATIP-plus grant from CNRS, by the Agence Nationale de la Recherche (programme JCJC). JM, AB and OG are supported by Agence Nationale de la Recherche (ANDY).

References and recommended reading

Papers of particular interest, published within the period of review, have been highlighted as:

- • of special interest
- •• of outstanding interest

1. Olins DE, Olins AL: **Chromatin history: our view from the bridge.** *Nat Rev Mol Cell Biol* 2003, **4**:809-814.

2. Cremer T, Cremer C, Lichter P: **Recollections of a scientific**
•• **journey published in human genetics: from chromosome**

territories to interphase cytogenetics and comparative genome hybridization. *Hum Genet* 2014, **133**:403-416.
An excellent, historical perspective of chromatin structure in cell nucleus.

3. Flemming W: *Zellsubstanz, Kern und Zelltheilung*. Edited by Leipzig FCWV; 1882.

4. Rabl C: **Über Zelltheilung**. *Morphol Jahrbuch* 1885:214-330.

5. Guacci V, Hogan E, Koshland D: **Centromere position in budding yeast: evidence for anaphase A**. *Mol Biol Cell* 1997, **8**:957-972.

6. Jin Q, Trelles-Sticken E, Scherthan H, Loidl J: **Yeast nuclei display prominent centromere clustering that is reduced in nondividing cells and in meiotic prophase**. *J Cell Biol* 1998, **141**:21-29.

7. Jin QW, Fuchs J, Loidl J: **Centromere clustering is a major determinant of yeast interphase nuclear organization**. *J Cell Sci* 2000, **113**:1903-1912.

8. Bystricky K, Heun P, Gehlen L, Langowski J, Gasser SM: **Long-range compaction and flexibility of interphase chromatin in budding yeast analyzed by high-resolution imaging techniques**. *Proc Natl Acad Sci U S A* 2004, **101**:16495-16500.

9. Heitz E: **Das heterochromatin der moose**. *Jahrb Wiss Botanik* 1928:762-818.

10. Tooze J, Davies HG: **Light- and electron-microscope studies on the spleen of the newt *Triturus cristatus*: the fine structure of erythropoietic cells**. *J Cell Sci* 1967, **2**:617-640.

11. Berezney R, Coffey DS: **Identification of a nuclear protein matrix**. *Biochem Biophys Res Commun* 1974, **60**:1410-1417.

12. Misteli T: **Protein dynamics: implications for nuclear architecture and gene expression**. *Science* 2001, **291**:843-847.

13. Marshall WF, Straight A, Marko JF, Swedlow J, Dernburg A, Belmont A, Murray AW, Agard DA, Sedat JW: **Interphase chromosomes undergo constrained diffusional motion in living cells**. *Curr Biol* 1997, **7**:930-939.

14. Heun P, Laroche T, Shimada K, Furrer P, Gasser SM: **Chromosome dynamics in the yeast interphase nucleus**. *Science* 2001, **294**:2181-2186.

15. Michaelis C, Ciosk R, Nasmyth K: **Cohesins: chromosomal proteins that prevent premature separation of sister chromatids**. *Cell* 1997, **91**:35-45.

16. van Steensel B, Dekker J: **Genomics tools for unraveling chromosome architecture**. *Nat Biotechnol* 2010, **28**:1089-1095.

17. Dekker J, Rippe K, Dekker M, Kleckner N: **Capturing chromosome conformation**. *Science* 2002, **295**:1306-1311.

18. Bau D, Marti-Renom MA: **Genome structure determination via 3C-based data integration by the Integrative Modeling Platform**. *Methods* 2012, **58**:300-306.

19. •• Rosa A, Zimmer C: **Computational models of large-scale genome architecture**. *Int Rev Cell Mol Biol* 2014, **307**:275-349.
A comprehensive overview of computational models of genome architecture of the last 25 years.

20. • Tokuda N, Terada TP, Sasai M: **Dynamical modeling of three-dimensional genome organization in interphase budding yeast**. *Biophys J* 2012, **102**:296-304.
Model of yeast chromosomes as chains moving under the constraints of nuclear confinement and chromatin-chromatin interactions.

21. •• Tjong H, Gong K, Chen L, Alber F: **Physical tethering and volume exclusion determine higher-order genome organization in budding yeast**. *Genome Res* 2012, **22**:1295-1305.
Model supporting the view that volume exclusion and physical tethering is sufficient to recapitulate most of the yeast genome contact map.

22. •• Wong H, Marie-Nelly H, Herbert S, Carrivain P, Blanc H, Koszul R, Fabre E, Zimmer C: **A predictive computational model of the dynamic 3D interphase yeast nucleus**. *Curr Biol* 2012, **22**:1881-1890.
Computational model reaching similar conclusion as 21, but with the additional notion of heteropolymer model to explain the spatial segregation and the shape of the nucleolus.

23. Duan Z, Andronescu M, Schutz K, McIlwain S, Kim YJ, Lee C, Shendure J, Fields S, Blau CA, Noble WS: **A three-dimensional model of the yeast genome**. *Nature* 2010, **465**:363-367.

24. Lesne A, Riposo J, Roger P, Cournac A, Mozziconacci J: **3D genome reconstruction from chromosomal contacts**. *Nat Methods* 2014, **11**:1141-1143.

25. Lieberman-Aiden E, van Berkum NL, Williams L, Imakaev M, Ragoczy T, Telling A, Amit I, Lajoie BR, Sabo PJ, Dorschner MO *et al.*: **Comprehensive mapping of long-range interactions reveals folding principles of the human genome**. *Science* 2009, **326**:289-293.

26. Halverson JD, Smrek J, Kremer K, Grosberg AY: **From a melt of rings to chromosome territories: the role of topological constraints in genome folding**. *Rep Prog Phys* 2014, **77**:022601.

27. • Dixon JR, Selvaraj S, Yue F, Kim A, Li Y, Shen Y, Hu M, Liu JS, Ren B: **Topological domains in mammalian genomes identified by analysis of chromatin interactions**. *Nature* 2012, **485**:376-380.
Identification of topological domains as large, megabase-sized local chromatin interaction domains, as structural constituent of the genome organization.

28. Barbieri M, Chotalia M, Fraser J, Lavitas LM, Dostie J, Pombo A, Nicodemi M: **Complexity of chromatin folding is captured by the strings and binders switch model**. *Proc Natl Acad Sci U S A* 2012, **109**:16173-16178.

29. Marie-Nelly H, Marbouty M, Cournac A, Liti G, Fischer G, Zimmer C, Koszul R: **Filling annotation gaps in yeast genomes using genome-wide contact maps**. *Bioinformatics* 2014, **30**:2105-2113.

30. •• Williamson I, Berlivet S, Eskeland R, Boyle S, Illingworth RS, Paquette D, Dostie J, Bickmore WA: **Spatial genome organization: contrasting views from chromosome conformation capture and fluorescence in situ hybridization**. *Genes Dev* 2014, **28**:2778-2791.
Extensive high resolution study of the murin HoxD with 3C methods and FISH reveales that products captured by 3C do not always reflect spatial proximity, and must be interpreted with caution.

31. Belmont AS: **Large-scale chromatin organization: the good, the surprising, and the still perplexing**. *Curr Opin Cell Biol* 2014, **26**:69-78.

32. Yaffe E, Tanay A: **Probabilistic modeling of Hi-C contact maps eliminates systematic biases to characterize global chromosomal architecture**. *Nat Genet* 2011, **43**:1059-1065.

33. • Cournac A, Marie-Nelly H, Marbouty M, Koszul R, Mozziconacci J: **Normalization of a chromosomal contact map**. *BMC Genomics* 2012, **13**:436.
A procedure of contact map normalization is described in detail in this work

34. Neumann FR, Dion V, Gehlen LR, Tsai-Pflugfelder M, Schmid R, Taddei A, Gasser SM: **Targeted INO80 enhances subnuclear chromatin movement and ectopic homologous recombination**. *Genes Dev* 2012, **26**:369-383.

35. Drubin DA, Garakani AM, Silver PA: **Motion as a phenotype: the use of live-cell imaging and machine visual screening to characterize transcription-dependent chromosome dynamics**. *BMC Cell Biol* 2006, **7**:19.

36. Gartenberg MR, Neumann FR, Laroche T, Blaszczyk M, Gasser SM: **Sir-mediated repression can occur independently of chromosomal and subnuclear contexts**. *Cell* 2004, **119**:955-967.

37. Berger AB, Cabal GG, Fabre E, Duong T, Buc H, Nehrbass U, Olivo-Marin JC, Gadal O, Zimmer C: **High-resolution statistical mapping reveals gene territories in live yeast**. *Nat Methods* 2008, **5**:1031-1037.

38. Teraoka I: **Polymer solutions: an introduction to physical properties**. *Polymer solutions*. John Wiley & Sons, Inc.; 2002:i-xv.

39. Weber SC, Spakowitz AJ, Theriot JA: **Bacterial chromosomal loci move subdiffusively through a viscoelastic cytoplasm**. *Phys Rev Lett* 2010, **104**:238102.

40. Hajjoul H, Mathon J, Ranchon H, Goiffon I, Mozziconacci J,
•• Albert B, Carrivain P, Victor JM, Gadal O, Bystricky K *et al.*: **High-throughput chromatin motion tracking in living yeast reveals the flexibility of the fiber throughout the genome.** *Genome Res* 2013, **23**:1829-1838.

Analysis of chromatin motion of multiple loci supports subdiffusive behavior of chromatin. Rouse polymer model is used to extract some biophysical properties of chromatin.

41. Verdaasdonk JS, Vasquez PA, Barry RM, Barry T, Goodwin S,
• Forest MG, Bloom K: **Centromere tethering confines chromosome domains.** *Mol Cell* 2013, **52**:819-831.

Chromosome motion strongly depends on tethering at the centromere. Detachment of centromere increased mobility, and modeling was used to evaluate forces dictating chromosome territorial organization

42. O'Toole ET, Winey M, McIntosh JR: **High-voltage electron tomography of spindle pole bodies and early mitotic spindles in the yeast *Saccharomyces cerevisiae*.** *Mol Biol Cell* 1999, **10**:2017-2031.

43. Gotta M, Laroche T, Formenton A, Maillet L, Scherthan H, Gasser SM: **The clustering of telomeres and colocalization with Rap1, Sir3, and Sir4 proteins in wild-type *Saccharomyces cerevisiae*.** *J Cell Biol* 1996, **134**:1349-1363.

44. Bystricky K, Laroche T, van Houwe G, Blaszczyk M, Gasser SM: **Chromosome looping in yeast: telomere pairing and coordinated movement reflect anchoring efficiency and territorial organization.** *J Cell Biol* 2005, **168**:375-387.

45. Albert B, Mathon J, Shukla A, Saad H, Normand C, Leger-Silvestre I, Villa D, Kamgoue A, Mozziconacci J, Wong H *et al.*: **Systematic characterization of the conformation and dynamics of budding yeast chromosome XII.** *J Cell Biol* 2013, **202**:201-210.

46. Backlund MP, Joyner R, Weis K, Moerner WE: **Correlations of**
•• **three-dimensional motion of chromosomal loci in yeast revealed by the double-helix point spread function microscope.** *Mol Biol Cell* 2014, **25**:3619-3629.

Novel type of fluorescent microscopy to analyse in 3D tracking loci was used, and confirmed sub-diffusive behavior of chromatin *in vivo*.

47. Cai LH, Panyukov S, Rubinstein M: **Mobility of spherical probe objects in polymer liquids.** *Macromolecules* 2011, **44**:7853-7863.

48. Weber SC, Thompson MA, Moerner WE, Spakowitz AJ, Theriot JA:
• **Analytical tools to distinguish the effects of localization error, confinement, and medium elasticity on the velocity autocorrelation function.** *Biophys J* 2012, **102**:2443-2450.

Analysis of loci trajectories are classically analyzed using mean-square displacement (MSD). Other type of analysis were used to explore chromatin motion *in vivo*.

49. Thompson M, Haeusler RA, Good PD, Engelke DR: **Nucleolar clustering of dispersed tRNA genes.** *Science* 2003, **302**:1399-1401.

50. Chen M, Gartenberg MR: **Coordination of tRNA transcription with export at nuclear pore complexes in budding yeast.** *Genes Dev* 2014, **28**:959-970.

51. Brickner JH, Walter P: **Gene recruitment of the activated INO1 locus to the nuclear membrane.** *PLoS Biol* 2004, **2**:e342.

52. Ahmed S, Brickner DG, Light WH, Cajigas I, McDonough M, Froyshteter AB, Volpe T, Brickner JH: **DNA zip codes control an ancient mechanism for gene targeting to the nuclear periphery.** *Nat Cell Biol* 2010, **12**:111-118.

53. Casolari JM, Brown CR, Komili S, West J, Hieronymus H, Silver PA: **Genome-wide localization of the nuclear transport machinery couples transcriptional status and nuclear organization.** *Cell* 2004, **117**:427-439.

54. Saner N, Karschau J, Natsume T, Gierlinski M, Retkute R,
• Hawkins M, Nieduszynski CA, Blow JJ, de Moura AP, Tanaka TU: **Stochastic association of neighboring replicons creates replication factories in budding yeast.** *J Cell Biol* 2013, **202**:1001-1012.

Super-resolution microscopy was used to investigate spatial organization of individual replicon. Model was used to quantify replication factories formation.

55. Mine-Hattab J, Rothstein R: **Increased chromosome mobility facilitates homology search during recombination.** *Nat Cell Biol* 2012, **14**:510-517.

56. Dion V, Kalck V, Horigome C, Towbin BD, Gasser SM: **Increased mobility of double-strand breaks requires Mec1, Rad9 and the homologous recombination machinery.** *Nat Cell Biol* 2012, **14**:502-509.

57. Seeber A, Dion V, Gasser SM: **Checkpoint kinases and the INO80 nucleosome remodeling complex enhance global chromatin mobility in response to DNA damage.** *Genes Dev* 2013, **27**:1999-2008.

58. Mizuguchi T, Fudenberg G, Mehta S, Belton JM, Taneja N,
•• Folco HD, FitzGerald P, Dekker J, Mirny L, Barrowman J *et al.*: **Cohesin-dependent globules and heterochromatin shape 3D genome architecture in S. pombe.** *Nature* 2014.

High resolution contact map (10 kb) in *S. pombe* reveal the role of cohesin complexes in boundaries of 'globules', small region of chromatin locally interacting. Cohesin loss disrupt globules, except in heterochromatin domains of the genome.

1.3 Extended discussion-the dynamics of the rDNA

Most of the research on the chromatin dynamics is focused on the non-rDNA chromatin (see "Introduction" 1.2.7). The dynamics of the non-rDNA chromatin follows a behavior consistent with the Rouse regime. However, in our novel dataset, we observed two regimes of the Rouse dynamics of the non-rDNA chromatin. We propose that such behavior is caused by the very extended fluorescent tagging.

Our group's previous work also suggested that the motion of the rDNA has two regimes: increasing slowly for short time scales (t < 5s, scaling exponent ~0.25) and then more abruptly after 5s (scaling exponent ~0.7) (Albert et al., 2013). In my new tracking, we failed to reproduce two regimes, most likely because of the specific selection of very bright fluorescent tags in rDNA. Our results further confirmed that the motion of the rDNA is very different than non-rDNA chromatin and it can be fitted well with one regime: the MSD of rDNA followed by a behavior with scaling exponent of ~0.7 (Figure 28).

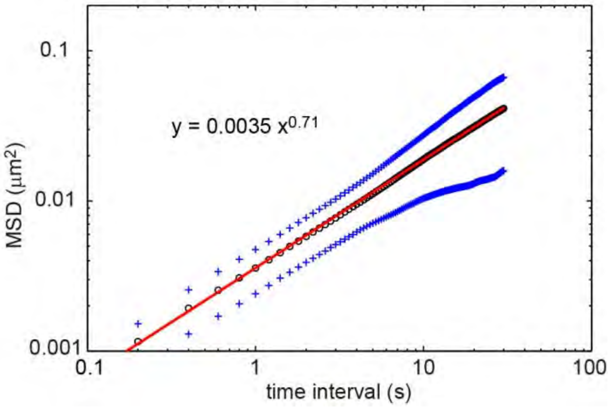

Figure 28. The dynamics of rDNA.

The black dataset represents the average MSD over 41 trajectories for a selected bright locus located at rDNA on chromosome XII. Standard errors are indicated as blue plus symbol. The motion of the rDNA followed by a power law with scaling exponent of ~0.7 (red line).

rDNA on chromosome XII, which is organized in the nucleolus, plays a key role in the ribosomes formation (see "Introduction" 2.1.3). The nucleolus has a totally different confinement compared with the nucleoplasm. Compare with the nucleoplasm, nucleolus is a more crowded region, so the motion of rDNA is both slower and following different constrains than non-rDNA. In addition, the repetitive nature of the rDNA, its peculiar chromatin structure, and the very high transcription rate may also play a role in this different mobility. It will be interesting to compare the dynamics of rDNA in the nucleolus with 25 copies and 200 copies. Further study on the rDNA dynamics are still required to investigate rDNA organization.

2. The influence of transcription on chromatin dynamics

2.1 Objective and summary

We have shown that the chromatin dynamics of non-rDNA loci were consistent with the Rouse polymer model, which describes chromosome as an ideal chain of beads connected by elastic springs. The characteristic length of these springs is characterized by only one adjustable parameter compatible with the very high flexibility of the fiber. However, the estimated flexibility of such ideal chain did not match the typical length scales of a 10-nm fibers. Then, we cooperated with Aurélien Bancaud's laboratory to study the biophysical properties of the chromatin in living yeast cells.

In this draft, we first tested the Rouse polymer model of chromosome motion *in vivo* and compared with the ideal Rouse motion of purified chromosome fragements *in vitro* (Marius's work). The results revealed that, opposed to ideal chain, chromatin polymer must be modeled uncoupling viscous drag and persistence length. *In vivo*, viscous friction is drastically increased, to a large extent due to transcription. To analyze the influence of transcription on the chromatin dynamics, we then constructed two temperature sensitive (TS) strains which would be transcriptionally inactivated after the temperature is high (with the help of Marta Kwapisz). We studied the chromatin moiton in a reference strain (WT) and a TS strain before and after transcription was inactived. The results revealed that upon transcription inactivation, chromatin motion increased, making chromatin properties closer to ideal chain. Altogether our study sheds new light on the structural properties of chromosomes based on direct measurements *in vivo*. We propose that the chromatin in living cells is best modeled with an alternative Rouse model: the "branched Rouse model".

2.2 Draft of manuscript: "Analysis of chromatin fluctuations in yeast reveals the transcription-dependent properties of chromosomes"

Analysis of chromatin fluctuations in yeast reveals the transcription-dependent properties of chromosomes

Marius Socol*, Renjie Wang*, Pascal Carrivain, Jean-Marc Victor, Kerstin Bystricky, Olivier Gadal and Aurélien Bancaud

Introduction

Characterizations using biochemical techniques or live cell microscopy have revealed the dynamic nature of eukaryotic chromosomes for molecular interactions and for spatial fluctuations. This behavior as well as the recurrent detection of irregular 10-nm fibers by cryo-TEM of thin nuclear sections has led to a new model of chromosome structure, which folds into a liquid-like state (Maeshima et al., 2010). However, the mechanical and structural parameters underlying these folding properties remain unclear.

We and others have recently showed that is chromosome motion in yeast was characterized by an anomalous sub-diffusive behavior with an anomalous parameter persistent over four time decades (Albert et al., 2013; Cabal et al., 2006; Hajjoul et al., 2013; Marshall et al., 1997; Verdaasdonk et al., 2013; Wang et al., 2015; Weber et al., 2010). We further suggested that this response offered a unique window to the characterization of chromosome structural properties using Rouse polymer model. This model describes chromosomes as a chain of beads connected by elastic springs. The length of these springs, which is referred to as the Kuhn length (*b* in the following), is related to the flexibility of the fiber. Our previous estimates indicated an unexpectedly low value of the Kuhn length of less than 5 nm that did not match the typical length scales of a 10-nm fiber.

We thus reasoned that the unrealistically low flexibility of chromatin required a clarification. Hence we validate the Rouse model to measure the flexibility of biomolecules, and show that the flexibility of chromatin is five-fold enhanced for chromatin over that of naked DNA *in vitro*. We then confirm our recent result (Hajjoul et al., 2013) that the dynamics of chromosomes is consistent with a very low value of the Kuhn length of ~1 nm in wild type cells, and therefore seek whether this unexpected response is related to transcription. In Pol II TS mutant *rpb1-1*, we show that transcription inactivation induces a global increase of chromatin dynamics, which is not associated with variation in nucleoplasmic viscosity. Because high-resolution nucleosome mapping did not show changes in nucleosome positioning 20 minutes after transcription shutdown (Weiner et al., 2010), we conclude that the viscous drag is increased for active transcription, possibly due to the binding of RNA nucleo-protein complexes on the fiber. This result, which allows us to estimate the Kuhn length and hydrodynamic radius of chromosomes of ~5 nm, is discussed in light of simulations of chromatin, which show the key role of nucleosomes to determine a flexible fiber.

Results

We designed a minimal *in vitro* system in which macromolecule motion can be explored in defined environments. We purified chromosome fragments of several Mbp with short fluorescent tracks of ~50 kbp. Because the level of crowding in the nucleoplasm is expected to screen out hydrodynamic interactions (Hajjoul et al., 2013), we used a high proportion of poly-vinylpyrrolidone (PVP, 360 kDa) to obtain a crowded solution with purely viscoelastic constraints and no shear thinning (Lacroix et al., 2016). The mean square displacement (MSD) of DNA fluorescent loci (left panel of Fig. 1A) as well as the step distribution function (SDF, Fig. 1B) was consistent with the Rouse model (see methods section, Rouse 1953), in which the temporal evolution of the MSD is characterized by a power law regime associated to an exponent of 0.5. The validity of this model has been extensively documented for concentrated solutions of synthetic polymers (Ewen and Richter, 1997). By minimizing of the residual between the fit and the MSD or SDF data (right panel of Fig. 1A), we measured the Kuhn length of DNA of 105+/-5 nm, in agreement with the reference value of the literature. Furthermore we carried out the same experiment with a solution containing 2% of low molecular weight PVP (40kDa). These conditions are below the overlapping concentration, so that hydrodynamic interactions should dictate DNA fluctuations. Accordingly, the Zimm model (see methods section, Fig. 1C), which depends on the solvent viscosity and not on the polymer flexibility, yielded an improved fit in comparison to the Rouse model. Therefore the analysis of fluctuations allowed us to extract quantitative measurements of DNA mechanical parameters.

Using the same genomic material, we subsequently reconstituted chromatin fibers with purified assembly and remodeling factors with a repeat of 165 bp (see methods), and probed the dynamics of fluorescent loci in a crowded polymer solution (Fig. 1D). Using the MSD and the SDF (Fig. 1D), we evaluated the Kuhn length of ~20 nm for nucleosome arrays, and hence confirmed that chromatin flexibility is greater than that of DNA *in vitro*. Altogether our in vitro system allowed us to demonstrate that chromatin is more flexible than DNA in the bulk, but measured Kuhn length *in vitro* is still higher than our earlier reports on chromosomes *in vivo*.

We then developed a systematic approach, which combined particle motion analysis and steady state localization by genemap analysis (Berger et al., 2008), to characterize a fluorescent locus on Gal genes (chromosome II) *vs*. a control locus on chromosome XII (position 680) (Fig. 2A, B). We first focused on the behavior of chromosomes in the presence of three different carbon sources, namely glucose, galactose, and raffinose. The metabolic pathways of glucose and galactose induce well-defined and distinct transcriptional state: Gal genes are active, inactive or poised for transcription in the presence of galactose, glucose, or raffinose, respectively. Locus on chromosome XII is a control away of Gal genes. We observed that the dynamics of the chromatin locus on chromosome XII were similar in glucose, galactose and raffinose (supplementary Fig. S1A) and their localization remained central (Fig. 2A). Motion analysis inferred from the MSD further confirmed the relevance of the Rouse dynamics with MSD~0.009 $\Delta t^{0.54}$ (black dashed lines in the upper panel). For Gal genes, we detected the well-documented relocalization of the locus at the periphery in the presence galactose (bottom panel in Fig. 2B). While we measured the same dynamics as for chromosome XII with glucose or raffinose (supplementary Fig. S1B), motion appeared to be 21% more dynamic in galactose (red dataset in Fig. 2B) whether the locus localization was peripheral or central (not shown). Consequently the activation of Gal genes induces a *local* onset in dynamics that may be attributed to active motion directed by transcribing polymerases (Ghosh and Gov, 2014). Focusing the reference behavior in glucose, which corresponds to 5 out of 6 experimental conditions, we recorded the SDF (Fig. 2C), and observed that this dataset together with the MSD were consistent with the Rouse model. The fit with the "ideal" Rouse model yielded a very small value of the Kuhn length of ~1-2 nm assuming that the viscosity of the nucleoplasm was 7 mPa.s (Fig. 2D, see more below). This study confirmed our recent report on the flexibility of chromatin in living yeast (Albert et al., 2013; Hajjoul et al., 2013), yet it did not allow us decipher the molecular origin of this apparent flexibility.

Next we wished to investigate the effect of transcription on chromosome dynamics using RNA polymerase II temperature-sensitive mutant *rpb1-1*, which shuts down mRNA synthesis rapidly at 37°C (Peccarelli and Kebaara, 2014). Ten minutes after transcription arrest, we detected an enhancement of ~50% of chromosome dynamics for both chromosome II and XII (right panels of Fig. 3A-B), whereas temperature modulation in wild type cells only induced a marginal increase of the amplitude of fluctuations (left panels of Fig. 3A-B). Interestingly we did not detect significant change in localization for the two different loci in WT or TS strains at 25 and 37°C (lower panels Fig. 3A-B), and we noted that the chain behavior inferred from SDF analysis (Fig. 3C) remained consistent with the Rouse model. In order to rule out effects in viscosity associated to transcription arrest, we monitoring the spatial redistribution of Tet-GFP molecules after photobleaching (supplementary Fig. S2). The similar relaxation kinetics in WT or TS cells at 25°C and 37°C indicated that 10 minutes of transcription shutdown indicated that the viscosity was roughly constant in every condition. Furthermore given that high-resolution nucleosome mapping did not show changes in nucleosome position 20 minutes after transcription shutdown (Weiner et al., 2010), we attributed the augmentation in fluctuation amplitude to a change in chromatin hydrodynamic friction. Indeed the Rouse model is dictated by the balance between elastic forces with viscous drag (see equation 1). Hence active transcription appears to increase the effective size of the chromatin fiber, likely through the loading of protein complexes as well as RNA molecules, and hence to slow down the motion of chromosomes globally. According to this interpretation, chromosomes should not be described with the ideal Rouse model, but with the “branched-Rouse” model with an intrinsic flexibility of the chromatin backbone and a drag coefficient determined by the load of nucleo-protein complexes around it. We therefore fitted our data with two parameters, the Kuhn length and the hydrodynamic radius a (Fig. 3C). The region of the parameter space associated to consistent fits had a parabolic profile, and this region was shifted towards larger values of the Kuhn length upon transcription arrest (right panel of Fig. 3C). In this situation, the ideal Rouse model, in which friction and flexibility are proportional, predicts a Kuhn length of ~5-7 nm. Given our argument that the fiber properties are similar at 25°C or 37°C, we conclude that the hydrodynamic radius is ~10 nm with active transcription and only ~5 nm after transcription shutdown.

We finally asked whether a high degree of flexibility was reasonable for the fiber. For this we run simulations of a fiber with the crystal structure of nucleosomes (i.e. DNA wrapped two times around DNA) or with open nucleosomes, meaning that the most labile interaction between DNA and histones at SHL=+/-6.5 is released.

Material and methods

DNA and chromatin preparation for in vitro experiments

Genomic DNA was extracted from U2OS cells, which had been treated to allow the stable incorporation of dUTP-Cy3 tracks of 50 kbp during replication (Lacroix et al., 2016). Chromatin was reconstituted using a reconstitution kit (Active Motif) with ~10 ng of this genetic material together with 1 μg of unlabeled λ-DNA. DNA or chromatin was subsequently diluted in a low ionic strength buffer (2X TBE, pH=8.3) with variable proportions of Poly-vinylpyrrolidone (Sigma-Aldrich) of 360 or 40 kDa. The dynamic viscosity was set to 6 or 2.3 mPas with 2% PVP 360 or 40 kDa, respectively. Note that our experiments were performed with a small proportion of Polystyrene Carboxylated Fluorescent beads of 100 nm in diameter (Invitrogen) in order to monitor the viscosity during the experiments based on the analysis of the diffusion coefficient of these objects.

Yeast strains

Genotypes of the strains used in this study are described in supplementary Table S1. To obtain haploid yeast strains carrying *rpb1-1* (*rpb1-G1437D*) thermosensitive mutation, genomic loci, Nop1p and Nup49p labeled with GFP or mcherry following crosses were made. For CMK8-1A, YGC242 strain was crossed with D439-5b. For CMK9-4D, JEZ14-1a was crossed with CMK8-5B. Obtained diploids were sporulated and haploid spores were selected.

Cell culture

Yeast media were used as previously described (Rose et al., 1990). YPD is made of 1% yeast extract, 2% peptone and 2% dextrose. SC is made of 0.67% nitrogen base w/o amino acids (BD Difco, USA), 2% dextrose supplemented with amino acids mixture (AA mixture Bio101, USA), adenine and uracil. Cells were grown overnight at 30 °C (or other temperature we used) in YP media containing 2% carbon source, cells were diluted at 10^6 cells/mL in rich glucose, galactose or raffinose containing media. Cells were harvested when OD_{600} reached 4×10^6 cells/mL and rinsed twice with the corresponding SC media. Cells were then spread on slides coated with corresponding SC patch containing 2% agar and 2% of corresponding carbon source. Cover slides were sealed with "VaLaP" (1/3 vaseline, 1/3 lanoline, 1/3 paraffin). Microscopy was performed during the first 10 to 20 min after the encapsulation of the cells in chamber.

Confocal microscopy for gene map acquisition

Confocal microscopy was performed with an Andor Revolution Nipkow-disk confocal system installed on a Olympus IX-81, featuring a CSU22 confocal spinning disk unit (Yokogawa) and an EMCCD camera (DU 888, Andor). The system was controlled using the mode "Revolution FAST" of Andor Revolution IQ1 software (Andor). Images were acquired using an Olympus 100× objective (Plan APO, 1.4 NA, oil immersion). Single laser lines used for excitation were diode pumped solid state lasers (DPSSL) exciting GFP fluorescence at 488 nm (50 mW, Coherent) and mCherry fluorescence at 561 nm (50 mW, CoboltJive). A Semrock bi-bandpass emission filter (Em01-R488/568-15) allowed collection of green and red fluorescence. Pixel size was 65 nm. For 3D analysis, Z-stacks of 41 images with a 250 nm Z-step were used.

Wide field microscopy for single particle tracking

Images were acquired with a Zeiss Microscope endowed with an sCMOS camera (Zyla, Andor) and equipped with a 40× objective (Plan APO, 1.4 NA, oil immersion). The light source was a Lumencor system, and we used the same Semrock bi-bandpass filter. The pixel size was set to 160 nm. A heating system (PE94, Linkam) was used to monitor the temperature at 37°C whenever necessary. Acquisitions were performed with inter-frame intervals of 40 to 200 ms for a total frame number of 300. For each condition, we recorded the motion of chromosomes in ~30 cells.

Image analysis and data proceeding

The motion of chromosome loci was processed with the TrackMate Plugin (Schindelin et al., 2012). Data obtained by movies processing were analyzed with a Matlab script to extract the mean square displacement (MSD) in 2D. We only considered long trajectories with more than

~100 consecutive tracked positions, and derived the MSD for time intervals lower than 50% of the total duration, and then averaged series of MSD during time steps smaller than 40 inter-frame intervals. For the extraction of gene maps, confocal stacks were processed with the Matlab script Nucloc, available at http://www.nucloc.org/ (MathWorks) (Berger et al., 2008).

Data processing

The Rouse model describes a polymer as a series of beads of radius *a* separated by elastic springs of stiffness *k*. For a finite chain with *N* monomers, the mean square displacement reads:

$$MSD(\tau) = 2Q_{11}^2\tau + 2\sum_{j\geq 2}^{N} Q_{1j}^2 . \frac{1-e^{-\lambda_j \tau/\tau_0}}{\lambda_j} \quad \text{Eq. (1)}$$

with

$$\begin{cases} Q_{i1} = \frac{1}{\sqrt{N}} \; Q_{ij} = \sqrt{\frac{2}{N}} * \cos\left[\frac{\left(i-\frac{1}{2}\right)(j-1)\pi}{N}\right] \\ \lambda_j = 2\frac{k}{\xi}\left[1 - \cos\left(\frac{(j-1)\pi}{N}\right)\right. \end{cases} \quad \text{Eq. (2)}$$

The friction term for individual monomers ξ is $6\pi\eta_s a$ with η_s the solution dynamic viscosity, and the relaxation time τ_0 is equal to ξ/k with $k = \frac{3k_B T}{b^2}$ according to fluctuation dissipation arguments. *b* is the Kuhn length, and a is equal to *b/2* in the standard model. Note that we set N to ~3000 in all our fits in order to focus on the Rouse regime, given its relevance over a broad temporal scale (Hajjoul et al., 2013).

For the Zimm model, which takes into account long-range hydrodynamic interactions, the following equation was used:

$$MSD(\tau) = \frac{2\Gamma_{1/3}}{\pi^2} N b^2 * \left(\frac{\tau}{\tau_Z}\right)^{2/3} \quad \text{Eq. (3)}$$

with the Zimm time scale $\tau_Z = \frac{\eta_s R_F^3}{\sqrt{3\pi} k_B T}$, $\Gamma_{1/3} = 2.67\;9$. Note that for a Gaussian chain with $R_F^2 \sim N b^2$, Eq. (3) only depends on the solvent dynamic viscosity.

The step distribution function in two dimensions, *i.e.* in the focal plane of the objective (Saxton, Lateral diffusion of single particle), is calculated according to:

$$P(r,\tau) = \frac{2r}{MSD(\tau)} e^{-r^2/MSD(\tau)} \qquad \text{Eq. (4)}$$

Fluorescence photobleaching/activation experiments

Cells were grown in glucose medium, and then placed on a Zeiss LSM710 confocal microscope with temperature control using an agarose pad. The experiment was carried out either at 24°C or during the first 10 minutes after setting the temperature to 37°C. Imaging was carried out with 40X water immersion objective and using small regions of interest around individual cells in order to reach fast inter-frame intervals of ~20 ms. 10 images were recorded before photobleaching half of the nucleus, as described in (Beaudouin et al., 2006) and fluorescence recovery was measured in the bleached region. At least 14 cells were used in each of the four conditions: wild type and TS cells at 25°C or 37°C. Because the bleaching time was slighly different from cell to cell, temporal traces were registered by setting the time of the image before the bleach to 0, and all the datapoints were combined into a single dataset, which was eventually smoothed with a box filter.

FIGURE LEGENDS

Figure 1: Dynamics of DNA and reconstituted chromatin *in vitro*. (A) The left panel shows the MSD over time for a locus on genomic DNA. The fluorescent loci consist of dUTP-Cy3 tracks randomly incorporated along purified chromosome fragments. Using a "crowded" solution with 2% polyvinylpyrrolidone (PVP, 360 KDa), we measured a set of MSD (black diamonds) and the average response (red squares), which was fitted with the Rouse model (black solid line) for a Kuhn length of 105 ± 5 nm, as shown by the residual of the fit in the right plot. Note that the solid green line corresponds to the MSD expected for the Zimm model for a viscosity of 6 mPa.s. **(B)** The three plots represent the probability distribution function for 3 time intervals (as indicated in inset), and the corresponding fits obtained with the Rouse model for a Kuhn length of 100 nm in agreement with the value obtained for MSD fitting. **(C)** The green dataset represents the average MSD for chromosome loci immersed in a 2% PVP (40 kDa) solution. The green and black solid lines show the Zimm and Rouse model, respectively, for a viscosity of 2.3 mPas and a Kuhn length of 100 nm. **(D)** In the upper left panel, the MSD temporal evolution is reported for fluorescent loci on chromosome fragments equipped with nucleosomes (see methods). This data is consistent with the Rouse model for a Kuhn length of 22 nm, as shown by the residual plotted in the lower left panel. Note that the level of crowding is enhanced in this experiment with a PVP concentration (360 kDa) of 3.2% and a dynamic viscosity of 14.7 mPa.s. In the right panel, we plot the probability density function for 3 time intervals and the corresponding fit with the Rouse model for a Kuhn length of 20 nm.

Figure 2: Chromatin dynamics in living yeast. (A) The chromatins we studied on chromosome XII and II are shown at the top (red arrows). The plot represents the temporal evolution of the MSD at 25°C for a locus on Chromosome XII using glucose or galactose as carbon source (cyan or red dataset, respectively). The dashed black lines represent the Rouse model dataset we published before. The two genemaps below are recorded in the same experimental conditions. Yellow circles and red ellipsoids depict the 'median' nuclear envelope and nucleolus, respectively. N represents the number of nuclei used to generate the probability density map. **(B)** The same study as in **(A)** is carried out for the *GAL1* gene on chromosome II. **(C)** The step distribution function for three different time intervals is represented for the locus on chromosome XII. The total number of events is ~3000 for each

dataset. The corresponding solid correspond to the behavior expected with the Rouse model, showing the consistency of the model with the entire dataset. **(D)** The fit with the “ideal” Rouse model yielded a very small value of the Kuhn length of ~1-2 nm, as shown by the residual plotted. Note that the viscosity is set to 7 mPas based on the literature.

Figure 3: Interplay between transcription and chromosome dynamics. (A) The upper panels represent the temporal evolution of the MSD for chromosome XII in wild type or temperature sensitive mutants (left and right plots) at two different temperatures of 25 and 37°C (cyan and red datasets, respectively). The genemaps below correspond to the average locus distribution in each experimental condition. Yellow circle and red ellipsoids respectively depict the ‘median’ nuclear envelope and nucleolus. *N* represents the number of nuclei used to generate the probability density map. **(B)** The same experiment as in **(A)** is reported for the *GAL1* gene on chromosome II. The dashed black lines represent the Rouse model dataset we published before. **(C)** The two graphs represent the step distribution function for the *GAL1* gene in the temperature sensitive strain at 25°C and 37°C (left and right plots, respectively). The line plots correspond to the predictions of the Rouse model for a set of parameters (*a,b*) shown in the lower panels. The standard Rouse model with *a=b/2* is shown by the white line.

Figure S1: Chromatin dynamics in different carbon sources. (A) The plot represents the temporal evolution of the MSD at 25°C for a locus on Chromosome XII using glucose or raffinose as carbon source (cyan or red dataset, respectively). The dashed black lines represent the Rouse model dataset we published before. The two genemaps below are recorded in the same experimental conditions. Yellow circles and red ellipsoids depict the ‘median’ nuclear envelope and nucleolus, respectively. N represents the number of nuclei used to generate the probability density map. **(B)** The same study as in **(A)** is carried out for the *GAL1* gene on chromosome II.

Figure S2: Flurescence photobleaching/activation tests of GFP-tagged nucleus of wild type and TS strains. (A) The first image shows GFP steady-state distribution in the nucleus before photobleaching. 10 images were recorded (here we showed one) before photobleaching half of the nucleus and fluorescence recovery was measured in the bleached region (white rectangle). Then we detected the recovery of the fluorescence (see t>0 s). **(B)** The fluorescence intensity gradually increased with the time after photobleaching, and after 1s, the intensity almost recovered stable. For each conditions, there were more than 14 samples. **(C)** Similar with **(B)**, the relative intensity recovery curves.

Table S1: Genotypes of strains used in this study.

Name	**Genotype**
YGC242	*MATalpha, his3Δ0, leu2Δ0, ura3Δ851, ade2-801, lys2-Δ202, LYS2::TETR-GFP, nup49-Δ::HIS-MX, interGAL1-FUR4::(tetO*112)-NAT; carrying plasmid pASZ11-NUPNOP (GFP-NUP49, mCherry-NOP1, ADE2)*
JEZ14-1a	*MATa, his3-Δ1, leu2-Δ0, ura3-Δ0, ade2-801, lys2-801, LYS2::TETR-GFP, nup49-Δ::HPH-MX6, interYLR188W-YLR189C::ura3::TetO-NAT*
D439-5b	*MATa, rpb1-1, leu2-Δ1, ura3-52, trp1-Δ63, lys2-801, his3-Δ200*
CMK8-5B	*MATalpha, rpb1-1, lys2, leu2, ura3, nup49-Δ::HISMX; carrying plasmid pASZ11-NUPNOP (GFP-NUP49, mCherry-NOP1, ADE2)*
CMK8-1A	*MATa, rpb1-1, his3, leu2, ura3, lys2, LYS2::TETR-GFP, interGAL1-FUR4::(tetO*112)-NAT); carrying plasmid pASZ11-NUPNOP(GFP-NUP49, mCherry-NOP1, ADE2)*
CMK9-4D	*MATa, rpb1-1, his3, leu2, ura3, lys2, LYS2::TETR-GFP, nup49-Δ::HPH-MX6, interYLR188W-YLR189C::ura3::TetO-NAT; carrying plasmid pASZ11-NUPNOP (GFP-NUP49, mCherry-NOP1, ADE2)*

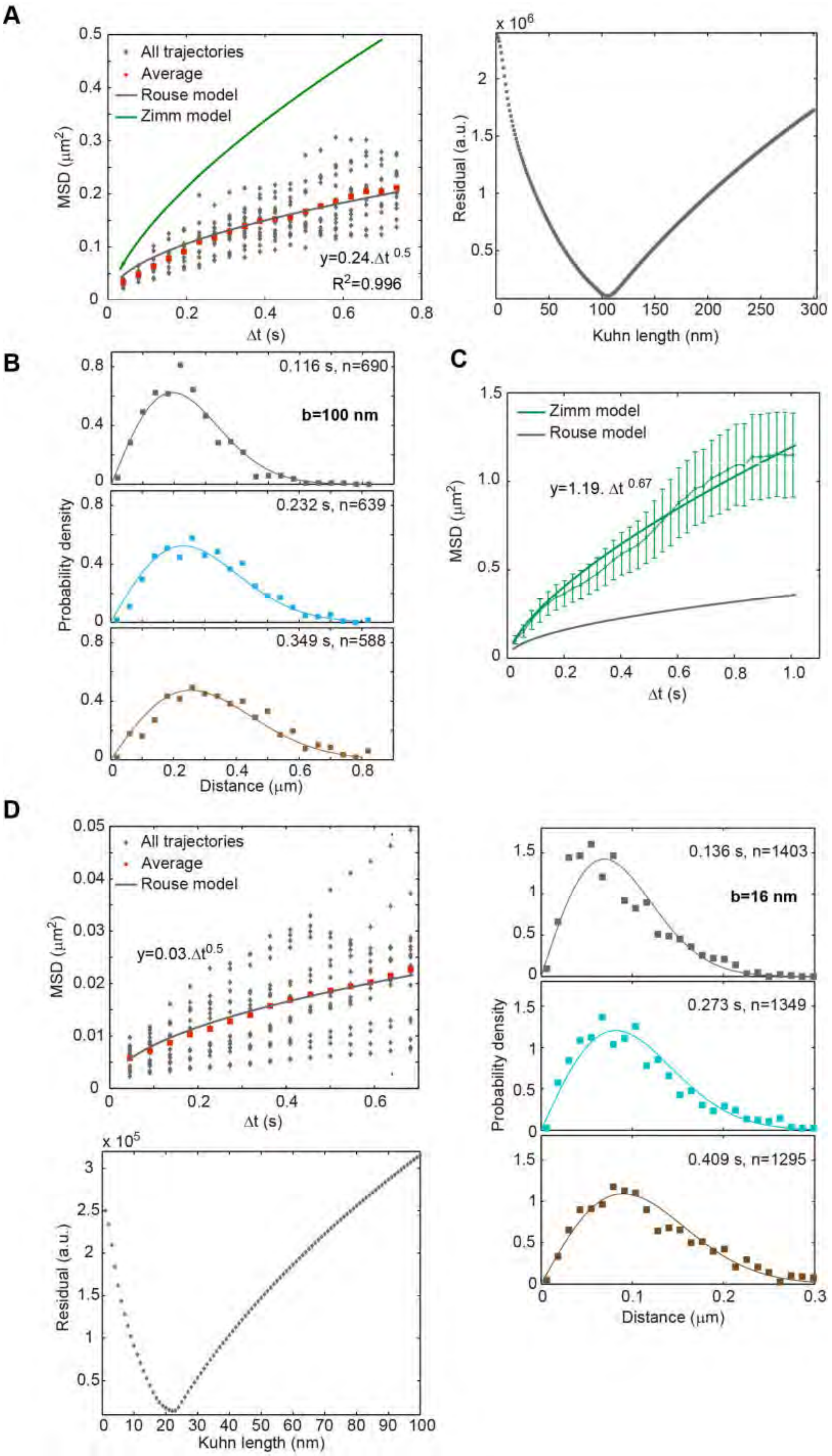
A
All trajectories
Average
Rouse model
Zimm model
MSD (μm²)
Δt (s)
y=0.24.Δt 0.5
R²=0.996
x 10⁶
Residual (a.u.)
Kuhn length (nm)
B
0.116 s, n=690
b=100 nm
0.232 s, n=639
0.349 s, n=588
Probability density
Distance (μm)
C
Zimm model
Rouse model
y=1.19. Δt 0.67
MSD (μm²)
Δt (s)
D
All trajectories
Average
Rouse model
y=0.03.Δt0.5
MSD (μm²)
Δt (s)
x 10⁵
Residual (a.u.)
Kuhn length (nm)
0.136 s, n=1403
b=16 nm
0.273 s, n=1349
0.409 s, n=1295
Probability density
Distance (μm)

Figure 1

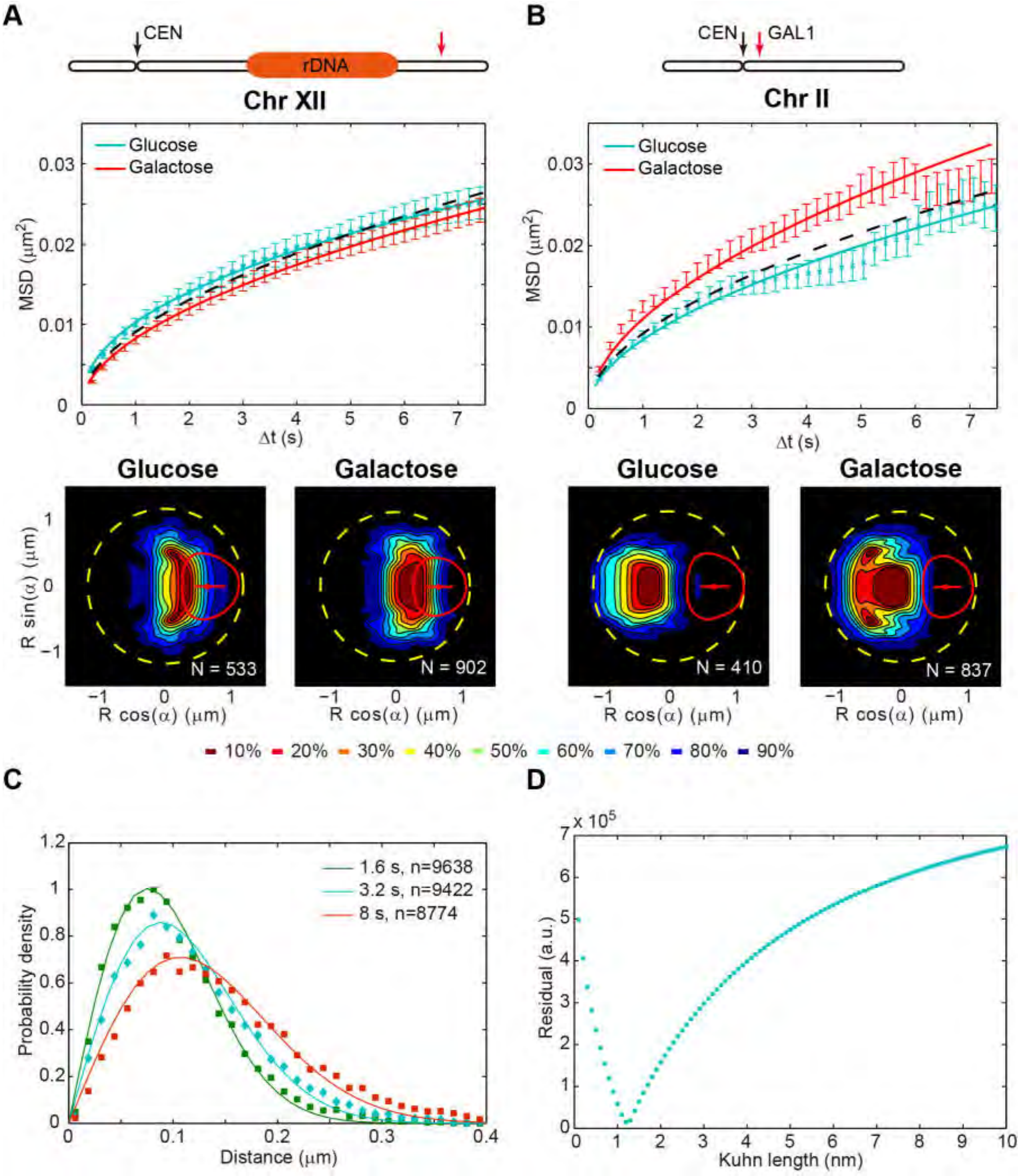
A
CEN
rDNA
Chr XII
Glucose
Galactose
MSD (µm²)
Δt (s)
B
CEN
GAL1
Chr II
Glucose
Galactose
Glucose
Galactose
R sin(α) (µm)
R cos(α) (µm)
N = 533
N = 902
N = 410
N = 837
10% 20% 30% 40% 50% 60% 70% 80% 90%
C
1.6 s, n=9638
3.2 s, n=9422
8 s, n=8774
Probability density
Distance (µm)
D
x 10^5
Residual (a.u.)
Kuhn length (nm)

Figure 2

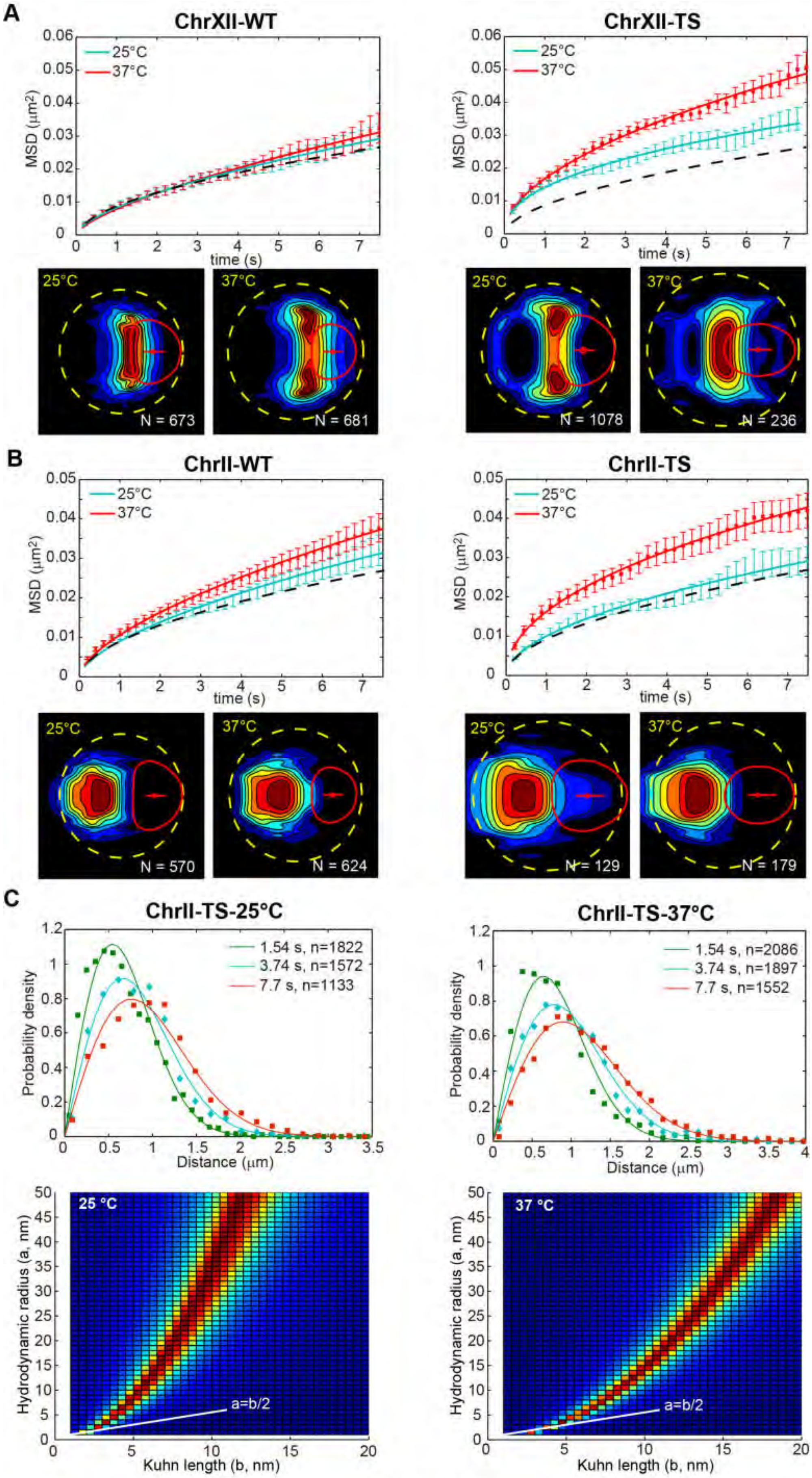
A
ChrXII-WT
25°C
37°C
MSD (μm²)
time (s)
N = 673
N = 681
ChrXII-TS
N = 1078
N = 236
B
ChrII-WT
N = 570
N = 624
ChrII-TS
N = 129
N = 179
C
ChrII-TS-25°C
1.54 s, n=1822
3.74 s, n=1572
7.7 s, n=1133
Probability density
Distance (μm)
ChrII-TS-37°C
1.54 s, n=2086
3.74 s, n=1897
7.7 s, n=1552
25 °C
37 °C
Hydrodynamic radius (a, nm)
Kuhn length (b, nm)
a=b/2

Figure 3

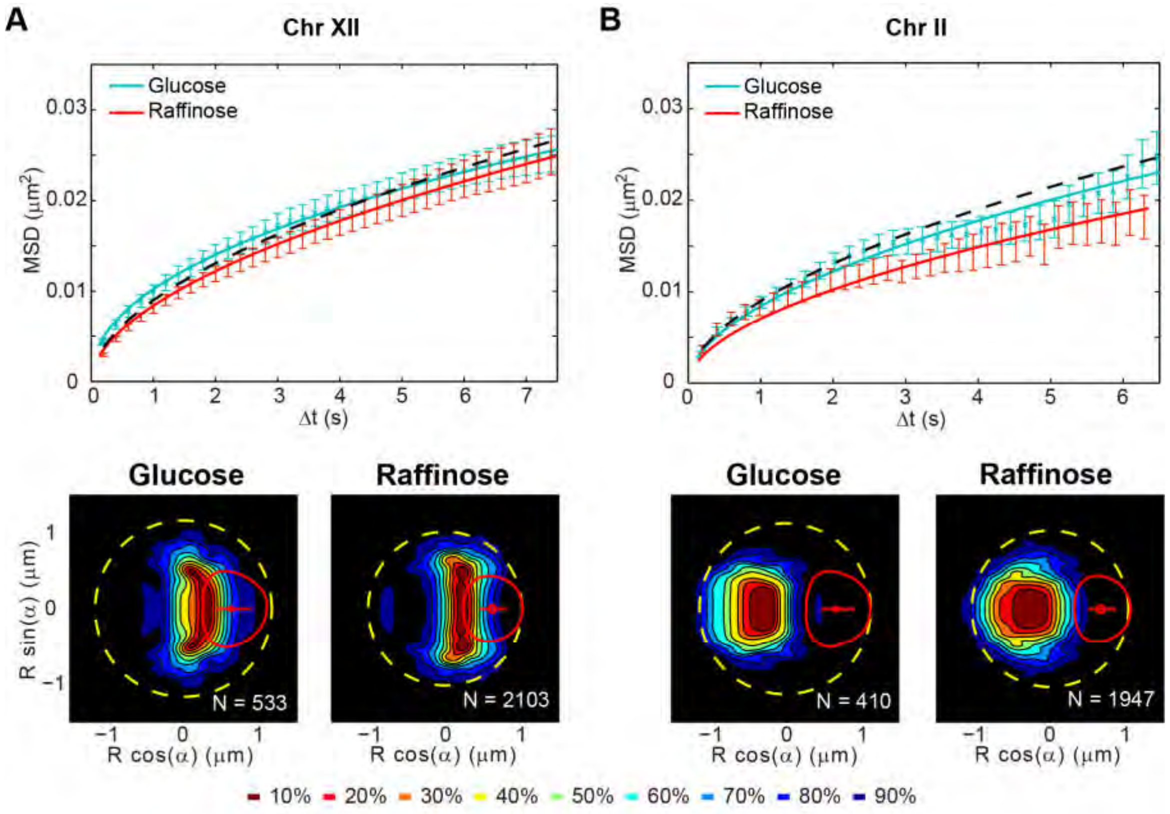
A
Chr XII
Glucose
Raffinose
MSD (μm^2)
0
0.01
0.02
0.03
0 1 2 3 4 5 6 7
Δt (s)
B
Chr II
Glucose
Raffinose
MSD (μm^2)
0
0.01
0.02
0.03
0 1 2 3 4 5 6
Δt (s)
Glucose
Raffinose
Glucose
Raffinose
R sin(α) (μm)
1
0
−1
N = 533
N = 2103
N = 410
N = 1947
−1 0 1
R cos(α) (μm)
10% 20% 30% 40% 50% 60% 70% 80% 90%

Figure S1

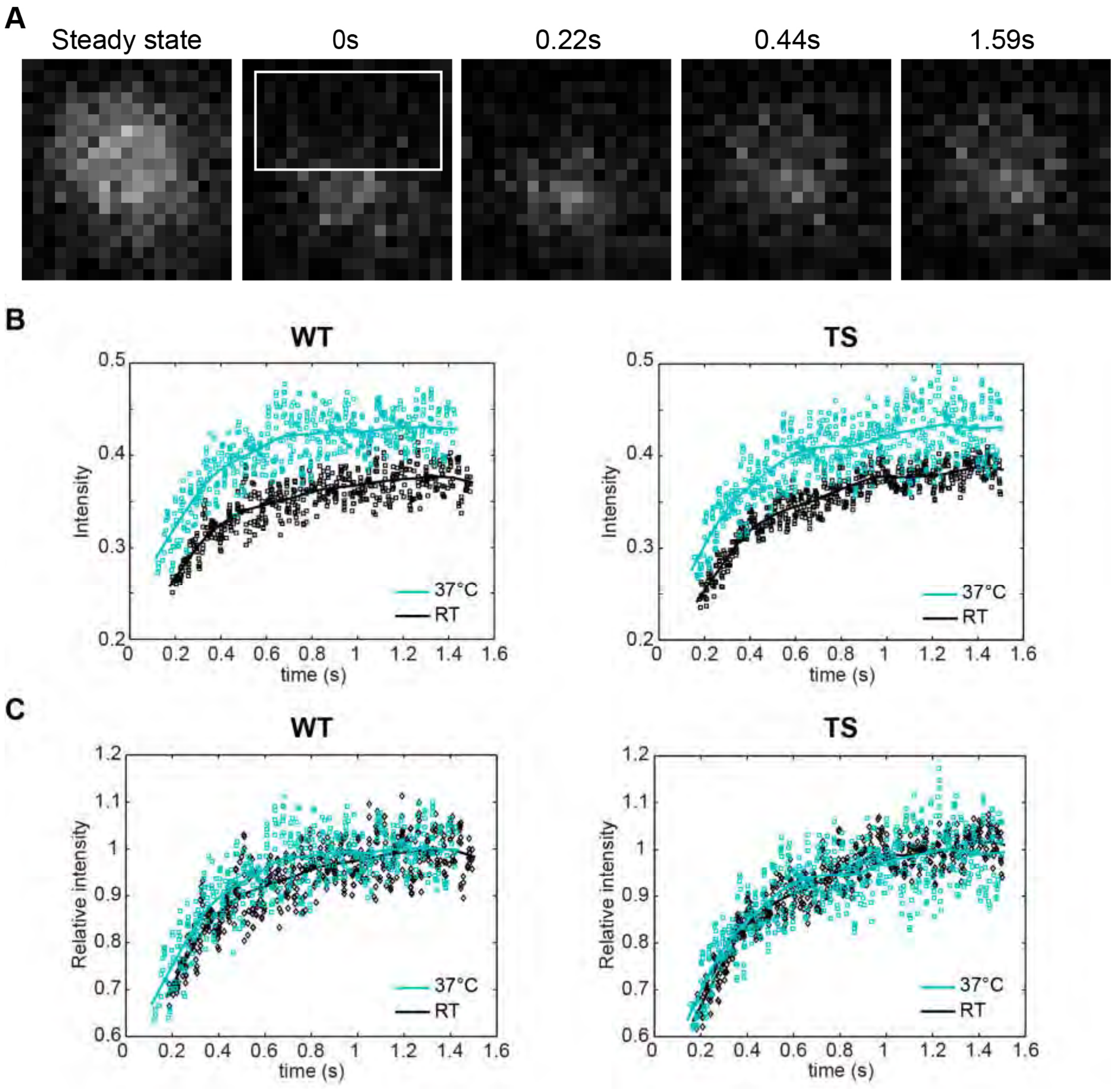
A
Steady state
0s
0.22s
0.44s
1.59s
B
WT
TS
Intensity
time (s)
37°C
RT
0.2
0.3
0.4
0.5
0
0.2
0.4
0.6
0.8
1
1.2
1.4
1.6
C
WT
TS
Relative intensity
time (s)
37°C
RT
0.6
0.7
0.8
0.9
1
1.1
1.2

Figure S2

3. Determination of the nuclear geometry in living yeast cells

3.1 Objective and summary

The nuclear shape and size have significant links with the chromosome organization (see “Introduction” 2). So the second axis of my PhD project was to create an accurate technique to determine the nuclear shape and size in 3D in living yeast cells.

In the following part, I will present a new algorithm I created, “NucQuant”, based on the published method “Nucloc” which was used to track the ‘gene territory’ (see “Introduction” 1.2.6). “NucQuant” is an automated fluorescent localization method including post-acquisition correction of the measurement bias due to spherical aberration along Z-axis. It can accurately interpolate the NE position in a large cell population. Based on this method, we determined the nuclear shape and size of yeast cells growing in different carbon source. Combining microfluidic technology with “NucQuant” we also accurately estimated the geometry of the nuclei in 3D along entire cell cycle. Finally, we determined the nuclear shape and size in quiescent cells. The NPC distribution was also studied by using this technique (see manuscript 3).

In the extended discussion section, I also present how this method can be used to determine the heterogeneity of the nuclear morphology and the nucleolar organization at the nuclear periphery. In addition, this technique also can be used to analyze the distribution of the NPC in different cell cycle stages.

3.2 Submitted manuscript: "High resolution microscopy reveals the nuclear shape of budding yeast during cell cycle and in various biological states"

High resolution microscopy reveals the nuclear shape of budding yeast during cell cycle and in various biological states

Renjie Wang, Alain Kamgoue, Christophe Normand, Isabelle Léger, and Olivier Gadal

High resolution microscopy reveals the nuclear shape of budding yeast during cell cycle and in various biological states

Renjie Wang[1], Alain Kamgoue[1], Christophe Normand[1], Isabelle Léger[1], Thomas Mangeat[2] and Olivier Gadal[1]

[1]Laboratoire de Biologie Moléculaire Eucaryote, Centre de Biologie Intégrative (CBI), Université de Toulouse, CNRS, UPS, 31000 France
[2]Laboratoire de biologie cellulaire et moléculaire du contrôle de la prolifération, Centre de Biologie Intégrative (CBI), Université de Toulouse, CNRS, UPS, 31000 France

Corresponding author:
Olivier Gadal
Equipe Organisation et Dynamique Nucléaire
LBME du CNRS, Bâtiment IBCG
Toulouse University
118 route de Narbonne
F-31000 Toulouse, France
Phone: +33(0)5 61 33 59 39
Fax: +33 (0)5 61 33 58 86
E-mail: olivier.gadal@ibcg.biotoul.fr

Summary statement:

- Novel enhanced resolution method to explore the 3D geometry of the nuclear envelope.
- Increased NPC density near SPB and nucleolus
- Stereotyped asymmetry of nuclear envelope toward nucleolus.

Keywords: localization microscopy; nuclear pore complex; nuclear geometry; super resolution microscopy

Running title: Yeast nuclear geometry in 3D.

Abstract

How does the spatial organization of the genome depend on the nuclear shape is unknown, mostly because accurate nuclear size and shape measurement is technically challenging. In large cell populations of the yeast *Saccharomyces cerevisiae*, we assessed the geometry (size and shape) of nuclei in three dimensions (3D) with a resolution of 30 nm. We improved an automated fluorescent localization method by implementing a post-acquisition correction of the spherical microscopic aberration along the Z-axis, to detect the three dimensional (3D) positions of nuclear pore complexes (NPCs) in the nuclear envelope (NE). We used here this method called Nucquant, to accurately estimate the geometry of nuclei in 3D along the cell cycle. To increase robustness of the statistics, we aggregated thousands of detected NPC from a cell population in a single representation using nucleolus or spindle pole body (SPB) as references to align nuclei along the same axis. We could detect asymmetric changes of the nucleus associated with the modification of nucleolar size. Stereotypical modification of the nucleus toward nucleolus further confirmed the asymmetric properties of the nuclear envelope.

Introduction

Structural organization of the genome is a key determinant in all genome transactions, including transcription and genome stability. In eukaryotic cells in interphase, genomic DNA is segregated away from the cytoplasm by the nuclear envelope (NE). Components of the inner nuclear membrane (INM) or nuclear pore complexes (NPCs) are crucial players in the spatial regulation of gene expression or genome stability (Towbin et al., 2009). Modification of the nuclear radius or altered sphericity affects the ability of loci to interact with NPCs and INM (Zhao et al., 2016). The confinement of *S. cerevisiae* genome in the cell's nucleus persists throughout the cell cycle because they have a closed mitosis. Only few structural features are involved in the inner organization of the budding yeast nucleus in interphase: the spindle pole body (SPB), centromeres, telomeres and the nucleolus. The SPB, the budding yeast microtubule-organizing center, is embedded into the nuclear envelope. Except a short time window after centromere's replication, SPB anchors each centromere via a microtubule spindle during the entire cell cycle (Winey and O'Toole, 2001). Telomeres are associated to the NE (Taddei et al., 2010). In exponentially growing cells, nuclear volume is subdivided into two third containing the nucleoplasm and one third the nucleolus (Léger-Silvestre et al., 1999). The SPB and the nucleolus being diametrically opposed in interphase (Yang et al., 1989), the SPB, the nuclear center and the nucleolar centroid define a central axis around which chromosomes are organized. This axis enabled the design of chromatin models as space-filling polymer, which accurately recapitulate most of the known features of the genome organization (Tjong et al., 2012; Wong et al., 2012). Importantly, the Alber's lab has shown that an accurate simulation of chromosome positioning largely depends on constrains imposed by the shape of the nucleoplasm (Tjong et al., 2012). Therefore, the nuclear volume and shape should be precisely defined to explore eukaryotic genome organization.

Nucleus in budding yeast is often described as a sphere of radius ~1µm, ignoring described variations of size: the median nuclear volume can vary up to two fold between yeast strains (Berger et al., 2008); carbon source has major impact on the nuclear size (Jorgensen et al., 2007); each yeast nucleus undergoes a two-fold increase in volume from G1 to S phase (Jorgensen et al., 2007; Winey et al., 1997). Additionally, budding yeast nucleus is not a perfect sphere and size determination cannot always rely on spherical approximation (Zhao et al., 2016). Vacuole is also known to modify nuclear shape (Severs et al., 1976). During closed mitosis, the nucleus adopts a number of non-spherical conformations: microtubule spindle cycle modifies nuclear shape (Yeh et al., 1995) and bud constriction constrains nuclear morphology (Boettcher et al., 2012). The chromatids segregation process is asymmetric: the mother cell's nucleus is one half larger than the daughter cell's nucleus (Heun et al., 2001). In the nucleus, SPB and nucleolus are known to impact on nuclear shape. During mitosis, SPB can affect locally NE sphericity (Koning et al., 1993). In interphasic cells growing exponentially in medium containing glucose, the nucleolus is described as a crescent shape nuclear domain flanking the NE. During cell cycle delay (S or G2), NE expansion is constrained toward nucleolus (Witkin et al., 2012). All these observations highlight the highly dynamic NE and the variability of nuclear size and shape (Stone et al., 2000; Webster et al., 2009). Accurate determination of the NE position using fluorescence microscopy is technically challenging and is mostly performed in two dimensions (2D) (Dultz et al., 2016). Recent technics have been proposed to explore the nuclear geometry in 3D (Zhao et al., 2016).

Here, we developed “NucQuant”, an optimized automated image analysis algorithm, accurately interpolating the nuclear envelop position in a large number of cell's nuclei in three dimensions (3D). Super-resolution fluorescence localization microscopy is now a well-established concept used to break resolution barrier in fluorescence microscopy: 200 nm in X-Y and about 500 nm in Z-axis (Nelson and Hess, 2014). Localization microscopy measures the position of isolated objects, single molecules (e.g. PALM, FPALM, STORM) or point-like structures, with an uncertainty of a few tens of nanometers. Isolated point-like structures can be fitted with the characteristic Gaussian distribution of fluorescence around local maxima approximating the point spread function of the optical setup (Thomann et al., 2002). GFP tagged NPC components appear as typical punctate ring staining the nuclear envelope (NE) (Wimmer et al., 1992). This bright staining originates from a high number of nucleoporins per NPC (up to 64) and the presence of 60 to 180 NPCs per nucleus (Rout et al., 2000; Winey et al., 1997). The punctate staining is caused by the non-random distribution of NPC within the NE (Winey et al., 1997), resulting in local clusters of NPCs. Therefore, adjacent NPCs, convolved by optical set-up, appear as punctuated bright spots within the NE. Therefore, GFP tagged nucleoporins represent ideal point-like structures to follow the NE shape and size by localization microscopy (Berger et al., 2008). We localized fluorescently labeled NPC and corrected detection bias due to optical spherical aberration along the Z-axis to accurately compute an approximation of the NE in 3D. Such approach allowed us to precisely measure the size and shape of the yeast nucleus along the cell cycle or in cells growing on different carbon sources: we could recapitulate the considerable level of plasticity of NE. Using the nucleolus or SPB as spatial landmark to align nuclei along the same axis and aggregate thousands of detected NPCs from a cell population in a single representation, we could evaluate the NPC density along the NE in different physiological conditions. We detected a low NPCs density in the NE at the nucleolar/nucleoplasmic interface and stereotypical modifications of the NE correlated with nucleolar size variations.

Results

Localization microscopy using confocal fluorescent imaging of Nuclear Pore Complexes is a super-resolution microscopic technique

“Localization microscopy” relies on detection of the centroid of point-like structures, and is classically not limited by diffraction, but by signal-to-noise ratio of individual detections. To label NPC, we fused GFP or mRFP dimers with abundant NPC components (Nup49, Nup57, Nup2 or Nup159). We developed an algorithm “NucQuant”, adapted from previously described automated image analysis pipeline using spinning-disk fluorescence microscopy and MATLAB codes (Berger et al., 2008). We could detect a median of 22 peripheral spots per cell's nucleus. Each detected spot should roughly correspond to a group of 3 to 9 closely spaced NPCs, hereafter called cNPCs (Winey et al., 1997). Importantly, 22 spots detection per nucleus provided sufficient connecting points to evaluate the NE position in 3D.

Refractive index mismatch between optical setup and biological object is known to generate spherical aberration along Z-axis (Fig. 1A and B). We measured and corrected this detection bias in our measurements. For exponentially growing cells in glucose, electron microscopy and X-ray tomography established that the yeast nucleus in interphase is mostly spherical (Larabell and Le Gros, 2004; Murata et al., 2014; Wei et al., 2012; Winey et al., 1997). We analyzed about 1000 round cell's nuclei and could generate a statistically robust dataset of about 20,000 cNPC detections (Fig, 1C). The nuclear sphericity allowed measurement of detection bias in our localization dataset. In a sphere, distances between detected cNPCs and the nuclear center are the same in each dimension (X, Y and Z) (Fig. S1A and C). Simulating the elongation along Z axis (Fig S1A to B) modified the distribution of normalized distances between detected cNPCs and nuclear center along X, Y and Z axis (compare Fig. S1C and D). Similar over-estimation along Z-axis was clearly detected in our experimental measurement (Fig. 1C). In our experimental dataset, post-acquisition correction of localized cNPCs was performed as suggested previously (see Materials and Methods; Fig S1E) (Cabal et al., 2006). This correction was calculated using round nuclei for each cell population that we analyzed, and was applied subsequently to the entire population (including non-round nuclei ; Fig S1F). Note that spherical aberration was always detectable, but modified for different objectives or microscope setups (confocal laser scanning- versus laser spinning disk- microscopes) (Fig. S1G, H).

To evaluate the resolution of our detection method after spherical aberration correction, we made use of the known distribution of nucleoporins in NPC near the central channel (Nsp1 complex subunits: Nup49 and Nup57), toward the nuclear basket (Nup2) and localized in the cytoplasmic filaments (Nup159) (Fig. 2A) (Alber et al., 2007; Dilworth et al., 2001; Grandi et al., 1995; Rout et al., 2000). To analyze the distribution of detected cNPCs, we computed their radial distances to the nuclear center. Labeling simultaneously two nucleoporins respectively with GFP or mRFP, we detected about 20,000 cNPCs in each color from cell's nuclei population. Radial distribution of detected cNPCs was plotted as cumulative frequency of either distances to the nuclear center or a fitted ellipsoid approximation of the NE using GFP or mRFP signals (Fig. 2B, C, D, E). As expected, median distances (to the nuclear center or to the fitted NE) between constituents of the Nsp1 subcomplex (Nup49-GFP and Nup57-mRFP) were equivalent (+4 to +9 nm; Fig. 2B). Median distance separating nuclear basket (Nup2-mRFP; intranuclear structure) to cytoplasmic filaments (Nup159-GFP; most distant structure to nuclear center) was from +48 to +51 nm (Fig. 2C). Adding the distance measured from nuclear basket to central channel (+20 to +26 nm) to the distance from central channel to cytoplasmic filaments (+13 to +26nm) allowed to determine *in vivo* the cNPC length perpendicular to the NE (from +33 to 52 nm) (Fig. 2D, E). This distance, measured *in vivo,* is largely compatible with the 50 nm separating nuclear basket from the cytoplasmic filaments measured by transmitted electron microscopy (TEM) after immuno-detection of Protein-A tagged nucleoporins from purified NE (Alber et al., 2007). Furthermore, *in vivo* fluorescently tagged Nup159 and the nucleoporin Nup60 which colocalized with Nup2 on the inner side of NPC, were shown to be separated by 60 nm using structured illumination microscopy (Guet et al., 2015).

We concluded that localization of cNPCs in the NE can be used to achieve robust super-resolution detection with sufficient accuracy to distinguish longitudinal position of nucleoporins within NPC. Therefore, we used the accuracy of cNPC detections to explore the nuclear envelop in 3D.

3D-NE model for complex shaped nuclei along the cell cycle

An asynchronous cell population contains cells in all cell cycle phases. The most abundant cells are in G1-S with quasi-round nuclei that in previous works were analyzed thanks to a spherical or ellipsoid fitting (Berger et al., 2008; Figure 2). To improve the NE fitting, the nuclear size and shape of quasi-round nuclei were explored using cNPCs position. The high number of detected cNPCs per nucleus allowed a precise interpolation of the NE geometry. We generated a 3D model of the NE using detected cNPCs. We also tested model prediction against simulated NPCs positions for a sphere or an ellipsoid (Fig. S2). NE shape in 2D was detected at very high resolution in electron microscopic micrographs of sections of cells fixed by high-pressure freezing followed by freeze substitution. This cell preparation resulted in optimal morphological preservation of NE (Fig. 3A). Direct connection of adjacent detected cNPCs in 2D resulted in a non-accurate estimation of the NE (Fig. 3A). Then, we computed a smooth estimation of NE by connecting adjacent detected cNPCs using spline interpolation (spline-NE model) (see Materials and Methods; Fig. 3A and 3B). Using this approach, nuclear surfaces and volumes were systematically underestimated (Figs. 3A-B; S2A). In such spline-NE model, detected cNPCs must be the most distant points of the NE to the nuclear center. This geometric constraint could trigger bias in the NE approximation on yeast sections. To prevent such bias, we generated additional anchoring points of the NE using the three closest cNPCs (Fig. 3A, 3C, see material and methods). Using simulated NPC positions, this method, called 3D-NE model slightly overestimated nuclear size for small number of NPCs (<20), but was more accurate than spline-NE for high number of NPCs (Fig. S2B). From the 3D-NE model, we could extract the surface (S_n) and volume (V_n) of each nucleus accurately in interphasic cells with quasi-round nuclei (Fig. 3C right panel).

Cells in G2/M displayed non-spherical nuclei with complex shapes ranging from elongated, constricted-, sausages-, hourglass- shaped structures (Yeh et al., 1995). In non-spherical nuclei, the spatial coordinates of cNPCs distributed as more than one cluster (Figure 3D, upper graphs). 3D-NE model using only one cluster was indeed not accurate and resulted in cNPC at constriction ring appearing inside the fitted nucleus (Fig 3D, low right panel). Splitting cNPCs into two clusters, the 3D-NE model performed on each cluster was more accurate (Figure 3D, right panel). If two clusters 3D-NE model approach generated overlapping volumes, then the algorithm subtracts surface and volume of the intersection. During late anaphase, a significant number of cNPCs were also detected in a long NE tube connecting the two nuclei (extended hourglass shape). Such configuration was explored by defining a third cluster of cNPCs (Fig. 3E). Therefore, considering 1, 2 or 3 cNPCs clusters, nuclei at each stage of cell cycle can be fitted using the 3D-NE model.

Quantification of the nuclear geometry during the cell cycle

Using the improved 3D-NE model described above, we investigated the nuclear size and shape modifications along the cell cycle. To avoid any potential perturbations of the nucleus caused by hormonal synchronization, living yeast cells were first observed in a microfluidic setup for an entire cell cycle (about 90 min), with image acquisitions every 15 min (Fig. 4A). Using our algorithm, we could accurately estimate surface and volume of nuclei along the cell cycle, allowing calculation of sphericity (Fig. 4B). Sphericity is defined as the ratio of the surface of a theoretical sphere having the same volume as the analyzed nucleus, to the measured surface of the considered nucleus (Wadell, 1935); see material and methods). Here, we analyzed 20 cells using the microfluidic setup. During interphase, nuclei increased in volume from 3 to 4.2 μm^3. Nuclear division resulted in a new daughter's cell nucleus of 2 μm^3, and a mother's cell nucleus of larger size (3.4 μm^3) in agreement with previous reports (Fig 4B, Table S1) (Heun et al., 2001). Sphericity is high in interphase (0-45min), and is largely reduced in mitosis (60 to 90 min). After mitosis, mother and daughter nuclei are both close to a sphere (Fig 4B; right panel). Acquisition time interval of 15 min in the microfluidic setup was established to reduce bleaching of fluorophore but increased the probability to miss some transient nuclear shapes (Yeh et al., 1995). To overcome this limitation, we analysed nuclei in a large assychronous cell populations. Indeed, the fraction of cells in one cell cycle phase in a large population is proportional to its duration; we thus converted percentage of cells in time. We could classify six stages along the 90 min cell cycle and measured sphericity for each stage (Figure 4C). Cells in G1 (stage 1) and in S phase (stage 2) have quasi spherical nuclei (sphericity>0.99). In late S, rapid (3-8 min) extention of intranuclear microtubule spindle provokes a small compression of nuclei (stage 3). Prior to nuclei entering through the bud constriction, stage 4 was characterized by elongated nuclei (4 - 1 min) along spindle axis. From stage 1 to 4, fitting 3D NE-model with one cluster was appropriate. Once nuclei entered through bud constriction (stages 5 and 6), two or three clusters had to be used to fit the NE. In stage 5, sphericity is reduced by bud construction and spindle elongation (from 0.98 to 0.8). At the end of mitosis, hour-glass shaped nuclei were elongated with a tube connecting the two nuclei (sphericity <0.8).

In conclusion, our approach allowed the quantification of cell cycle nuclear variations in *S. cerevisiae* assessed in single living cells and in large cell populations.

Geometry of interphasic nuclei in different metabolic conditions

It was reported that the nuclear size is reduced when carbon source is changed from glucose to less favorable ones (galactose, raffinose or ethanol) (Jorgensen et al., 2007). We tested if we could measure such reduced nuclear size and any potential perturbations of the NE shape for these different diets. Each carbon source impacted the cell doubling time: 90 min in 2% glucose, 120 min in 2% galactose, 130 min in 2% raffinose and 220 min in 3% ethanol. Sphericity stayed high in all conditions, but was reduced while doubling time increased (Fig. 5A). When changing from most to less favorable carbon sources, we could measure gradual reduction of about two-fold of the nuclear volume, and an associated five-fold reduction of the nucleolar volume (Table S2).

Such drastic modification of the nucleoplasm/nucleolus ratio may affect internal nuclear organization. In glucose, the SPB and the nucleolus are roughly opposed in interphasic cells, defining a central axis (alignment of SPB, nuclear center and nucleolar centroid). We then explored the 3D geometry of the SPB relative to the nucleolus when the nucleolar volume was modified. We described the SPB and the nucleolus positions using probability density maps (Berger et al., 2008; Therizols et al., 2010). Briefly, we made use of labeled nucleolus with the mCherry tagged Nop1 protein (yeast orthologs of fibrillarin). An abundant SPB constituent Spc42 tagged with GFP was used to detect SPB, which could be distinguished from NPC signal in the same green channel thanks to its high fluorescence. SPB is duplicated during S phase and the two SPBs are pulled apart during G2/M. Only cells in G1 and early S phase with a single spot corresponding to SPB were considered for analysis. SPB was positioned relative to two reference points: the nuclear center and the centroid of the nucleolus. This approach enabled to define a cylindrical coordinates system with an oriented axis in which we described the position of the SPB by its distance from the nuclear center (R) and the angle from the central axis (α) (Fig. 5B). In galactose or raffinose, the SPB was indeed opposite to the nucleolus as it was in glucose, with a median angle α of 30°. When the less favorable carbon source ethanol was used, this angle significantly increased to 40° (Fig. 5C). We next generated probability density map of SPB distribution. We used nuclear and nucleolar center as landmarks. To align the all nuclei analyzed in the same coordinates system, we translated all nuclear centers to the origin and rotated them around the origin so that nucleolar centroids (secondary landmark) became aligned on the X-axis. This allowed to rotate SPB positions around the central axis (Fig. 5B, φ =angle around central axis) and into a single plane (φ=0; cylindrical projection), essentially without loss of information. Kernel density estimation was then used to define a SPB density map, similarly to the previously described probability density map of genomic loci (Berger et al., 2008; Therizols et al., 2010). On the SPB density map (Fig. 5D), the yellow dashed circle represents the median nucleus periphery and the median nucleolus is displayed as solid red (glucose) or orange (other carbon sources) curves. SPB remains opposed nucleolus, but nucleolus was reduced massively, up to 5 fold (compare red to orange solid lines) (Fig. 5D).

We then decided to evaluate the distribution of detected cNPCs using the same central axis, to generate an NPC map using similar kernel density distribution. Plotting NPC maps, we could quantify the probability density of cNPCs in the NE of yeast growing in glucose, galactose, raffinose or ethanol (Fig. 5E). On this NPC density map, the white dashed circle represents the median nucleus periphery in glucose medium, while yellow dash circles correspond to median nucleus in other carbon sources. As previously described, nucleus size was drastically reduced when the growth rate was reduced (compare yellow to white dashed circle; see also Table S2(Jorgensen et al., 2007). cNPC density along NE appeared non-uniform. To quantify differences in cNPCs density between the yeast growing in different carbon sources, we plotted variation of cNPC density along the central axis (Fig. 5F). In all carbon sources tested, detected cNPCs appeared slightly depleted in the NE at the nucleolus/nucleoplasm border. In glucose and ethanol, cNPC density slightly increased in the NE flanking the nucleolus. The cNPC non-uniformed density along the NE can reflect either a non-uniform distribution on each individual cell, or aggregation of heterogeneous nuclei in the population. In order to explore this possible heterogeneity, we then sorted nuclei, from a cells growing in glucose, according to their volume in three classes (small, medium and large), and plotted NPC map (Fig. 5G). In the NE flanking the nucleolus, the cNPC density was higher in small nuclei than in large nuclei. At the SPB (opposed to the nucleolus) similar variation of cNPC density was also detected. Similar heterogeneity was observed in population growing in galactose and raffinose media (data not shown).

In conclusion, when changing carbon source, yeast nucleus in interphasic cells remains largely spherical. However, in less favorable carbon source, sphericity is reduced and SPB position deviates from the nuclear-nucleolar central axis. Further, we could always observe a depletion of detected cNPCs at the interface of nucleoplasm-nucleolus. cNPC density in NE flanking nucleolus varies with nuclear size. Therefore, reduction of the nucleolar volume correlates with reorganization of SPB position and modification of cNPC density along NE.

Exploration of the NE during quiescence

We next explored the nuclear size and shape during quiescence establishment that has a drastic impact on the nucleolar size. Upon nutrients depletion, ribosome biogenesis is quickly repressed, resulting in the compaction of the nucleolus (Tsang et al., 2003). In quiescent cells, following an extended period of nutrients depletion, Sagot's laboratory showed that the SPB assembles a long monopolar array of stable microtubules, associated with a displacement of the nucleolus (Laporte et al., 2013). As shown in Fig 6A, this observation would lead in our quantitative approach in an increase of the α angle. We determined the SPB density map upon glucose depletion and quiescence establishment (from 2h depletion to 7 days; Fig. 6B). During establishment of quiescence, the nucleolar volume decreased and the SPB distribution deviated progressively from the central axis. The α angle (α) progressively increased during quiescence establishment, with median distribution from 30° in exponential growing cells to 70° after 7 days of nutrients depletion (Fig. 6C).

We next evaluated the distribution of cNPCs along the NE during quiescence establishment. Importantly, since the SPB and the nucleolus were not aligned, we performed NPC map using either nucleolus (Fig. 7A) or SPB (Fig. 7C) as secondary landmark. Before depletion, the NPC map defined accurately the median nucleus. After seven days, cNPC distribution was spread around the median nucleus reflecting the great heterogeneity of the NE size and/or shape amongst quiescent cells (Fig. 7A, C). However, some stereotypical patterns in cNPC distribution were clearly visible: depletion of detected cNPC at the nucleolus/nucleoplasm interface, and the cNPC concentration toward the nucleolus observed in optimal growth conditions were strengthened during starvation. Such distribution was illustrated by plotted variations of cNPC density along the central axis (Fig. 7B). Using SPB as secondary landmark (Fig. 7C), NPC maps revealed an increased number of cNPCs detected at close proximity of the SPB during quiescence establishment. Indeed, maximum radial distance ratio of cNPC along X and Y axis gradually increased during starvation establishment (Fig. 7D). We also visually detected a change of nuclear shape from spherical to elongated in more than 60% of cell's nuclei (Fig. 7E). We hypothesized that the stable monopolar array of microtubules could displace the nucleolus and modify the NE shape (Laporte et al., 2013). To test which of those modification was caused by starvation, or by the long monopolar array of stable microtubules, we evaluated nuclear shape and nucleolar position in *dyn1*Δ mutant, in which microtubule spindle is disrupted (Laporte et al., 2013). As expected, elongated nuclear shape were not observed in the mutant (Fig. 7F). Surprisingly, SPB deviation from the nuclear-nucleolar centroid axis increased during quiescence establishment was independent of spindle establishment (Fig. 7G). In conclusion, we have detected a loss of axial symmetry (SPB- nuclear/nucleolar center alignment) in quiescent cells. Furthermore, stable microtubules were involved in NE deformation, but not in the loss of axial symmetry.

Modification of the NE shape during G1 cell cycle arrest

In all tested conditions (varying carbon sources, and quiescence), the nucleolar volume was reduced. We thus analyzed NE geometry in G1 arrested cells in which the nucleolar volume is increased (Stone et al., 2000). A well-established method to analyze cell cycle progression is to synchronize cells in bulk culture. Asynchronous cells (*MAT a*) were blocked in G1 using alpha factor treatment. Progressively, the fraction of cells in G1 was increasing. Arrest lasting for more than an entire cell cycle progression resulted in a cell population with almost all cells in G1 phase. Quick wash of the alpha factor allowed cells to progress synchronously through the cell cycle as illustrated in Fig. 8A. However, cell cycle arrest is known to influence NE morphology: upon alpha factor treatment, budding yeast nuclei adopt an unusual dumbbell shape, reflecting a spatial separation of chromosomal and nucleolar domains and an increase of the nucleolar volume (Stone et al., 2000). SPB density map analysis revealed that SPB maximum density remained opposed to the nucleolus during alpha factor treatment, but had a considerably broader distribution (Fig. 8B). Although the angle of the SPB to the central axis was not affected during the treatment (Fig. 8C), the distance from the SPB to the nucleolar centroid was significantly increased and variable from cell to cell (Fig. 8D). NPC map using nucleolar centroid as secondary landmark allowed us to visualize the stereotypical dumbbell shape previously reported, and the two-fold increased nucleolar volume (Stone et al., 2000) (Fig. 8E). In 80% of the cells, nucleolus was at the center of one lobe of the dumbbell. As in asynchronous cells, we detected cNPCs depletion at the NE interface between nucleoplasm and nucleolus. Using SPB as secondary landmark, NPC map revealed a fuzzy distribution toward the nucleolus (Fig. 8F). Visual inspection of the SPB position along NE showed a deviation from the central axis of the dumbbell shaped nuclei in more than 55% of the cells (43.2% + 12.2%). It was reported that microtubules emanating from the SPB are not involved in such nuclear reorganization (Stone et al., 2000). We propose that heterogeneity in measured distances between SPB to nucleolus, and in the position of the SPB in dumbbell shape nuclei resulted in a blurred NPCs density map (Fig 8F). We quantitated this heterogeneity measuring sphericity, which decrease to a mediane value of 0.85 upon treatment, and an increased standard deviation (Fig. 8G).

In conclusion, upon alpha factor treatment, increased nucleolar volume did not modify the nuclear central axis, but did change specifically NE morphology flanking the nucleolus and correlated with an increased NE surface.

Discussion

In this paper, we explored the *S. cerevisiae* nuclei geometry in living cells using high resolution microscopy detection of closely spaced nuclear pore complexes (cNPCs) embedded in the nuclear envelope. On one hand, nuclear geometry was extrapolated from the analysis of single living cells along the cell cycle and in cell populations. Heterogeneity of the 3D nuclear geometry could be quantified using the developed “NucQuant” algorithm. On the other hand, the aggregation of numerous aligned individual cNPCs detected in nuclei in large living cells populations allowed us to generate NPC density maps. Using either SPB or nucleolus as landmarks, the maps revealed an asymmetric distribution of the cNPCs. We also generated SPB density maps to explore, with robust statistics, the distribution of SPB positions relative to the nucleolus. Moreover, analysis of starving cells with or without stable microtubules bundle and G1 arrested cells displayed modifications of the nuclear shape with stereotypical deformations of the NE toward the nucleolus.

The need for new approaches to evaluate nuclear geometry in living cells

NE morphology is dynamic and due to limited resolution of fluorescent microscopy, is mostly described qualitatively. Most of the existing measurements are diffraction limited, *i.e.* 200 nm lateral (X-Y) and 500 nm axial (Z) resolution, and often biased by optical spherical aberrations. Other techniques with higher resolution have been reported. Initially, transmission electron microscopy (TEM) performed on ultra-thin sections of yeast nuclei, revealed heterogeneous appearance of NE probably mostly due to chemical fixation artefacts (I. Léger, unpublished results). When using sample-preserving fixation, such as high-pressure cryo-fixation followed by cryo-substitution, TEM of ultra-thin (60-80 nm) sections of NE showed a smooth double membrane envelope with circular or ellipsoidal contours. When performed on ultra-thin serial sections of an entire nucleus, TEM became directly informative of the nuclear shape and volume. However, data collection of serial sections analyzed by TEM is a time-consuming technical performance and was reported for sampling of less than 100 nuclei (Winey et al., 1997). Innovative imaging techniques, relying on cryo-fixation but with less tedious exploration of 3D space, as high-voltage scanning transmission electron tomography of thick sections (Murata et al., 2014), focused ion beam combined with scanning electron microscopy (FIB-SEM) (Wei et al., 2012), and soft-X-ray tomography (Larabell and

Le Gros, 2004) are very promising. However, they are not compatible with *in vivo* imaging, and they have not yet been combined with high-throughput image analysis algorithms required to extract statistically robust dataset. Recently, 3D membrane reconstruction approach that used fluorescently tagged nuclear envelope or endoplasmic reticulum membrane marker proteins was published to precisely map the nuclear volume (Zhao et al., 2016). Here, we show that super-resolution localization microscopy of cNPC allow both, accurate nuclear size and shape determination and proper correction of spherical aberration along the Z axis. Therefore, both methods are complementary to evaluate NE shape and NPC distribution.

Discontinuous increase of the nuclear size along the cell cycle

S. cerevisiae nuclei in interphasic cells appear quasi-round. Quantifying their sphericity in 3D with the NucQuant approach, we confirmed this observation. Moreover, exploring heterogeneity in interphasic cell's nucleus, we could also recapitulate previously observed modifications of the nuclear shape in interphase, triggered by microtubules spindle prior to mitosis (Yeh et al., 1995). However, proportions of these clamped and elongated nuclei in asynchronous population were low reflecting very transient states. Additionally, following a single cell's nucleus over time, thanks to a microfluidic setup, allowed us to measure the NE surface and the nuclear volume, showing a slight deviation from a sphere in G1 and S phases. Previous studies suggested continuous increase of the nuclear volume during the cell cycle (Jorgensen et al., 2007). On the contrary, we observed a discontinuous increase of the NE surface: at mitotic onset (60 min), we detected a fast and significant NE expansion while the nucleus size slightly increased from G1 to M. The measured timing of this rapid NE surface increase is fully compatible with the activation timing of polo kinase cdc5 described to be required for NE expansion at mitotic onset (Walters et al., 2014).

Non-homogeneous distribution of closely spaced NPC (cNPC) near SPB and nucleolus

We observed non-uniform distribution of detected cNPCs along the NE. The analysis of size-sorted interphasic nuclei showed that the cNPCs density in NE near the SPB or flanking the nucleolus was different in small round early G1 nuclei versus large round late S nuclei. In quiescence, depletion of cNPCs at the nucleolus/nucleoplasm interface and the cNPC concentration toward the SPB and toward the nucleolus observed in optimal growth conditions were strengthened. This may reflect different physical properties of the NE near the SPB and at the nucleolus. A relationship between SPB and NPCs has been previously described: when SPB is ready to be duplicated, in late G1, (i.e. small nuclei or quiescent cells), cNPCs are frequently detected near SPB (Winey and O'Toole, 2001). The authors proposed that that local NE bending by NPCs was required for insertion of the newly synthetized SPB. The variation of cNPCs concentration near the SPB that we measured could reflect this involvement of NPCs in the SPB duplication. However, such specific enrichment is not detectable in artificially arrested cells in G1.

Specific interplay between the NE, the nucleolus and NPCs are also known. NE flanking the nucleolus is depleted of NPC associated proteins such as Mlp1, Mlp2, (Galy et al., 2004), Pml39 (Palancade et al., 2005) and of the inner nuclear membrane protein Esc1 (Taddei et al., 2004) suggesting that the NPCs and the inner membrane flanking the nucleolus are specialized. The NE flanking the nucleolus is also known to correlate with a local modification of the NE rigidity (Witkin et al., 2012). Is the nucleolus physically connected to the NE? Previous works established a connection between the NE and the nucleolus via INM non-NPC associated proteins, Nur1 and Heh1 distributed in the entire NE and involved in peripheral tethering of ribosomal DNA (Mekhail et al., 2008). We propose that NPCs are physically anchored to the NE. Indeed, we observed cNPCs concentration at the NE flanking the nucleolus or at the interface nucleolus/nucleoplasm was highly variable according to the cells physiology.Nucleolar volume is rapidly changing following inhibition or activation, of ribosome biogenesis (Trumtel et al., 2000). Upon quiescence caused by starvation, or changing carbon source, nucleolar volume decreased but nucleolus remained associated to the NE. Therefore, a significant fraction of the NE at the interface nucleolus/nucleoplasm lost its nucleolar connection. A physical connection of NPCs with the nucleolar component would explain their local concentration at the remaining NE flanking the nucleolus and their depletion at the nucleolus-nucleoplasm NE interface. Further, such observations suggest that physical association between NPCs flanking nucleolus and nucleolar components is kept upon ribosome biogenesis inhibition.

Nuclear geometry alteration

One important parameter in modeling genome organization in *Saccharomyces cerevisiae* is the confinement of the genomic material in the nucleoplasm (Tjong et al., 2012; Wong et al., 2012). SPB being roughly opposite to the nucleolus in interphase, and nucleolus forming a nuclear compartment excluding 90% of the genomic material, a central axis was used to define yeast nuclear geometry (angle α=0; SPB-nuclear center to nuclear center-nucleolar centroid) (Berger et al., 2008). Here, we observed that this central axis geometry was strongly correlated with nucleolar activity. When nucleolar activity was maximized (short cell cycle in rich glucose medium), deviation to ideal central axis organization was low (<30°). Upon G1 arrest, which stops cell growth, but which keeps a large nucleolar volume, this angle was unchanged. When nucleolar volume was reduced in conditions where growth rate was impaired using unfavorable carbon source, the angle increased. Finally, in quiescent cells in which the nucleolar volume was further reduced, this angle increased to 70°. Moreover, this large modification of nuclear geometry in quiescence did not depend on stable long monopolar array of microtubules. Therefore, we propose that nucleolar size, and not directly growth rate, is involved in keeping internal geometry of the nucleus around the central axis.

Conclusion

In conclusion, we have developed NucQuant, a set of computational tools to quantify the nuclear geometry (size and shape) of *S. cerevisiae*. The statistical robustness and accurate measurements obtained with this approach recapitulated known stereotypical rearrangements of the yeast nucleus, and uncovered heterogeneity of cNPC concentration along NE. Model of the yeast chromosomes had already been computed based on geometry of round shaped nuclei (mostly in G1 cells). Models of chromosomes in nuclei of quiescent cells did not take into account the modifications of the nuclear morphology as quantified in our work (Guidi et al., 2015). Quantification of stereotypical modifications of the nuclear morphology, observed when changing carbon source, upon quiescence or in G1 arrested cells, will now allow to refine chromosomes structure models by integrating changes of the nuclear confinement defined by nuclear shape and size and by modifications of the nucleolar compartment. Numerous observations point to a relationship between the nuclear size and shape and pathological process or aging (Webster et al., 2009). However, apparent heterogeneity from nucleus to nucleus limits our ability to study mechanistic insight. Probabilistic density maps, presented here for a model organism, might drive future effort for metazoan cell nucleus analysis, as already proposed for endomembrane organization (Schauer et al., 2010).

Materials and Methods

Plasmids and yeast strains

Genotypes of the strains used in this study are described in supplementary Table S3. Plasmids used in this study are listed in Table S4. Yeast strains were constructed using homologous recombination.

Fluorescence and electron microscopy of yeast cells

Yeast media were used as previously described (Rose et al., 1990). Home-made PDMS chamber connected with microfluidic pump (Fluigent S.A.) allowed trapping cells under constant flow of growth medium for more than 2 hours. Confocal microscopy was performed as previously described (Albert et al., 2013). Electron microscopy was performed as previously described (Albert et al., 2011).

NucQuant: Post-acquisition correction of z aberration

Confocal images were processed and analyzed with a Matlab script NucQuant, the modification version of nucloc (http://www.nucloc.org/).

We calculated the distances between the nuclear center and the cNPCs. For each nucleus these distances were normalized by nucleus mean radius (R). This distribution was best fitted by the second-degree polynomial curve: $ax^2 + bx + c$. This equation could be used to correct the aberration along z axis: $d_{correct}/R = d/R-(ax^2 + bx)$.

NPC clustering by k-means

To reconstruct the nuclear envelope, we measured the distribution of NPCs in the clusters. After extracting the NPC positions and correcting the z aberration $(\boldsymbol{x_i, y_i, z_i})$, we used the k-means clustering method with Euclidian squared distance (Matlab) group the NPCs in different clusters $(\mathbf{C^k})$.

Spline-NE

Clustering allows us to distribute detected NPCs in each cluster $(x^k_i, y^k_i, z^k_i)_{i=1..N}$, where N is the size of cluster C^k. The first configuration of the nucleus envelope represented by the cluster C^k is given by the polyhedral patch of the set $(x^k_i, y^k_i, z^k_i)_{i=1..N}$. Since the size of C^k is very low for a smooth surface, we did three times refining using existing method (Shirman, L. A., PhD thesis, University of California, 1990). This spline interpolation give us the refining sets $(x^k_i, y^k_i, z^k_i)_{i=1..N3}$ and $(x^k_i, y^k_i, z^k_i)_{i=1..N4}$ to make the surface more smooth.

3D-NE

The first configuration of the nucleus envelope represented by the cluster C^k is given by the patch of the set $(x^k_i, y^k_i, z^k_i)_{i=1..N}$. In this patch, the surface of the nucleus envelope consists of many Delaunay triangulations which were formed by connecting the neighboring three NPCs. For one time refining, we generated one anchoring point of NE for each Delaunay triangulation. The new point at the direction from the cluster center to each Delaunay triangulation mass center, and the distance of the new point to the cluster center is the mean distance of these three NPCs to the cluster center (Fig. 3C). After three times refining, we can get enough points to generate the precise envelope. Software implementing these methods is available to download at GitHub (https://github.com/ogadal/nucquant).

Acknowledgements

We are grateful to Michael Pilsl and Jorge Perez-Fernandez for strains construction and initial characterization of the nuclear shape. We thank Aurélien Bancaud for helpful advice. This work benefited from the assistance of the imaging platform of Toulouse TRI.

Author's contributions

RW performed microscopy, analyzed data, wrote image analysis scripts and wrote the manuscript; AK conceived and wrote image analysis scripts and analyzed data; CN constructed strains, analyzed data and wrote the manuscript; IL performed electron microscopy and wrote the manuscript; TM computed spherical aberration and wrote the manuscript; OG designed experiments, analyzed data, and wrote the manuscript. All authors reviewed the results and approved the final version of the manuscript.

Funding

This work was supported by the Agence Nationale de la Recherche (ANDY) and IDEX of Toulouse University (Clemgene and Nudgene).

Figure legends

Figure 1. Detection and correction of the aberrations along Z axis. (**A**) Yeast nucleus in exponential phase with nuclear pores labeled in green and the nucleolus in red (maximum intensity projections of a 3D image stack in X-Y plane and X-Z plane). Yellow crosses show detected NPCs, green crosses show the nucleus center, blue crosses show nucleolus centroid. Green circles show the expected edge of the nucleus and white ellipse shows the detected edge. Strain yCNOD99-1a. Scale bar, 1 µm. (**B**) Immersion layer refractive index=1.51, cover slip 170 µm and refractive index=1.51, Sample refractive index=1.38. Objective lens: NA=1.4×100, lambda=520 nm. Linear Z-level shift of PSF mass center and the real Z-axial position of the fluorophore. (**C**) The normalized distances distribution of the detected NPCs to the nuclear center along X-level, Y-level and Z-level before correction of the aberration along Z axis. d= distances of NPCs to the nuclear center, R= radius of each nucleus. Strain yCNOD99-1a, a=0.26, b=0.0029, c=0.81. (**D**) The normalized distances distribution along X-level, Y-level and Z-level after correction of the aberration along Z axis. $d_{correct}$ =corrected distances of NPCs to the nuclear center.

Figure 2. The resolution of NucQuant after correction of the aberration along Z axis. (**A**) Nuclear pore complex (NPC) architecture and nucleoporins localization in the NPC. (**B-E**) Cumulative frequency of distances to the nuclear center (left panels) and of distances to the fitted ellipsoid approximation of the NE (right panels) using GFP or mRFP-tagged nucleoporins. (**B**) GFP-Nup49 and mRFP-Nup57 (Strain yRW3-1a). (**C**) GFP-Nup159 and mRFP-Nup2 (Strain yRW7-1a). (**D**) GFP-Nup49 and mRFP-Nup2 (Strain yRW4-1a). (**E**) GFP-Nup159 and mRFP-Nup57 (Strain yRW8-1a).

Figure 3. Extrapolation of nucleus envelope using detected NPCs. (**A**) 2D models building nuclear envelopes are represented onto electron microscopic micrographs of nuclear sections on which the positions of NPCs are visually detected (black arrows in the left panel ; strain BY4741). In the second image, the NE is built by connecting adjacent NPCs. In the third image, the NE is built by spline interpolation. In the right panel, the NE is fitted by generating anchoring spots in NE. Scale bars, 100 nm. (**B-C**) Based on the 3D confocal microscopic images, we could detect the NPC positions (blue spheres; strain yCNOD99-1a). Using the spline-NE model (**B**), we refined the connection to get a smooth nuclear envelope. Red circles represent the spots that were used to refine the connection. 3D-NE model (**C**) generates additional anchoring spots (blue empty circle) in the NE to get the accurate nucleus envelope.

(D) The fitted nuclear envelope based on 3D-NE model for the nuclei characterized by 1 or 2 NPCs clusters respectively (Upper graphs: X, Y, Z coordinates of detected NPCs ; black cross = centroid of detected cluster(s); cluster 1 in red, cluster 2 in green; scale bar, 1 µm; strain yCNOD99-1a). **(E)** The fitted nuclear envelope based on 3D-NE model for the anaphase nuclei characterized using 3 NPCs- clusters (cluster 3 in blue; strain yCNOD203-1a) .

Figure 4. The living yeast nuclear geometry during cell cycle. (**A**) Time course during a complete cell cycle of a single cell immobilized in a microfluidic device: NPCs in green and nucleolus in red (maximum intensity projections of a 3D image stack; Strain yCNOD99-1a) (**B**) The fitted nuclear envelope based on 3D-NE model for the nuclei in the different cell cycle phases. Surface of the NE and volume of nuclei allowed to calculate sphericity. (**C**) 3D-NE model fitting of different nuclear shapes (stages 1 to 6) along the cell cycle. The cell cycle is represented as a circle: the percentage of cells from a large population, in each cell cycle phase was converted to duration (min). For each stage (panels 1 to 6), the DIC and the fluorescent (GFP-Nup49 and Bim1-tDimerRFP) pictures are displayed (stages 1 to 6; strain yCNOD203-1a). The fitting using the 3-D NE model is also shown for each stage and was used to calculate sphericity. Scale bar, 1µm.

Figure 5. The nuclear geometry according to the carbon sources. (**A**) Cumulative distribution of sphericity of the interphase nuclei cultured in different carbon sources. Strain yCNOD99-1a **(B)** Cylindrical coordinates system with an oriented axis in which the position of the SPB is described by its distance from the nuclear center (R) and the angle from the central axis (α). Nucleolus is displayed in red. Angle Φ represent rotation around central axis. **(C)** Cumulative frequency of the angle α between SPB and the central axis. Strain yRW11-1a **(D)** SPB probability density maps based on analysis of nuclei comparing glucose to different carbon sources containing media. In glucose, dashed yellow circle: nuclear envelope determined according to the 3D-NE method; red curve: median nucleolus; red dot: median nucleolar centroid. Compare nucleolar size in glucose (red) to nucleolar size in other carbons sources (orange). N represents the number of nuclei used to generate the cumulative percentage maps. **(E)** NPCs probability density maps based on analysis of nuclei in exponential phase cells growing in different carbon sources (strain ycnod99-1a). Compare median nuclear size in glucose (white dashed circle) to other carbon sources (yellow dashed circles). N represents the number of cNPCs used to generate the cumulative percentage maps. **(F)** Plotted variation of NPC density along the central axis. **(G)** The heterogeneity of the

NPCs distribution in interphasic cells. Nuclei were sorted according to their size (1/3 small, 1/3 medium, 1/3 large nuclei ; strain yCNOD99-1a). Scale bars, 1 µm.

Figure 6. The reorganization of the nuclear central axis during quiescence. (**A**) The nuclear central axis (SPB/nuclear center/nucleolar centroid) is broken after the cells enter quiescence. Red ellipse: nucleolus; green circle: SPB; black cross: nucleus centroid; blue cross: nucleolus centroid; α: angle of SPB to the nuclear-nucleolar centroid axis. (**B**) SPB probability density maps based on analysis of nuclei after indicated time of starvation (see Materials and Methods). Representative fluorescent pictures (GFP-Nup49, Spc42-GFP and mCherry-Nop1) are displayed. Scale bars, 1 µm. (**C**) Cumulative frequency of the angle α upon incubation in glucose depleted medium (from 2 h to 7 days). Strain yRW11-1a.

Figure 7. The NE structure and NPC distribution during quiescence. (**A**) NPC probability density maps using nucleolus as secondary landmark upon time progressive incubation in glucose depleted medium. Representative fluorescent pictures (GFP-Nup49 and mCherry-Nop1) are displayed. (Strain yCNOD99-1a). (**B**) Plotted variation of NPC density along the central axis during progressive starvation. (**C**) NPC probability density maps using SPB as secondary landmark upon time progressive incubation in glucose depleted medium. Small red dot: SPB median position. Representative fluorescent pictures (GFP-Nup49 and SPC42-mRFP) are displayed. (Strain yRW9-1a). (**D**) Maximum radial distance ratio of cNPC along X and Y axis. (Strain yRW9-1a). (**E**) After the cells enter quiescence, the percentage of different nuclear geometries at incubation times in carbon depleted medium (Strain yCNOD99-1a). (**F**) In the *dyn1*Δ mutant, percentage of the elongated nuclei versus sphere-like nuclei after 48h hours to 7 days carbon depletion (Strain yRW19-1a). (**G**) SPB probability density maps based on analysis of nuclei from *dyn1*Δ mutant cells after indicating time of starvation (Strain yRW20-1a). Scale bars, 1 µm.

Figure 8. Modification of the nuclear envelope after treatment with alpha factor. (**A**) DNA content in asynchronous culture, after 2h alpha factor treatment and after alpha factor removal determined by flow cytometry (strain yCNOD99-1a). **(B)** SPB probability density maps before and after treatment with alpha factor using nucleolus as secondary landmark. Representative fluorescent pictures (GFP-Nup49, SPC42-GFP and mCherry-Nop1) are displayed (strain yRW11-1a). (**C**) Cumulative frequency of the angle SPB-central axis. (**D**) Cumulative frequency of the distances from SPB to the nucleolar centroid. (**E**) NPC probability density maps in asynchronous population (left map), after two hours alpha factor

blocking (right map) and 15 min after release in G1 (low map), using nucleolus as secondary landmark. Representative fluorescent pictures (GFP-Nup49 and mCherry-Nop1) are displayed (strain yCNOD99-1a). Drawings depict the different nuclear shapes and the position and size of the nucleolus after 2 hours treatment with alpha factor. (**F**) NPC probability density maps before and after treatment with alpha factor using SPB as secondary landmark. Representative fluorescent pictures (SPC42-GFP and Nup57-tDimerRFP) are displayed (strain yRW10-1a). Drawings depict the percentage of different nuclear geometries after 2 h treatment with alpha factor. (**G**) Cumulative distribution of sphericity. Scale bars, 1 μm.

Figure S1. Optical spherical aberration along the Z axis. (**A**) Normalized distances distribution of random spots on a sphere surface. (**B**) Normalized distances distribution of random spots on an ellipsoid surface (Rz>Rx=Ry, R=(Rx+Ry+Rz)/3). (**C**) Simulated normalized distances distribution of the spots on a sphere surface along the three dimensions (sphere radius is 1 μm; the standard localization deviation of simulated spots is 0.03 μm). (**D**) Normalized distances distribution of spots on a sphere surface along the three dimensions with spherical aberration introducing linear distance overestimation along Z axis. (**E**) Using NPCs detection and approximation of the nucleus as a sphere, the over-estimation along Z axis was measured. (**F**) Computed corrected position along Z axis. (**G**) The silicon immersion objective (left panel; Olympus; NA~1.35) decreased the aberrations compared to oil-immersion objective (right panel; Olympus; NA~1.4). (**H**) Spherical aberration along Z-axis using confocal laser scanning microscope.

Figure S2. Evaluation of the spline-NE model and 3D-NE model. We simulated a sphere of radius=1 μm (volume=blue dashed line) and an ellipsoid (volume=green dashed line) of Rx=Ry=1 μm, Rz=1.5 μm. We calculated the volume of this sphere (blue line) or ellipsoid (green line) for different number of NPCs using either the spline-NE model (**A**) or the 3D-NE model (**B**), considering that the standard localization deviation of simulated NPCs is 0 μm.

References

Alber, F., Dokudovskaya, S., Veenhoff, L. M., Zhang, W., Kipper, J., Devos, D., Suprapto, A., Karni-Schmidt, O., Williams, R., Chait, B. T. et al. (2007). Determining the architectures of macromolecular assemblies. *Nature* **450**, 683-94.

Albert, B., Leger-Silvestre, I., Normand, C., Ostermaier, M., Perez-Fernandez, J., Panov, K., Zomerdijk, J., Schultz, P. and Gadal, O. (2011). RNA polymerase I-specific subunits promote polymerase clustering to enhance the rRNA gene transcription cycle. *J. Cell Biol.* **192**, 277-293.

Albert, B., Mathon, J., Shukla, A., Saad, H., Normand, C., Leger-Silvestre, I., Villa, D., Kamgoue, A., Mozziconacci, J., Wong, H. et al. (2013). Systematic characterization of the conformation and dynamics of budding yeast chromosome XII. *J Cell Biol* **202**, 201-10.

Berger, A. B., Cabal, G. G., Fabre, E., Duong, T., Buc, H., Nehrbass, U., Olivo-Marin, J. C., Gadal, O. and Zimmer, C. (2008). High-resolution statistical mapping reveals gene territories in live yeast. *Nat Methods* **5**, 1031-7.

Boettcher, B., Marquez-Lago, T. T., Bayer, M., Weiss, E. L. and Barral, Y. (2012). Nuclear envelope morphology constrains diffusion and promotes asymmetric protein segregation in closed mitosis. *J Cell Biol* **197**, 921-37.

Brachmann, C. B., Davies, A., Cost, G. J., Caputo, E., Li, J., Hieter, P. and Boeke, J. D. (1998). Designer deletion strains derived from Saccharomyces cerevisiae S288C: a useful set of strains and plasmids for PCR-mediated gene disruption and other applications. *Yeast* **14**, 115-32.

Cabal, G. G., Genovesio, A., Rodriguez-Navarro, S., Zimmer, C., Gadal, O., Lesne, A., Buc, H., Feuerbach, F., Olivo-Marin, J., Hurt, E. et al. (2006). SAGA interacting factors confine sub-diffusion of transcribed genes to the nuclear envelope. *Nature* **441**, 770-3.

Cioci, F., Vu, L., Eliason, K., Oakes, M., Siddiqi, I. N. and Nomura, M. (2003). Silencing in yeast rDNA chromatin: reciprocal relationship in gene expression between RNA polymerase I and II. *Mol Cell* **12**, 135-45.

Dilworth, D. J., Suprapto, A., Padovan, J. C., Chait, B. T., Wozniak, R. W., Rout, M. P. and Aitchison, J. D. (2001). Nup2p dynamically associates with the distal regions of the yeast nuclear pore complex. *J Cell Biol* **153**, 1465-78.

Dultz, E., Tjong, H., Weider, E., Herzog, M., Young, B., Brune, C., Mullner, D., Loewen, C., Alber, F. and Weis, K. (2016). Global reorganization of budding yeast chromosome conformation in different physiological conditions. *J Cell Biol* **212**, 321-34.

Galy, V., Gadal, O., Fromont-Racine, M., Romano, A., Jacquier, A. and Nehrbass, U. (2004). Nuclear retention of unspliced mRNAs in yeast is mediated by perinuclear Mlp1. *Cell* **116**, 63-73.

Grandi, P., Schlaich, N., Tekotte, H. and Hurt, E. C. (1995). Functional interaction of Nic96p with a core nucleoporin complex consisting of Nsp1p, Nup49p and a novel protein Nup57p. *Embo J* **14**, 76-87.

Guet, D., Burns, L. T., Maji, S., Boulanger, J., Hersen, P., Wente, S. R., Salamero, J. and Dargemont, C. (2015). Combining Spinach-tagged RNA and gene localization to image gene expression in live yeast. *Nat Commun* **6**, 8882.

Guidi, M., Ruault, M., Marbouty, M., Loiodice, I., Cournac, A., Billaudeau, C., Hocher, A., Mozziconacci, J., Koszul, R. and Taddei, A. (2015). Spatial reorganization of telomeres in long-lived quiescent cells. *Genome Biol* **16**, 206.

Heun, P., Laroche, T., Raghuraman, M. K. and Gasser, S. M. (2001). The positioning and dynamics of origins of replication in the budding yeast nucleus. *J Cell Biol* **152**, 385-400.

Huh, W. K., Falvo, J. V., Gerke, L. C., Carroll, A. S., Howson, R. W., Weissman, J. S. and O'Shea, E. K. (2003). Global analysis of protein localization in budding yeast. *Nature* **425**, 686-91.

Jorgensen, P., Edgington, N. P., Schneider, B. L., Rupes, I., Tyers, M. and Futcher, B. (2007). The size of the nucleus increases as yeast cells grow. *Mol Biol Cell* **18**, 3523-32.

Koning, A. J., Lum, P. Y., Williams, J. M. and Wright, R. (1993). DiOC6 staining reveals organelle structure and dynamics in living yeast cells. *Cell Motil Cytoskeleton* **25**, 111-28.

Laporte, D., Courtout, F., Salin, B., Ceschin, J. and Sagot, I. (2013). An array of nuclear microtubules reorganizes the budding yeast nucleus during quiescence. *J Cell Biol* **203**, 585-94.

Laporte, D., Courtout, F., Tollis, S. and Sagot, I. (2016). Quiescent Saccharomyces cerevisiae forms telomere hyperclusters at the nuclear membrane vicinity through a multifaceted mechanism involving Esc1, the Sir complex, and chromatin condensation. *Mol Biol Cell* **27**, 1875-84.

Larabell, C. A. and Le Gros, M. A. (2004). X-ray tomography generates 3-D reconstructions of the yeast, saccharomyces cerevisiae, at 60-nm resolution. *Mol Biol Cell* **15**, 957-62.

Léger-Silvestre, I., Trumtel, S., Noaillac-Depeyre, J. and Gas, N. (1999). Functional compartmentalization of the nucleus in the budding yeast Saccharomyces cerevisiae. *Chromosoma* **108**, 103-13.

Longtine, M. S., McKenzie, A., 3rd, Demarini, D. J., Shah, N. G., Wach, A., Brachat, A., Philippsen, P. and Pringle, J. R. (1998). Additional modules for versatile and economical PCR-based gene deletion and modification in Saccharomyces cerevisiae. *Yeast* **14**, 953-61.

Mekhail, K., Seebacher, J., Gygi, S. P. and Moazed, D. (2008). Role for perinuclear chromosome tethering in maintenance of genome stability. *Nature* **456**, 667-70.

Murata, K., Esaki, M., Ogura, T., Arai, S., Yamamoto, Y. and Tanaka, N. (2014). Whole-cell imaging of the budding yeast Saccharomyces cerevisiae by high-voltage scanning transmission electron tomography. *Ultramicroscopy* **146**, 39-45.

Nelson, A. J. and Hess, S. T. (2014). Localization microscopy: mapping cellular dynamics with single molecules. *J Microsc* **254**, 1-8.

Palancade, B., Zuccolo, M., Loeillet, S., Nicolas, A. and Doye, V. (2005). Pml39, a novel protein of the nuclear periphery required for nuclear retention of improper messenger ribonucleoparticles. *Mol Biol Cell* **16**, 5258-68.

Rose, M. D., Winston, F. and Hieter, P. (1990). Methods in Yeast Genetics. A Laboratory Manual: Cold Spring Harbor, NY,.

Rout, M. P., Aitchison, J. D., Suprapto, A., Hjertaas, K., Zhao, Y. and Chait, B. T. (2000). The yeast nuclear pore complex: composition, architecture, and transport mechanism. *J Cell Biol* **148**, 635-51.

Schauer, K., Duong, T., Bleakley, K., Bardin, S., Bornens, M. and Goud, B. (2010). Probabilistic density maps to study global endomembrane organization. *Nat Methods* **7**, 560-6.

Severs, N. J., Jordan, E. G. and Williamson, D. H. (1976). Nuclear pore absence from areas of close association between nucleus and vacuole in synchronous yeast cultures. *J Ultrastruct Res* **54**, 374-87.

Siniossoglou, S., Lutzmann, M., Santos-Rosa, H., Leonard, K., Mueller, S., Aebi, U. and Hurt, E. (2000). Structure and assembly of the Nup84p complex. *J Cell Biol* **149**, 41-54.

Stone, E. M., Heun, P., Laroche, T., Pillus, L. and Gasser, S. M. (2000). MAP kinase signaling induces nuclear reorganization in budding yeast. *Curr Biol* **10**, 373-82.

Sung, M. K., Ha, C. W. and Huh, W. K. (2008). A vector system for efficient and economical switching of C-terminal epitope tags in Saccharomyces cerevisiae. *Yeast* **25**, 301-11.

Taddei, A., Hediger, F., Neumann, F. R., Bauer, C. and Gasser, S. M. (2004). Separation of silencing from perinuclear anchoring functions in yeast Ku80, Sir4 and Esc1 proteins. *Embo J* **23**, 1301-12.

Taddei, A., Schober, H. and Gasser, S. M. (2010). The budding yeast nucleus. *Cold Spring Harb Perspect Biol* **2**, a000612.

Therizols, P., Duong, T., Dujon, B., Zimmer, C. and Fabre, E. (2010). Chromosome arm length and nuclear constraints determine the dynamic relationship of yeast subtelomeres. *Proc Natl Acad Sci U S A* **107**, 2025-30.

Thomann, D., Rines, D. R., Sorger, P. K. and Danuser, G. (2002). Automatic fluorescent tag detection in 3D with super-resolution: application to the analysis of chromosome movement. *J Microsc* **208**, 49-64.

Thomas, B. J. and Rothstein, R. (1989). Elevated recombination rates in transcriptionally active DNA. *Cell* **56**, 619-30.

Tjong, H., Gong, K., Chen, L. and Alber, F. (2012). Physical tethering and volume exclusion determine higher-order genome organization in budding yeast. *Genome Res* **22**, 1295-305.

Towbin, B. D., Meister, P. and Gasser, S. M. (2009). The nuclear envelope--a scaffold for silencing? *Curr Opin Genet Dev* **19**, 180-6.

Trumtel, S., Leger-Silvestre, I., Gleizes, P. E., Teulieres, F. and Gas, N. (2000). Assembly and functional organization of the nucleolus: ultrastructural analysis of Saccharomyces cerevisiae mutants. *Mol Biol Cell* **11**, 2175-89.

Tsang, C. K., Bertram, P. G., Ai, W., Drenan, R. and Zheng, X. F. (2003). Chromatin-mediated regulation of nucleolar structure and RNA Pol I localization by TOR. *Embo J* **22**, 6045-56.

Wadell, H. (1935). Volume, shape, and roundness of quartz particles. *J. Geol.* **43**, 250-280.

Walters, A. D., May, C. K., Dauster, E. S., Cinquin, B. P., Smith, E. A., Robellet, X., D'Amours, D., Larabell, C. A. and Cohen-Fix, O. (2014). The yeast polo kinase Cdc5 regulates the shape of the mitotic nucleus. *Curr Biol* **24**, 2861-7.

Webster, M., Witkin, K. L. and Cohen-Fix, O. (2009). Sizing up the nucleus: nuclear shape, size and nuclear-envelope assembly. *J Cell Sci* **122**, 1477-86.

Wei, D., Jacobs, S., Modla, S., Zhang, S., Young, C. L., Cirino, R., Caplan, J. and Czymmek, K. (2012). High-resolution three-dimensional reconstruction of a whole yeast cell using focused-ion beam scanning electron microscopy. *Biotechniques* **53**, 41-8.

Wimmer, C., Doye, V., Grandi, P., Nehrbass, U. and Hurt, E. C. (1992). A new subclass of nucleoporins that functionally interact with nuclear pore protein NSP1. *Embo J* **11**, 5051-61.

Winey, M. and O'Toole, E. T. (2001). The spindle cycle in budding yeast. *Nat Cell Biol* **3**, E23-7.

Winey, M., Yarar, D., Giddings, T. H., Jr. and Mastronarde, D. N. (1997). Nuclear pore complex number and distribution throughout the Saccharomyces cerevisiae cell cycle by three-dimensional reconstruction from electron micrographs of nuclear envelopes. *Mol Biol Cell* **8**, 2119-32.

Witkin, K. L., Chong, Y., Shao, S., Webster, M. T., Lahiri, S., Walters, A. D., Lee, B., Koh, J. L., Prinz, W. A., Andrews, B. J. et al. (2012). The budding yeast nuclear envelope adjacent to the nucleolus serves as a membrane sink during mitotic delay. *Curr Biol* **22**, 1128-33.

Wong, H., Marie-Nelly, H., Herbert, S., Carrivain, P., Blanc, H., Koszul, R., Fabre, E. and Zimmer, C. (2012). A predictive computational model of the dynamic 3D interphase yeast nucleus. *Curr Biol* **22**, 1881-90.

Yang, C. H., Lambie, E. J., Hardin, J., Craft, J. and Snyder, M. (1989). Higher order structure is present in the yeast nucleus: autoantibody probes demonstrate that the nucleolus lies opposite the spindle pole body. *Chromosoma* **98**, 123-8.

Yeh, E., Skibbens, R., Cheng, J., Salmon, E. and Bloom, K. (1995). Spindle dynamics and cell cycle regulation of dynein in the budding yeast, Saccharomyces cerevisiae. *J. Cell Biol.* **130**, 687-700.

Zhao, Y., Schreiner, S. M., Koo, P. K., Colombi, P., King, M. C. and Mochrie, S. G. (2016). Improved Determination of Subnuclear Position Enabled by Three-Dimensional Membrane Reconstruction. *Biophys J* **111**, 19-24.

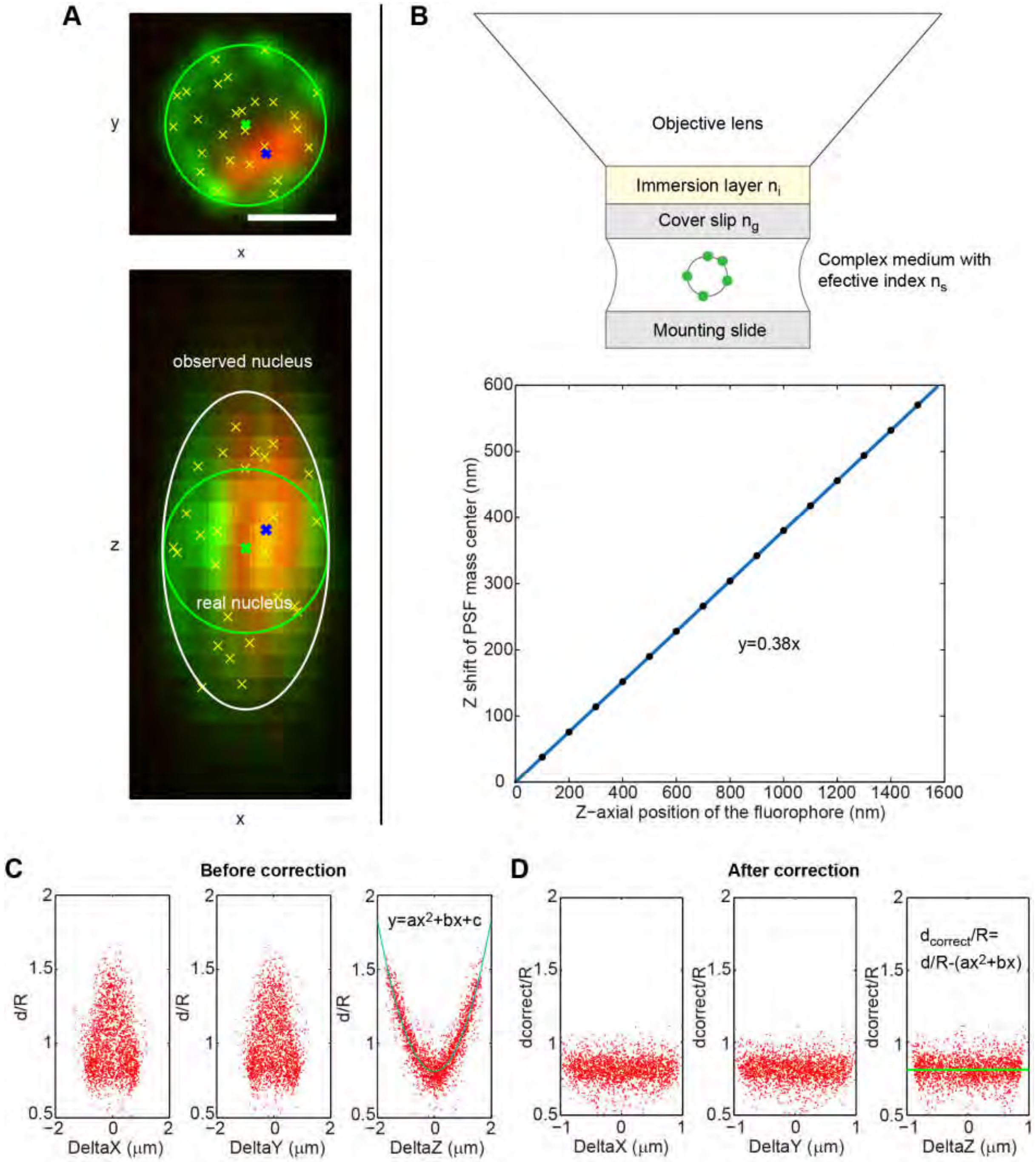
A
y
x
observed nucleus
z
real nucleus
x
B
Objective lens
Immersion layer n_i
Cover slip n_g
Complex medium with efective index n_s
Mounting slide
Z shift of PSF mass center (nm)
Z-axial position of the fluorophore (nm)
y=0.38x
0
100
200
300
400
500
600
0
200
400
600
800
1000
1200
1400
1600
C
Before correction
d/R
DeltaX (μm)
DeltaY (μm)
DeltaZ (μm)
y=ax²+bx+c
D
After correction
dcorrect/R
DeltaX (μm)
DeltaY (μm)
DeltaZ (μm)
$d_{correct}/R= d/R-(ax^2+bx)$

Figure 1

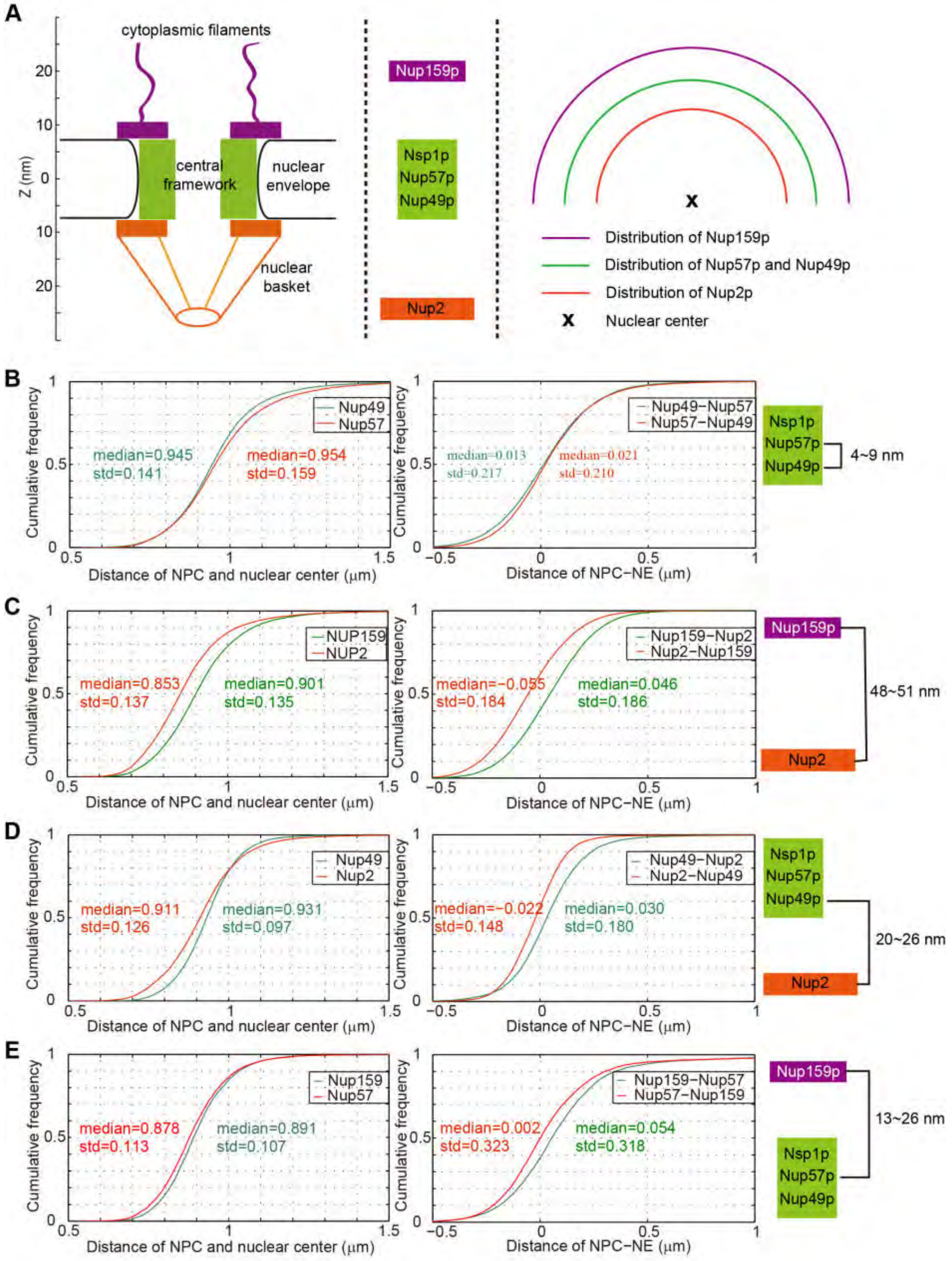
A
cytoplasmic filaments
central framework
nuclear envelope
nuclear basket
Z (nm)
20
10
0
10
20
Nup159p
Nsp1p
Nup57p
Nup49p
Nup2
x
Distribution of Nup159p
Distribution of Nup57p and Nup49p
Distribution of Nup2p
x Nuclear center
B
Cumulative frequency
Nup49
Nup57
median=0.945
std=0.141
median=0.954
std=0.159
Distance of NPC and nuclear center (μm)
Nup49−Nup57
Nup57−Nup49
median=0.013
std=0.217
median=0.021
std=0.210
Distance of NPC−NE (μm)
Nsp1p
Nup57p
Nup49p
4~9 nm
C
NUP159
NUP2
median=0.853
std=0.137
median=0.901
std=0.135
Nup159−Nup2
Nup2−Nup159
median=−0.055
std=0.184
median=0.046
std=0.186
Nup159p
Nup2
48~51 nm
D
Nup49
Nup2
median=0.911
std=0.126
median=0.931
std=0.097
Nup49−Nup2
Nup2−Nup49
median=−0.022
std=0.148
median=0.030
std=0.180
Nsp1p
Nup57p
Nup49p
Nup2
20~26 nm
E
Nup159
Nup57
median=0.878
std=0.113
median=0.891
std=0.107
Nup159−Nup57
Nup57−Nup159
median=0.002
std=0.323
median=0.054
std=0.318
Nup159p
Nsp1p
Nup57p
Nup49p
13~26 nm
0
0.5
1
1.5
−0.5

Figure 2

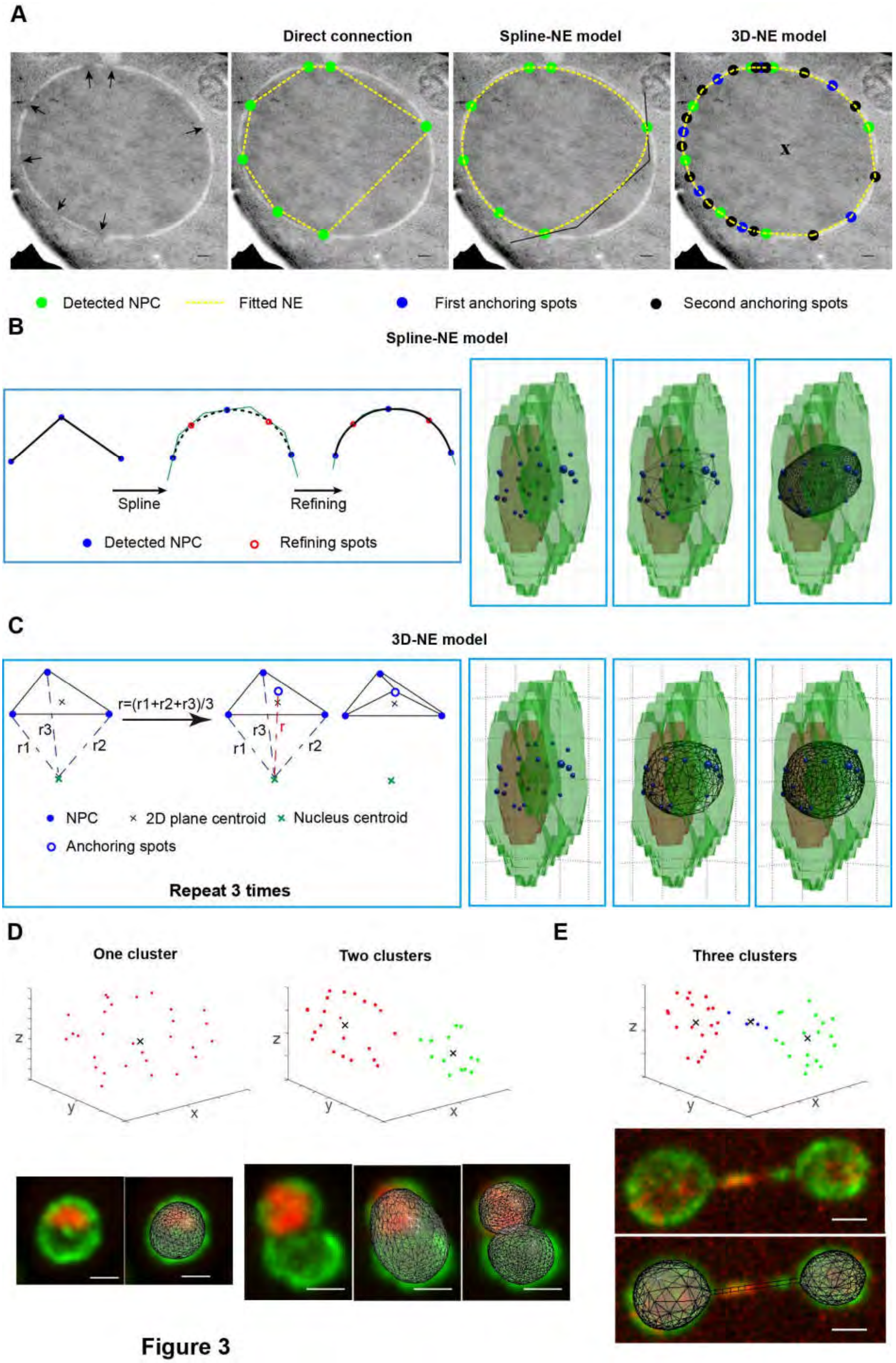
A
Direct connection
Spline-NE model
3D-NE model
x
● Detected NPC
Fitted NE
● First anchoring spots
● Second anchoring spots
B
Spline-NE model
Spline
Refining
● Detected NPC
○ Refining spots
C
3D-NE model
r=(r1+r2+r3)/3
r1
r2
r3
r
● NPC
× 2D plane centroid
× Nucleus centroid
○ Anchoring spots
Repeat 3 times
D
One cluster
Two clusters
z
y
x
E
Three clusters

Figure 3

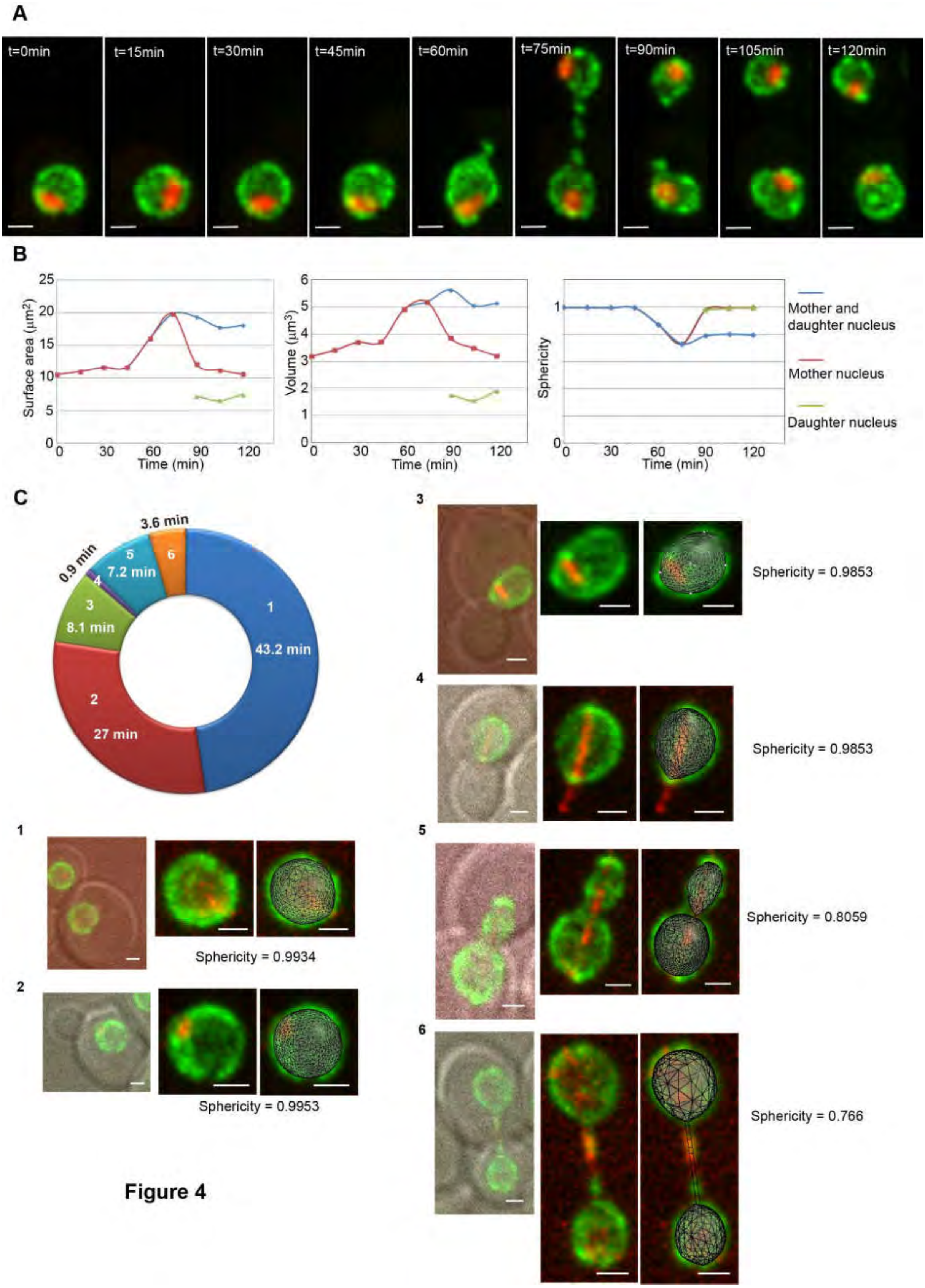
A
t=0min
t=15min
t=30min
t=45min
t=60min
t=75min
t=90min
t=105min
t=120min
B
Surface area (μm²)
25
20
15
10
5
0
0
30
60
90
120
Time (min)
Volume (μm³)
6
5
4
3
2
1
0
Sphericity
1
0
Mother and daughter nucleus
Mother nucleus
Daughter nucleus
C
3.6 min
0.9 min
5
7.2 min
6
4
3
8.1 min
1
43.2 min
2
27 min
1
Sphericity = 0.9934
2
Sphericity = 0.9953
3
Sphericity = 0.9853
4
Sphericity = 0.9853
5
Sphericity = 0.8059
6
Sphericity = 0.766

Figure 4

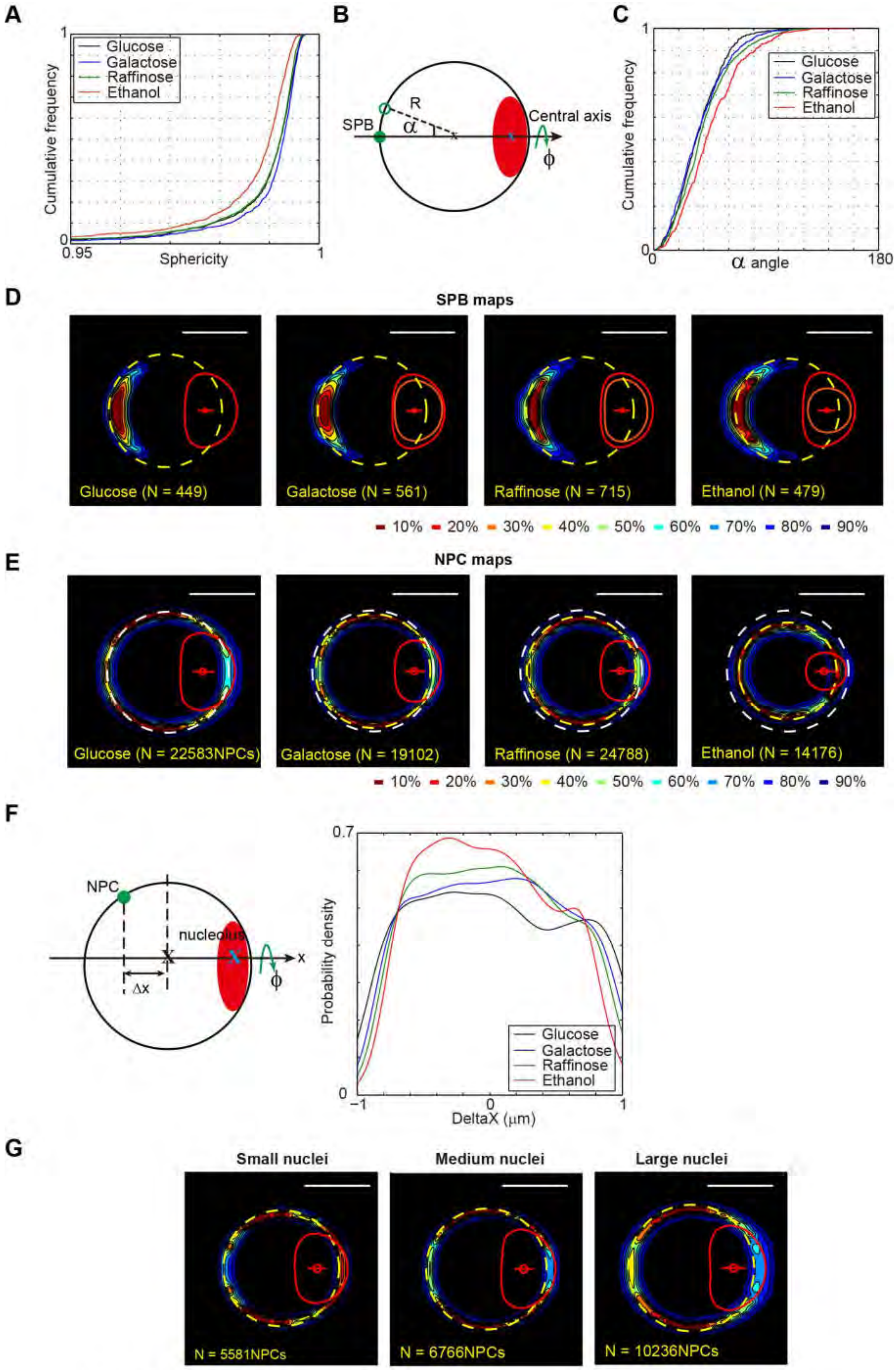
A
Cumulative frequency
Sphericity
0.95
1
0
1
Glucose
Galactose
Raffinose
Ethanol
B
SPB
R
α
Central axis
ϕ
C
Cumulative frequency
α angle
0
180
1
Glucose
Galactose
Raffinose
Ethanol
D
SPB maps
Glucose (N = 449)
Galactose (N = 561)
Raffinose (N = 715)
Ethanol (N = 479)
10% 20% 30% 40% 50% 60% 70% 80% 90%
E
NPC maps
Glucose (N = 22583NPCs)
Galactose (N = 19102)
Raffinose (N = 24788)
Ethanol (N = 14176)
10% 20% 30% 40% 50% 60% 70% 80% 90%
F
NPC
nucleolus
x
Δx
ϕ
Probability density
0.7
0
DeltaX (μm)
−1
0
1
Glucose
Galactose
Raffinose
Ethanol
G
Small nuclei
Medium nuclei
Large nuclei
N = 5581NPCs
N = 6766NPCs
N = 10236NPCs

Figure 5

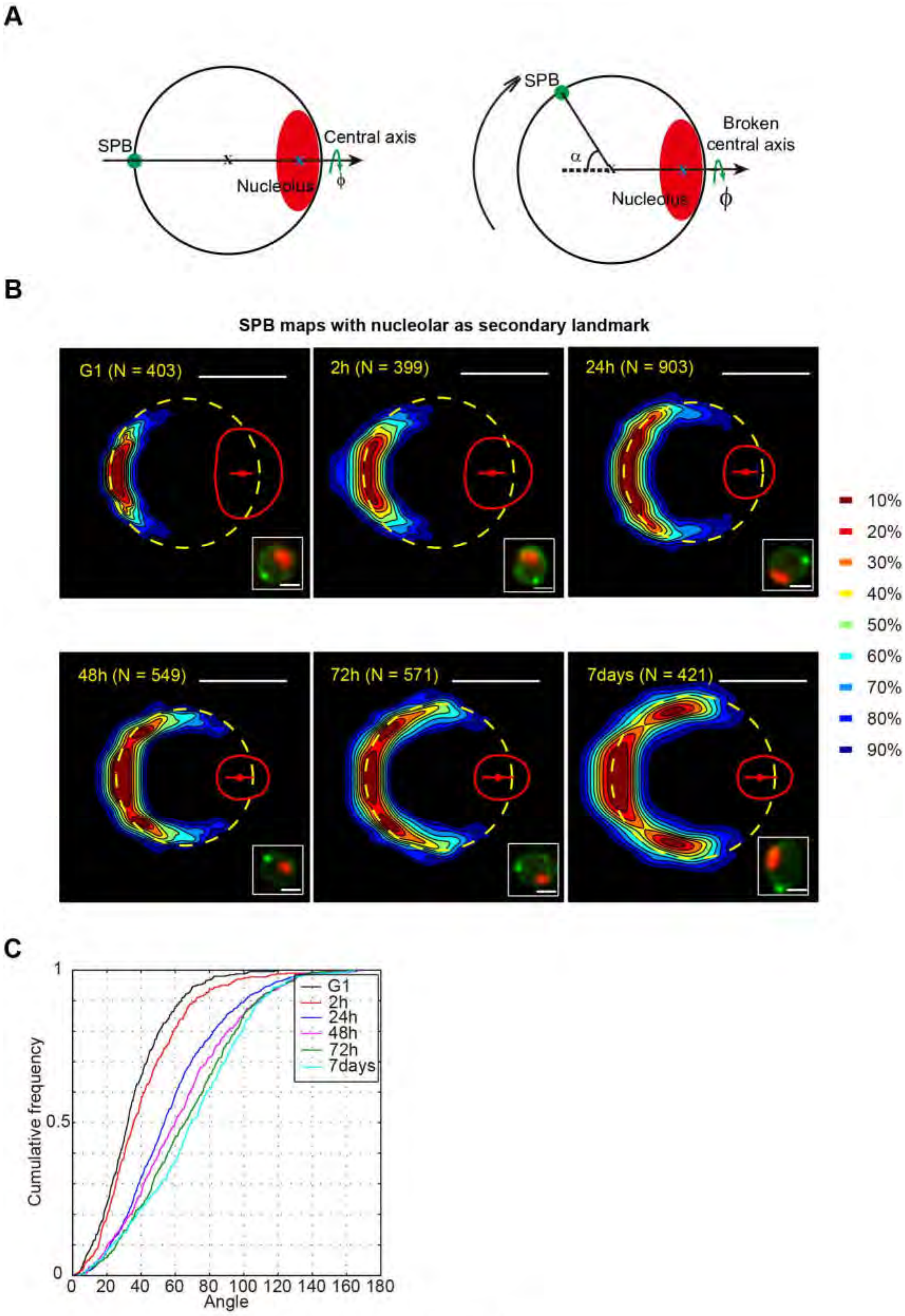
A
SPB
Central axis
x
Nucleolus
ϕ
SPB
α
Broken central axis
Nucleolus
ϕ
B
SPB maps with nucleolar as secondary landmark
G1 (N = 403)
2h (N = 399)
24h (N = 903)
48h (N = 549)
72h (N = 571)
7days (N = 421)
10%
20%
30%
40%
50%
60%
70%
80%
90%
C
Cumulative frequency
0
0.5
1
0 20 40 60 80 100 120 140 160 180
Angle
G1
2h
24h
48h
72h
7days

Figure 6

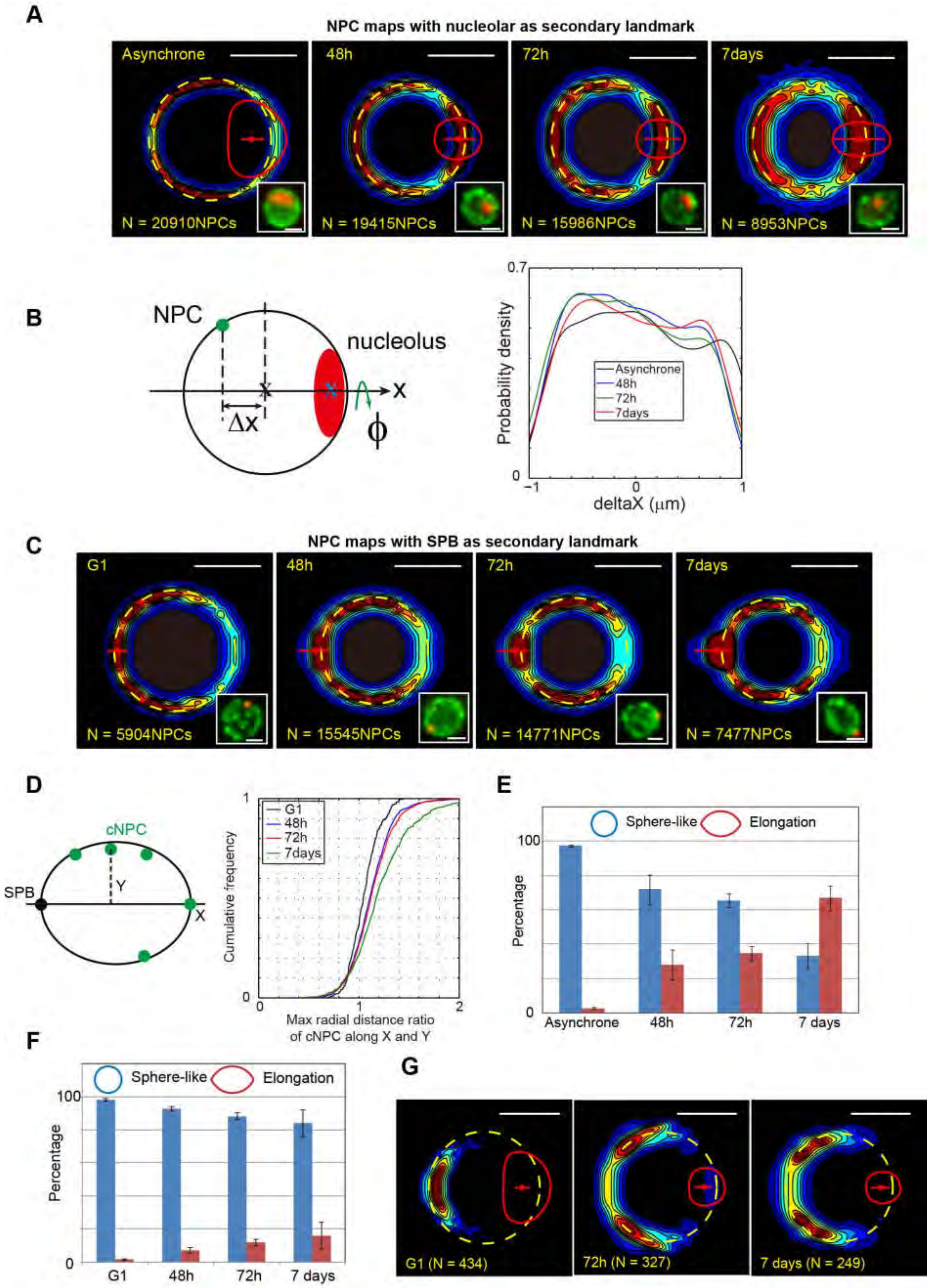
A
NPC maps with nucleolar as secondary landmark
Asynchrone
48h
72h
7days
N = 20910NPCs
N = 19415NPCs
N = 15986NPCs
N = 8953NPCs
B
NPC
nucleolus
X
Δx
ϕ
0.7
Probability density
0
−1
0
1
deltaX (μm)
Asynchrone
48h
72h
7days
C
NPC maps with SPB as secondary landmark
G1
48h
72h
7days
N = 5904NPCs
N = 15545NPCs
N = 14771NPCs
N = 7477NPCs
D
cNPC
SPB
Y
X
1
0
Cumulative frequency
0
1
2
G1
48h
72h
7days
Max radial distance ratio
of cNPC along X and Y
E
Sphere-like
Elongation
100
0
Percentage
Asynchrone
48h
72h
7 days
F
Sphere-like
Elongation
100
0
Percentage
G1
48h
72h
7 days
G
G1 (N = 434)
72h (N = 327)
7 days (N = 249)

Figure 7

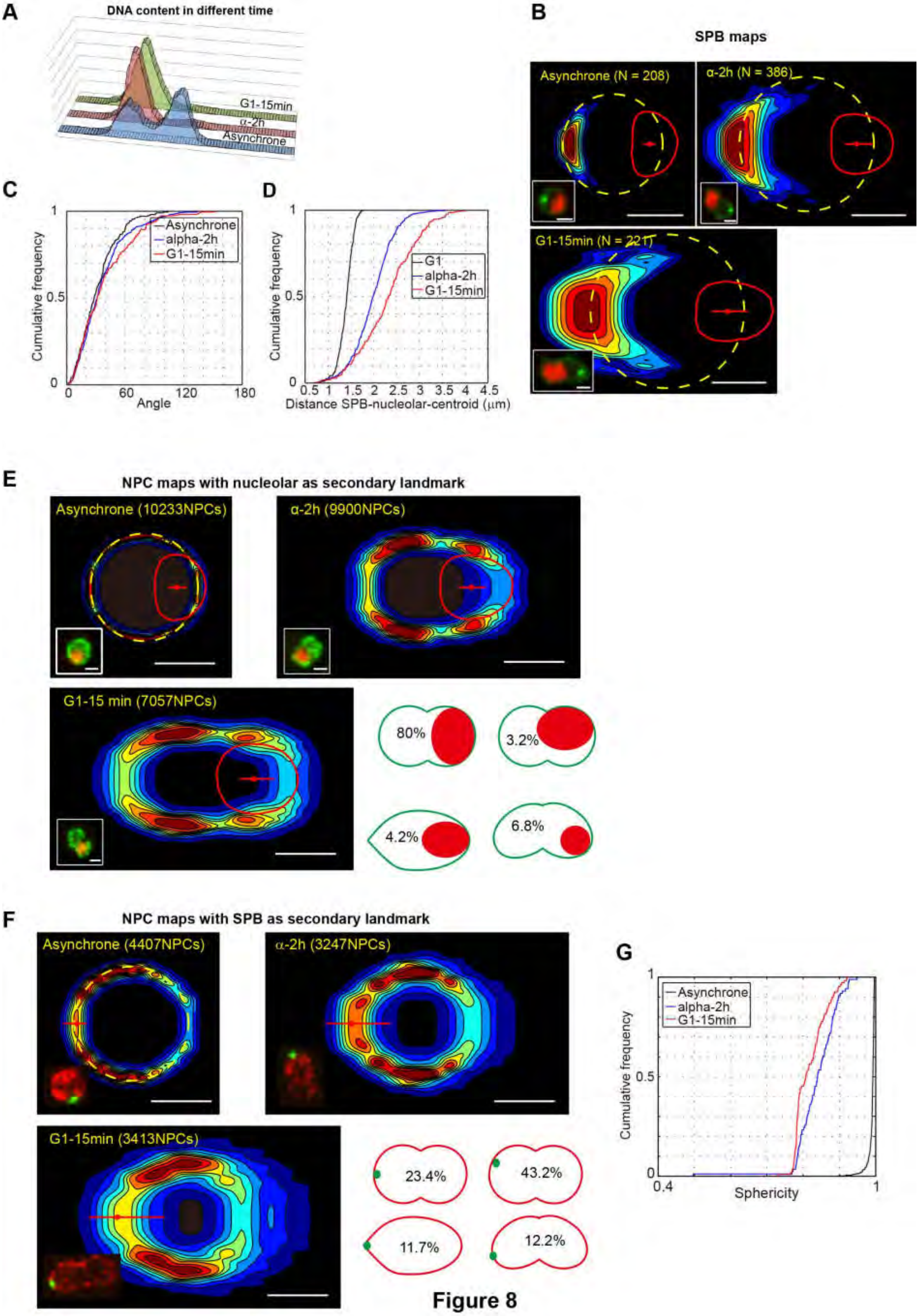
A
DNA content in different time
G1-15min
α-2h
Asynchrone
B
SPB maps
Asynchrone (N = 208)
α-2h (N = 386)
G1-15min (N = 221)
C
Cumulative frequency
1
0.5
0
0
60
120
180
Angle
Asynchrone
alpha-2h
G1-15min
D
Cumulative frequency
1
0.5
0
0.5 1 1.5 2 2.5 3 3.5 4 4.5
Distance SPB-nucleolar-centroid (μm)
G1
alpha-2h
G1-15min
E
NPC maps with nucleolar as secondary landmark
Asynchrone (10233NPCs)
α-2h (9900NPCs)
G1-15 min (7057NPCs)
80%
3.2%
4.2%
6.8%
F
NPC maps with SPB as secondary landmark
Asynchrone (4407NPCs)
α-2h (3247NPCs)
G1-15min (3413NPCs)
23.4%
43.2%
11.7%
12.2%
G
Cumulative frequency
1
0.5
0
0.4
1
Sphericity
Asynchrone
alpha-2h
G1-15min

Figure 8

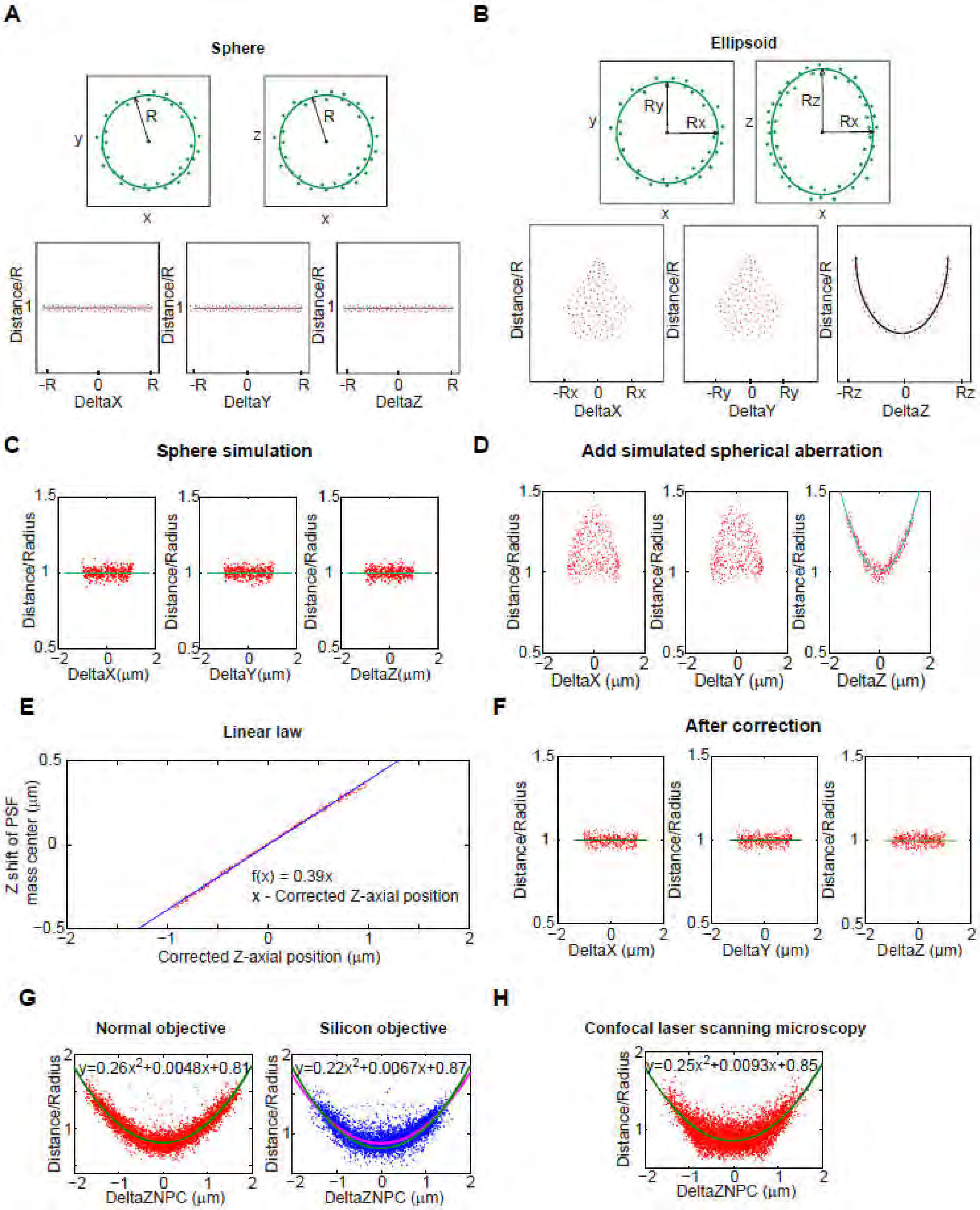
A
Sphere
y
x
z
x
R
Distance/R
1
-R
0
R
DeltaX
DeltaY
DeltaZ
B
Ellipsoid
Ry
Rx
Rz
-Rx
0
Rx
-Ry
Ry
-Rz
Rz
C
Sphere simulation
Distance/Radius
1.5
1
0.5
−2
0
2
DeltaX(μm)
DeltaY(μm)
DeltaZ(μm)
D
Add simulated spherical aberration
DeltaX (μm)
DeltaY (μm)
DeltaZ (μm)
E
Linear law
Z shift of PSF mass center (μm)
0.5
0
−0.5
−2
−1
1
2
f(x) = 0.39x
x - Corrected Z-axial position
Corrected Z-axial position (μm)
F
After correction
G
Normal objective
y=0.26x²+0.0048x+0.81
Silicon objective
y=0.22x²+0.0067x+0.87
DeltaZNPC (μm)
H
Confocal laser scanning microscopy
y=0.25x²+0.0093x+0.85

Figure S1

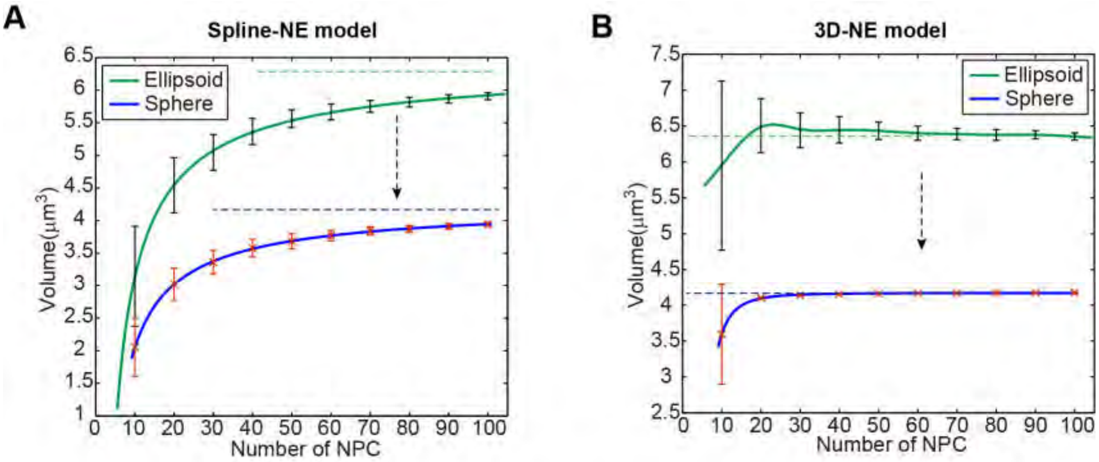
A
Spline-NE model
Ellipsoid
Sphere
Volume(μm³)
6.5
6
5.5
5
4.5
4
3.5
3
2.5
2
1.5
1
0
10
20
30
40
50
60
70
80
90
100
Number of NPC
B
3D-NE model
Ellipsoid
Sphere
Volume(μm³)
7.5
7
6.5
6
5.5
5
4.5
4
3.5
3
2.5
0
10
20
30
40
50
60
70
80
90
100
Number of NPC

Figure S2

Table S1. The volume of the nuclei along one cell cycle

t/min	0	15	30	45	60	75	90	105	120
Cell 1	3.92	4.26	4.52	4.71	5.11	3.57+1.69*	3.76+1.81*	4.22+2.12*	4.58+2.66*
					G2	End of mitois			
Cell 2	4.14	4.11	4.13	4.67	5.26	5.08	3.82+1.78*	3.76+1.66*	4.05+1.73*
						G2	End of mitosis		
Cell 3	3.99	3.9	4.51	5.12	5.12	3.39+1.52*	3.54+1.55*	3.68+1.61*	4.11+1.89*
				G2	Anaphase				
Cell 4	2.99	3.4	3.9	4.1	3.83	2.98+0.81*	3.35+1.03*	3.55+1.29*	3.86+1.45*
					Anaphase				
Cell 5	3.29	3.5	3.59	3.76	3.91	4.23	3.11+1.76*	3.44+1.89*	3.16+1.87*
						G2			
Cell 6	2.95	3.38	3.57	4.07	4.34	2.9+1.87*	3.04+1.81*	3.22+2.01*	3.21+2.28*
					Anaphase				
Cell 7	3.2	3.42	3.71	3.71	4.92	4.88	3.23+1.56*	3.49+1.55*	3.21+1.92*
					G2	Anaphase			
Cell 8	4	4.02	2.49+1.57*	2.93+1.57*	3.19+1.82*	3.28+1.96*	3.24+1.63*	3.6	3.9
	G2	Anaphase							
Cell 9	3.91	3.99	4.1	5.53	5.1	3.09+1.99*	3.04+1.72*	3.51+2.35*	3.74+2.95*
				G2	Anaphase				
Cell 10	3.47	4.43	4.07	5.2	5.1	5.74	3.79+2.6*	3.8+2.63*	4.13+2.83*
					G2	Anaphase			

* represent the daughter nucleus.

Table S2. Summary nuclear and nucleolus size distribution in asynchronous cultures

Carbon source	NO. cells	Doubling time (min)	G1 percentage (%)	Median size of nucleus		$V_{nucleolus}$ (μm^3)
				Surface (μm^2)	Volume (μm^3)	
Glucose	1054	90	42.2	10.99±1.36	3.41±0.60	1.38±1.15
Galactose	1061	120	45.4	9.77±1.16	2.83±0.50	0.82±0.82
Raffinose	1451	130	49.8	8.82±1.23	2.44±0.51	0.84±0.61
Ethanol	1116	220	71.1	6.84±1.15	1.66±0.41	0.29±0.21

Table S3: Genotypes of strains used in this study

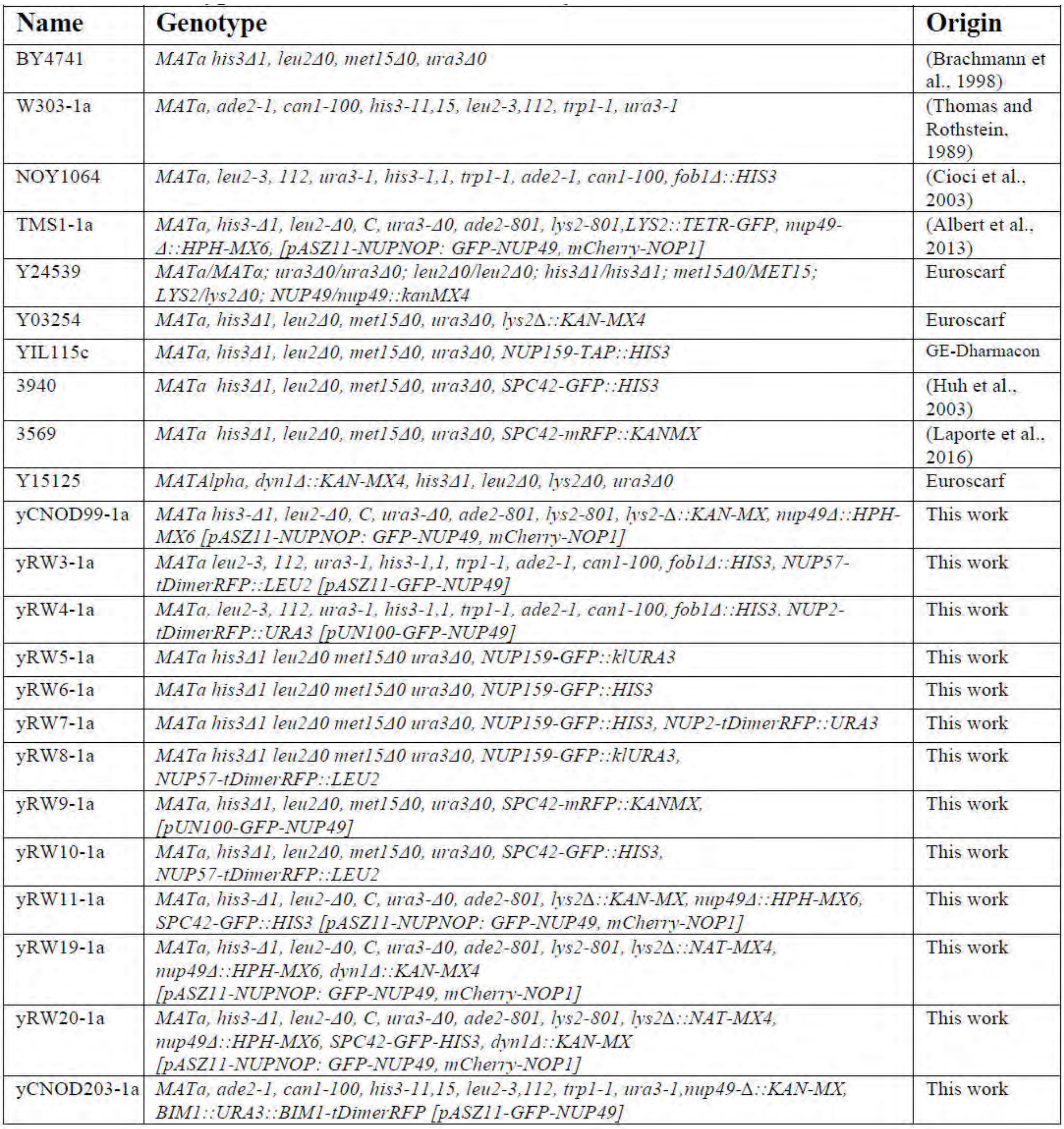

Name	**Genotype**	**Origin**
BY4741	*MATa his3Δ1, leu2Δ0, met15Δ0, ura3Δ0*	(Brachmann et al., 1998)
W303-1a	*MATa, ade2-1, can1-100, his3-11,15, leu2-3,112, trp1-1, ura3-1*	(Thomas and Rothstein, 1989)
NOY1064	*MATa, leu2-3, 112, ura3-1, his3-1,1, trp1-1, ade2-1, can1-100, fob1Δ::HIS3*	(Cioci et al., 2003)
TMS1-1a	*MATa, his3-Δ1, leu2-Δ0, C, ura3-Δ0, ade2-801, lys2-801,LYS2::TETR-GFP, nup49-Δ::HPH-MX6, [pASZ11-NUPNOP: GFP-NUP49, mCherry-NOP1]*	(Albert et al., 2013)
Y24539	*MATa/MATα; ura3Δ0/ura3Δ0; leu2Δ0/leu2Δ0; his3Δ1/his3Δ1; met15Δ0/MET15; LYS2/lys2Δ0; NUP49/nup49::kanMX4*	Euroscarf
Y03254	*MATa, his3Δ1, leu2Δ0, met15Δ0, ura3Δ0, lys2Δ::KAN-MX4*	Euroscarf
YIL115c	*MATa, his3Δ1, leu2Δ0, met15Δ0, ura3Δ0, NUP159-TAP::HIS3*	GE-Dharmacon
3940	*MATa his3Δ1, leu2Δ0, met15Δ0, ura3Δ0, SPC42-GFP::HIS3*	(Huh et al., 2003)
3569	*MATa his3Δ1, leu2Δ0, met15Δ0, ura3Δ0, SPC42-mRFP::KANMX*	(Laporte et al., 2016)
Y15125	*MATAlpha, dyn1Δ::KAN-MX4, his3Δ1, leu2Δ0, lys2Δ0, ura3Δ0*	Euroscarf
yCNOD99-1a	*MATa his3-Δ1, leu2-Δ0, C, ura3-Δ0, ade2-801, lys2-801, lys2-Δ::KAN-MX, nup49Δ::HPH-MX6 [pASZ11-NUPNOP: GFP-NUP49, mCherry-NOP1]*	This work
yRW3-1a	*MATa leu2-3, 112, ura3-1, his3-1,1, trp1-1, ade2-1, can1-100, fob1Δ::HIS3, NUP57-tDimerRFP::LEU2 [pASZ11-GFP-NUP49]*	This work
yRW4-1a	*MATa, leu2-3, 112, ura3-1, his3-1,1, trp1-1, ade2-1, can1-100, fob1Δ::HIS3, NUP2-tDimerRFP::URA3 [pUN100-GFP-NUP49]*	This work
yRW5-1a	*MATa his3Δ1 leu2Δ0 met15Δ0 ura3Δ0, NUP159-GFP::klURA3*	This work
yRW6-1a	*MATa his3Δ1 leu2Δ0 met15Δ0 ura3Δ0, NUP159-GFP::HIS3*	This work
yRW7-1a	*MATa his3Δ1 leu2Δ0 met15Δ0 ura3Δ0, NUP159-GFP::HIS3, NUP2-tDimerRFP::URA3*	This work
yRW8-1a	*MATa his3Δ1 leu2Δ0 met15Δ0 ura3Δ0, NUP159-GFP::klURA3, NUP57-tDimerRFP::LEU2*	This work
yRW9-1a	*MATa, his3Δ1, leu2Δ0, met15Δ0, ura3Δ0, SPC42-mRFP::KANMX, [pUN100-GFP-NUP49]*	This work
yRW10-1a	*MATa, his3Δ1, leu2Δ0, met15Δ0, ura3Δ0, SPC42-GFP::HIS3, NUP57-tDimerRFP::LEU2*	This work
yRW11-1a	*MATa, his3-Δ1, leu2-Δ0, C, ura3-Δ0, ade2-801, lys2Δ::KAN-MX, nup49Δ::HPH-MX6, SPC42-GFP::HIS3 [pASZ11-NUPNOP: GFP-NUP49, mCherry-NOP1]*	This work
yRW19-1a	*MATa, his3-Δ1, leu2-Δ0, C, ura3-Δ0, ade2-801, lys2-801, lys2Δ::NAT-MX4, nup49Δ::HPH-MX6, dyn1Δ::KAN-MX4 [pASZ11-NUPNOP: GFP-NUP49, mCherry-NOP1]*	This work
yRW20-1a	*MATa, his3-Δ1, leu2-Δ0, C, ura3-Δ0, ade2-801, lys2-801, lys2Δ::NAT-MX4, nup49Δ::HPH-MX6, SPC42-GFP-HIS3, dyn1Δ::KAN-MX [pASZ11-NUPNOP: GFP-NUP49, mCherry-NOP1]*	This work
yCNOD203-1a	*MATa, ade2-1, can1-100, his3-11,15, leu2-3,112, trp1-1, ura3-1,nup49-Δ::KAN-MX, BIM1::URA3::BIM1-tDimerRFP [pASZ11-GFP-NUP49]*	This work

Table S4: Plasmids used in this study

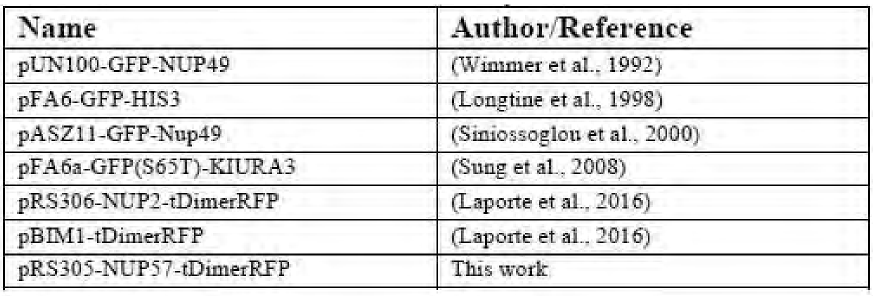

Name	Author/Reference
pUN100-GFP-NUP49	(Wimmer et al., 1992)
pFA6-GFP-HIS3	(Longtine et al., 1998)
pASZ11-GFP-Nup49	(Siniossoglou et al., 2000)
pFA6a-GFP(S65T)-KIURA3	(Sung et al., 2008)
pRS306-NUP2-tDimerRFP	(Laporte et al., 2016)
pBIM1-tDimerRFP	(Laporte et al., 2016)
pRS305-NUP57-tDimerRFP	This work

3.3 Extended discussion

In this part, I will further discuss our results about the nuclear geometry, and add some unpublished dataset. I will focus this discussion on a shape descriptor called "sphericity index", the intranuclear position of the nucleolus and the NPC distribution during cell cycle.

3.3.1 Heterogeneity of the nuclear shape in cell population

The cell nucleus is typically spheroidal or ellipsoid (Albert et al., 2012; Berger et al., 2008). However, the nuclear shape has high plasticity: in a same strain, the nuclei also will have different shape from cell to cell (see “Introduction” part). To study the heterogeneity of the nuclear shape in interphase of one cell population, we measured sphericity of each cell nucleus. Sphericity is one criterion to reflect how round an object is. The sphericity of a given object is the ratio between the surface area of a sphere which would have the same volume as that object to the surface area of the object (Wadell, 1935). For one perfect sphere, the sphericity index equals to 1 and is maximal. A sphericity index lower than 1 indicates deviation from a perfect sphere. For one ellipsoid, the sphericity is ~0.92 when a:b:c=1:1:2 (Figure 29A). We tested the sphericity of yeast nucleus when carbon source is changed from the most (glucose) to the less favorable carbon source (ethanol). We confirmed that most of the nuclei in interphase were close to spherical (the median sphericity is over 0.99). However, about 20% of nucleus are rather ellipsoidal (sphericity below 0.95) (Figure 29B, the samples are presented in Figure 29D). We also found that when the carbon source was changed to the less favorable carbon source ethanol, the sphericity clearly decreased compare with the favorable carbon source (Figure 29B). So we supposed that, together with the growth rate and NPC distribution (see manuscript) which are influenced by the carbon source, the nuclear shape is also impacted by the carbon source. We have known that after the cells enter quiescence, ~ 70% nuclear lost their sphericity. So, we also explored the heterogeneity of the nuclear shape after the cells enter quiescence. The results clearly showed that after 7 days starvation, most of the nuclei lost their sphericity (Figure 29C).

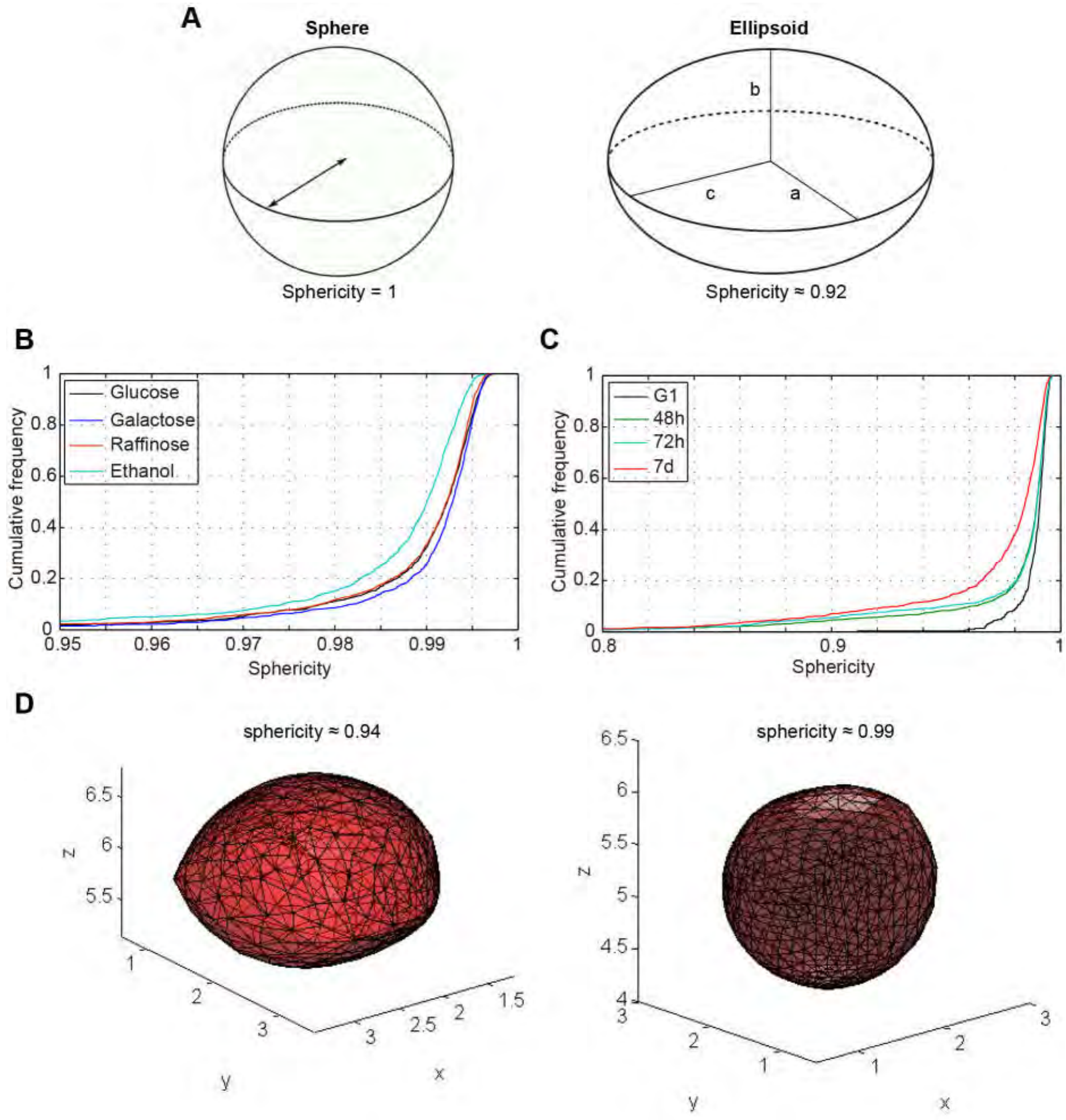

Figure 29. The heterogeneity of the nuclear shape.

A. The sphericity of sphere and ellipsoid. The sphericity of one perfect sphere is 1, and the ellipsoid (a:b:c=1:1:2) is ~0.92.

B. The influence of the carbon source on the nuclear shape, the sphericity of the nuclei decreases while less favorable carbon (ethanol) source is used.

C. The sphericity distribution of the nuclei after the cells enter quiescence. After 7 days starvation, the nuclei lost their sphericity.

D. Exemples of two nuclei with different sphericity. The less spherical nucleus looks shorter along Z-axis.

3.3.2 The organization of the nucleolus

The budding yeast has 100-200 ribosomal DNA (rDNA) units tandemly located on chromosome XII and is confined in the nucleolus. Only half of the rDNA copies are actively transcribed in *S. cerevisiae* (Dammann et al., 1993). During my PhD, we wanted to quantitate the intra-nuclear position of the nucleolus. In budding yeast, the nucleolus contacts extensively with the nuclear envelope (NE) (Figure 30A). The nuclear periphery was always seen as the silenced region ("genes poor region"), so the study of the nuclear periphery is important to help us to understand the relation between the chromosome organization and transcription activity. Using our methods, we could accurately explore in 3D the peripheral location of the nucleolus.

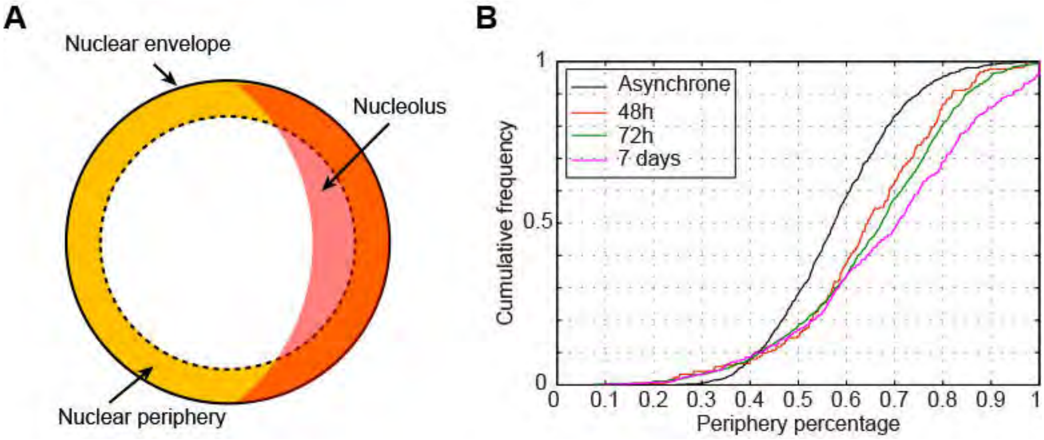

Figure 30. The change of the nucleolus structure after the cells enter quiescence.

A. Schematic of the nucleus, nucleolus and the nuclear periphery region. Here, the periphery region was defined as the region occupy 1/3 of the total nucleus at the periphery.

B. After the cells enter quiescence, the nucleolus contacts the nuclear envelope more extensively.

We have shown after the cells enter quiescence, the growth of cells was stopped and the nucleolar size decreased (see manuscript Figure 7A). We were wondering if this change in the nucleolar size impacts its localization respect to the nuclear periphery. To answer this question, we calculated the fraction of the nucleolus located at the nuclear periphery. We defined periphery as 1/3 of the nuclear volume uniformally distributed along the NE. The nucleolar periphery percentage is the proportion of the nucleolus at the nuclear periphery. It is clear that with such definition, the nucleolus was not restricted to the peripheral region: in asynchrone cells, we measured a median of ~60% of the nucleolus located at the nuclear periphery. After cells entered quiescence, the percentage of the nucleolus at nuclear periphery is massively increased (Figure 30B). We conclude that when ribosome production is repressed, peripheral location of nucleolus is increasing.

Chapter III

Conclusion and perspectives

My thesis is containing two parts about the chromatin dynamics and the nuclear geometry in living yeast cells.

1. The dynamics of non-rDNA and rDNA chromatin

In the first part of my thesis, I studied the motion of the non-rDNA chromatin and rDNA chromatin in exponentially growing yeast cells. To track the motions of loci we labeled them thanks to the FROS approach and chose clones with very bright signal. Bright signals (high signal to noise ratio) were obtained by increasing the number of bacterial operator binding sites *tet*O (and subsequently the length of the labeled sequence) and significantly improved the accuracy of detection of tagged loci. For an isolated Rouse polymer chain, the motion of a locus composed of N monomers, with a known stiffness characterized by the Kuhn length (*Lk*) is described by three consecutive regimes (see Results 1.2, the review of Wang et al., 2015). For very short time scale, the motion of non-rDNA loci is not restricted by elastic interactions with their neighboring polymer segments, leading to a regime of free diffusion. However, in our experimental conditions, due to the increased length of the labeled DNA sequence, the initial free diffusive dynamics was slower than a short labeled sequence. The transition to the Rouse motion hence is delayed, leading to an exponent ~0.7 (see Results 1.2). After this transition, the movement of a locus was consistent with the Rouse dynamics with an exponent ~0.54 (compatible with our previous work, see Hajjoul et al., 2013 and Albert et al., 2013). For long time scales, because of the confinement of the nucleus, and the tethering of centromeres (CEN) and telomeres (TEL) to nuclear structures, the entire chromosome cannot diffuse freely: the chromatin dynamics can be modeled as two-regime Rouse model. This two-regime response was not detected in our previous work because of the shorter number of *tetO* sites in chosen FROS labeled sequences (Albert et al., 2013).

For the rDNA chromatin dynamics analysis, we also chose the clone with a very bright signal. The dynamics of the rDNA was very different than non-rDNA chromatin and fitted well with one regime: the MSD of rDNA followed a behavior with scaling exponent of ~0.7. The nucleolus, a nuclear body organized around the rDNA on the chromosome XII, is a totally different confinement compared with the nucleoplasm: the nucleolus is a more crowded region, so the motion of rDNA is slower and follows different constrains than non-rDNA. In addition, the repetitive nature of the rDNA, its peculiar chromatin structure, and the very high transcription rate may also play a role in this different mobility. It will be interesting to compare the dynamics of rDNA in the nucleolus within strains containing 25 or 200 rDNA copies. The MSD fitting of rDNA dynamics is similar with the Zimm polymer model. Further studies on the rDNA dynamics are still required to investigate rDNA organization. Mutants of RNA polymerase I and early ribosomal RNA processing could also be informative.

2. Interplay between the chromosome organization and chromatin motion

Chromosome organization in the nucleus is still debated. In this thesis, I contributed to define which polymer model can accurately predict the motion and organization of chromatin in the nucleus. Starting from an ideal Rouse chain, we tried to elucidate which chromatin properties are affecting the motion *in vivo*.

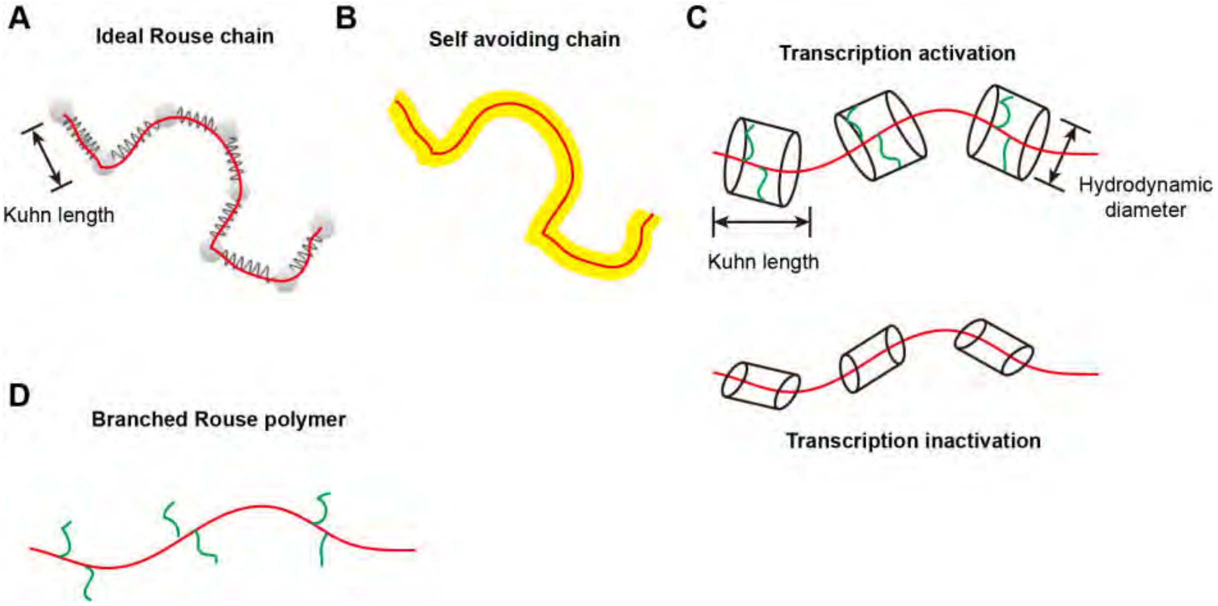

Figure 31. The “ideal” Rouse model and the chromosome models in living yeast cells.

A. The “ideal” Rouse chain, the chain can be seen as N beads (monomers) connected by harmonic springs, the monomers can cross each other. The MSD of an “ideal” Rouse chain can be fitted with an exponent of 0.5.

B. The self avoiding Rouse chain in vivo.The chromosome segments cannot cross each other freely.

C. The activation of transcription induce the binding of RNA nucleo-protein complexes (green lines) on the chromosome which will lead to an increased hydrodynamic diameter of the chromatin fibers, independently of the Kuhn length. Upon transcription inactivation, hydrodynamic radius is lower.

D. The branched Rouse polymer model *in vivo*. The red curve represents the chromosome, green curves represent the RNA nucleo-protein complexes.

“Ideal” Rouse chain can be seen as *N* beads connected by harmonic springs (Figure 32A). There are no excluded volume interactions between the beads and the chain can cross itself, like "ghost chain". The length of the springs, or the length of the monomers (Kuhn length), is characterized by only parameter defining the flexibility of the chain: the shorter the length, the more flexible the chain. In the “Results” section 2.2, we have confirmed that in living yeast cells, the chromatin motion followed the Rouse dynamics. However, the motion of the chromatin was not perfectly fitted by an ideal Rouse model because the MSD of chromatin dynamics was fitted with an unexpected exponent ~0.54 (“ideal” Rouse model is 0.5). We propose that chromosome segments cannot cross each other freely. According to this model, a chromosome should be considered as a self-avoiding chain (Hajjoul et al., 2013) (Figure 32B).

Based on chromatin dynamics *in vivo*, we confirmed the Kuhn length of ~1 nm in wild type (WT) cells which is much smaller than the one measured in *in vitro* system and appears unrealistic (see “Results” 2.2, Figure 1D). Then we wanted to see whether this unexpected response was related to the transcription activity. To study how transcription influences the chromatin dynamics, we then analyzed the mobility changes of loci (a locus on chromosome XII and the *GAL1* gene on chromosome II) after transcriptional inactivation. To achieve this, we constructed two polymerase II temperature sensitive (TS) mutant strains in which the transcriptional inactivation occurs after temperature shift from 25°C to 37 °C. The motion analysis revealed that upon transcription inactivation, chromatin dynamics increased ~50%, making chromatin properties closer to ideal chain (see “Results” 2.2, Figure 3A, B). We propose that for the same Kuhn length, the hydrodynamic radius of chromosomes was smaller after transcription inactivation (see “Results” 2.2, Figure 3C). Activation of the transcription induces the binding of RNA nucleo-protein complexes on the chromosome which will lead to the increase of the viscous friction (this will lead to the decrease of the chromatin dynamics) and the hydrodynamic diameter of the chromosome (Figure 32C). We propose that the chromatin in living cells is best modeled using an alternative Rouse model: the “branched Rouse polymer”, the RNA nucleo-protein complexes binds on the Rouse chromosome (Figure 32D). Therefore, we propose that chromatin polymer have to be modeled using two independent parameters: Kuhn length (flexibility) and hydrodynamic radius. The relation between the Kuhn length and the hydrodynamic diameter are still not clear; further studies are needed.

3. Determination of the nuclear shape and size

Chromosomes are space-filling polymers in the nucleus. Therefore, the nuclear organization and geometry should have significant influence on the chromosome organization. However, the interplay between them is still debated because the research on the nuclear shape and size is technically challenging.

This question leads to the second part of my PhD work, in which I developed one algorithm, “NucQuant” used to quantify the nuclear shape and size of living yeast with high accuracy. This approach benefits from“Localization microscopy” approach that can measure the position of isolated objects with a resolution of a few tens of nanometers (Thomann et al., 2002). Because of the mismatch of the refractive index (see Results 3.2, Figure 1), the accuracy of “localization microscopy” along the Z-axis is much lower than in X-Y plane (Kirshner et al., 2013) and results in spherical aberrations along the Z-axis. The “NucQuant” algorithm includes a post-acquisition correction to revise this aberration. After correction of the Z aberration, “NucQuant” could interpolate the nuclear envelope (NE) based on the 3D-NE method. In this approach, one assumes that between detected nuclear pore complexes (NPCs), NE adopts a spherical shape keeping distance NE-nuclear center constant. This hypothesis can lead to approximation errors. Spline-NE estimation is not based on this hypothesis, only assuming a smooth NE shape. However, our spline-NE approach systematically underestimated the nuclear size because the number of detected NPCs was too low (around 20-30). However, it is still a good method to detect the nuclear envelope without additional hypothesis if the number of detected NPCs is high enough (more than 100, see “Results” 3.2, Figure S2). Actually, if one can improve the resolution of the algorithm to increase the number of detected NPCs, spline-NE will be the most promising way to analyze the nuclear shape. To go further in the characterization of the yeast nuclear geometry, we have tested a novel kind of super-resolution microscopy, based on structured-illumination microscopy, which has the ability to increase the number of detected NPC (Figure 33).

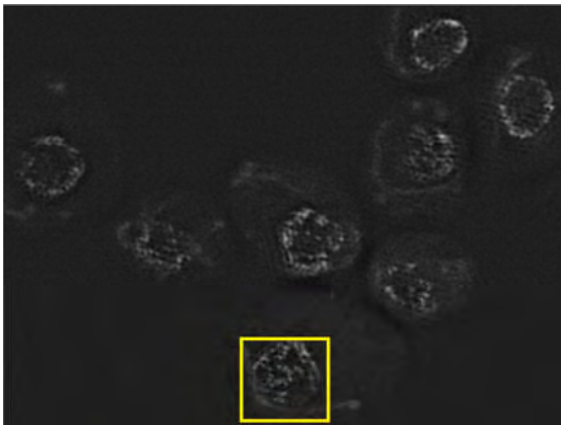

Figure 32. The detection of the nuclear shape based on structured-illumination microscopy. With the improvement of the resolution, it is possible to see the clusters of the NPC (see the yellow rectangle).

To validate this technique, we labeled different nucleoporins (Nups) in the NPC and were able to assign their locations in the thickness of the NE. The results showed that this method was highly accurate and has the potential to be used to calculate the median distances among Nups.

Then, we used this method to analyze the nuclear shape and size of yeast growing in different conditions. By using this method, cell's nuclei can be studied individually or in a bulk population. Combining the microfluidic technology with "NucQuant", we determined the nuclear shape and size of the yeast nucleus along the cell cycle and we could confirm the continuous increase of the nuclear volume from G1 to M (Jorgensen et al., 2007). Our results also revealed a significant increased NE surface at mitotic onset. Polo kinase cdc5 is known to be required for NE expansion at mitotic onset (Walters et al., 2014). Even if we did not detect the NE increased surface toward the nucleolus prior to mitosis, time window of rapid NE expansion are fully compatible with the activation timing polo kinase cdc5 (Walters et al., 2014).

Yeast nuclear genome has an axial symmetry around the so-called central axis: SPB/nuclear center/nucleolar centroid. Our results showed that the symmetry of the nucleus around the central axis was broken upon reduction of the nucleolar volume. After alignment of all of the nuclei into the same coordinates and projection of all the detected NPCs into a same plane, we were able to calculate the NPCs probability density distribution map (we called it as "NPCmap"). By analyzing the NPCmap of yeast cells, we also found that, the NPCs were heterogeneously distributed along the NE. NPCs are depleted of the NE at the interface nucleoplasm/nucleolus. Upon reduction of the nucleolar volume, NPCs are concentrated in the NE flanking the nucleolus, suggesting a physical link between NPC and the nucleolar content. Our study also revealed that from the G1 phase to the begining of the G2 phase (while the nucleolus volume is increasing gradually), the NPCs were moving away from the NE flanking the nucleolus. We observed that after cell division, i.e. at the early state of the G1 phase, the NPCs are concentrated at the NE flanking the nucleolus. This might be a consequence of mitosis, with the hour-glass shaped nucleus and the nucleolus being the last nuclear domain to segregate. In late G1, S and G2 phase, the surface of the nucleus is increased from the NE flanking the nucleolus (Walters et al., 2014). Thus the NPCs at this site are gradually shifted away from the nucleolus.

Finally, because we could determine the NE with high accuracy in 3D, we also could use this method to detect the nuclear periphery organization. The quantification of the nucleolar portion localized at the nuclear periphery revealed that when ribosome production is repressed, peripheral location of the nucleolus is increasing. In fact, some genes, such as *GAL1*, *HXK1*, *INO1*, *TSA2*, *HSP104*, *SUC2* and *MFA2*, are recruited to nuclear periphery upon transcriptional activation (Brickner and Walter, 2004; Burns and Wente, 2014; Cabal et al., 2006; Taddei et al., 2006). Labeling the NPC and a gene of interest with different fluorochromes, we could also accurately calculate the localization of the gene relative to the NE in 3D.We also could use this technique to analyze the localization of the rDNA in the nucleolus, combined the motion of rDNA chromatin to analyze the rDNA organization.

REFERENCE

Absolom, D., and M.H. Van Regenmortel. 1977. Nucleosome structure studied with purified antibodies to histones H2B, H3 and H4. *Febs Lett*. 85:61-64.

Adkins, N.L., M. Watts, and P.T. Georgel. 2004. To the 30-nm chromatin fiber and beyond. *Biochim Biophys Acta*. 1677:12-23.

Alber, F., S. Dokudovskaya, L.M. Veenhoff, W. Zhang, J. Kipper, D. Devos, A. Suprapto, O. Karni-Schmidt, R. Williams, B.T. Chait, M.P. Rout, and A. Sali. 2007. Determining the architectures of macromolecular assemblies. *Nature*. 450:683-694.

Albert, B., I. Leger-Silvestre, C. Normand, and O. Gadal. 2012. Nuclear organization and chromatin dynamics in yeast: biophysical models or biologically driven interactions? *Biochim Biophys Acta*. 1819:468-481.

Albert, B., J. Mathon, A. Shukla, H. Saad, C. Normand, I. Leger-Silvestre, D. Villa, A. Kamgoue, J. Mozziconacci, H. Wong, C. Zimmer, P. Bhargava, A. Bancaud, and O. Gadal. 2013. Systematic characterization of the conformation and dynamics of budding yeast chromosome XII. *The Journal of cell biology*. 202:201-210.

Albiez, H., M. Cremer, C. Tiberi, L. Vecchio, L. Schermelleh, S. Dittrich, K. Kupper, B. Joffe, T. Thormeyer, J. von Hase, S. Yang, K. Rohr, H. Leonhardt, I. Solovei, C. Cremer, S. Fakan, and T. Cremer. 2006. Chromatin domains and the interchromatin compartment form structurally defined and functionally interacting nuclear networks. *Chromosome research : an international journal on the molecular, supramolecular and evolutionary aspects of chromosome biology*. 14:707-733.

Amitai, A., and D. Holcman. 2013. Polymer model with long-range interactions: analysis and applications to the chromatin structure. *Phys Rev E Stat Nonlin Soft Matter Phys*. 88:052604.

Antonin, W., and H. Neumann. 2016. Chromosome condensation and decondensation during mitosis. *Current opinion in cell biology*. 40:15-22.

Arnone, J.T., A.D. Walters, and O. Cohen-Fix. 2013. The dynamic nature of the nuclear envelope: lessons from closed mitosis. *Nucleus*. 4:261-266.

Backlund, M.P., R. Joyner, K. Weis, and W.E. Moerner. 2014. Correlations of three-dimensional motion of chromosomal loci in yeast revealed by the double-helix point spread function microscope. *Molecular biology of the cell*. 25:3619-3629.

Bak, A.L., J. Zeuthen, and F.H. Crick. 1977. Higher-order structure of human mitotic chromosomes. *Proceedings of the National Academy of Sciences of the United States of America*. 74:1595-1599.

Bansal, M. 2003. DNA structure: Revisiting the Watson-Crick double helix. *Curr Sci India*. 85:1556-1563.

Barbi, M., J. Mozziconacci, J.M. Victor, H. Wong, and C. Lavelle. 2012. On the topology of chromatin fibres. *Interface focus*. 2:546-554.

Beaudouin, J., F. Mora-Bermudez, T. Klee, N. Daigle, and J. Ellenberg. 2006. Dissecting the contribution of diffusion and interactions to the mobility of nuclear proteins. *Biophysical journal*. 90:1878-1894.

Bednar, J., R.A. Horowitz, S.A. Grigoryev, L.M. Carruthers, J.C. Hansen, A.J. Koster, and C.L. Woodcock. 1998. Nucleosomes, linker DNA, and linker histone form a unique structural motif that directs the higher-order folding and compaction of chromatin. *Cell Biology*. 95:14173-14178.

Belton, J.M., R.P. McCord, J.H. Gibcus, N. Naumova, Y. Zhan, and J. Dekker. 2012. Hi-C: a comprehensive technique to capture the conformation of genomes. *Methods*. 58:268-276.

Berger, A.B., G.G. Cabal, E. Fabre, T. Duong, H. Buc, U. Nehrbass, J.C. Olivo-Marin, O. Gadal, and C. Zimmer. 2008. High-resolution statistical mapping reveals gene territories in live yeast. *Nature methods*. 5:1031-1037.

Bernal, M.A., C.E. deAlmeida, S. Incerti, C. Champion, V. Ivanchenko, and Z. Francis. 2015. The Influence of DNA Configuration on the Direct Strand Break Yield. *Comput Math Methods Med*. 2015:417501.

Bernard, P., J.F. Maure, J.F. Partridge, S. Genier, J.P. Javerzat, and R.C. Allshire. 2001. Requirement of heterochromatin for cohesion at centromeres. *Science*. 294:2539-2542.

Bertalan, Z., C.A. La Porta, H. Maiato, and S. Zapperi. 2014. Conformational mechanism for the stability of microtubule-kinetochore attachments. *Biophysical journal*. 107:289-300.

Boettcher, B., T.T. Marquez-Lago, M. Bayer, E.L. Weiss, and Y. Barral. 2012. Nuclear envelope morphology constrains diffusion and promotes asymmetric protein segregation in closed mitosis. *The Journal of cell biology*. 197:921-937.

Bolzer, A., G. Kreth, I. Solovei, D. Koehler, K. Saracoglu, C. Fauth, S. Muller, R. Eils, C. Cremer, M. R.Speicher, and T. Cremer. 2005. Three-dimensional maps of all chromosomes in human male fibroblast nuclei and prometaphase rosettes. *PLoS Biology*. 3:826-842.

Bonnet, A., H. Bretes, and B. Palancade. 2015. Nuclear pore components affect distinct stages of intron-containing gene expression. *Nucleic Acids Res*. 43:4249-4261.

Botta, M., S. Haider, I.X. Leung, P. Lio, and J. Mozziconacci. 2010. Intra- and inter-chromosomal interactions correlate with CTCF binding genome wide. *Molecular systems biology*. 6:426.

Brickner, J.H., and P. Walter. 2004. Gene recruitment of the activated INO1 locus to the nuclear membrane. *PLoS Biol*. 2:e342.

Bupp, J.M., A.E. Martin, E.S. Stensrud, and S.L. Jaspersen. 2007. Telomere anchoring at the nuclear periphery requires the budding yeast Sad1-UNC-84 domain protein Mps3. *Journal of Cell Biology*. 179:845-854.

Burns, L.T., and S.R. Wente. 2014. From hypothesis to mechanism: uncovering nuclear pore complex links to gene expression. *Molecular and cellular biology*. 34:2114-2120.

Bystricky, K., P. Heun, L. Gehlen, J. Langowski, and S.M. Gasser. 2004. Long-range compaction and flexibility of interphase chromatin in budding yeast analyzed by high-resolution imaging techniques. *Proceedings of the National Academy of Sciences of the United States of America*. 101:16495-16500.

Bystricky, K., T. Laroche, G. van Houwe, M. Blaszczyk, and S.M. Gasser. 2005. Chromosome looping in yeast: telomere pairing and coordinated movement reflect anchoring efficiency and territorial organization. *Journal of Cell Biology*. 168:375-387.

Cabal, G.G., A. Genovesio, S. Rodriguez-Navarro, C. Zimmer, O. Gadal, A. Lesne, H. Buc, F. Feuerbach-Fournier, J.C. Olivo-Marin, E.C. Hurt, and U. Nehrbass. 2006. SAGA interacting factors confine sub-diffusion of transcribed genes to the nuclear envelope. *Nature*. 441:770-773.

Casolari, J.M., C.R. Brown, S. Komili, J. West, H. Hieronymus, and P.A. Silver. 2004. Genome-wide localization of the nuclear transport machinery couples transcriptional status and nuclear organization. *Cell*. 117:427-439.

Cheeseman, I.M., and A. Desai. 2008. Molecular architecture of the kinetochore-microtubule interface. *Nature reviews. Molecular cell biology*. 9:33-46.

Choi, J., and T. Majima. 2011. Conformational changes of non-B DNA. *Chemical Society reviews*. 40:5893-5909.

Cockell, M.M., and S.M. Gasser. 1999. The nucleolus: nucleolar space for RENT. *Current biology : CB*. 9:R575-576.

Corbett, A.H., and P.A. Silver. 1997. Nucleocytoplasmic transport of macromolecules. *Microbiology and molecular biology reviews : MMBR*. 61:193-211.

Cournac, A., R. Koszul, and J. Mozziconacci. 2016. The 3D folding of metazoan genomes correlates with the association of similar repetitive elements. *Nucleic Acids Res*. 44:245-255.

Cremer, M., F. Grasser, C. Lanctot, S. Muller, M. Neusser, R. Zinner, I. Solovei, and T. Cremer. 2008. Multicolor 3D fluorescence in situ hybridization for imaging interphase chromosomes. *Methods Mol Biol*. 463:205-239.

Cremer, T., and M. Cremer. 2010. Chromosome Territories. *Cold Spring Harbor perspectives in biology*. 2.

D'Angelo, M.A., and M.W. Hetzer. 2008. Structure, dynamics and function of nuclear pore complexes. *Trends Cell Biol*. 18:456-466.

Dammann, R., R. Lucchini, T. Koller, and J.M. Sogo. 1993. Chromatin structures and transcription of rDNA in yeast Saccharomyces cerevisiae. *Nucleic Acids Res*. 21:2331-2338.

Davey, C.A., D.F. Sargent, K. Luger, A.W. Maeder, and T.J. Richmond. 2002. Solvent mediated interactions in the structure of the nucleosome core particle at 1.9 angstrom resolution. *J Mol Biol*. 319:1097-1113.

De Lucia, F., M. Alilat, A. Sivolob, and A. Prunell. 1999. Nucleosome dynamics. III. Histone tail-dependent fluctuation of nucleosomes between open and closed DNA conformations. Implications for chromatin dynamics and the linking number paradox. A relaxation study of mononucleosomes on DNA minicircles. *J Mol Biol*. 285:1101-1119.

Dekker, J., M.A. Marti-Renom, and L.A. Mirny. 2013. Exploring the three-dimensional organization of genomes: interpreting chromatin interaction data. *Nature Reviews Genetics*. 14:390-403.

Dekker, J., K. Rippe, M. Dekker, and N. Kleckner. 2002. Capturing chromosome conformation. *Science*. 295:1306-1311.

Dilworth, D.J., A. Suprapto, J.C. Padovan, B.T. Chait, R.W. Wozniak, M.P. Rout, and J.D. Aitchison. 2001. Nup2p dynamically associates with the distal regions of the yeast nuclear pore complex. *The Journal of cell biology*. 153:1465-1478.

Doluca, O., J.M. Withers, and V.V. Filichev. 2013. Molecular Engineering of Guanine-Rich Sequences: Z-DNA, DNA Triplexes, and G-Quadruplexes. *Chem Rev*. 113:3044-3083.

Dorigo, B., T. Schalch, K. Bystricky, and T.J. Richmond. 2003. Chromatin fiber folding: requirement for the histone H4 N-terminal tail. *J Mol Biol*. 327:85-96.

Dostie, J., T.A. Richmond, R.A. Arnaout, R.R. Selzer, W.L. Lee, T.A. Honan, E.D. Rubio, A. Krumm, J. Lamb, C. Nusbaum, R.D. Green, and J. Dekker. 2006. Chromosome Conformation Capture Carbon Copy (5C): A massively parallel solution for mapping interactions between genomic elements. *Genome Res*. 16:1299-1309.

Duan, Z., M. Andronescu, K. Schutz, S. McIlwain, Y.J. Kim, C. Lee, J. Shendure, S. Fields, C.A. Blau, and W.S. Noble. 2010. A three-dimensional model of the yeast genome. *Nature*. 465:363-367.

Dultz, E., H. Tjong, E. Weider, M. Herzog, B. Young, C. Brune, D. Mullner, C. Loewen, F. Alber, and K. Weis. 2016. Global reorganization of budding yeast chromosome conformation in different physiological conditions. *The Journal of cell biology*. 212:321-334.

Dundr, M., T. Misteli, and M.O. Olson. 2000. The dynamics of postmitotic reassembly of the nucleolus. *The Journal of cell biology*. 150:433-446.

Eckert-Boulet, N., and M. Lisby. 2009. Regulation of rDNA stability by sumoylation. *DNA repair*. 8:507-516.

Ewen, B., and D. Richter. 1997. Neutron spin echo investigations on the segmental dynamics of polymers in melts, networks and solutions. *Adv Polym Sci*. 134:1-129.

Finch, J.T., and A. Klug. 1976. Solenoidal model for superstructure in chromatin. *Proceedings of the National Academy of Sciences of the United States of America*. 73:1897-1901.

Fischle, W., Y. Wang, and C.D. Allis. 2003. Histone and chromatin cross-talk. *Current opinion in cell biology*. 15:172-183.

Gal, N., D. Lechtman-Goldstein, and D. Weihs. 2013. Particle tracking in living cells: a review of the mean square displacement method and beyond. *Rheologica Acta*. 52:425-443.

Galy, V., O. Gadal, M. Fromont-Racine, A. Romano, A. Jacquier, and U. Nehrbass. 2004. Nuclear retention of unspliced mRNAs in yeast is mediated by perinuclear Mlp1. *Cell*. 116:63-73.

Gehlen, L.R., G. Gruenert, M.B. Jones, C.D. Rodley, J. Langowski, and J.M. O'Sullivan. 2012. Chromosome positioning and the clustering of functionally related loci in yeast is driven by chromosomal interactions. *Nucleus*. 3:370-383.

Gehlen, L.R., S. Nagai, K. Shimada, P. Meister, A. Taddei, and S.M. Gasser. 2011. Nuclear Geometry and Rapid Mitosis Ensure Asymmetric Episome Segregation in Yeast. *Current Biology*. 21:25-33.

Ghosh, A., and M. Bansal. 2003. A glossary of DNA structures from A to Z. *Acta crystallographica. Section D, Biological crystallography*. 59:620-626.

Ghosh, A., and N.S. Gov. 2014. Dynamics of active semiflexible polymers. *Biophysical journal*. 107:1065-1073.

Goffeau, A., B.G. Barrell, H. Bussey, R.W. Davis, B. Dujon, H. Feldmann, F. Galibert, J.D. Hoheisel, C. Jacq, M. Johnston, E.J. Louis, H.W. Mewes, Y. Murakami, P. Philippsen, H. Tettelin, and S.G. Oliver. 1996. Life with 6000 genes. *Science*. 274:546, 563-547.

Goldman, R.D., Y. Gruenbaum, R.D. Moir, D.K. Shumaker, and T.P. Spann. 2002. Nuclear lamins: building blocks of nuclear architecture. *Gene Dev*. 16:533-547.

Gotta, M., T. Laroche, A. Formenton, L. Maillet, H. Scherthan, and S.M. Gasser. 1996. The clustering of telomeres and colocalization with Rap1, Sir3, and Sir4 proteins in wild-type Saccharomyces cerevisiae. *The Journal of cell biology*. 134:1349-1363.

Grandi, P., N. Schlaich, H. Tekotte, and E.C. Hurt. 1995. Functional interaction of Nic96p with a core nucleoporin complex consisting of Nsp1p, Nup49p and a novel protein Nup57p. *The EMBO journal*. 14:76-87.

Greenland, K.B., H. Ding, M. Costanzo, C. Boone, and T.N. Davis. 2010. Identification of Saccharomyces cerevisiae spindle pole body remodeling factors. *PloS one*. 5:e15426.

Grewal, S.I., and S. Jia. 2007. Heterochromatin revisited. *Nature reviews. Genetics*. 8:35-46.

Grewal, S.I., and D. Moazed. 2003. Heterochromatin and epigenetic control of gene expression. *Science*. 301:798-802.

Grigoryev, S.A., G. Arya, S. Correll, C.L. Woodcock, and T. Schlick. 2009. Evidence for heteromorphic chromatin fibers from analysis of nucleosome interactions. *Proceedings of the National Academy of Sciences of the United States of America*. 106:13317-13322.

Grob, A., and B. McStay. 2014. Construction of synthetic nucleoli and what it tells us about propagation of sub-nuclear domains through cell division. *Cell Cycle*. 13:2501-2508.

Guet, D., L.T. Burns, S. Maji, J. Boulanger, P. Hersen, S.R. Wente, J. Salamero, and C. Dargemont. 2015. Combining Spinach-tagged RNA and gene localization to image gene expression in live yeast. *Nat Commun*. 6:8882.

Guidi, M., M. Ruault, M. Marbouty, I. Loiodice, A. Cournac, C. Billaudeau, A. Hocher, J. Mozziconacci, R. Koszul, and A. Taddei. 2015. Spatial reorganization of telomeres in long-lived quiescent cells. *Genome Biol*. 16:206.

Hajjoul, H., S. Kocanova, I. Lassadi, K. Bystricky, and A. Bancaud. 2009. Lab-on-Chip for fast 3D particle tracking in living cells. *Lab Chip*. 9:3054-3058.

Hajjoul, H., J. Mathon, H. Ranchon, I. Goiffon, J. Mozziconacci, B. Albert, P. Carrivain, J.M. Victor, O. Gadal, K. Bystricky, and A. Bancaud. 2013. High-throughput chromatin motion tracking in living yeast reveals the flexibility of the fiber throughout the genome. *Genome Res*. 23:1829-1838.

Hall, I.M., K. Noma, and S.I.S. Grewal. 2003. RNA interference machinery regulates chromosome dynamics during mitosis and meiosis in fission yeast. *Proceedings of the National Academy of Sciences of the United States of America*. 100:193-198.

Han, R., Z. Li, Y. Fan, and Y. Jiang. 2013. Recent advances in super-resolution fluorescence imaging and its applications in biology. *Journal of genetics and genomics = Yi chuan xue bao*. 40:583-595.

Hansen, J.C. 2002. Conformational dynamics of the chromatin fiber in solution: determinants, mechanisms, and functions. *Annu Rev Biophys Biomol Struct*. 31:361-392.

Hattier, T., E.D. Andrulis, and A.M. Tartakoff. 2007. Immobility, inheritance and plasticity of shape of the yeast nucleus. *BMC cell biology*. 8:47.

Hernandez-Verdun, D., P. Roussel, M. Thiry, V. Sirri, and D.L. Lafontaine. 2010. The nucleolus: structure/function relationship in RNA metabolism. *Wiley interdisciplinary reviews. RNA*. 1:415-431.

Heun, P., T. Laroche, M.K. Raghuraman, and S.M. Gasser. 2001. The positioning and dynamics of origins of replication in the budding yeast nucleus. *The Journal of cell biology*. 152:385-400.

Hudson, D.F., K.M. Marshall, and W.C. Earnshaw. 2009. Condensin: Architect of mitotic chromosomes. *Chromosome research : an international journal on the molecular, supramolecular and evolutionary aspects of chromosome biology*. 17:131-144.

Huet, S., C. Lavelle, H. Ranchon, P. Carrivain, J.M. Victor, and A. Bancaud. 2014. Relevance and limitations of crowding, fractal, and polymer models to describe nuclear architecture. *International review of cell and molecular biology*. 307:443-479.

Huh, W.K., J.V. Falvo, L.C. Gerke, A.S. Carroll, R.W. Howson, J.S. Weissman, and E.K. O'Shea. 2003. Global analysis of protein localization in budding yeast. *Nature*. 425:686-691.

Ishii, K., G. Arib, C. Lin, G. Van Houwe, and U.K. Laemmli. 2002. Chromatin boundaries in budding yeast: the nuclear pore connection. *Cell*. 109:551-562.

Jani, D., E. Valkov, and M. Stewart. 2014. Structural basis for binding the TREX2 complex to nuclear pores, GAL1 localisation and mRNA export. *Nucleic Acids Res*. 42:6686-6697.

Jaspersen, S.L., and S. Ghosh. 2012. Nuclear envelope insertion of spindle pole bodies and nuclear pore complexes. *Nucleus*. 3:226-236.

Jaspersen, S.L., A.E. Martin, G. Glazko, T.H. Giddings, Jr., G. Morgan, A. Mushegian, and M. Winey. 2006. The Sad1-UNC-84 homology domain in Mps3 interacts with Mps2 to connect the spindle pole body with the nuclear envelope. *The Journal of cell biology*. 174:665-675.

Jaspersen, S.L., and M. Winey. 2004. The budding yeast spindle pole body: structure, duplication, and function. *Annual review of cell and developmental biology*. 20:1-28.

Jin, Q., E. Trelles-Sticken, H. Scherthan, and J. Loidl. 1998. Yeast nuclei display prominent centromere clustering that is reduced in nondividing cells and in meiotic prophase. *J Cell Biol*. 141:21-29.

Jorgensen, P., N.P. Edgington, B.L. Schneider, I. Rupes, M. Tyers, and B. Futcher. 2007. The size of the nucleus increases as yeast cells grow. *Mol Biol Cell*. 18:3523-3532.

Joti, Y., T. Hikima, Y. Nishino, F. Kamada, S. Hihara, H. Takata, T. Ishikawa, and K. Maeshima. 2012. Chromosomes without a 30-nm chromatin fiber. *Nucleus*. 3:404-410.

Kim, K.D., H. Tanizawa, O. Iwasaki, C.J. Corcoran, J.R. Capizzi, J.E. Hayden, and K. Noma. 2013. Centromeric motion facilitates the mobility of interphase genomic regions in fission yeast. *Journal of cell science*. 126:5271-5283.

Kirshner, H., F. Aguet, D. Sage, and M. Unser. 2013. 3-D PSF fitting for fluorescence microscopy: implementation and localization application. *Journal of microscopy*. 249:13-25.

Klein, F., T. Laroche, M.E. Cardenas, J.F.X. Hofmann, D. Schweizer, and S.M. Gasser. 1992. Localization of Rap1 and Topoisomerase-Ii in Nuclei and Meiotic Chromosomes of Yeast. *Journal of Cell Biology*. 117:935-948.

Knockenhauer, K.E., and T.U. Schwartz. 2016. The Nuclear Pore Complex as a Flexible and DynamicGate. *Cell*. 164:1162-1171.

Knop, M., G. Pereira, and E. Schiebel. 1999. Microtubule organization by the budding yeast spindle pole body. *Biology of the cell / under the auspices of the European Cell Biology Organization*. 91:291-304.

Kobayashi, T. 2003. The replication fork barrier site forms a unique structure with Fob1p and inhibits the replication fork. *Molecular and cellular biology*. 23:9178-9188.

Kobayashi, T., and T. Horiuchi. 1996. A yeast gene product, Fob1 protein, required for both replication fork blocking and recombinational hotspot activities. *Genes Cells*. 1:465-474.

Koning, A.J., P.Y. Lum, J.M. Williams, and R. Wright. 1993. Dioc6 Staining Reveals Organelle Structure and Dynamics in Living Yeast-Cells. *Cell Motil Cytoskel*. 25:111-128.

Kupiec, M. 2014. Biology of telomeres: lessons from budding yeast. *FEMS microbiology reviews*. 38:144-171.

Lacroix, J., S. Pelofy, C. Blatche, M.J. Pillaire, S. Huet, C. Chapuis, J.S. Hoffmann, and A. Bancaud. 2016. Analysis of DNA replication by optical mapping in nanochannels. *Small*. doi: 10.1002 /smll.201503795.

Lam, A.L., D.E. Pazin, and B.A. Sullivan. 2005. Control of gene expression and assembly of chromosomal subdomains by chromatin regulators with antagonistic functions. *Chromosoma*. 114:242-251.

Laporte, D., F. Courtout, B. Salin, J. Ceschin, and I. Sagot. 2013. An array of nuclear microtubules reorganizes the budding yeast nucleus during quiescence. *The Journal of cell biology*. 203:585-594.

Larabell, C.A., and M.A. Le Gros. 2004. X-ray tomography generates 3-D reconstructions of the yeast, Saccharomyces cerevisiae, at 60-nm resolution. *Molecular biology of the cell*. 15:957-962.

Laroche, T., S.G. Martin, M. Gotta, H.C. Gorham, F.E. Pryde, E.J. Louis, and S.M. Gasser. 1998. Mutation of yeast Ku genes disrupts the subnuclear organization of telomeres. *Current biology : CB*. 8:653-656.

Lau, A.C., and G. Csankovszki. 2014. Condensin-mediated chromosome organization and gene regulation. *Frontiers in genetics*. 5:473.

Leger-Silvestre, I., S. Trumtel, J. Noaillac-Depeyre, and N. Gas. 1999. Functional compartmentalization of the nucleus in the budding yeast Saccharomyces cerevisiae. *Chromosoma*. 108:103-113.

Lesne, A., J. Riposo, P. Roger, A. Cournac, and J. Mozziconacci. 2014. 3D genome reconstruction from chromosomal contacts. *Nature methods*. 11:1141-1143.

Leung, A.K., and A.I. Lamond. 2003. The dynamics of the nucleolus. *Critical reviews in eukaryotic gene expression*. 13:39-54.

Lieberman-Aiden, E., N.L. van Berkum, L. Williams, M. Imakaev, T. Ragoczy, A. Telling, I. Amit, B.R. Lajoie, P.J. Sabo, M.O. Dorschner, R. Sandstrom, B. Bernstein, M.A. Bender, M. Groudine, A. Gnirke, J. Stamatoyannopoulos, L.A. Mirny, E.S. Lander, and J. Dekker. 2009. Comprehensive mapping of long-range interactions reveals folding principles of the human genome. *Science*. 326:289-293.

Loiodice, I., M. Dubarry, and A. Taddei. 2014. Scoring and manipulating gene position and dynamics using FROS in budding yeast. *Current protocols in cell biology / editorial board, Juan S. Bonifacino ... [et al.]*. 62:Unit 22 17 21-14.

Longtine, M.S., A. McKenzie, 3rd, D.J. Demarini, N.G. Shah, A. Wach, A. Brachat, P. Philippsen, and J.R. Pringle. 1998. Additional modules for versatile and economical PCR-based gene deletion and modification in Saccharomyces cerevisiae. *Yeast*. 14:953-961.

Lopez-Soler, R.I., R.D. Moir, T.P. Spann, R. Stick, and R.D. Goldman. 2001. A role for nuclear lamins in nuclear envelope assembly. *Journal of Cell Biology*. 154:61-70.

Louis, E.J. 1995. The chromosome ends of Saccharomyces cerevisiae. *Yeast*. 11:1553-1573.

Lu, X.J., Z. Shakked, and W.K. Olson. 2000. A-form conformational motifs in ligand-bound DNA structures. *J Mol Biol*. 300:819-840.

Luders, J., and T. Stearns. 2007. Microtubule-organizing centres: a re-evaluation. *Nature reviews. Molecular cell biology*. 8:161-167.

Luger, K., A.W. Mader, R. K.Richmond, D.F. Sargent, and T.J. Richmond. 1997. Crystal structure of the nucleosome core particle at 2.8 A resolution. *nature*. 389:251-260.

Maeshima, K., and M. Eltsov. 2008. Packaging the genome: the structure of mitotic chromosomes. *Journal of biochemistry*. 143:145-153.

Maeshima, K., S. Hihara, and M. Eltsov. 2010. Chromatin structure: does the 30-nm fibre exist in vivo? *Current opinion in cell biology*. 22:291-297.

Maeshima, K., R. Imai, S. Tamura, and T. Nozaki. 2014. Chromatin as dynamic 10-nm fibers. *Chromosoma*. 123:225-237.

Maeshima, K., and U.K. Laemmli. 2003. A two-step scaffolding model for mitotic chromosome assembly. *Developmental cell*. 4:467-480.

Manuelidis, L. 1985. Individual Interphase Chromosome Domains Revealed by Insitu Hybridization. *Human Genetics*. 71:288-293.

Marshall, W.F., A. Straight, J.F. Marko, J. Swedlow, A. Dernburg, A. Belmont, A.W. Murray, D.A. Agard, and J.W. Sedat. 1997. Interphase chromosomes undergo constrained diffusional motion in living cells. *Current biology : CB*. 7:930-939.

McIntosh, J.R., and E.T. O'Toole. 1999. Life cycles of yeast spindle pole bodies: Getting microtubules into a closed nucleus. *Biology of the Cell*. 91:305-312.

McStay, B., and I. Grummt. 2008. The epigenetics of rRNA genes: from molecular to chromosome biology. *Annual review of cell and developmental biology*. 24:131-157.

Meister, P., L.R. Gehlen, E. Varela, V. Kalck, and S.M. Gasser. 2010. Visualizing yeast chromosomes and nuclear architecture. *Methods in enzymology*. 470:535-567.

Mekhail, K., J. Seebacher, S.P. Gygi, and D. Moazed. 2008. Role for perinuclear chromosome tethering in maintenance of genome stability. *Nature*. 456:667-670.

Melese, T., and Z. Xue. 1995. The nucleolus: an organelle formed by the act of building a ribosome. *Current opinion in cell biology*. 7:319-324.

Mine-Hattab, J., V. Recamier, I. Izeddin, R. Rothstein, and X. Darzacq. 2016. Fast imaging of DNA motion reveals distinct sub-diffusion regimes at the site of DNA damage. *bioRxiv*.

Miyazaki, N., M. Esaki, T. Ogura, and K. Murata. 2014. Serial block-face scanning electron microscopy for three-dimensional analysis of morphological changes in mitochondria regulated by Cdc48p/p97 ATPase. *J Struct Biol*. 187:187-193.

Montavon, T., and D. Duboule. 2012. Landscapes and archipelagos: spatial organization of gene regulation in vertebrates. *Trends Cell Biol*. 22:347-354.

Moser, S.C., and J.R. Swedlow. 2011. How to be a mitotic chromosome. *Chromosome Research*. 19:307-319.

Murata, K., M. Esaki, T. Ogura, S. Arai, Y. Yamamoto, and N. Tanaka. 2014. Whole-cell imaging of the budding yeast Saccharomyces cerevisiae by high-voltage scanning transmission electron tomography. *Ultramicroscopy*. 146:39-45.

Nagano, T., Y. Lubling, T.J. Stevens, S. Schoenfelder, E. Yaffe, W. Dean, E.D. Laue, A. Tanay, and P. Fraser. 2013. Single-cell Hi-C reveals cell-to-cell variability in chromosome structure. *Nature*. 502:59-64.

Naumova, N., M. Imakaev, G. Fudenberg, Y. Zhan, B.R. Lajoie, L.A. Mirny, and J. Dekker. 2013. Organization of the mitotic chromosome. *Science*. 342:948-953.

Naumova, N., E.M. Smith, Y. Zhan, and J. Dekker. 2012. Analysis of long-range chromatin interactions using Chromosome Conformation Capture. *Methods*. 58:192-203.

Nelson, A.J., and S.T. Hess. 2014. Localization microscopy: mapping cellular dynamics with single molecules. *Journal of microscopy*. 254:1-8.

Neusser, M., V. Schubel, A. Koch, T. Cremer, and S. Muller. 2007. Evolutionarily conserved, cell type and species-specific higher order chromatin arrangements in interphase nuclei of primates. *Chromosoma*. 116:307-320.

Niepel, M., C. Strambio-de-Castillia, J. Fasolo, B.T. Chait, and M.P. Rout. 2005. The nuclear pore complex-associated protein, Mlp2p, binds to the yeast spindle pole body and promotes its efficient assembly. *The Journal of cell biology*. 170:225-235.

Nishino, Y., M. Eltsov, Y. Joti, K. Ito, H. Takata, Y. Takahashi, S. Hihara, A.S. Frangakis, N. Imamoto, T. Ishikawa, and K. Maeshima. 2012. Human mitotic chromosomes consist predominantly of irregularly folded nucleosome fibres without a 30-nm chromatin structure. *Embo Journal*. 31:1644-1653.

Nozaki, T., K. Kaizu, C.G. Pack, S. Tamura, T. Tani, S. Hihara, T. Nagai, K. Takahashi, and K. Maeshima. 2013. Flexible and dynamic nucleosome fiber in living mammalian cells. *Nucleus-Austin*. 4:349-356.

Osborne, M.A., G. Schlenstedt, T. Jinks, and P.A. Silver. 1994. Nuf2, a spindle pole body-associated protein required for nuclear division in yeast. *The Journal of cell biology*. 125:853-866.

Ostergaard, S., L. Olsson, and J. Nielsen. 2000. Metabolic engineering of Saccharomyces cerevisiae. *Microbiology and molecular biology reviews : MMBR*. 64:34-50.

Palancade, B., M. Zuccolo, S. Loeillet, A. Nicolas, and V. Doye. 2005. Pml39, a novel protein of the nuclear periphery required for nuclear retention of improper messenger ribonucleoparticles. *Mol Biol Cell*. 16:5258-5268.

Peccarelli, M., and B.W. Kebaara. 2014. Measurement of mRNA Decay Rates in Saccharomyces cerevisiae Using rpb1-1 Strains. *Jove-J Vis Exp*.

Petes, T.D., B. Byers, and W.L. Fangman. 1973. Size and structure of yeast chromosomal DNA. *Proc Natl Acad Sci*. 70:3072-3076.

R., N.C., L.S. W., and W.J. R. 1997. Does *Saccharomyces* need an organized nucleolus? *Chromosoma*. 105:444-451.

Raska, I., K. Koberna, J. Malinsky, H. Fidlerova, and M. Masata. 2004. The nucleolus and transcription of ribosomal genes. *Biology of the cell / under the auspices of the European Cell Biology Organization*. 96:579-594.

Recouvreux, P., C. Lavelle, M. Barbi, E.S.N. Conde, E. Le Cam, J.M. Victor, and J.L. Viovy. 2011. Linker histones incorporation maintains chromatin fiber plasticity. *Biophysical journal*. 100:2726-2735.

Rieder, C.L., and R.E. Palazzo. 1992. Colcemid and the mitotic cycle. *Journal of cell science*. 102 (Pt 3):387-392.

Robinson, P.J., L. Fairall, V.A. Huynh, and D. Rhodes. 2006. EM measurements define the dimensions of the "30-nm" chromatin fiber: evidence for a compact, interdigitated structure. *Proceedings of the National Academy of Sciences of the United States of America*. 103:6506-6511.

Robinson, P.J.J., and D. Rhodes. 2006. Structure of the '30 nm' chromatin fibre: A key role for the linker histone. *Curr Opin Struc Biol*. 16:336-343.

Rodriguez, A., and P. Bjerling. 2013. The links between chromatin spatial organization and biological function. *Biochemical Society transactions*. 41:1634-1639.

Rose, M.D., F. Winston, and P. Hieter. 1990. Methods in Yeast Genetics. A Laboratory Manual. Cold Spring Harbor, NY,.

Rout, M.P., J.D. Aitchison, A. Suprapto, K. Hjertaas, Y. Zhao, and B.T. Chait. 2000. The yeast nuclear pore complex: composition, architecture, and transport mechanism. *The Journal of cell biology*. 148:635-651.

Routh, A., S. Sandin, and D. Rhodes. 2008. Nucleosome repeat length and linker histone stoichiometry determine chromatin fiber structure. *Proceedings of the National Academy of Sciences of the United States of America*. 105:8872-8877.

Ryan, K.J., and S.R. Wente. 2000. The nuclear pore complex: a protein machine bridging the nucleus and cytoplasm. *Current opinion in cell biology*. 12:361-371.

Sanyal, A., D. Bau, M.A. Marti-Renom, and J. Dekker. 2011. Chromatin globules: a common motif of higher order chromosome structure? *Current opinion in cell biology*. 23:325-331.

Saxton, M.J. 1994. Single-particle tracking: models of directed transport. *Biophysical journal*. 67:2110-2119.

Schalch, T., S. Duda, D.F. Sargent, and T.J. Richmond. 2005. X-ray structure of a tetranucleosome and its implications for the chromatin fibre. *Nature*. 436:138-141.

Schardin, M., T. Cremer, H.D. Hager, and M. Lang. 1985. Specific Staining of Human-Chromosomes in Chinese-Hamster X Man Hybrid Cell-Lines Demonstrates Interphase Chromosome Territories. *Human Genetics*. 71:281-287.

Schindelin, J., I. Arganda-Carreras, E. Frise, V. Kaynig, M. Longair, T. Pietzsch, S. Preibisch, C. Rueden, S. Saalfeld, B. Schmid, J.Y. Tinevez, D.J. White, V. Hartenstein, K. Eliceiri, P. Tomancak, and A. Cardona. 2012. Fiji: an open-source platform for biological-image analysis. *Nature methods*. 9:676-682.

Schwartz, T.U. 2016. The Structure Inventory of the Nuclear Pore Complex. *J Mol Biol*. 428:1986-2000.

Shogren-Knaak, M., H. Ishii, J.M. Sun, M.J. Pazin, J.R. Davie, and C.L. Peterson. 2006. Histone H4-K16 acetylation controls chromatin structure and protein interactions. *Science*. 311:844-847.

Simmons Kovacs, L.A., C.L. Nelson, and S.B. Haase. 2008. Intrinsic and cyclin-dependent kinase-dependent control of spindle pole body duplication in budding yeast. *Molecular biology of the cell*. 19:3243-3253.

Simonis, M., P. Klous, E. Splinter, Y. Moshkin, R. Willemsen, E. de Wit, B. van Steensel, and W. de Laat. 2006. Nuclear organization of active and inactive chromatin domains uncovered by chromosome conformation capture-on-chip (4C). *Nat Genet*. 38:1348-1354.

Sivolob, A., C. Lavelle, and A. Prunell. 2003. Sequence-dependent nucleosome structural and dynamic polymorphism. Potential involvement of histone H2B N-terminal tail proximal domain. *J Mol Biol*. 326:49-63.

Sosa, B.A., A. Rothballer, U. Kutay, and T.U. Schwartz. 2012. LINC Complexes Form by Binding of Three KASH Peptides to Domain Interfaces of Trimeric SUN Proteins. *Cell*. 149:1035-1047.

Stone, E.M., P. Heun, T. Laroche, L. Pillus, and S.M. Gasser. 2000. MAP kinase signaling induces nuclear reorganization in budding yeast. *Current biology : CB*. 10:373-382.

Strahl, B.D., and C.D. Allis. 2000. The language of covalent histone modifications. *Nature*. 403:41-45.

Stuurman, N., S. Heins, and U. Aebi. 1998. Nuclear lamins: Their structure, assembly, and interactions. *J Struct Biol*. 122:42-66.

Sung, M.K., C.W. Ha, and W.K. Huh. 2008. A vector system for efficient and economical switching of C-terminal epitope tags in Saccharomyces cerevisiae. *Yeast*. 25:301-311.

Taddei, A., and S.M. Gasser. 2006. Repairing subtelomeric DSBs at the nuclear periphery. *Trends Cell Biol*. 16:225-228.

Taddei, A., and S.M. Gasser. 2012. Structure and function in the budding yeast nucleus. *Genetics*. 192:107-129.

Taddei, A., F. Hediger, F.R. Neumann, C. Bauer, and S.M. Gasser. 2004. Separation of silencing from perinuclear anchoring functions in yeast Ku80, Sir4 and Esc1 proteins. *The EMBO journal*. 23:1301-1312.

Taddei, A., H. Schober, and S.M. Gasser. 2010. The budding yeast nucleus. *Cold Spring Harbor perspectives in biology*. 2:a000612.

Taddei, A., G. Van Houwe, F. Hediger, V. Kalck, F. Cubizolles, H. Schober, and S.M. Gasser. 2006. Nuclear pore association confers optimal expression levels for an inducible yeast gene. *Nature*. 441:774-778.

Takagi, M., and N. Imamoto. 2014. Control of nuclear size by NPC proteins. *Advances in experimental medicine and biology*. 773:571-591.

Teraoka, I., and P. Cifra. 2002. Polymer chains in semidilute solutions confined to a square channel: mean-field Gaussian chain theory and comparison with simulation results. *Polymer*. 43:3025-3033.

Texari, L., G. Dieppois, P. Vinciguerra, M.P. Contreras, A. Groner, A. Letourneau, and F. Stutz. 2013. The nuclear pore regulates GAL1 gene transcription by controlling the localization of the SUMO protease Ulp1. *Molecular cell*. 51:807-818.

Therizols, P., T. Duong, B. Dujon, C. Zimmer, and E. Fabre. 2010. Chromosome arm length and nuclear constraints determine the dynamic relationship of yeast subtelomeres. *Proceedings of the National Academy of Sciences of the United States of America*. 107:2025-2030.

Thiry, M., T. Cheutin, M.F. O'Donohue, H. Kaplan, and D. Ploton. 2000. Dynamics and three-dimensional localization of ribosomal RNA within the nucleolus. *Rna*. 6:1750-1761.

Thiry, M., and D.L. Lafontaine. 2005. Birth of a nucleolus: the evolution of nucleolar compartments. *Trends Cell Biol*. 15:194-199.

Thomann, D., D.R. Rines, P.K. Sorger, and G. Danuser. 2002. Automatic fluorescent tag detection in 3D with super-resolution: application to the analysis of chromosome movement. *Journal of microscopy*. 208:49-64.

Thomas, J.O., and V. Furber. 1976. Yeast chromatin structure. *Febs Lett*. 66:274-280.

Thompson, R.E., D.R. Larson, and W.W. Webb. 2002. Precise nanometer localization analysis for individual fluorescent probes. *Biophysical journal*. 82:2775-2783.

Tjong, H., K. Gong, L. Chen, and F. Alber. 2012. Physical tethering and volume exclusion determine higher-order genome organization in budding yeast. *Genome Res*. 22:1295-1305.

Tooze, J., and H.G. Davies. 1967. Light- and electron- microscope studies on the spleen of the newt Triturus cristatus: the fine structure of erythropoietic cells. *Journal of cell science*. 2:617-640.

Towbin, B.D., P. Meister, and S.M. Gasser. 2009. The nuclear envelope--a scaffold for silencing? *Current opinion in genetics & development*. 19:180-186.

Trumtel, S., I. Leger-Silvestre, P.E. Gleizes, F. Teulieres, and N. Gas. 2000. Assembly and functional organization of the nucleolus: ultrastructural analysis of Saccharomyces cerevisiae mutants. *Molecular biology of the cell*. 11:2175-2189.

Tsang, C.K., P.G. Bertram, W. Ai, R. Drenan, and X.F. Zheng. 2003. Chromatin-mediated regulation of nucleolar structure and RNA Pol I localization by TOR. *Embo J*. 22:6045-6056.

Umbarger, M.A., E. Toro, M.A. Wright, G.J. Porreca, D. Bau, S.H. Hong, M.J. Fero, L.J. Zhu, M.A. Marti-Renom, H.H. McAdams, L. Shapiro, J. Dekker, and G.M. Church. 2011. The three-dimensional architecture of a bacterial genome and its alteration by genetic perturbation. *Molecular cell*. 44:252-264.

van Steensel, B., and J. Dekker. 2010. Genomics tools for unraveling chromosome architecture. *Nat Biotechnol*. 28:1089-1095.

Verdaasdonk, J.S., P.A. Vasquez, R.M. Barry, T. Barry, S. Goodwin, M.G. Forest, and K. Bloom. 2013. Centromere tethering confines chromosome domains. *Molecular cell*. 52:819-831.

Vjestica, A., and S. Oliferenko. 2012. Nuclear Geometry: Mitotic Nucleus Flares Out When Arrested. *Current Biology*. 22:R489-R491.

Wadell, H. 1935. Volume, shape, and roundness of quartz particles. *J. Geol*. 43:250-280.

Wainright, P.O., G. Hinkle, M.L. Sogin, and S.K. Stickel. 1993. Monophyletic origins of the metazoa: an evolutionary link with fungi. *Science*. 260:340-342.

Walters, A.D., C.K. May, E.S. Dauster, B.P. Cinquin, E.A. Smith, X. Robellet, D. D'Amours, C.A. Larabell, and O. Cohen-Fix. 2014. The yeast polo kinase Cdc5 regulates the shape of the mitotic nucleus. *Current biology : CB*. 24:2861-2867.

Wang, F., C. Ying, G. Shang, M. Jiao, and Z. Hongfang. 2013. The new evidence of nucleolar ultrastructural dynamic change: fibrillar centre (FC) fusion in G1 phase and regeneration in S phase. *Micron*. 49:15-20.

Wang, R., J. Mozziconacci, A. Bancaud, and O. Gadal. 2015. Principles of chromatin organization in yeast: relevance of polymer models to describe nuclear organization and dynamics. *Current opinion in cell biology*. 34:54-60.

Watson, J.D., and F.H. Crick. 1953. Molecular structure of nucleic acids; a structure for deoxyribose nucleic acid. *Nature*. 171:737-738.

Weber, S.C., A.J. Spakowitz, and J.A. Theriot. 2010. Bacterial Chromosomal Loci Move Subdiffusively through a Viscoelastic Cytoplasm. *Physical Review Letters*. 104.

Webster, M., K.L. Witkin, and O. Cohen-Fix. 2009. Sizing up the nucleus: nuclear shape, size and nuclear-envelope assembly. *Journal of cell science*. 122:1477-1486.

Webster, M.T., J.M. McCaffery, and O. Cohen-Fix. 2010. Vesicle trafficking maintains nuclear shape in Saccharomyces cerevisiae during membrane proliferation. *Journal of Cell Biology*. 191:1079-1088.

Wei, D., S. Jacobs, S. Modla, S. Zhang, C.L. Young, R. Cirino, J. Caplan, and K. Czymmek. 2012. High-resolution three-dimensional reconstruction of a whole yeast cell using focused-ion beam scanning electron microscopy. *Biotechniques*. 53:41-48.

Weiner, A., A. Hughes, M. Yassour, O.J. Rando, and N. Friedman. 2010. High-resolution nucleosome mapping reveals transcription-dependent promoter packaging. *Genome Res*. 20:90-100.

Wente, S.R., and M.P. Rout. 2010. The nuclear pore complex and nuclear transport. *Cold Spring Harbor perspectives in biology*. 2:a000562.

Wimmer, C., V. Doye, P. Grandi, U. Nehrbass, and E.C. Hurt. 1992. A new subclass of nucleoporins that functionally interact with nuclear pore protein NSP1. *Embo J*. 11:5051-5061.

Winey, M., and B. Byers. 1993. Assembly and functions of the spindle pole body in budding yeast. *Trends in genetics : TIG*. 9:300-304.

Winey, M., and E.T. O'Toole. 2001. The spindle cycle in budding yeast. *Nature cell biology*. 3:E23-27.

Winey, M., D. Yarar, T.H. Giddings, Jr., and D.N. Mastronarde. 1997. Nuclear pore complex number and distribution throughout the Saccharomyces cerevisiae cell cycle by three-dimensional reconstruction from electron micrographs of nuclear envelopes. *Molecular biology of the cell*. 8:2119-2132.

Witkin, K.L., Y. Chong, S. Shao, M.T. Webster, S. Lahiri, A.D. Walters, B. Lee, J.L. Koh, W.A. Prinz, B.J. Andrews, and O. Cohen-Fix. 2012. The budding yeast nuclear envelope adjacent to the nucleolus serves as a membrane sink during mitotic delay. *Curr Biol*. 22:1128-1133.

Wong, H., H. Marie-Nelly, S. Herbert, P. Carrivain, H. Blanc, R. Koszul, E. Fabre, and C. Zimmer. 2012. A predictive computational model of the dynamic 3D interphase yeast nucleus. *Current biology : CB*. 22:1881-1890.

Woodcock, C.L., S.A. Grigoryev, R.A. Horowitz, and N. Whitaker. 1993. A Chromatin Folding Model That Incorporates Linker Variability Generates Fibers Resembling the Native Structures. *Proceedings of the National Academy of Sciences of the United States of America*. 90:9021-9025.

Yamaguchi, M., Y. Namiki, H. Okada, Y. Mori, H. Furukawa, J. Wang, M. Ohkusu, and S. Kawamoto. 2011. Structome of Saccharomyces cerevisiae determined by freeze-substitution and serial ultrathin-sectioning electron microscopy. *Journal of electron microscopy*. 60:321-335.

Yang, C.H., E.J. Lambie, J. Hardin, J. Craft, and M. Snyder. 1989. Higher-Order Structure Is Present in the Yeast Nucleus - Autoantibody Probes Demonstrate That the Nucleolus Lies Opposite the Spindle Pole Body. *Chromosoma*. 98:123-128.

Yeh, E., R.V. Skibbens, J.W. Cheng, E.D. Salmon, and K. Bloom. 1995. Spindle Dynamics and Cell-Cycle Regulation of Dynein in the Budding Yeast, Saccharomyces-Cerevisiae. *Journal of Cell Biology*. 130:687-700.

Yoder, T.J., C.G. Pearson, K. Bloom, and T.N. Davis. 2003. The Saccharomyces cerevisiae spindle pole body is a dynamic structure. *Molecular biology of the cell*. 14:3494-3505.

Zakian, V.A. 1996. Structure, function, and replication of Saccharomyces cerevisiae telomeres. *Annual review of genetics*. 30:141-172.

Zimmer, C., and E. Fabre. 2011. Principles of chromosomal organization: lessons from yeast. *Journal of Cell Biology*. 192:723-733.

Zirbel, R.M., U.R. Mathieu, A. Kurz, T. Cremer, and P. Lichter. 1993. Evidence for a nuclear compartment of transcription and splicing located at chromosome domain boundaries. *Chromosome Research*. 1:93-106.

APPENDIX

1. Utilization of “NucQuant”

In this part, I will present how to use “NucQuant” to analyze the nuclear shape and size for possible users.

1.1 Installation

The version of the Matlab “NucQuant” can be used is 2012b and the later versions.

Because to acquire the NPCmap we used R package, so we also need install the R (version is 2.9.2). Then we need install some packages in R, we need open the R as administrator. We need install the packages of rscproxy (1.3-1), mvtnorm (0.9-8), ks (1.6.8), rpanel (1.0-5), nuclocR and the R.matlab (3.0.1) packages successively. Then we also need install the Scilab.

Note 1: The version of the R packages should be compatible with the R just as shown above.

Note 2: Environment variables. Make sure that the PATH environment variable includes the bin directory of R. The way to change the PATH environment variable is: Start Menu → Control panel → System → Environment variables. Add the PATH environment variable of the bin directory of R to the end. Such as **C:\Users\gadal\Documents\R\R-2.9.2\bin**.

Note 3: Be careful in the code of nucquant_NPCmap.m (line 185), we also need make sure the path here is right.

1.2 How to use “NucQuant”

“NucQuant” containing many algorithms, when we open the nucquant_platform, this interface containing all of the algorithms inside (Figure 1). I will explain this by introducing how to use “NucQuant” to analyze the nuclear shape and size.

Note 1: Before using “NucQuant”, set the folder of the nucquant files as path in Matlab. To avoid unexpected errors, copy the figures into the folder of nucquant files and the output data will also be saved in this folder. For each experiment, after analysis, remember move the all output dataset out or it will influence the analysis of next experiment figures.

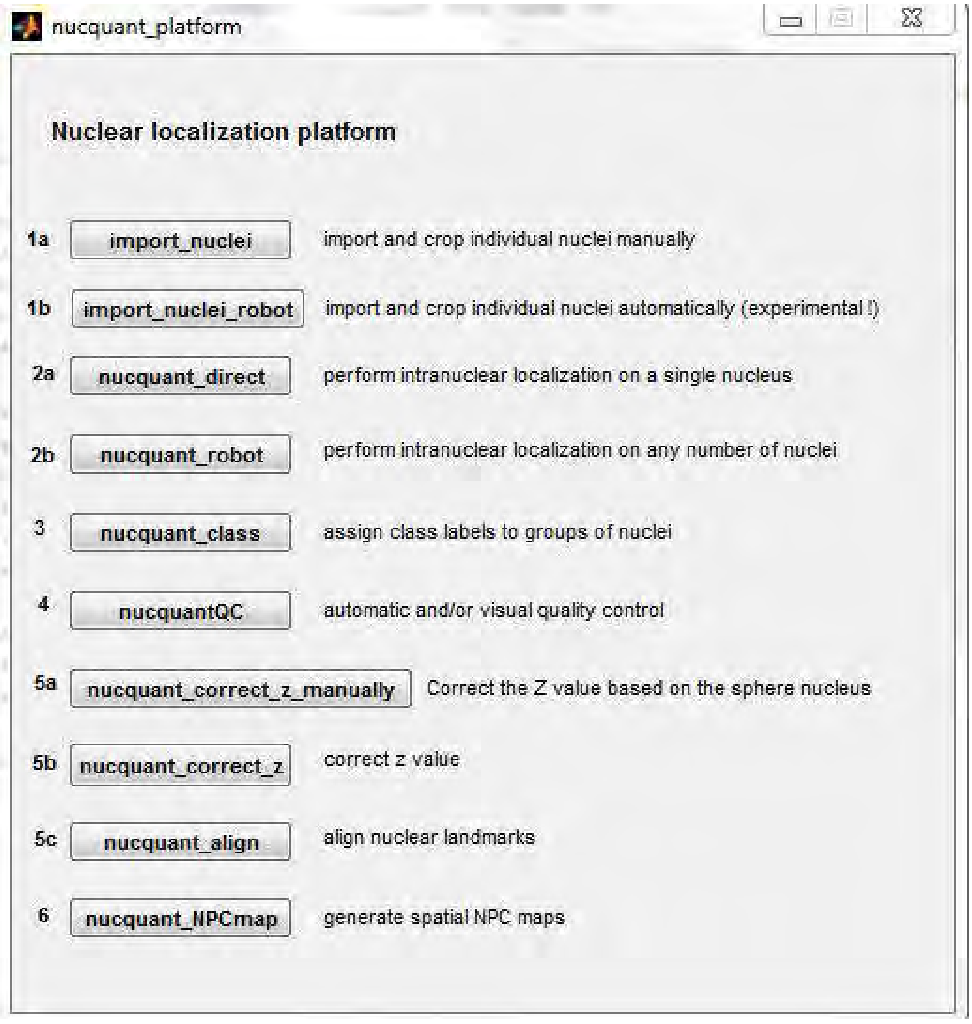

nucquant_platform

Nuclear localization platform

1a	import_nuclei	import and crop individual nuclei manually
1b	import_nuclei_robot	import and crop individual nuclei automatically (experimental !)
2a	nucquant_direct	perform intranuclear localization on a single nucleus
2b	nucquant_robot	perform intranuclear localization on any number of nuclei
3	nucquant_class	assign class labels to groups of nuclei
4	nucquantQC	automatic and/or visual quality control
5a	nucquant_correct_z_manually	Correct the Z value based on the sphere nucleus
5b	nucquant_correct_z	correct z value
5c	nucquant_align	align nuclear landmarks
6	nucquant_NPCmap	generate spatial NPC maps

Figure 1. The interface of “NucQuant”.

1.2.1 Input the figures and crop the cells

The figures we acquired are from the spinning andor confocal microscopy (saved as .tiff type). For 3D analysis, Z-stacks of 41 images (two channels) with a 250 nm Z-step were used. For the analysis, we need to know some parameters which are very important in the “NucQuant”. The refactive index of the sample medium (YPD, SC we used 1.33), the numerical aperture (NA) of the objective lens (default setting is 1.4), the emission wavelength (default setting is 0.5), the voxel dimension along x (65 nm), y (65 nm) and z (we used 250 nm) and the number of color channels (default setting is 2).

Input the figures have two methods: manually (import_nuclei) and automatically (import_nuclei_robot). Manually method will remind you to change these parameters when you choose one figure. Automatically method, these parameters are default setting inside the code of IHM.m (line 71-76), we also can change the parameters in the interface after we choose the automatically way.

Note: For manually way, we can crop the cells we are interested by manually. For the automatically way, the software will crop the nuclei with close-spherical shape (interphase nuclei) automatically.

1.2.2 Extract the NPC position, nuclear center, nucleolus segmentation and the nucleolar centroid

After crop the cells, we also have two ways to extract the information of each nucleus, nucquant_direct for the users to see the extraction of single nucleus; nucquant_robot will detect the information of each nucleus automatically can save them into the output file.

Note 1: When we choose to extract the information of each nucleus, the interface of 'nucquant_gui' will appear. In this interface, the things we should note are the 'Figures' part (Figure 2, red rectangle). 'Show, don't save' means the software will show us the extracted information for each nucleus in figures version. This is suitable for us to check single nucleus. Although for robot extraction we also can let it show and save the data, it is very slow!

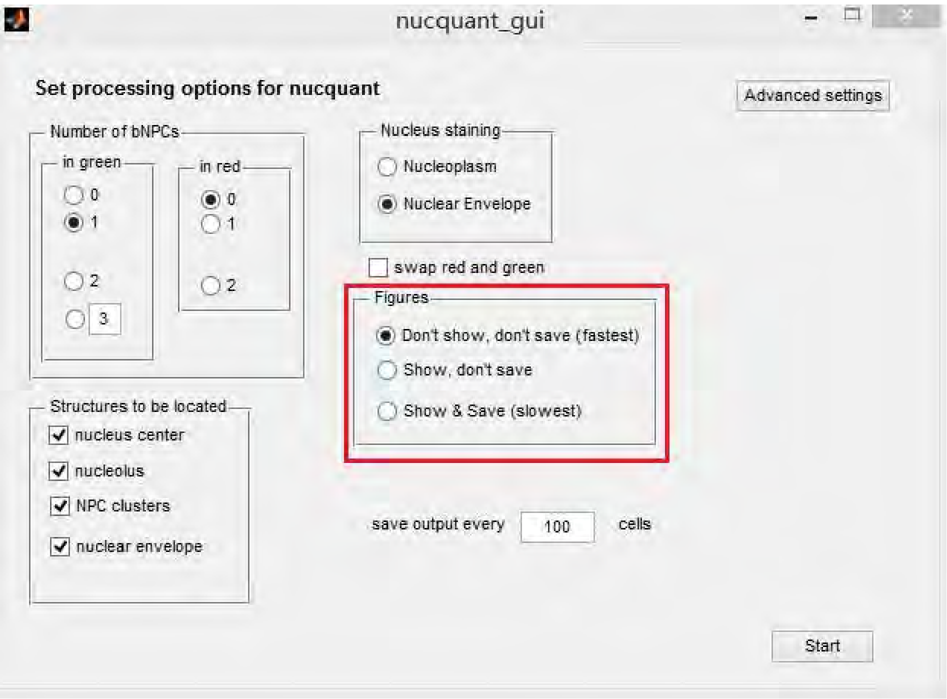

nucquant_gui

Set processing options for nucquant

Advanced settings

Number of bNPCs
in green
○ 0
● 1
○ 2
○ 3

in red
● 0
○ 1
○ 2

Nucleus staining
○ Nucleoplasm
● Nuclear Envelope

☐ swap red and green

Figures
● Don't show, don't save (fastest)
○ Show, don't save
○ Show & Save (slowest)

Structures to be located
☑ nucleus center
☑ nucleolus
☑ NPC clusters
☑ nuclear envelope

save output every 100 cells

Start

Figure 2. Extract the nucleus information.

Note 2: In the code, we will first to find the birghtest spot in the figure as the bNPC, then choose the other potential NPCs based on their thresholding. Then we choose the spot whose distance to the nucleus center is 0.5-2.0 μm as the true NPCs. For different experiment, we also can change this value in the code of nucleolus.m (line 314-315).

1.2.3 Class the data

This step is default, all of the data are classified as ‘renjie’, and you can change this in the code of nucquant_class.m (line 63).

1.2.4 Quality control

Quality control step is for the automatically crop, extraction data. The quality control principle is the ellipsoid approximated radius (default value is like the distance of NPC to the center, 0.5-2.0μm) and the number of NPC (default is 3). You can change these settings in the code of nucquant_QC.m (line 184-196).

Note: After quality control step, the data will be saved in the output which named as ‘QC_Okauto_.....’. For the manually crop users, because manually select is a quality control step, you can change the ‘nucquant_class’ output files name to pass this step.

1.2.5 Correc the aberration along Z axis

For the interphase spherical nuclei we just need choose ‘nucquant_correct_z’ to correct the z coordinates of the detected NPC, the nucleolus center and so on. In addtion, this choice also automatically caculate the nuclear volume, surface and the sphericity of the nucleus based on 3D-NE method we created (See the results part). For this step, after correction, the output file containing four parameters (a, b, c and d) which can be used to correct the z coordinates for the non-spherical nuclei. They are needed for the choice ‘nucquant_correct_z_manually’ which is for the non-spherical nuclei.

Note: For non-spherical nuclei, because it is not sure about the shape of the nucleus (one cluster, two clusters or three clusters), so ‘nucquant_correct_z_manually’ just correct Z aberration, it does not calculate the volume and surface of the nucleus automatically. To calculate this, we need use 3D-NE code (in which containing the code to calculate the nucleus shape and size for different shape)

1.2.6 Align the nuclei

For the interphase nuclei or the nuclei with similar geometry, we could use nucleus center and nucleolus center (or spindle pole body) as the two landmarks to align all of the labeled NPCs and project them into one single plane.

Note: This step will automatically input the output file named as ‘QC_Okcorrect_.....’ which come from the correction step.

1.2.7 Calculate the NPC distribution

Based on the align file we can calculate the probability density of the NPC, and the software will output one heatmap of the NPC.

2. Published: "Decoding the principles underlying the frequency of association with nucleoli for RNA Polymerase III-transcribed genes in budding yeast"

During my PhD project, I also participated another research on the tRNA genes (see manuscript attached below). I used “Nucloc” to study the ‘gene territories’ of tRNA genes and revealed the association between tRNA genes and the nucleolus.

Decoding the principles underlying the frequency of association with nucleoli for RNA polymerase III–transcribed genes in budding yeast

Praveen Belagal[a], Christophe Normand[a], Ashutosh Shukla[b], Renjie Wang[a], Isabelle Léger-Silvestre[a], Christophe Dez[a], Purnima Bhargava[b,*], and Olivier Gadal[a,*]
[a]Laboratoire de Biologie Moléculaire Eucaryote, Centre de Biologie Intégrative, Université de Toulouse, CNRS, UPS, 31000 Toulouse, France; [b]Centre for Cellular and Molecular Biology, Council of Scientific and Industrial Research, Hyderabad 500007, India

ABSTRACT The association of RNA polymerase III (Pol III)–transcribed genes with nucleoli seems to be an evolutionarily conserved property of the spatial organization of eukaryotic genomes. However, recent studies of global chromosome architecture in budding yeast have challenged this view. We used live-cell imaging to determine the intranuclear positions of 13 Pol III–transcribed genes. The frequency of association with nucleolus and nuclear periphery depends on linear genomic distance from the tethering elements—centromeres or telomeres. Releasing the hold of the tethering elements by inactivating centromere attachment to the spindle pole body or changing the position of ribosomal DNA arrays resulted in the association of Pol III–transcribed genes with nucleoli. Conversely, ectopic insertion of a Pol III–transcribed gene in the vicinity of a centromere prevented its association with nucleolus. Pol III–dependent transcription was independent of the intranuclear position of the gene, but the nucleolar recruitment of Pol III–transcribed genes required active transcription. We conclude that the association of Pol III–transcribed genes with the nucleolus, when permitted by global chromosome architecture, provides nucleolar and/or nuclear peripheral anchoring points contributing locally to intranuclear chromosome organization.

Monitoring Editor
Karsten Weis
ETH Zurich

Received: Mar 4, 2016
Revised: Aug 10, 2016
Accepted: Aug 18, 2016

INTRODUCTION

Eukaryotic chromatin is a complex three-dimensional (3D) entity. Its organization within the nucleus can influence genome stability and gene expression (Misteli, 2007). Global genome organization in budding yeast has been clearly determined. The nucleolus, which is organized into a crescent-shaped structure adjacent to the nuclear envelope (NE), contains almost exclusively the genes encoding ribosomal DNA (rDNA) from the right arm of chromosome XII (Yang *et al.*, 1989; Léger-Silvestre *et al.*, 1999). In cycling cells, diametrically opposite the nucleolus, the kinetochore complex at the centromeres (CENs) is tethered to the spindle pole body (SPB) via microtubules throughout the cell cycle (Yang *et al.*, 1989; Bystricky *et al.*, 2005; Duan *et al.*, 2010; Zimmer and Fabre, 2011). Telomeres (TELs) are localized in clusters at the nuclear envelope (Klein *et al.*, 1992; Gotta *et al.*, 1996), such that the chromosome arms extend from the CEN toward the nucleolus and the nuclear periphery. Therefore, in cycling cells, chromosomes adopt a Rabl-like conformation (Jin *et al.*, 2000). Computational models based on small numbers of biophysical constraints and reproducing most of these features have recently been developed (Tjong *et al.*, 2012; Wong *et al.*, 2012; Gursoy *et al.*, 2014; Gong *et al.*, 2015). By studying budding yeast chromosome XII by live-cell imaging, we confirmed that the nuclear positions of loci were globally well predicted by such models (Albert *et al.*, 2013). Models introducing constraints due to nuclear biochemical activity have been reported to provide a better fit to experimental contact frequency maps (Gehlen *et al.*, 2012; Tokuda *et al.*, 2012). Recent imaging studies in different physiological conditions affecting the yeast transcriptome revealed a global shift of many positions on chromosome II to the periphery of the nucleus (Dultz *et al.*, 2016). This peripheral recruitment of chromosome arms is consistent with

---

*Address correspondence to: Purnima Bhargava (purnima@ccmb.res.in), Olivier Gadal (gadal@biotoul.fr).

Abbreviations used:

the presence of transcription-dependent anchoring points along the length of the chromosome (Tjong *et al*., 2012). However, the tethering sites organizing chromosomes locally remain largely unidentified (Dultz *et al*., 2016).

Each of the three nuclear RNA polymerases transcribes a specific subset of genes. RNA polymerase (Pol) II transcribes all protein-coding genes and many noncoding (nc) RNA genes. Pol I synthesizes only one type of RNA—the precursor of large rRNAs. Pol III specializes in the synthesis of a few hundred ncRNAs, mostly involved in translation: the 5S rRNA, tRNAs, and abundant small nc-RNAs. There is a well-documented correlation between the frequent association of a gene with a nuclear substructure and its transcriptional activity (Takizawa *et al*., 2008). Pol I transcription is the model system for this preferential localization of genes. Indeed, assembly of the nucleolus, the largest nuclear body, is initiated by rDNA transcription by Pol I (Trumtel *et al*., 2000; Misteli, 2001; Hernandez-Verdun *et al*., 2002). Previous studies suggested that nucleolar association of Pol III-transcribed genes has been conserved during evolution. Nucleolus-associated domains in metazoan genomes are significantly enriched in tRNA genes (tDNAs; Nemeth *et al*., 2010). In budding yeast, tDNAs scattered over the various chromosomes appear to be colocalized in a cluster close to or within the nucleolus on fluorescence in situ hybridization (FISH) microscopy (Thompson *et al*., 2003; Haeusler and Engelke, 2004). Recent studies of budding yeast also reported transcription-dependent recruitment of a tDNA to the nuclear pore complex (NPC) during mitosis (Chen and Gartenberg, 2014). Pol III–transcribed genes may behave as local tethering sites for the organization of chromosome arms.

In this study, we investigated the intranuclear position of individual Pol III–transcribed genes in three dimensions. We measured distances from genes of interest to both nuclear and nucleolar centers (Berger *et al*., 2008). FISH studies previously demonstrated a concentration of tRNA gene families (*Leu(CAA)*; *Lys(CUU)*, *Gly(GCC)*, *Gln(UUG)*, and *Glu(UUC)*) in or near the nucleolus (Thompson *et al*., 2003). We used fluorescent operator-repressor system (FROS) insertion to label individual Pol III–transcribed genes and determine their position within the nucleus in vivo (Berger *et al*., 2008). We found that some, but not all, Pol III–transcribed genes were frequently associated with the periphery of the nucleolus and/or away from the nuclear center. Proximity to the centromere or telomere prevented nucleolar recruitment, suggesting a hierarchical organization of locus positions. Centromere proximity constrained loci to be at the nuclear periphery close to SPB. Telomere proximity precluded central localization in the nucleus, resulting in loci close to SPB for short-arm chromosomes or away from SPB for long-arm chromosomes (Therizols *et al*., 2010). Centromere inactivation or the insertion of a centromere at an ectopic site at some distance from a tDNA resulted in the nucleolar association of the Pol III–-transcribed gene; peripheral position was kept, but shifted away from SPB toward the nucleolus. The nucleolar association of tDNA was alleviated by nutrient starvation, which inhibits Pol III transcription, However, Pol III transcription was not limited to nucleolus-associated genes. We evaluated the contribution of the gene itself to the intranuclear positioning of its host locus and showed that Pol III–transcribed genes controlled the local organization of the chromosome arms via nucleolar and/or nuclear envelope tethering.

RESULTS

Identification of Pol III–transcribed genes generating unique, detectable transcripts

Pol III–transcribed genes can be classified into three groups, types I–III, on the basis of their internal promoter organization (Figure 1A). Most tRNAs are encoded by large multigene families scattered throughout the yeast genome, with a mean of 4 genes encoding the same tRNA and up to 16 genes for *Gly(GCC)*. Even within multigene families, the isogenes encoding different tRNAs display very high levels of sequence identity, making it difficult to design gene-specific probes for estimating the abundance of a specific transcript. Furthermore, within a set of tRNA genes encoding the same anticodon, individual copies are not equivalent, and the deletion of individual genes may affect yeast fitness to very different extents (Bloom-Ackermann *et al*., 2014). We performed a comprehensive survey to identify base-pair polymorphisms in tRNA sequences in each of the 20 families. In total, 69 tRNA species are produced from the 273 tDNAs of the yeast nuclear genome (Figure 1B, circles). We identified 33 unique tRNA species (circles labeled with 1 in Figure 1B) produced from single genes. Six of these 33 unique tDNAs bore unique anticodons. However, if a unique anticodon-encoding gene is lost, other tRNAs can decode the codon through wobble base pairing; as a result, only four of these six genes were considered essential (Bloom-Ackermann *et al*., 2014).

We mapped 30 representative loci from the 278 different Pol III–transcribed genes in yeast by in vivo microscopy (gene names in blue in Figure 1B). We previously determined the intranuclear positions of 5 of these loci on chromosome XII: *SNR6*, the 5S gene in rDNA, and three tDNAs (*tP(UGG)L*, *tA(UGC)L*, and *tL(UAA)L*; Albert *et al*., 2013). We explored the positions of Pol III–transcribed genes further by labeling *SCR1* (the gene encoding the RNA component of the signal recognition particle [SRP]) and seven other tDNAs: three of the four essential tDNAs (*TRT2*, *SUP61*, and *TRR4*) and *tG(CCC)*, represented by only two tDNAs—*SUF3* and *SUF5*—which display low but significant levels of sequence polymorphism (see later discussion). We also labeled *SUP4*, the deletion of which causes a strong growth defect, despite its membership in the large *tY(GUA)* family, which contains eight isoforms (Bloom-Ackermann *et al*., 2014). The *SUP53* tDNA, for which expression can be assessed indirectly from the suppressor activity of a nonsense mutation (unpublished data), was also included in our study.

Intranuclear position of Pol III–transcribed genes

We determined the positions of individual Pol III–transcribed genes in the nuclear space in vivo by FROS labeling (TetO/TetR–green fluorescent protein [GFP]). The linear position of each gene on the chromosomes is shown in Figures 2A and 3A. We previously showed that, for Pol III–transcribed genes, a single nucleosome dynamics upstream for *SNR6* and downstream for tDNAs controlled differences in transcription (Arimbasseri and Bhargava, 2008; Mahapatra *et al*., 2011; Kumar and Bhargava, 2013). The positions of FROS insertions close (from 60 to 800 base pairs) to genes of interest were therefore selected with care to ensure that the FROS insertion point affected neither adjacent nucleosome occupancy nor RNA Pol III recruitment. Pol III occupancy in the vicinity of tDNAs was assessed by chromatin immunoprecipitation (ChIP) and quantitative PCR (qPCR). Nucleosome position was determined by mononucleosome MNase protection assays, followed by qPCR. Pol III occupancy and nucleosome positioning were similar in the untagged and tagged cells (Supplemental Figure S1).

Gene position was determined by the NucLoc method (Berger *et al*., 2008; Therizols *et al*., 2010). Images were acquired from living, exponentially growing cells in culture by the confocal fluorescence imaging of large numbers of nuclei (>1000). Images were analyzed with dedicated software (see *Materials and Methods*). Briefly, for each cell with a spherical nucleus (including the G1, S, and early G2/M phases), nuclear and nucleolar volumes were determined on the basis

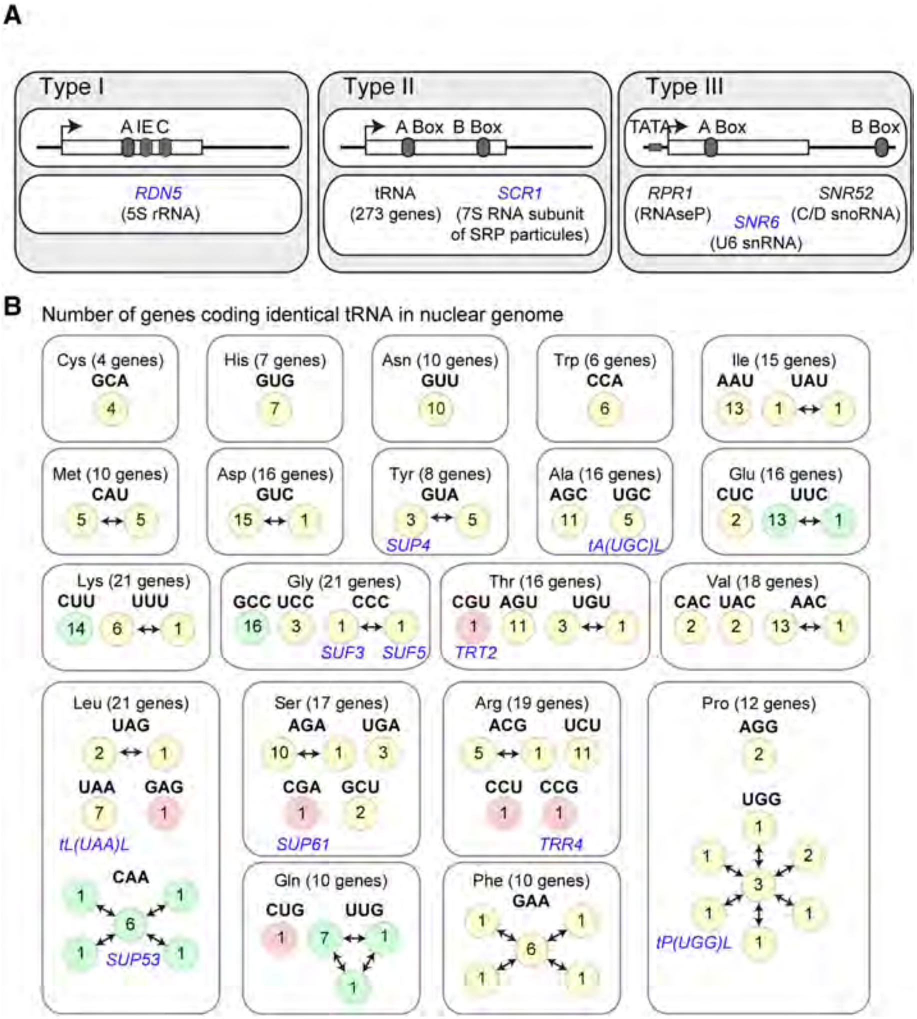

FIGURE 1: Schematic representation of Pol III–transcribed genes. (A) Pol III–transcribed genes can be classified on the basis of internal promoter organization into types I–III. Positions of boxes A, IE, B, and C (gray oval) relative to the transcription start site (arrow) and the transcribed region (rectangle). (B) It is challenging to find individual tRNA genes (tDNAs) to label from which a unique gene product can be unambiguously identified. The 273 tDNAs generate 69 different tRNAs (circles) in budding yeast. Each family, defined on the basis of the amino acid targeted (rectangles) and the anticodon (bold), contains 1–16 genes (colored circles and numbers of identical genes). Double arrows link tRNAs within a family responsible for decoding the same anticodon but with different sequences. Unique genes for the decoding of a specific anticodon are shown in red and those with a known nucleolar distribution (Thompson *et al.*, 2003) in green. The FROS used for labeling was inserted near the genes highlighted in blue.

of the fluorescent Nup49-GFP (nuclear pore complex) and Nop1-mCherry (nucleolar protein) signals, respectively. Locus position was determined relative to two references: the 3D positions of the centers of the nucleus and the nucleolus. Nucleus geometry was explored by measuring the angle (α) between the locus–nuclear center axis and the nuclear center–nucleolar center axis. By construction, nucleolar center is at α = 180°. SPB is peripheral and opposed to the nucleolus (α ≈ 0). Peripheral location of a locus away from SPB will result in a larger α (~45–180°). The distance between the locus and the nuclear center was used, together with α, to generate a color-coded statistical map of locus positions in which the percentage indicated within a contour represents the probability of finding the locus within that contour. On these maps, the average nuclear circumference is depicted as a yellow circle, and the median nucleolus (including 50% of all nucleoli) is displayed as a red isocontour (see Figures 2B and 3B).

The previously characterized intranuclear positions of the 5S rDNA and *SNR6* gene loci (Albert *et al.*, 2013) are shown in Figure 2B. As expected, 5S rDNA, which is interspersed with RNA polymerase I–transcribed rRNA gene repeats (35S rDNA) in the budding yeast genome, was restricted to the nucleolus (Figure 2B; Berger *et al.*, 2008; Albert *et al.*, 2013). The *SNR6* locus, which is located 86 kb away from the rDNA, toward the centromere on the right arm of chromosome XII, appeared to be mostly localized at the nucleolar periphery. We also determined the intranuclear positions of two tDNA loci: *SUP53* and *SUP4*. A transcriptionally active *SUP53* gene has been reported to be associated with the nucleolus (Thompson *et al.*, 2003). Using our FROS strain, we found that *SUP53*, which is located 23 kb from the centromere on the left arm of chromosome III, was excluded from nucleolar periphery, whereas *SUP4*, sited 107 kb from the centromere on the right arm of chromosome X, was detected in a large volume within the nuclear space, frequently interacting with the nucleolus (Figure 2B). Similarly, *SUF3* and *SUF5*, both located >250 kb from the centromere and telomere, were frequently found to be associated with the nucleolar periphery. We found that *SUF3* was also frequently located in the periphery of the nucleus. The 5S rRNA gene, *SUP4*, *SUP53*, *SUF3*, and *SUF5* all belong to multigene families in which functionally equivalent transcripts can be produced from multiple genes, and so it was not possible to determine the proportion of transcriptionally active genes among the loci localized.

We next localized three essential tDNAs (*TRT2*, *TRR4*, and *SUP61*) with unique anticodons as transcriptionally active Pol III loci. We also determined the position of *SCR1*, an essential non-tRNA Pol III transcript (Figure 3, A and B). The genomic positions of the loci are shown in Figure 3A, and localization maps are displayed in Figure 3B. *TRT2* is located close to the left telomere (47 kb) on chromosome XI and was found to have a perinuclear distribution reminiscent of subtelomeric sequences, rarely coming into contact with the nucleolus (Therizols *et al.*, 2010). The *TRR4* locus is located 350 kb from the rDNA and 261 kb from the right telomere, on the right arm of chromosome XII. *TRR4* nuclear position appears both at the nucleolar and nuclear periphery. *SCR1* is located on the right arm of chromosome V, 290 kb from CEN and 135 kb from the telomere. Like *SUF3* and *TRR4*, *SCR1* was preferentially associated with the nucleolus and nuclear periphery. *SUP61* is located 113 kb from the centromere and it appeared to be excluded from the nucleolar periphery, in close proximity to the nuclear envelope. Both *SUP4* and *SUP61* are located ~100 kb from centromere, but the maps of these genes were markedly different. *HMR*, a heterochromatin domain attached to the nuclear envelope, is located 66 kb from the *SUP61* locus.

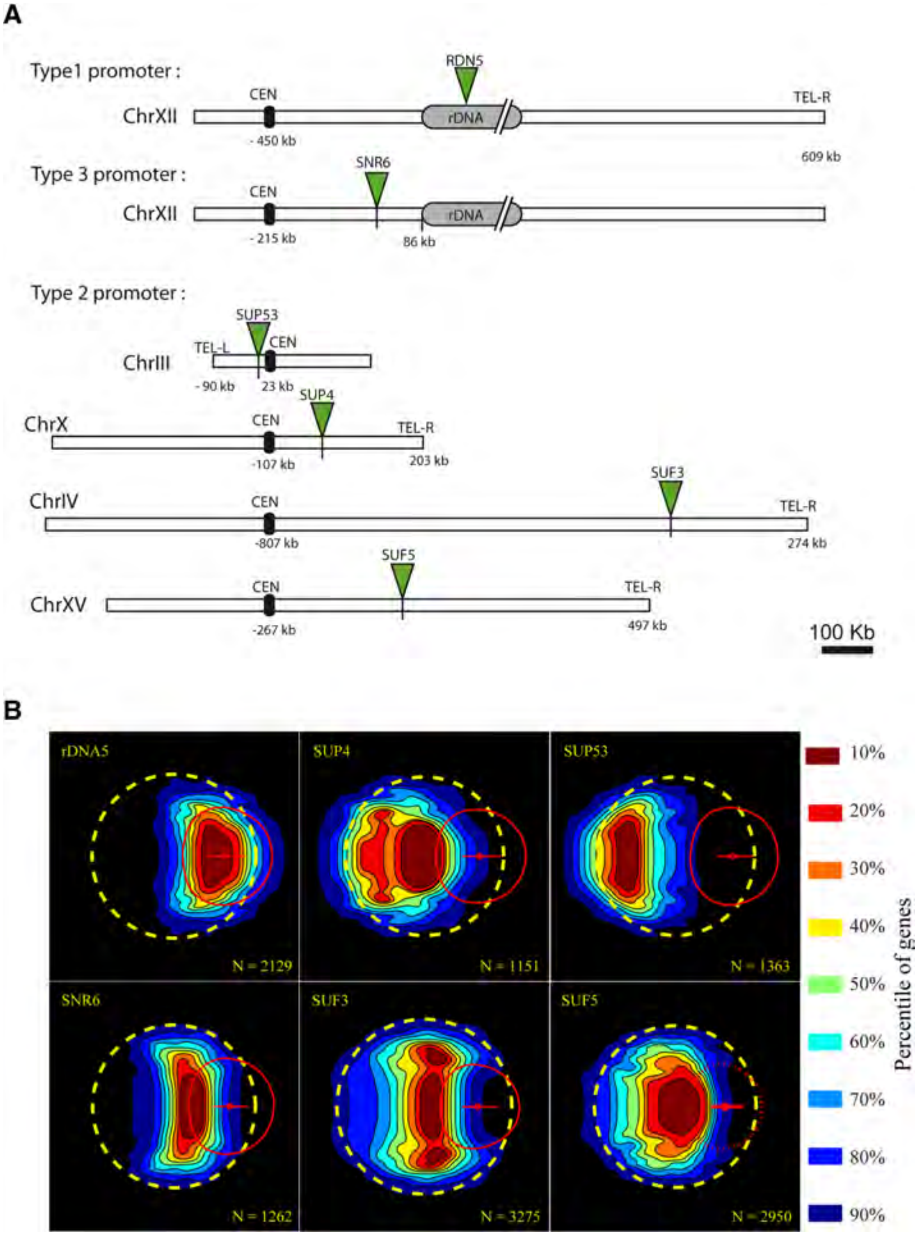

FIGURE 2: Positions of Pol III–transcribed genes on the chromosomes and in the intranuclear space. (A) FROS insertions near *RDN5, SNR6, SUP53, SUP4, SUF3*, and *SUF5* genes on the chromosome relative to CEN, rDNA, and left and right TELs. The distance of the FROS insertion (green triangle) relative to the two closest tethering elements (kilobases) is indicated. (B) Gene map of the FROS-labeled loci. Yellow circle and red ellipsoids correspond to nuclear envelope and nucleolus, respectively. *N*, number of nuclei used to generate the probability density map. The probability of finding the locus within the various regions of the nucleus is indicated by the percentage enclosed within the contour concerned.

SUP61, *tT(UGU)G1*, and *tT(AGU)C* were recently reported to be preferentially associated with the NPC during mitosis (Chen and Gartenberg, 2014). We explored the possible cell cycle–regulated positioning of another Pol III–transcribed gene, *SCR1*. In our aggregate population analysis, *SCR1* was preferentially found in two positions: nucleolus and nuclear periphery (Figure 3B). We manually sorted nuclei by cell shape to analyze G1 (unbudded), S (small buds), and G2/M (choosing large buds with round nuclei, excluding anaphase) phases. Perinucleolar recruitment was observed mostly in G1 (Figure 3C, left). Marked recruitment to the nuclear periphery was observed in S phase and conserved in G2/M (Figure 3C, middle and right).

A comparative analysis of all the intranuclear maps of Pol III–transcribed genes in this study (Table 1) showed that the close proximity of tethering elements (<100 kb from CEN, TEL, or HMR) prevented the association of Pol III–transcribed genes (*SUP53*, *TRT2*, and *SUP61*) with the nucleolus. Conversely, the close proximity of *SNR6* to rDNA on the right arm of chromosome XII was associated with an exclusively nucleolar location. For regions with no obvious constraints on their motion due to the Rabl-like chromosomal architecture, Pol III–transcribed genes displayed frequent, possibly cell cycle–regulated nucleolar interactions (*SUP4* and *SUF5*) or nucleolar/nuclear periphery interactions (*SRC1*, *TRR4*, and *SUF3*).

Proximity to centromeres prevents the association of Pol III–transcribed genes with nucleoli

Our mapping results suggest that the proximity of genes to tethering elements such as centromeres prevents them from associating with nucleoli. We investigated the interplay between Pol III–transcribed genes and centromeres, using a genetic system for the ectopic insertion of any gene at the *SUP53* locus, which is close (23 kb) to the centromere (Supplemental Figure S2). Because the SPB occupies a position diametrically opposite to that of the nucleolus, we hypothesized that proximity to the centromere would result in the locus being tethered away from the nucleolus. We changed the genomic locations of four Pol III–transcribed genes from the three Pol III classes: the 5S rRNA gene (type 1), one tDNA (*SUF3*), and two essential type III genes (*SNR6, SCR1*; Figure 4A). All were strongly associated with the nucleolus when in their wild-type genomic positions (Figure 4B, top). No growth defect was detected in any of the strains carrying an ectopic gene at the *SUP53* locus with deletion of the gene at its endogenous wild-type locus (unpublished data). We mapped each ectopic insertion and compared it to the wild-type position of the gene (Figure 4B, compare top to bottom). We observed no nucleolar recruitment for *SUF3*, *SNR6*, and *SCR1* inserted at the *SUP53* locus close to the centromere. In the budding yeast genome, the 5S rDNA is inserted between copies of the Pol I–transcribed rDNA repeat (35S rDNA). This organization is unusual, in that 5S rDNA arrays are clustered into arrays separately from the 35S rDNA in other organisms. In fission yeast, the insertion of a 35S rDNA sequence not including the 5S rDNA at the mating-type region induced relocalization of the gene from the SPB to the nucleolar periphery (Jakociunas *et al.*, 2013). The 5S rDNA (*RDN5*) gene is universally associated with nucleoli (Haeusler and Engelke, 2006). We therefore hypothesized that a single 5S rDNA at the *SUP53* locus would drive strong nucleolar association. However, the insertion of

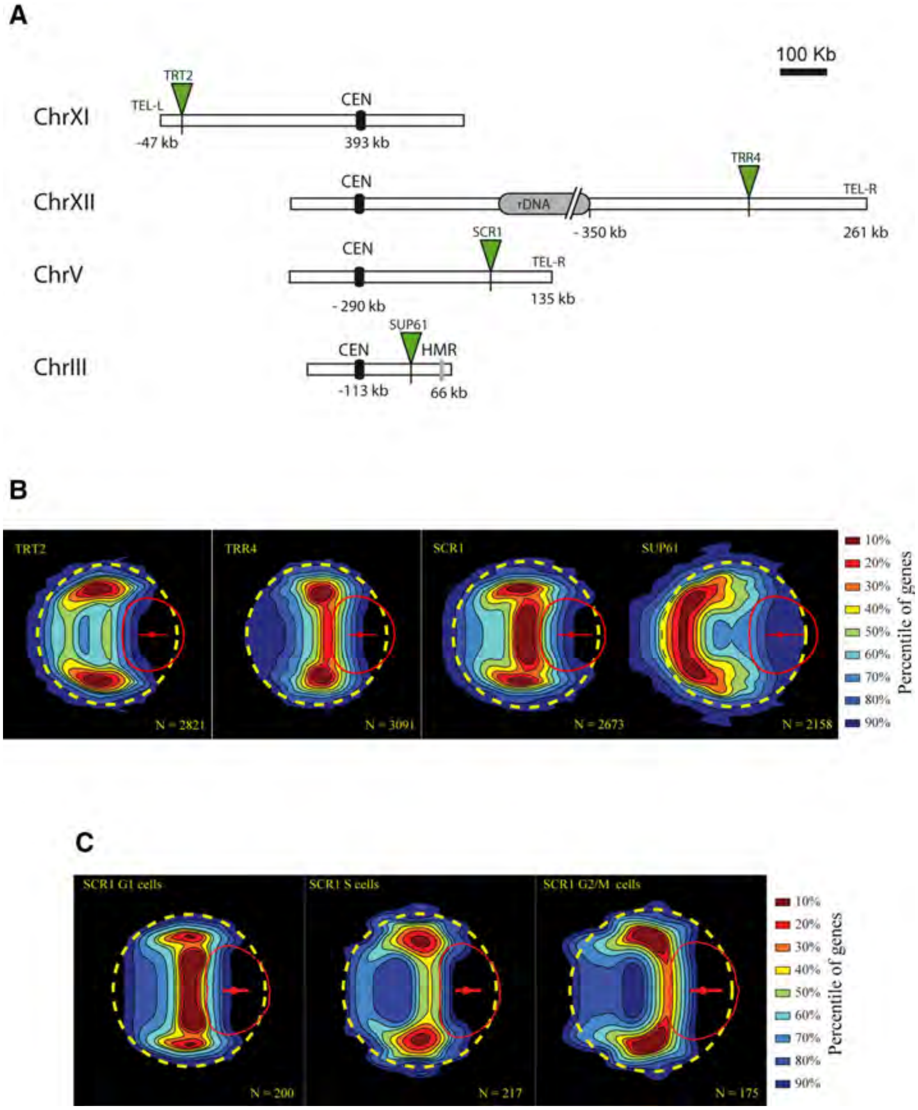

FIGURE 3: Positions of four essential Pol III–transcribed genes on chromosomes and in the intranuclear space. (A) FROS insertions near *TRT2, TRR4, SCR1*, and *SUP61* genes on the chromosome relative to *CEN*, rDNA, right and left TELs, and silent mating-type loci (*HMR*). The distance of the FROS insertion (green triangle) from the two closest tethering elements (kilobases) is indicated. (B) Gene map of the FROS-labeled loci. Yellow circle and red ellipsoids correspond to nuclear envelope and nucleolus, respectively. *N*, number of nuclei used to generate the probability density map. (C) Gene map of the FROS-labeled *SCR1* gene during the cell cycle.

RDN5 at *SUP53* was not sufficient to drag the locus to the nucleolus (Figure 4B, rightmost images). The identity of the Pol III–transcribed gene inserted in place of *SUP53* did not affect the intranuclear position of the locus (Figure 4C).

Our data suggest that the Pol III–transcribed genes tested could not direct the association of a centromere-proximal region to the nucleolar periphery or significantly modify gene position relative to that of the wild-type *SUP53* gene.

Pol III–transcribed SUP53 slides along the nuclear periphery toward the nucleolus when the chromosome III centromere is inactivated or displaced

The Pol III–transcribed, centromere-proximal *SUP53* locus is not found near the nucleolus in wild-type cells. We disrupted *CEN* function to determine whether CEN proximity (23 kb) prevented nucleolar association. We used a strong inducible promoter (*pGAL1-10*) to disengage the kinetochore from the centromere (Hill and Bloom, 1987; Reid *et al*., 2008). On induction, GAL genes were recruited to the nuclear periphery, as previously reported (Casolari *et al*., 2004). We inserted the *pGAL1-10* promoter at the chromosome III centromere (*CEN3*), close to *SUP53* (Figure 5A). Expression under *pGAL1-10* control caused a conditional knockdown of *CEN3* kinetochore attachment, strongly decreasing cell viability upon induction (Figure 5B), due to chromosome segregation defects resulting from kinetochore disassembly. As control, we checked that the wild-type *SUP53* locus position was unaffected by shifting the cells from repressed to induced conditions for up to 4 h (Figure 5C, left). We then induced *CEN3*–kinetochore dissociation using similar growth conditions and monitored locus positions (Figure 5C, middle). The location of *SUP53* was significantly affected by *CEN3*–kinetochore dissociation, with this locus predominantly occupying a peripheral position. The nucleolar recruitment of *SUP53* did not increase significantly even after 4 h of induction. *CEN3* kinetochore inactivation significantly modified the angle α between the locus–nuclear center axis and the central axis (Figure 5C, right). This angle was unaffected in wild-type (WT) cells incubated with galactose for 4 h (Figure 5D, left) but gradually increased after kinetochore disassembly (Figure 5D, right). *SUP53* thus remained at the nuclear periphery, appearing to deviate from the axis between the nuclear and nucleolar centers. No such effect was observed if a centromere other than *CEN3* was disrupted (*CEN9*; Supplemental Figure S3). It was not possible to explore longer periods of *CEN3* release due to cell morphology abnormalities. We overcame this problem by constructing a strain in which the endogenous *CEN3* was deleted and an ectopic centromere (*CEN6*) was inserted 14.2 kb from *TEL-R* and 212 kb from *SUP53* (Figure 5E, left). This strain displayed no growth defect (Supplemental Figure S3C). After permanent centromere release, *SUP53* gene was recruited to the nuclear and nucleolus periphery (Figure 5E, right). These results confirm that proximity to the centromere constrains the location of *SUP53*.

An ectopic location of rDNA alters the nucleolar association of Pol III–transcribed genes

SNR6 had a strictly perinucleolar location (Figure 2B). We suggest that this is largely due to the proximity of rDNA and *SNR6* (only 86 kb apart), anchoring the locus to the nucleolus. We tested this hypothesis by modifying a strain constructed by M. Nomura's laboratory, rDNA-CEN5, for gene position analysis. In this strain, all of the rDNA repeats of chromosome XII have been deleted

Reference	Gene name	Common name	Genomic location: +rDNA = 1–2 Mb of rDNA array				Nuclear location
			Chromosome number	Distance			
				CEN	rDNA	Other	
Albert *et al*. (2013)	*RDN5*	5S rRNA gene	XII	309 kb right	Inside	588 kb + rDNA from right telomere	Away from SPB; inside nucleolus
Albert *et al*. (2013)	*SNR6*	U6 snRNA gene	XII	216 kb right	86 kb left	674 kb + rDNA from right telomere	Away from SPB; nucleolar periphery
Albert *et al*. (2013)	*tP(UGG)L*	None	XII	58 kb left	359 kb left	93 kb from left telomere	Nucleoplasm
Albert *et al*. (2013)	*tA(UGC)L*	None	XII	64 kb right	237 kb left	261 kb from right telomere	Away from SPB; nucleoplasm/ nucleolar periphery
Albert *et al*. (2013)	*tL(UAA)L*	None	XII	812 kb + rDNA left	473 kb right	115 kb from right telomere	Away from SPB; nucleolar and nuclear periphery
This study	*tR(CCG)L*	*TRR4*	XII	668 kb + rDNA left	350 kb right	261 kb from right telomere	Away from SPB; nucleolar and nuclear periphery
This study	*SCR1*	7SL RNA gene	V	290 kb right	Not linked	135 kb from right telomere	Away from SPB; nucleolar and nuclear periphery
This study	*tL(CAA)C*	*SUP53*	III	23 kb	Not linked	90 kb from left telomere	Close to SPB, nuclear periphery; away from nucleolus
This study	*tS(CGA)C*	*SUP61*	III	113 kb right	Not linked	66 kb left of HMR locus	Close to SPB, nuclear periphery; away from nucleolus
This study	*tY(GUA)J2*	*SUP4*	X	107 kb	Not linked	203 kb from right telomere	Away from SPB; nucleoplasm/ nucleolar periphery
This study	*tG(CCC)D*	*SUF3*	IV	807 kb right	Not linked	274 kb from right telomere	Away from SPB; nucleolar and nuclear periphery
This study	*tT(CGU)K*	*TRT2*	XI	393 kb	Not linked	47 kb from left telomere	Nuclear periphery
This study	*tG(CCC)O*	*SUF5*	XV	267 kb	Not linked	765 kb from right telomere	Nucleolar periphery

TABLE 1: Gene-mapping results for Pol III–transcribed genes in the budding yeast nucleus.

and reinserted in the vicinity of the centromere on chromosome V (see *Materials and Methods* and Figure 6A; Oakes *et al*., 2006). As previously observed, the nucleolus was located diametrically opposite the SPB in the WT strain (Figure 6B; bottom). After ectopic rDNA insertion, the SPB was close to the nucleolus (Figure 6B, top; Oakes *et al*., 2006). The rDNA-CEN5 strain had impaired growth, and the nuclear radius was increased, making distance variation difficult to interpret. We explored the changes in nucleus geometry using the gene map and the α angle variation, which remains informative even if nucleus size is modified. In the rDNA-CEN5 strain, *SUP53* was confined to the nucleolar periphery (Figure 6C, left). In the rDNA-CEN5 strain, *SNR6* was not linked to rDNA and was located 215 kb from the centromere and 648 kb from the right telomere (Figure 6A). *SNR6* was more widely dispersed in the nucleus in the mutant rDNA-CEN5 strain than in the WT strain (Figure 6C, right). Its geometric position in these two strains could be described by the α angle distribution. In the WT strain, the distribution of α angles was centered on 105°, reflecting a perinucleolar location (Figure 6D). The distribution of α angles was broader and centered on 75° in the rDNA-CEN5 strain, reflecting a displacement of the locus away from the nucleolus. Therefore, in the rDNA-CEN5 strain, *SNR6* was not strictly perinucleolar but nevertheless remained frequently associated with the nucleolus, confirming that Pol III–transcribed genes located away from anchoring elements often interact with the nucleolar periphery.

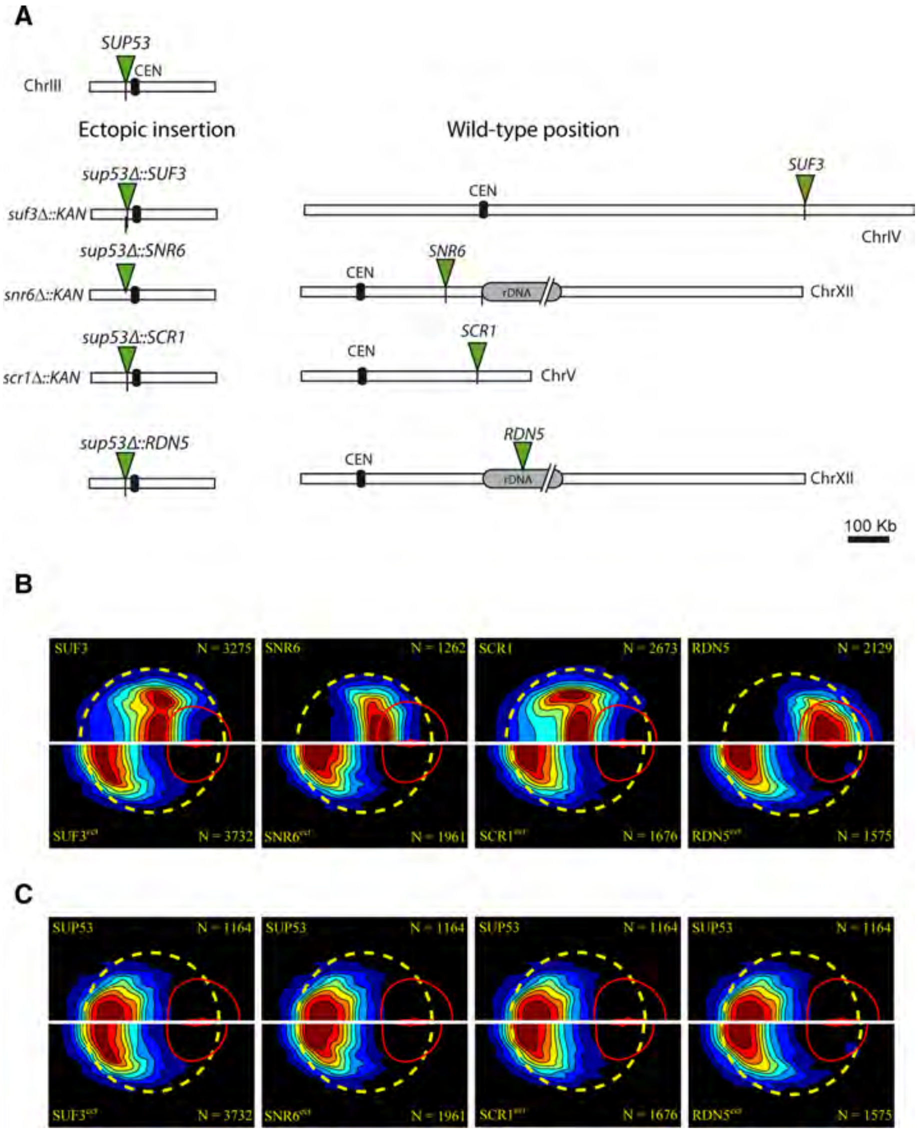

FIGURE 4: Positions of ectopically inserted genes. (A) Description of ectopic strains. *SNR6*, *SCR1*, *SUF3*, and a copy of *RDN5* were inserted separately at the *SUP53* locus. Except for *RDN5*, for which there are ~200 copies, the original copy of the inserted gene was deleted. (B) Gene maps for the original locus and the ectopic *SUP53* location for the *SNR6*, *SCR1*, *SUF3*, and *RDN5* genes. (C) Gene maps for *SUP53* at its native position and for ectopic insertions of *SNR6*, *SCR1*, *SUF3*, and *RDN5* at the *SUP53* locus (top and bottom, respectively).

Nucleolar association is not essential for the expression of Pol III–transcribed genes

We investigated the link between expression and the location of Pol III–transcribed genes in the nuclear space by comparing expression levels for *SNR6*, *SCR1*, and a tDNA, *SUF3*, in their wild-type (nucleolus-associated) and ectopic (close to the centromere, excluded from the nucleolar periphery) positions (Figure 7).

SNR6 and *SCR1* are single-copy genes. We used Northern blotting to determine the levels of their transcripts relative to those of an abundant Pol II transcript (snR46). *SNR6* and *SCR1* transcript levels were not affected by a change in the position of the locus within the genome (compare WT and ectopic, Figure 7, A and B). For *SCR1*, as a control, we evaluated transcript levels before and after FROS insertion. No change in transcript level was detected (Figure 7B, lane 2 vs. lane 3). Finally, we assessed the dependence of *SUF3* tDNA expression level on nucleolar association by primer extension (Figure 7C). As loading control, we designed a probe (o-Gly) for assessing overall RNA levels for 18 of the 21 tDNAs of the glycine family. We tried to generate a probe targeting either the *SUF3* or *SUF5* tRNA based on two polymorphisms found in *SUF3* and *SUF5* (Figure 7C, top). Gene-specific transcript levels were determined with total RNA from the WT, *suf3Δ*, and *suf5Δ* strains. The *SUF5* probe did not appear to be specific, whereas the *SUF3* signal was ~70% lower in the *suf3* deletion mutant than in wild type (no decrease in the *suf5* deletion mutant) and was therefore considered to display good specificity (Figure 7C, left). The ectopic insertion of *SUF3* away from the nucleolus had no major effect on transcript levels (Figure 7C, right). Thus Pol III–transcribed gene expression levels are not strictly dependent on nucleolar association.

Nontethered Pol III–transcribed genes drive association with the nucleolar periphery

Our results confirm that a Rabl-like chromosomal architecture constrains the spatial position of genes located close to centromeres and rDNA-anchoring elements. Furthermore, when not tethered by nearby structural elements, individual Pol III–transcribed genes are frequently associated with the nucleolar periphery.

We then investigated whether the association of the Pol III–transcribed locus *SUP4* with the nucleolus was directly dependent on Pol III activity. To distinguish between passive recruitment to the nucleolus and transcription-based recruitment, we cultured FROS-labeled cells for 2 h in dilute rich medium with no carbon source. This treatment efficiently shuts off Pol III transcription in vivo (Roberts *et al*., 2003), as demonstrated by the release of Pol III from genes (Figure 8A; Kumar and Bhargava, 2013). This starvation treatment halved the ratio of nucleolar-to-nuclear volumes in strains carrying labeled *SNR6*, *SUP4*, and *SUP53* loci (Figure 8B), reflecting a decrease in nucleolar volume in the absence of a change in nuclear volume. A decrease in nucleolar size is also observed when the global reprogramming of transcription is induced by rapamycin treatment, with only a minor effect on overall chromosome architecture (Albert *et al*., 2013).

We compared locations of the *SUP4* gene in expressed and nonexpressed conditions and of loci tethered by a centromere (SUP53) or close to rDNA (SNR6) as controls. The distance of the *SUP4* locus from the nucleolar center was modified in starved cells (Figure 8C). We quantified the observed effect by plotting the cumulative frequency distribution of distances between the loci and the center of the nucleolus and comparing normal and starvation conditions (Figure 8D, solid and dashed lines, respectively). No significant difference was detected for the centromere-associated locus *SUP53* (two-sample Kolmogorov–Smirnov test [ks-test2],

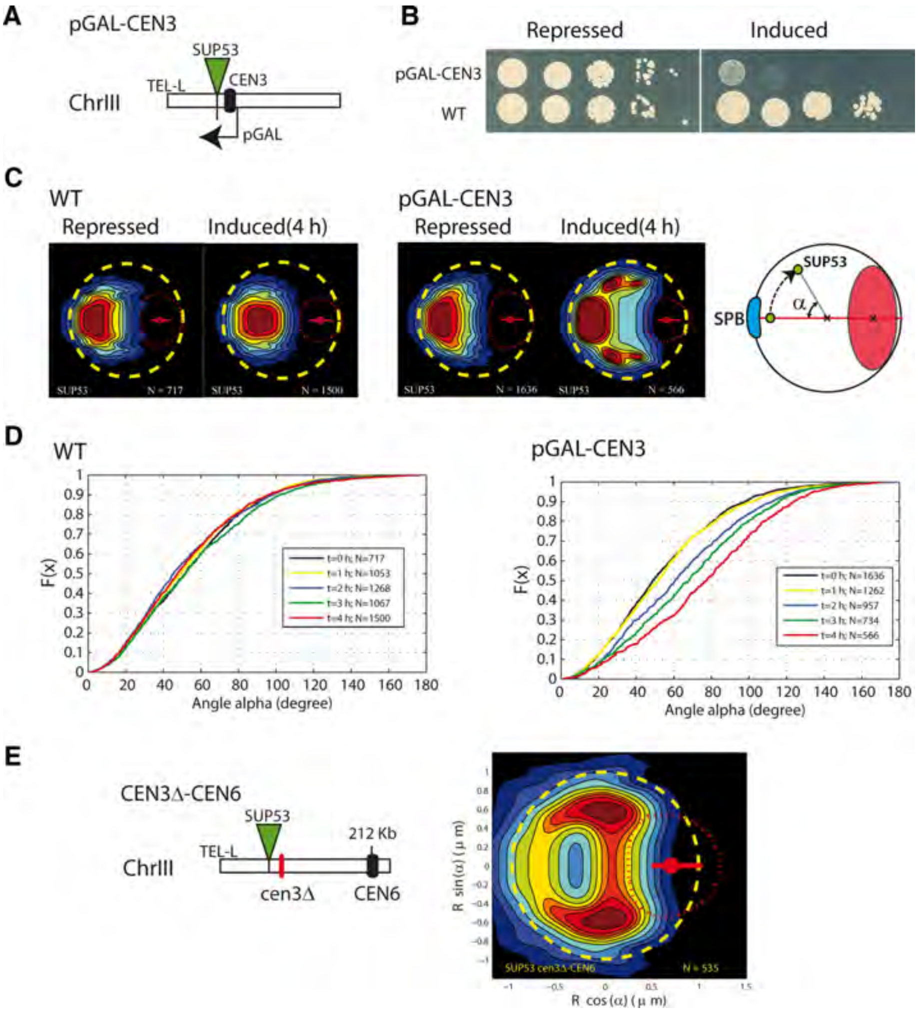

FIGURE 5: Releasing *CEN3* from the SPB results in *SUP53* relocalization. (A) Important features of chromosome III in pGAL-CEN3. (B) Evaluation of the growth of serial dilutions of WT and pGAL-CEN3 strains on media supplemented with glucose (repressed) or galactose (induced). (C) Gene map of the FROS-labeled *SUP53* locus in the WT (left) or pGAL-CEN3 (middle) in medium supplemented with glucose (repressed) and after 4 h of culture in medium supplemented with galactose (induced). Right, *SUP53* locus movement in galactose: the locus (green dot) deviates from the nuclear–nucleolar center axis (red line), resulting in an increase of α angle values. Red, nucleolus. Blue, positions occupied by the SPB. (D) Cumulative distribution function of the gene–nuclear center axis and the nuclear–nucleolar center axis angle α in WT (left) and pGAL-CEN3 (right) strains during the time-course experiment in galactose-supplemented medium. (E) Left, important features of chromosome III in the cen3Δ-CEN6 strain. Right, gene map of the FROS-labeled *SUP53* locus in the cen3Δ-CEN6 strain.

p = 0.05), consistent with CEN attachment to SPB, which is known to be independent of transcriptional inhibition (Albert *et al.*, 2013; Verdaasdonk *et al.*, 2013). The *SNR6* locus, located close to rDNA, appeared to be significantly (ks-test2, $p = 6 \times 10^{-13}$) closer to the center of the nucleolus (Figure 8D) after the change in nucleolar radius during starvation: mean nucleolar radius in the labeled strain was decreased from 0.7 to 0.5 µm by starvation (Figure 8D, light to dark gray). It has been shown that the decrease in nucleolar volume induced by rapamycin treatment results in a small but significant shift of locus positions toward the center of the nucleolus (Therizols *et al.*, 2010). However, *SUP4* did not follow this pattern, as it was located predominantly at the nucleolar periphery in glucose-containing medium and displayed a significant shift away from the nucleolar region upon nutrient stress (ks-test2; $p = 1 \times 10^{-6}$). This indicates that the association of *SUP4* with the nucleolus is driven by its transcription. Indeed, tRNA genes have been shown to dissociate from the nucleolus when transcription is abolished by promoter mutation (Thompson *et al.*, 2003).

For confirmation that the lower frequency of *SUP4* nucleolar association resulted directly from inhibition of the Pol III–mediated transcription of this gene rather than global reorganization due to glucose starvation, we deleted *SUP4* and monitored the position of the *sup4Δ* locus in glucose-rich medium. *SUP4* deletion resulted in a strong growth defect (unpublished data; Bloom-Ackermann *et al.*, 2014). Normal growth was restored by inserting an ectopic copy of the gene at *SUP53* locus (Figure 8E). *SUP4* gene deletion resulted in a greater distance between the deleted *SUP4* locus and the nucleolar center (Figure 8F; ks-test2; $p = 1.4 \times 10^{-12}$). Thus, in the cell population, the frequency of *SUP4* tDNA locus association with the nucleolar periphery depends on the presence of the gene. We then investigated the effects of deleting *SUF3*, *SUF5*, *SCR1*, *TRR4*, and *TRT2*, all located away from the tethering elements studied earlier (Supplemental Figure S4). All the deletions tested, except *SUF3*, induced a small but significant (ks-test2; $p = 10^{-3} - 10^{-9}$) shift of the locus away from the nucleolus. For *SUF3* tDNA, the perinuclear anchoring upon deletion of the tRNA gene was weakened.

In conclusion, our localization study confirmed that Pol III–transcribed genes located away from tethering elements were recruited to the nucleolus or its periphery. The association of the tDNA *SUP4* locus with the nucleolar periphery was specifically reduced by the inhibition of Pol III transcription or deletion of the gene. Nucleolar recruitment was observed for most of the genes tested. We also observed perinuclear anchoring of Pol III–transcribed genes away from tethering elements (i.e., *SUF3*). With the spectrum of genes studied here, we showed that Pol III–transcribed genes were able to tether the chromosome arm locally to either nuclear or nucleolar periphery.

DISCUSSION

The major finding of this study is that hierarchical constraints in chromosome organization control the position of Pol III–transcribed genes in the nucleus. The Rabl-like conformation of yeast chromosomes imposes a rigid scaffold that strongly modulates the frequency of associations between Pol III–transcribed genes and the nuclear and/or nucleolar periphery. Pol III–transcribed genes close to tethering elements, such as centromeres, HMR, or telomeres, interact with the nucleolus at very low frequency in cell populations. Here we confirmed that a locus near CEN is close to the NE and constrained by SPB, and a locus near TEL is at the NE. We showed that Pol III–transcribed genes located >100 kb from these

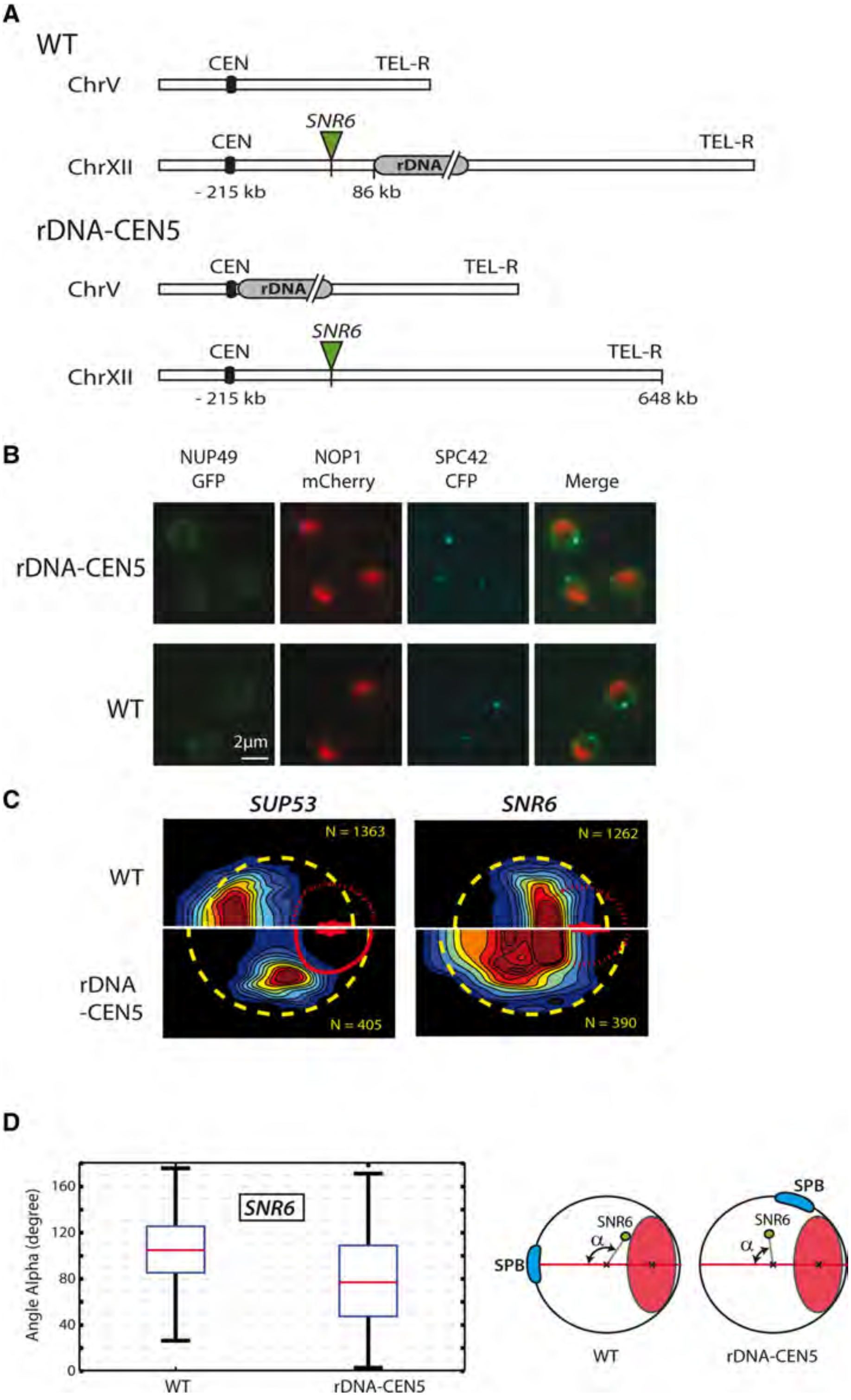

FIGURE 6: Ectopic insertion of rDNA modifies nucleolar associations. (A) Important chromosomal features in the WT and rDNA-CEN5 strains. (B) In vivo labeling of the SPB (SPC42-CFP, blue signal) and nucleolus (NOP1-mCherry) in the nucleus of the WT (left) and rDNA-CEN5 strains. (C) Gene map of the *SUP53* (left) and *SNR6* (right) loci in WT (top) and rDNA-CEN5 (bottom) strains. (D) Box plot of α angle distribution for *SNR6* locus in WT and rDNA-CEN5 strains. Median angle (for 20 individual nuclei) values. Red line, median α value. Edges of the box are 25th and 75th percentiles. Whiskers extend to 10th and 90th percentiles. Right, angle between *SNR6* locus (green dot) and nuclear–nucleolar center axis (red line). The region occupied by the SPB (blue) is close to the nucleolus in the rDNA-CEN5 strain.

tethering elements were frequently found close to the nucleolus and/or NE. Changing the position of genes relative to tethering elements (CEN and rDNA) allowed us to monitor the position of Pol III–transcribed genes free from constrains imposed by the Rabl-like configuration. Our results demonstrated that recruitment of a tDNA locus at the nucleolar periphery is driven by the Pol III–transcribed gene itself. Finally, for a subset of genes, we were also able to show that nucleolar association of the host locus depended on the presence of the Pol III–transcribed gene and was driven by its transcriptional status. For one case (*SUF3*), nucleolar association was not affected upon Pol III–transcribed gene deletion, but peripheral location was weakened.

Hierarchy of constraints driving chromosome organization in vivo

tRNA gene clustering at the nucleolus is believed to affect global chromosome folding in vivo, potentially competing with centromeric recruitment to the SPB (Haeusler and Engelke, 2006). We showed here, using ectopic insertions of essential Pol III–transcribed genes close to centromeres, that centromeric proximity prevented nucleolar recruitment of Pol III–transcribed genes. The genes studied included *SCR1* and *SNR6* genes, which can drive nucleolar recruitment. Permanent centromere release, manipulating *CEN3* location within the chromosome, was sufficient for the nucleolar recruitment of Pol III–transcribed genes. We conclude that the recruitment of Pol III–transcribed genes to the nucleolus or nuclear periphery contributes to higher-order chromosome organization in vivo when permitted by the strongest constraints imposed by the Rabl-like conformation.

Pol III–transcribed genes preferentially localize at the nuclear and nucleolar periphery

tRNA-encoding genes are recruited to the nuclear periphery in G2/M (Chen and Gartenberg, 2014), consistent with changes in the location of Pol III–transcribed genes during the cell cycle. We used yeast strains and automated data analysis methods developed primarily for the mapping, with high accuracy, of gene positions relative to the nucleolus. However, we were also able to demonstrate the frequent localization of *tL(UAA)L* (Albert *et al.*, 2013), *SUF3*, *TRR4*, and *SCR1* at the nuclear periphery. We found that *SCR1* was recruited to the nucleolar periphery mostly in G1. In the

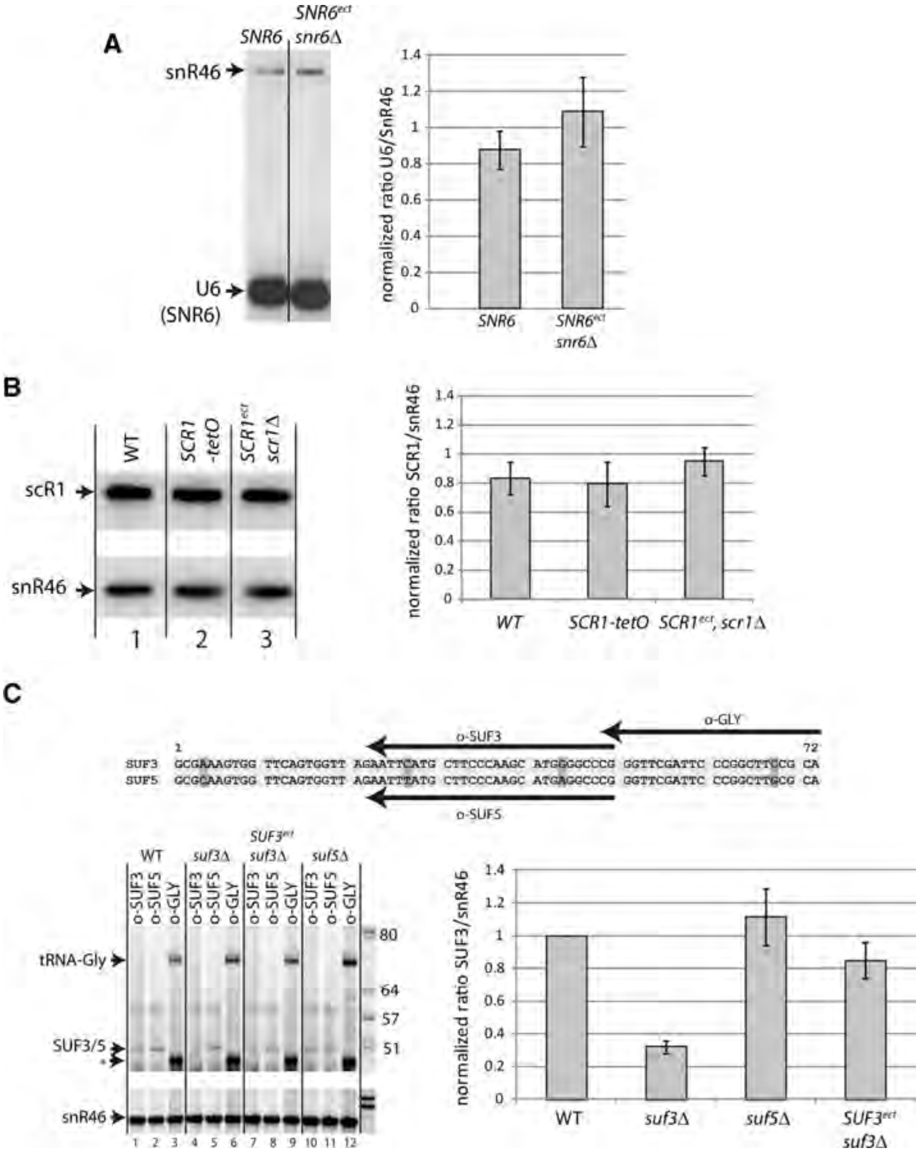

FIGURE 7: RNA accumulation from ectopically expressed Pol III–transcribed genes. (A) Quantification by northern blotting (top) of U6 transcript accumulation (bottom) relative to *SNR46* small nucleolar RNA in the wild-type strain (*SNR6*) and the strain with an ectopic *SNR6* insertion (*SNR6*^{ect}, *snr6Δ*). (B) Northern blot quantification of *SCR1* transcript accumulation relative to *SNR46* small nucleolar RNA in WT (lane1) and strains with tetO-labeled *SCR1* (lane 2) and ectopically inserted *SCR1* without a copy of *SCR1* at the native locus (*SCR1ect, scr1Δ*; lane 3). (C) Quantification by reverse transcription of *SUF3* and *SUF5* transcript accumulation relative to snR46 small nucleolar RNA (top, oligonucleotides used as primers for reverse transcription aligned with the *SUF3* and *SUF5* sequences: o-SUF3, specific to *SUF3* RNA; o-SUF5, specific to *SUF5* RNA; o-GLY was used to detect all glycine tRNAs produced from most of the tRNA^{Gly} genes). Asterisk indicates premature stop product (Figure 1).

S and G2/M phases, *SCR1* was frequently located at the nuclear periphery. tDNA docking at the nuclear envelope, exclusively in G2/M, is associated with a peak of tRNA expression during mitosis and requires Los1, the major exportin of nascent tRNA (Chen and Gartenberg, 2014). *SCR1* encodes the RNA component of the SRP particle; its location at the periphery of the nucleus during S phase may be explained by an expression pattern different from that of the tDNA.

The nucleolar and nuclear periphery regions are, therefore, preferential locations for Pol III–transcribed genes, although the locations of these genes may vary during the cell cycle.

Mechanism by which Pol III–transcribed genes associates with the nucleolus

Condensin-dependent clustering of Pol III–transcribed genes and microtubule-dependent nucleolar association of tDNAs from large families have been described (Thompson *et al.*, 2003; Haeusler *et al.*, 2008; Rodley *et al.*, 2011; Chen and Gartenberg, 2014; Rutledge *et al.*, 2015). These findings suggest that tRNA genes are involved in maintaining the spatial organization of the genome. Furthermore, chromosome conformation capture (3C) methods cluster tDNAs into two large groups: an rDNA-proximal cluster and a nonnucleolar, centromere-proximal cluster (Duan *et al.*, 2010; Rutledge *et al.*, 2015). However, some reported findings have recently been called into question. A different normalization procedure for 3C contact maps accounting for technical bias resulted in a lower estimated likelihood of Pol III–Pol III gene contacts (Cournac *et al.*, 2012). This would make a direct role for tDNA clustering in global chromosome organization less likely (Rutledge *et al.*, 2015).

By exploring individual loci by fluorescence microscopy rather than tDNA clusters by 3C-based methods, we were able to reproduce the frequent association with the nucleolar periphery of nontethered (>100 kb from *TEL*, *CEN*, and *HMR*) Pol III genes. The condensin complex is essential for the nucleolar clustering of Pol III–transcribed genes (Haeusler *et al.*, 2008). However, condensin is associated with all Pol III–transcribed genes, even those tethered away from the nucleolus (D'Ambrosio *et al.*, 2008), suggesting a role for other anchoring elements in nucleolar association. Nucleolar recruitment was abolished when Pol III transcription was inhibited. The transcripts of Pol III–transcribed genes have been reported to pass through the nucleolus during their maturation (Bertrand *et al.*, 1998). The nascent tRNAs themselves, therefore, may participate in recruiting their genes to the nucleolus. A recent study on human cells showed that Alu RNAs accumulating in the nucleolus could target other loci to the nucleolus (Caudron-Herger *et al.*, 2015). A similar mechanism in which RNA drives a DNA locus–nucleolar interaction may contribute to the association of Pol III–transcribed genes with the nucleolus in budding yeast.

Pol III–transcribed genes as a controller of local chromosome organization

Chromosome organization has been described quantitatively in yeast. Biophysical models of chromatin can be used to describe chromosomes or chromosomal rearrangements in cycling cells: the chromosomes adopt the Rabl-like configuration (Tjong *et al.*, 2012; Wong *et al.*, 2012). However, it has been suggested that other elements may tether chromosomes to the nuclear periphery (Dultz *et al.*, 2016). Our

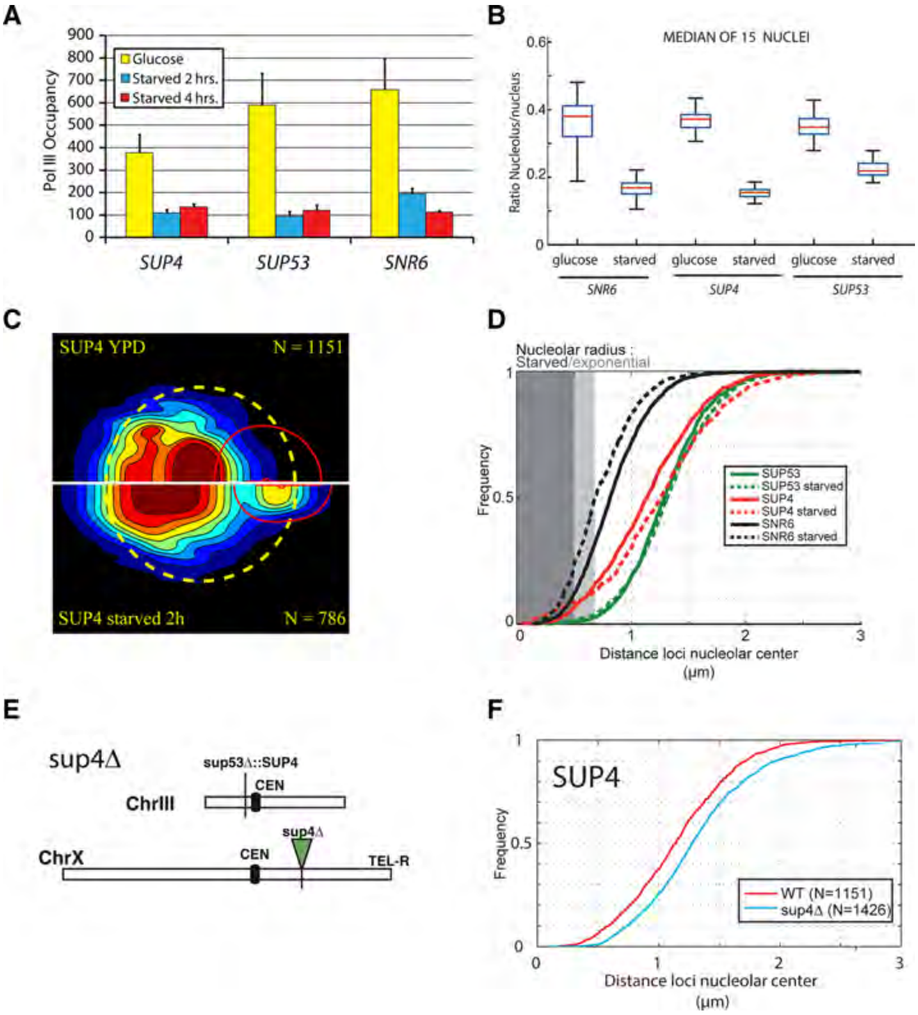

FIGURE 8: Nontethered Pol III–transcribed genes drive nucleolar periphery association. (A) Starvation results in the loss of Pol III from the genes. Pol III occupancy of genes was measured by ChIP of the 9xMyc-tagged RPC128 subunit after 2 and 4 h of starvation. Occupancy was measured by real-time PCR quantification of the loci by the $\Delta\Delta Ct$ method. (B) Nucleolar/nuclear volume ratio upon nutrient depletion. Cells exponentially growing or starved of nutrients for 2 h were analyzed with NucLoc software. Boxplots of the median nucleolar-to-nuclear volume ratio (see *Materials and Methods*) were generated. (C) Gene map comparison of the position of the *SUP4* locus in exponential growth (top) and nutrient deprivation (bottom) conditions. (D) Cumulative distribution function (CDF) of the locus–nucleolar center distance (micrometers) for FROS-tagged *SUP53* (green), *SUP4* (red), and *SNR6* (black) locus. Exponential growth (solid line) and starvation conditions (dashed line). (E) FROS insertion (green triangle) near the *sup4Δ* locus on chromosome X. The gene at the *SUP4* locus was deleted and inserted into the *SUP53* locus on chromosome III. (F) CDF of locus–nucleolar center distance (micrometers) for FROS-tagged *SUP4* locus with (WT, red) and without the *SUP4* gene (*sup4Δ*, blue). (G) Gene map comparison of the *SUP4* locus (top half) with the deleted gene locus (bottom half).

findings confirm that Pol III–transcribed genes anchor the chromosomes to the nucleolus and/or NE. We demonstrate here a direct role for the nucleolus in organizing chromatin in the nucleoplasm and contributing to chromosome organization in vivo through the anchoring of Pol III–transcribed genes to its periphery.

MATERIALS AND METHODS

Yeast strains

The genotypes of the strains used are described in Supplemental Table S1. The oligonucleotides used for PCR are listed in Supplemental Table S2. We used p29802 (Berger *et al.*, 2008) as a template for PCR amplification of the KAN-MX cassette. Strains for gene mapping were constructed as previously described (Albert *et al.*, 2013). The insertion point coordinates on the chromosome and oligonucleotides used to target integration are listed in Supplemental Table S1. yCNOD15-1c, BEN56-1a, yCNOD72-1a, and yJUK03-1a were constructed by transforming the TMS1-1a strain. Strains PRA5-1a, PRA6-4a, PRA4-8a, PRA3-5a, PRA1-5a, and PRA2-7a were constructed by transforming the TMS5-8d strain.

Strains with ectopic gene insertions

We chose the *SUP53* locus for ectopic insertion because its proximity to centromere III may compete with nucleolar association, and a neighboring auxotrophic marker (*LEU2*) facilitates the desired genome modification without the need to insert an unrelated marker. Briefly, the strain construction strategy described in Supplemental Figure S2 involved construction of a receptor strain, yCNOD98-1a, in which *SUP53* and the N-terminal part of the auxotrophic selection marker *LEU2* were deleted (Supplemental Figure S2A) and a platform plasmid bearing the genomic DNA of the locus, in which *SUP53* could be replaced by any other Pol III–transcribed gene, was introduced (Supplemental Figure S2B). The targeted gene was introduced via this platform construct. Finally, two successive modifications based on homologous recombination were used to drive the ectopic insertion of a Pol III–transcribed gene at the *SUP53* locus. *LEU2*-positive clones were selected, and the native locus was invalidated in the process. The yJUK10-1a strain was generated by PCR with the 1207/1208 primers and S288c genomic DNA to restore the wild-type *LEU2* gene in the TMS1-1a strain. yCNOD98-1a was built by replacing the *SUP53* and the N-terminal part of *LEU2* in strain yJUK10-1a with a *KAN-MX* cassette, using primers 983/982. The yCNOD98-1a strain was then transformed with *Sac*I-*Hin*dIII–digested plasmids (pCNOD44, pEB5, or pBEL7) to generate ectopic insertions of *SNR6*, *SUF3*, and *SCR1* (PRA14-1a), respectively. The extra copy at the wild-type locus was removed by inserting the *KAN-MX* cassette with primer pairs 1254/1255 (*SNR6*), 1286/1287 (*SUF3*), and 1298/1299 (*SCR1*) to generate strains BEL1-6a, PRA13-1a, and PRA15-2a, respectively. *SUF3* and *SUF5* were deleted in strain yJUK10-1a with primers 1286/1287 and 1292/1293 to generate BEL5-1a and BEL6-7a, respectively. TetO insertions were performed, as described for strain yJUK03-1a, in strains BEL1-6a, PRA13-1a, and PRA15-2a to generate strains BEL4-2a, PRA8-1a, and PRA11-1a, respectively.

Deletion strains

SUF5 was deleted from PRA2-7a by transformation with an integrative URA3 PCR fragment amplified with primers 1292/1293 from pSK-URA3-M13 used as a template. This deletion generated the yCNOD165-1a strain. yCNOD178-1a and yCNOD142-1a, carrying labeled deletions of *SUF3* and *SCR1*, respectively, were obtained by *his3Δ-tetO-NAT* insertion into the ectopic strains PRA13-1a (*SUF3ect*) and PRA15-2a (*SCR1ect*). The labeling strategies were identical to those used when generating strains PRA1-5a (*SUF3*) and PRA3_5a (*SCR1*). We deleted *TRT2*, *TRR4*, and *SUP4*, by introducing the *(sup53Δ-leu2ΔNter)::KAN-MX* cassette used for ectopic insertion into strains with labeled loci by mating PRA5-1a (*TRT2*) and PRA4-8a (*TRR4*) with yCNOD98-1a, and yCNOD72-1a (*SUP4*) with yCNOD148-7b, and then allowing sporylation to occur. Selected spores were transformed with *Sac*I/*Hin*dIII–digested pCNOD60 (*TRT2*), pCNOD58 (*TRR4*), or pCNOD45 (*SUP4*) to insert ectopic copies. The WT gene copies were deleted by transformation with URA3 amplified from pSK-URA3-M13 by integrative PCR with the primer pairs 1480/1481 (*TRT2*), 1302/1470 (*TRR4*), and 1256/1257 (*SUP4*). This generated strains yCNOD166-1a (*TRT2*), yCNOD163-1a (*TRR4*), and yCNOD190-2a (*SUP4*), respectively, carrying labeled deletions.

Ectopic rDNA at CEN5

Strain rDNA-CEN5 (yCNOD191-1a) was constructed as follows. MATalpha strain NOY2030 carrying rDNA at CEN5 (Oakes *et al.*, 2006) was converted into MATa, and spontaneous *URA3*$^+$ revertants were isolated. They were then mated with strain TMS5-8d, which is suitable for use for gene labeling. After meiosis, yCNOD130-4b spores carrying rDNA at CEN5 (checked by pulsed-field gel electrophoresis) and suitable markers were selected. These spores lacked the *TetR-GFP* gene, which was subsequently reintroduced in two steps. First, a large 3′ deletion (*lys2Δ::KAN*) was introduced into the *LYS2* gene (primers 1497/1498, template p29802). In the second step, a *Bgl*II-linearized *TetR-GFP* (pE219) plasmid was inserted into the *lys2Δ::KAN* allele. *SNR6* or *SUP53* was labeled in yCNOD191-1a, as described for yJUK03-1a and yCNOD15-1c. This labeling resulted in the strains yCNOD182-1a (*SNR6*) and yCNOD184-1a (*SUP53*). The centromere was labeled with *SPC42-CFP* in strain yCNOD130-4b (rDNA-CEN5), generating strains yCNOD186-1a and TMS1-1a (control), giving rise to yCNOD192-1a. A *CFP-KAN* PCR fragment was amplified by integrative PCR from pDH3 (pFA6-CFP-KAN) with oligonucleotides 1492 and 1493.

Conditional centromere

Strain yCNOD171-1a (pGAL-CEN3) is a derivative of strain yJUK03-1a. We inserted pGAL at *CEN3,* using pCEN03-UG (Reid *et al.*, 2008) according to the authors' protocol. The control strain pGAL-CEN9 (yCNOD174-1a) was generated like yCNOD171-1a but with pCEN09-UG. We generated yCNOD173-1a (cen3Δ-CEN6) by inserting the *Nco*I-linearized centromeric plasmid pCNOD69 into yCNOD171-1a at the *YCR101c* locus. Integration events were selected on SC-galactose minus leucine plates, leading to the selection of strain yCNOD172-1a. The pGAL-CEN3 conditional centromere was then fully deleted with a *KAN-MX* PCR fragment amplified with primers 1507/1508 and plasmid p29802. Transformants were selected on glucose-containing medium.

Plasmid construction

The plasmids used in this study are listed in Supplemental Table S3. For ectopic insertion, plasmids were constructed as follows. First, a PCR fragment containing *SUP53* and the N-terminal part of *LEU2* was amplified with the 1220/1219 primers from S288c genomic DNA and inserted as a *Sac*I/*Hin*dIII fragment into pUC19 to generate pCNOD40. pCNOD41, carrying *SUP53* flanked by *Xho*I and *Bam*HI sites, was then generated by site-directed mutagenesis of pCNOD40 with primers 980 and 981. *SUP4, TRR4, TRT2, SNR6, SUF3*, and *SCR1* were amplified from S288c genomic DNA by PCR with primer pairs 1221/1222, 1312/1313, 1486/1487, 1223/1224, 1304/1305, and 1347/1311, respectively. PCR fragments were inserted into pCNOD41 as *Xho*I/*Bam*HI fragments in place of *SUP53* to generate pCNOD45 (*SUP4*), pCNOD58 (*TRR4*), pCNOD60 (*TRT2*), pCNOD44 (*SNR6*), pBEL5 (*SUF3*), and pBEL7 (*SCR1*). A similar strategy was used to insert *RDN5* into pBEL8, except that pNOY373 was used as the template for PCR with primers 1308/1309. The integrative plasmid pCNOD69 was constructed by amplifying the *YCR101c* locus from S288c genomic DNA with primers 1494/1495 and inserting the resulting *Hin*dIII/*Bam*HI–digested fragment inserted into the vector pRS315.

Fluorescence microscopy of living yeast cells

Cell culture. Yeast media were used as previously described (Rose *et al.*, 1990). YPD consists of 1% yeast extract, 2% peptone, and 2% dextrose. SC consists of 0.67% nitrogen base without amino acids (BD Difco) and 2% dextrose supplemented with amino acid mixture (AA mixture; Bio101), adenine, and uracil. Cells were grown overnight at 30°C in YPD diluted to 10^6 cells/ml, harvested at a density of 4×10^6 cells/ml, and rinsed twice with the corresponding SC medium. Cells were spread on slides coated with a patch of SC medium supplemented with 2% agarose and 2% glucose. Cover slides were sealed with VaLaP (one-third Vaseline, one-third lanolin, one-third paraffin). For starvation experiments, cell cultures reaching a density of 4×10^6 cells/ml were washed twice with 15% YP without glucose, resuspended at a density of 4×10^6 cells/ml in this medium, and incubated for 2 h at 30°C. Cells were mounted on slides as described but with 15% SC without glucose.

Microscope image acquisition. *Gene position*. Confocal microscopy was performed within 20 min of mounting, using an Andor Revolution Nipkow-disk confocal system installed on an Olympus IX-81, featuring a CSU22 confocal spinning-disk unit (Yokogawa) and an electron-multiplying charge-coupled device camera (DU 888; Andor). The system was controlled with the Revolution FAST mode of Andor Revolution IQ1 software. Images were acquired with an Olympus 100× objective (Plan APO, 1.4 numerical aperture [NA], oil immersion). The single laser lines used for excitation were from diode-pumped solid-state lasers exciting GFP fluorescence at 488 nm (50 mW; Coherent) and mCherry fluorescence at 561 nm (50 mW; CoboltJive). A Semrock bi-bandpass emission filter (Em01-R488/568-15) was used to collect green and red fluorescence. Pixel size was 65 nm. For 3D analysis, *Z*-stacks of 41 images with a 250-nm *Z*-step were used. An exposure time of 200 ms was applied.

SPB imaging. Fluorescence imaging was performed with an Olympus inverted microscope equipped with a complementary metal-oxide semiconductor camera (Hamamatsu ORCA-Flash 4.0) and a SpectraX illumination system (Lumencore). Images were acquired with an Olympus UPlan SApo 100× objective lens (NA 1.4) and a dual-band cyan fluorescent protein (CFP)–yellow fluorescent protein Semrock filter set (excitation, 416/501-25; DM440/520-Di01-25×36; emission, 464/547-25) for CFP and a three-band Chroma filter set (69002 ET-DAPI/FITC/Texas Red) in combination with an eternal filter wheel equipped with Semrock filters with emission 465/537/623 and 520-40 for mCherry and GFP, respectively.

Image analysis to determine locus position. Confocal images were processed and analyzed with a Matlab (MathWorks) script, NucLoc, available from www.nucloc.org (Berger *et al.*, 2008). Cumulative distribution functions were generated with an existing function (Matlab). Boxplots of median ratios of distances to the center of the nucleolus or nucleus were generated in two steps by first calculating median distances for each of 100 nuclei and then plotting boxplots for the median values obtained.

RNA analysis

The sequences of the oligonucleotides used for RNA quantification are given in Supplemental Table S3. RNA was extracted and Northern blotting performed as previously described (Beltrame and Tollervey, 1992). Reverse transcription was performed with the Superscript II kit (Invitrogen) in accordance with the manufacturer's protocol. RNA species were resolved by electrophoresis on 8% polyacrylamide sequencing gels. Quantifications were performed by phosphorimaging (Typhoon; GE Healthcare) with MultiGauge software (Fujifilm).

Chromatin immunoprecipitation

The YPH500 RPC128-myc strain was grown to mid exponential growth phase ($OD_{600\ nm}$ = 0.8) and cross-linked by incubation with 1% formaldehyde for 30 min. ChIP samples were prepared as previously described (Arimbasseri and Bhargava, 2008; Mahapatra *et al.*, 2011; Kumar and Bhargava, 2013) with an anti-Myc antibody (05-724; Millipore). Real-time PCR was performed on the ChIP and control (input and no antibody) DNA to determine Pol III occupancy on *SNR6* (primers 1 and 2), *SUP4* (primers 3 and 4), and *SUP53* (primers 5 and 6) genes. Pol III occupancy was normalized relative to that on *TelVIR* (primers 7 and 8) used as a negative control and is expressed as fold enrichment relative to the negative control.

Mononucleosome MNase protection assay

Untagged control (TMS5-8a) and FROS insertion (for genes *TRT2*, *TRR4*, *SUF3*, *SUF5*, and *SUP61*) strains were grown to mid exponential growth phase (OD = 0.8) at 30°C. Cells were cross-linked by incubation with 1% formaldehyde for 10 min, and the reaction was quenched by adding 125 mM glycine. Cells were washed, and spheroplasts were generated with Zymolyase. Spheroplasts were subjected to controlled MNase digestion, and the digested DNA was purified and subjected to electrophoresis in 1.25% agarose gels. Naked genomic DNA (deproteinized) was digested with MNase to obtain a fragment distribution ranging from 100 to 300 base pairs for use as a control. The band corresponding to mononucleosomal DNA was excised from the gel, and the DNA was purified. Equal amounts of mononucleosomal DNA and digested genomic DNA were used as a template for real-time PCR. Nucleosome occupancy was investigated with primers designed to amplify 110 ± 10–base pair fragments close to the tDNA gene. Nucleosome occupancy was normalized relative to a control subtelomeric region of TelVIR.

ACKNOWLEDGMENTS

We thank Juliane Klehr for strain construction and initial characterization of the positions of loci. This work also benefited from the assistance of the imaging platform of Toulouse TRI. This work was supported by an ATIP-plus grant from the Centre National de la Recherche Scientifique, the Agence Nationale de la Recherche (ANDY), and the IDEX of Toulouse University (Clemgene and Nudgene). This work is a French–Indian collaborative effort funded by Indo-French Centre for the Promotion of Advanced Research Project 4103 between the laboratories of P.B. and O.G.

REFERENCES

Albert B, Mathon J, Shukla A, Saad H, Normand C, Leger-Silvestre I, Villa D, Kamgoue A, Mozziconacci J, Wong H, *et al.* (2013). Systematic characterization of the conformation and dynamics of budding yeast chromosome XII. J Cell Biol 202, 201–210.

Arimbasseri AG, Bhargava P (2008). Chromatin structure and expression of a gene transcribed by RNA polymerase III are independent of H2A.Z deposition. Mol Cell Biol 28, 2598–2607.

Beltrame M, Tollervey D (1992). Identification and functional analysis of two U3 binding sites on yeast pre-ribosomal RNA. EMBO J 11, 1531–1542.

Berger AB, Cabal GG, Fabre E, Duong T, Buc H, Nehrbass U, Olivo-Marin JC, Gadal O, Zimmer C (2008). High-resolution statistical mapping reveals gene territories in live yeast. Nat Methods 5, 1031–1037.

Bertrand E, Houser-Scott F, Kendall A, Singer RH, Engelke DR (1998). Nucleolar localization of early tRNA processing. Genes Dev 12, 2463–2468.

Bloom-Ackermann Z, Navon S, Gingold H, Towers R, Pilpel Y, Dahan O (2014). A comprehensive tRNA deletion library unravels the genetic architecture of the tRNA pool. PLoS Genet 10, e1004084.

Bystricky K, Laroche T, van Houwe G, Blaszczyk M, Gasser SM (2005). Chromosome looping in yeast: telomere pairing and coordinated movement reflect anchoring efficiency and territorial organization. J Cell Biol 168, 375–387.

Casolari JM, Brown CR, Komili S, West J, Hieronymus H, Silver PA (2004). Genome-wide localization of the nuclear transport machinery couples transcriptional status and nuclear organization. Cell 117, 427–439.

Caudron-Herger M, Pankert T, Seiler J, Nemeth A, Voit R, Grummt I, Rippe K (2015). Alu element-containing RNAs maintain nucleolar structure and function. EMBO J 34, 2758–2774.

Chen M, Gartenberg MR (2014). Coordination of tRNA transcription with export at nuclear pore complexes in budding yeast. Genes Dev 28, 959–970.

Cournac A, Marie-Nelly H, Marbouty M, Koszul R, Mozziconacci J (2012). Normalization of a chromosomal contact map. BMC Genomics 13, 436.

D'Ambrosio C, Schmidt CK, Katou Y, Kelly G, Itoh T, Shirahige K, Uhlmann F (2008). Identification of cis-acting sites for condensin loading onto budding yeast chromosomes. Genes Dev 22, 2215–2227.

Duan Z, Andronescu M, Schutz K, McIlwain S, Kim YJ, Lee C, Shendure J, Fields S, Blau CA, Noble WS (2010). A three-dimensional model of the yeast genome. Nature 465, 363–367.

Dultz E, Tjong H, Weider E, Herzog M, Young B, Brune C, Mullner D, Loewen C, Alber F, Weis K (2016). Global reorganization of budding yeast chromosome conformation in different physiological conditions. J Cell Biol 212, 321–334.

Gehlen LR, Gruenert G, Jones MB, Rodley CD, Langowski J, O'Sullivan JM (2012). Chromosome positioning and the clustering of functionally related loci in yeast is driven by chromosomal interactions. Nucleus 3, 370–383.

Gong K, Tjong H, Zhou XJ, Alber F (2015). Comparative 3D genome structure analysis of the fission and the budding yeast. PLoS One 10, e0119672.

Gotta M, Laroche T, Formenton A, Maillet L, Scherthan H, Gasser SM (1996). The clustering of telomeres and colocalization with Rap1, Sir3, and Sir4 proteins in wild-type Saccharomyces cerevisiae. J Cell Biol 134, 1349–1363.

Gursoy G, Xu Y, Liang J (2014). Computational predictions of structures of multichromosomes of budding yeast. Conf Proc IEEE Eng Med Biol Soc 2014, 3945–3948.

Haeusler RA, Engelke DR (2004). Genome organization in three dimensions: thinking outside the line. Cell Cycle 3, 273–275.

Haeusler RA, Engelke DR (2006). Spatial organization of transcription by RNA polymerase III. Nucleic Acids Res 34, 4826–4836.

Haeusler RA, Pratt-Hyatt M, Good PD, Gipson TA, Engelke DR (2008). Clustering of yeast tRNA genes is mediated by specific association of condensin with tRNA gene transcription complexes. Genes Dev 22, 2204–2214.

Hernandez-Verdun D, Roussel P, Gebrane-Younes J (2002). Emerging concepts of nucleolar assembly. J. Cell Sci 115, 2265–2270.

Hill A, Bloom K (1987). Genetic manipulation of centromere function. Mol Cell Biol 7, 2397–2405.

Jakociunas T, Domange Jordo M, Ait Mebarek M, Bunner CM, Verhein-Hansen J, Oddershede LB, Thon G (2013). Subnuclear relocalization and silencing of a chromosomal region by an ectopic ribosomal DNA repeat. Proc Natl Acad Sci USA 110, E4465–E4473.

Jin QW, Fuchs J, Loidl J (2000). Centromere clustering is a major determinant of yeast interphase nuclear organization. J Cell Sci 113, 1903–1912.

Klein F, Laroche T, Cardenas ME, Hofmann JF, Schweizer D, Gasser SM (1992). Localization of RAP1 and topoisomerase II in nuclei and meiotic chromosomes of yeast. J Cell Biol 117, 935–948.

Kumar Y, Bhargava P (2013). A unique nucleosome arrangement, maintained actively by chromatin remodelers facilitates transcription of yeast tRNA genes. BMC Genomics 14, 402.

Léger-Silvestre I, Trumtel S, Noaillac-Depeyre J, Gas N (1999). Functional compartmentalization of the nucleus in the budding yeast Saccharomyces cerevisiae. Chromosoma 108, 103–113.

Mahapatra S, Dewari PS, Bhardwaj A, Bhargava P (2011). Yeast H2A.Z, FACT complex and RSC regulate transcription of tRNA gene through differential dynamics of flanking nucleosomes. Nucleic Acids Res 39, 4023–4034.

Misteli T (2001). The concept of self-organization in cellular architecture. J Cell Biol 155, 181–185.

Misteli T (2007). Beyond the sequence: cellular organization of genome function. Cell 128, 787–800.

Nemeth A, Conesa A, Santoyo-Lopez J, Medina I, Montaner D, Peterfia B, Solovei I, Cremer T, Dopazo J, Langst G (2010). Initial genomics of the human nucleolus. PLoS Genet 6, e1000889.

Oakes ML, Johzuka K, Vu L, Eliason K, Nomura M (2006). Expression of rRNA genes and nucleolus formation at ectopic chromosomal sites in the yeast Saccharomyces cerevisiae. Mol Cell Biol 26, 6223–6238.

Reid RJ, Sunjevaric I, Voth WP, Ciccone S, Du W, Olsen AE, Stillman DJ, Rothstein R (2008). Chromosome-scale genetic mapping using a set of 16 conditionally stable Saccharomyces cerevisiae chromosomes. Genetics 180, 1799–1808.

Rodley CD, Pai DA, Mills TA, Engelke DR, O'Sullivan JM (2011). tRNA gene identity affects nuclear positioning. PLoS One 6, e29267.

Rose MD, Winston F, Hieter P (1990). Methods in Yeast Genetics. A Laboratory Manual, Cold Spring Harbor, NY: Cold Spring Harbor Laboratory Press.

Rutledge MT, Russo M, Belton JM, Dekker J, Broach JR (2015). The yeast genome undergoes significant topological reorganization in quiescence. Nucleic Acids Res 43, 8299–8313.

Sikorski RS, Hieter P (1989). A system of shuttle vectors and yeast host strains designed for efficient manipulation of DNA in Saccharomyces cerevisiae. Genetics 122, 19–27.

Takizawa T, Meaburn KJ, Misteli T (2008). The meaning of gene positioning. Cell 135, 9–13.

Therizols P, Duong T, Dujon B, Zimmer C, Fabre E (2010). Chromosome arm length and nuclear constraint determine the dynamic relationship of yeast subtelomeres. Proc Natl Acad Sci USA 107, 2025–2030.

Thompson M, Haeusler RA, Good PD, Engelke DR (2003). Nucleolar clustering of dispersed tRNA genes. Science 302, 1399–1401.

Tjong H, Gong K, Chen L, Alber F (2012). Physical tethering and volume exclusion determine higher-order genome organization in budding yeast. Genome Res 22, 1295–1305.

Tokuda N, Terada TP, Sasai M (2012). Dynamical modeling of three-dimensional genome organization in interphase budding yeast. Biophys J 102, 296–304.

Trumtel S, Leger-Silvestre I, Gleizes PE, Teulieres F, Gas N (2000). Assembly and functional organization of the nucleolus: ultrastructural analysis of Saccharomyces cerevisiae mutants. Mol Biol Cell 11, 2175–2189.

Wai H, Johzuka K, Vu L, Eliason K, Kobayashi T, Horiuchi T, Nomura M (2001). Yeast RNA polymerase I enhancer is dispensable for transcription of the chromosomal rRNA gene and cell growth, and its apparent transcription enhancement from ectopic promoters requires Fob1 protein. Mol Cell Biol 21, 5541–5553.

Wong H, Marie-Nelly H, Herbert S, Carrivain P, Blanc H, Koszul R, Fabre E, Zimmer C (2012). A predictive computational model of the dynamic 3D interphase yeast nucleus. Curr Biol 22, 1881–1890.

Yang CH, Lambie EJ, Hardin J, Craft J, Snyder M (1989). Higher order structure is present in the yeast nucleus: autoantibody probes demonstrate that the nucleolus lies opposite the spindle pole body. Chromosoma 98, 123–128.

Zimmer C, Fabre E (2011). Principles of chromosomal organization: lessons from yeast. J Cell Biol 192, 723–733.

3. Published: "High-throughput live-cell microscopy analysis of association between chromosome domains and the nucleolus in *S. cerevisiae*"

During my PhD project, I also one published one book chapter about the high-throughput live-cell microscopy analysis of association between chromosome domains and the nucleolus in S. cerevisiae on the Methods in Molecular Biology. This part is the protocol about how to track the chromatin dynamics and the ‘gene territories’.

Chapter 4

High-Throughput Live-Cell Microscopy Analysis of Association Between Chromosome Domains and the Nucleolus in *S. cerevisiae*

Renjie Wang, Christophe Normand, and Olivier Gadal

Abstract

Spatial organization of the genome has important impacts on all aspects of chromosome biology, including transcription, replication, and DNA repair. Frequent interactions of some chromosome domains with specific nuclear compartments, such as the nucleolus, are now well documented using genome-scale methods. However, direct measurement of distance and interaction frequency between loci requires microscopic observation of specific genomic domains and the nucleolus, followed by image analysis to allow quantification. The fluorescent repressor operator system (FROS) is an invaluable method to fluorescently tag DNA sequences and investigate chromosome position and dynamics in living cells. This chapter describes a combination of methods to define motion and region of confinement of a locus relative to the nucleolus in cell's nucleus, from fluorescence acquisition to automated image analysis using two dedicated pipelines.

Key words Nucleolus, FROS, Nuclear organization, Live-cell imaging, Fluorescence microscopy, Chromosome domain dynamics, Yeast, *Saccharomyces cerevisiae*

1 Introduction

Nuclear organization is investigated using a large panel of advanced molecular biology and imaging techniques. Chromosome conformation capture (3C) and derived methods are more and more popular to explore 3D organization of genomes [1]. However, contact frequencies obtained using 3C-derived methods are indicative of the frequency at which sequences are ligated together by cross-linking [2]. High frequency of product captured correlated strongly with spatial proximity but should be combined with direct imaging observation to exclude local discrepancy [3]. Thanks to the fluorescent labeling of chromosome loci in living cells, advanced imaging techniques can also provide considerable amount of data describing the spatial organization of chromosomes. Fluorescent labeling in living cells is mostly performed using Fluorescent

Attila Németh (ed.), *The Nucleolus: Methods and Protocols*, Methods in Molecular Biology, vol. 1455, DOI 10.1007/978-1-4939-3792-9_4, © Springer Science+Business Media New York 2016

operator-repressor system (FROS) fluorescent repressor-operator system, which combines the expression of a bacterial repressor fused to a fluorescent protein and the integration of operator sequence as tandem arrays at a specific locus (*see* **Note 1**). A unique FROS tagged locus appears as a bright fluorescent spot in the nucleus. However, to be informative, imaging data must be quantitative, and "high throughput" to generate statistically robust data comparable with 3C-derived dataset. Here, we describe two types of analysis to explore motion and position of a locus relative to the nucleolus. Motion addresses local biophysical properties of chromatin, while position gives information about confinement (gene territory within chromosome territory) and long-range nuclear organization [4, 5].

Locus motion can be followed using time-lapse imaging of fluorescently tagged loci. Time-lapse imaging can be used over broad time scales (from 0.2 to 400 s time intervals) and then the images analyzed by a dedicated image analysis system [6] which can be used to extract trajectories of loci in yeast cell nucleus with high precision (below 30 nm). Our previous work had explored the dynamics of chromosomes relative to the nucleolus [7, 8]. The nucleolar association of loci is evaluated using a double detection of loci and nucleolar region in the nucleus. When chromatin is out of the nucleolus, we propose that chromatin motion is described by the Rouse polymer model, which assumes that chromatin fiber behaves as a homogeneous series of beads connected by elastic springs [7]. The motion of nucleolar associated locus in yeast is not compatible with such model and remains largely uncharted [7, 8].

Trajectories are classically analyzed using mean-square displacement (MSD). For every time interval (s), the square of the mean displacement observed (μm^2) can be calculated. Confinement of a locus in areas of the nucleus appears as a plateau at longer time scale, defining a radius of constrains (Rc, expressed in μm) (typically measured at 200 s) [4]. However, for such long intervals, the number of distance measurements decreases, which increases the standard deviation of the measured Rc. Therefore, Rc only approximates the volume of the nucleus in which loci are confined. Typically, the explored volume for different loci (0.57–1.5 μm^3) can be determined using spherical approximations [9]. How to explore accurately association of the locus to the nucleolus? To analyze the spatial location of a given locus in yeast nucleus, 'Nucloc' algorithm determines, in each cell nucleus of a population, the three-dimensional position of the locus relative to the nuclear envelope, and the nuclear center and the nucleolus as landmarks [10]. Automated detection "pipeline" allows high-throughput analysis of a large number of cells (>1000). The 'Nucloc' algorithm [10] can create genemap: a high-resolution cumulative percentile map of subnuclear domains occupied by individual loci in a population of cells, thereby defining the domain in the nucleus in which locus is confined: the gene territory. Importantly, the dimensions of a gene territory, as defined by the volume in which 50% of the gene positions are detected in statistical maps, are compatible with explored volumes estimated using MSD (from 0.57 and 1.5 µm^3 using MSD to 0.8 and 1.2 µm^3, respectively, using gene territory) [8]. Therefore, motion analysis and high-resolution cumulative percentile maps of subnuclear domains occupied by individual locus are nice complementary methods.

Here, we present a detailed protocol to determine the motion of a FROS tagged locus relative to the nucleolus and explore the shape and the position of its confinement area. This protocol describes sample preparation, image analysis, and visualization of data generated. The protocol includes a specific focus on validation procedure of imaging data prior to automated processing and on controls required to assess quality of data collected.

2 Materials

2.1 Cell Culture

1. YP medium (1% w/v yeast extract, 2% w/v peptone) complemented with required sugar source (glucose, galactose, raffinose) 2% w/v each.
2. Synthetic medium (SC): Due to high autofluorescence of yeast extract in most optical setup, cells are washed and mounted on slide using synthetic medium (SC) 0.67% nitrogen base w/o amino acids, 2% w/v dextrose supplemented with amino acids mixture supplemented with adenine (20 mg/L).
3. Molecular biology grade agarose (2% w/v) is used to immobilize cells for microscopic inspection. We prepare an agar pad using SC media.
4. "VaLaP" is a mixture of 1/3 vaseline, 1/3 lanoline, and 1/3 paraffin which is used to seal coverslip.
5. Slide (Knittel Glass, Germany, 76 × 26 mm).
6. Coverslip (Knittel Glass, Germany, 22 × 22 mm).

2.2 Live-Cell Fluorescence Microscopy for Time-Lapse Imaging

1. An inverted microscope (Ti-E/B; Nikon).
2. A system for long-range time-lapse experiments (Perfect Focus System).
3. Filters tubes (e.g., Semrock; GFP (Ex: 482BP35; DM: 506; Em: 536BP40) and mCherry (Ex. 562BP40, DM593, Em.641BP75)).
4. EM CCD camera (e.g., DU-897; Andor Technology).
5. 100× oil immersion objective lens with variable NA (e.g., CFI Plan-fluor 100×, NA 0.7–1.30, Dt0.2) (*see* **Note 2**).

2.3 Live-Cell Fluorescence Microscopy for Determination of 3D Gene Position in Cell Population

1. A spinning disk confocal system (e.g., Andor Revolution Nipkow-disk confocal system).
2. A CSU22 confocal spinning disk unit (Yokogawa).
3. EM CCD camera (e.g., DU888, Andor).
4. 100× oil immersion objective lens (e.g., Plan APO, 1.4 NA, Olympus).
5. Diode pumped solid state lasers (e.g., DPSSL; at 488 nm (50 mW, Coherent) and mCherry fluorescence at 561 nm (50 mW, CoboltJive)).
6. Filters (e.g., Semrock bi-bandpass emission filter, Em01-R488/568-15).

2.4 Image Analysis Workstation

1. Tracking gene motion: Executable file derived from multiple-target tracing (MTT) [11] is freely available upon request [6]. This executable file used is compiled from Matlab application. Therefore, the compiled executable file can be used on image analysis workstation without Matlab installed. A freely accessible application named component Runtime (MCR; a standalone set of shared libraries to run compiled MATLAB applications) should be installed.
2. Determination of gene position: 'Nucloc' is a suite of Matlab programs, requiring Matlab (Mathworks) to be used (tested with releases R2007b and R2008a) including curve fitting, image processing optimization, signal processing statistic, and wavelet toolbox. The suite is freely available upon request (http://www.nucloc.org/) [10].

3 Methods

3.1 Preparation of the Samples

To determine locus motion and position relative to the nucleolus, we start our experiments with a strain bearing three fluorescent proteins (TetR-GFP, GFP-Nup49, and mCherry-Nop1) (No-FROS strain; *see* **Note 3**). Insertion of a transgene bearing high number of operator (250 repeats) results in individual yeast clones with various number of tetO repeats insertion in the genome (from about 50 to 250 repeats) (*see* **Note 4**). For each targeted locus, we prepare for imaging from two to four individual FROS labeled clones (the quality of the acquired images are evaluated postacquisition, *see* Subheading 3.3). For image acquisition, we need a device allowing long-term growth but maintaining cells immobile close to a microscopic coverslip. We immobilize the yeast cells and distribute them in a single cell monolayer (*see* **Note 5**).

1. Preculture the strain at 30 °C in YP media containing 2% w/v glucose and grow overnight.
2. Dilute cells at 10^6 cells/mL in 50 mL YP glucose media. For some mutant strains, culture condition should be modified to avoid autofluorescence (*see* **Note 6**).
3. Incubate at 30 °C till concentration reaches 4×10^6 cells/mL (at least two doublings after dilution).
4. Collect 1 mL cultured cells and centrifuge $1000 \times g$, 3.5 min at room temperature (low speed centrifugation is used to preserve nuclear organization). Additional steps are required when preparing fixed cell samples (*see* **Note 7**).
5. Rinse cell pellet twice with 1 mL of SC media complemented with suitable sugar.
6. Resuspend cells and concentrate in 5–10 μL SC media.

   Steps 7–11 can be done during cell culture (**step 3**).
7. Prepare 20 mL 2% w/v agarose in SC media containing 2% w/v of sugar. Melt agarose slowly in microwave oven (defrosts program for several minutes). An Erlenmeyer in water filled beaker is used. Melt agarose is kept in 50 °C water bath before pouring pads.
8. Align side by side three microscopy slides on the bench and stick with laboratory tape on the two slides on each side. The one in the middle, that will be used to pour pad, can be freely moved. The tape thickness will define the thickness of the agarose pad. For long time imaging, we increased thickness with a second tape.
9. Drop 80 μL (thickness 2 tapes) or 40 μL (thickness 1 tape) of melted agarose on the central glass slide.
10. A regular slide is immediately placed across the top to create a flat surface on the pad. Press against the top slide for 1 min (*see* **Note 8**).
11. Recovering the slide is the tricky part. Remove the central slide with the cross slide. Slowly move the two slides against each other without damaging the pad. A slide with a pad can be stored in wet atmosphere for 1–2 h.
12. Place 3 μL of the concentrated cells on the pad and cover by a regular coverslip. Gently press to distribute the cells into a monolayer.
13. Seal the coverslip with "VaLaP". "VaLaP" is melted at 150 °C and applied with a cotton swab.

    Live microscopy with such agar pad should be limited to 20 min after mounting, at temperature from 20 to 37 °C.

3.2 Image Acquisition

1. For observation of a gene motion, image acquisition was performed on wide-field microscope equipped with a single photon sensitivity camera. Time interval is usually set to 200 ms but can vary from 20 ms to 10 s depending on the time range to be analyzed.
2. For observation of the gene territory, microscopy was performed with a spinning disk microscope with a sensitive camera with large field of view. For 3D analysis, Z-stacks of 41 images with a 250 nm Z-step were used. Exposure time was 200 ms.

3.3 Validation of the Acquired Fluorescent Images

Gene motion and gene territories are both automated imaging pipeline, allowing high-throughput image analysis. Automation has a clear cost: without proper calibration, it will generate meaningless dataset. Therefore, such optimized algorithms require a well-calibrated and homogeneous fluorescent signal in the cell population (*see* **Note 9**). In case of low signal-to-noise ratio (SNR) for FROS labeling, detection of locus can be inaccurate (*see* **Note 10**). Furthermore, automatic detection of FROS tagged locus can generate meaningless dataset (*see* **Note 11**). Postacquisition control must be performed before running automated image analysis for time-lapse imaging (tracking gene motion) or confocal stack (gene position):

1. Evaluate qualitatively the fluorescent signal obtained in each FROS tagged clone (*see* **Note 12**).
2. From a representative set of acquisition (10–20 cell's nucleus), measure locus intensity ($I_{\max}$), background mean (I_{noise}), and standard deviation (σ_{noise}) intensity (Fig. 1).
3. Determine SNR (dB) of your acquisition (*see* **Note 13**).

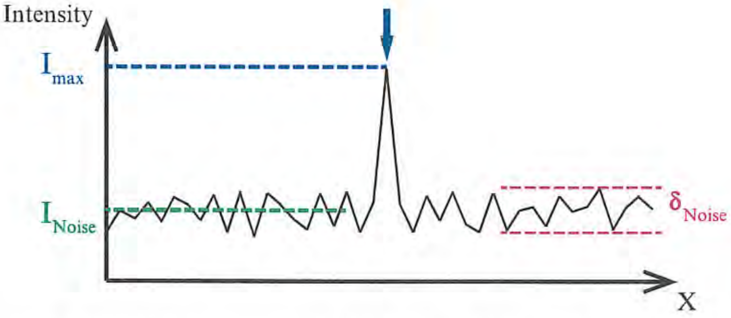

Fig. 1 Signal-to-noise ratio determination. One-dimensional representation of an intensity plot is shown. A point-like fluorescent object (*blue arrow*) is detected. The signal-to-noise ratio depends on the intensity of the signal ($I_{\max}$), the background intensity (I_{noise}), and the variance of the background. The signal-to-noise ratio can be estimated using two different equations, which give different results: $\text{SNR} = (I_{\max} - I_{\text{noise}})/\delta_{\text{noise}}$ or $\text{SNR} = (I_{\max} - I_{\text{noise}})/\sqrt{I_{\max}}$

3.4 Image Analysis and Visualization of Data

3.4.1 Tracking Gene Motion

To determine trajectory with high resolution, we use a freely accessible executable script [6]. This script is based on the algorithm Multiple-Target Tracing (MTT), an advanced version of SPT [11]. MTT's derived executable file can generate dynamic maps at high densities of tracked loci, thereby providing global representation of chromosome dynamics in nucleus. In MTT, the detection, estimation of positions, and reconnection are done sequentially.

1. Detect the position $r(t)$ of a fluorescently labeled locus in each frame of a time-lapse movie (Fig. 2a) (*see* **Note 14**).
2. Evaluate extracted trajectories (*see* **Note 15**). Raw measurement is the sum of true motion and experimental errors. Visual inspection of the tracking allows rejection of aberrant tracking. User should also evaluate microscopic slide drift, easily detectable by correlated motion of all genes in the frame of view.
3. Determine the contribution of nuclear motion to gene trajectories (*see* **Note 16**).
4. Estimate accuracy of extracted trajectories (*see* **Note 17**).
5. Compute ensemble-averaged MSD from high quality trajectories (Fig. 2b, *see* **Note 18**). To identify possible heterogeneity in the data, rather than mean displacement, step distribution for a given time interval can also be informative [12]. The loci in nucleolus have a different behavior compared with the loci on the same chromosome but in nucleoplasm (Fig. 2c vs d).

3.4.2 Determination and Validation of Genemap

1. Detect cells by importing the confocal stack of images (Fig. 3a). Individual round nuclei (*see* **Note 19**) are detected and cropped as region of interest (ROI). Automation of the script allows processing of about 1000 nuclei without user input. Cells also can be selected manually.
2. 3D localization of FROS position is automatically performed by detection of chosen landmarks (one or two tagged loci; NPC labeling and nucleolus) (Fig. 3b).
3. Quality control of extracted distances is performed (*see* **Note 20**).
4. Evaluate position of loci in cell nucleus. At this stage, distances distribution can be generated (locus-NE, locus-Nuclear center, Locus-Nucleolar centroid) (Fig. 3c).
5. Alignment is computed to generate probability map (Fig. 4). After alignment (Fig. 4a), loci are projected in two-dimension (2D) by cylindrical projection, preserving distance to nuclear and nucleolar center (*see* **Note 21**).
6. Generate the 2D locus probability map in color-coded histogram (Fig. 4b). Rather than histogram, we now use kernel density representation (Fig. 4c), which allows a smooth visualization of color-coded locus probability density map and does not rely on arbitrary histogram bin [13] (*see* **Note 22**).

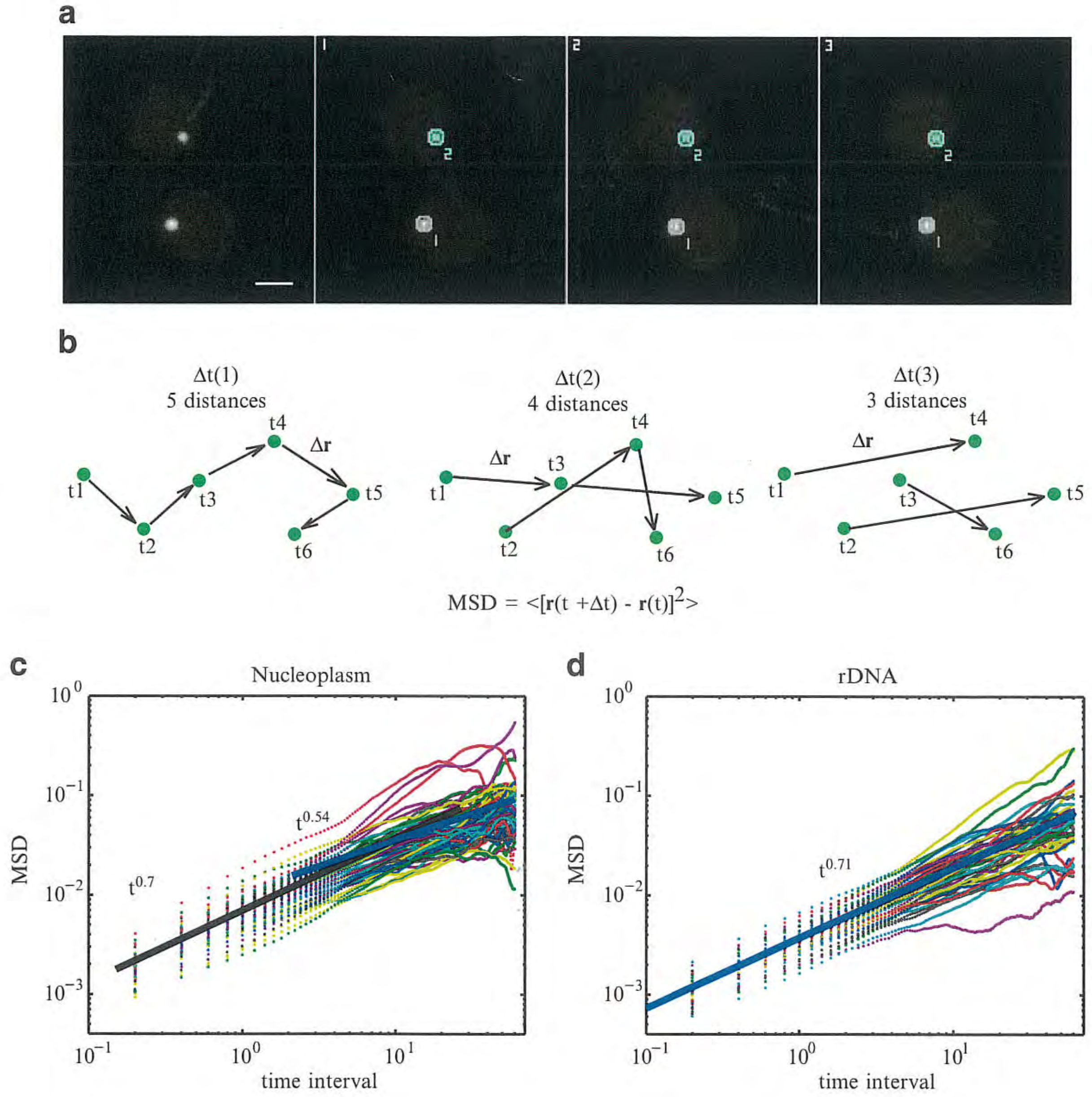

Fig. 2 Mean square displacement (MSD) calculation and interpretation. (**a**) Locus position determined using an MTT-derived algorithm. *Left* is the initial fluorescent image, which is followed by images taken at 200 ms intervals in time-lapse imaging. Scale bar 1 μm. (**b**) Robust MSD calculation requires high numbers of data points. From six positions, detected from t1 to t6 by MTT, the MSD value at $\Delta t(1)$ can be calculated from the mean of five distances. For $\Delta t(2)$ and $\Delta t(3)$, MSD values are the mean of four and three distances, respectively. Robustness of MSD decreases when time intervals (Δt) are increasing. (**c**) MSD extracted from 45 trajectories for one selected FROS labeled locus (position 380 kb on chromosome XII). The *black* and *blue solid lines* represent the average MSD of these trajectories. Motion of loci in the nucleoplasm scale with an exponent of 0.54. (**d**) MSD extracted from 41 trajectories for FROS inserted in rDNA. Blue line represents average MSD. The motion of loci in the nucleolus scales with an exponent of 0.7, which is clearly different from the motion of loci in the nucleoplasm

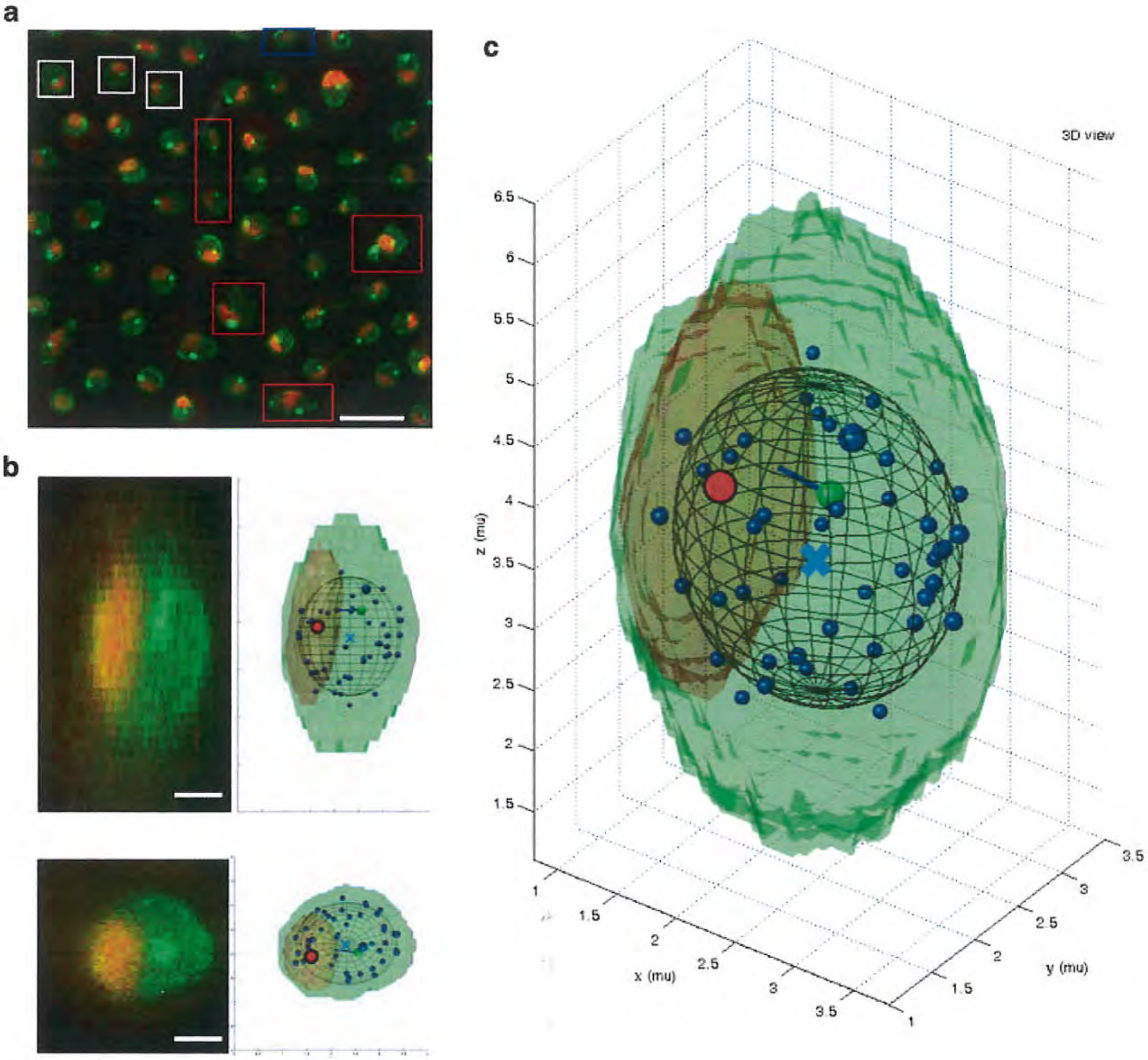

Fig. 3 Determination of three-dimensional position of gene and nuclear landmarks: nuclear center, nuclear periphery, and nucleolus. (**a**) Selection of interphase cells can be performed manually or automatically. Selected nuclei (*white box*) are round and correspond to G1/S phase. The nucleus at the edge of the field of view (*blue box*), mitotic cells, and cells with abnormal shape are excluded (*red boxes*). (**b**) X-projected (*upper panel*) or Z-projected (*lower panel*) fluorescent stack (*left*) and extracted position (*right*). The 'Nucloc' package extracts point-like structures (gene-*green* and NPC-*blue*) and performs thresholding of GFP and mCherry signal used, respectively, to determine nuclear center (*blue cross*) and nucleolar centroid (*red circle*). (**c**) 3D representation of the detection output of 'Nucloc'

4 Conclusion

Both methods give access to different chromatin properties and can be combined using the FROS tagged strains. The robustness and accuracy of the datasets generated by our automated gene motion tracking pipelines are of high quality. Confinement can be best explored using Genemap visualization (Fig. 4), which allows determination of gene territories (50% of distribution). Possible interpretation of such data is still the topic of extensive discussion.

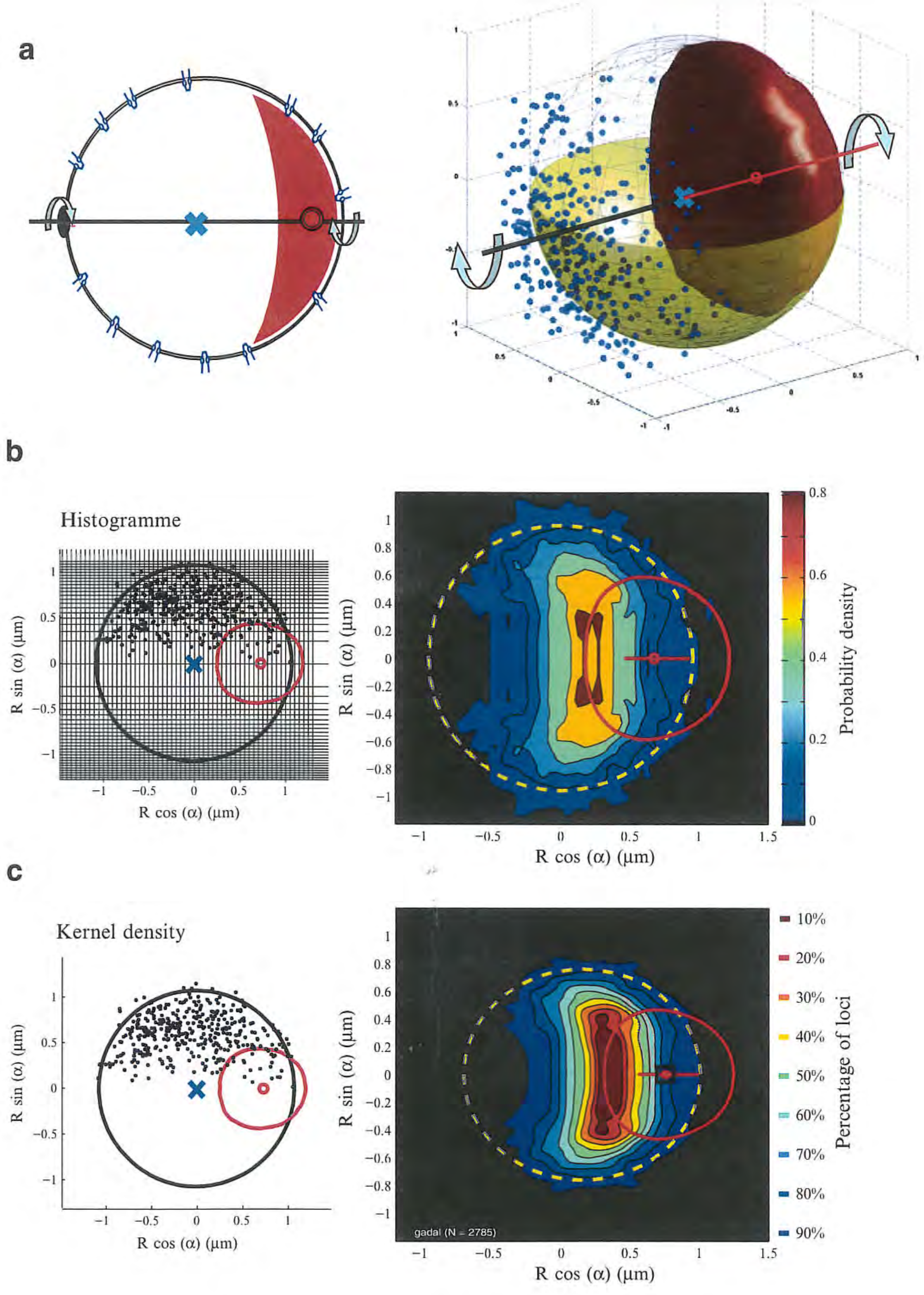

Fig. 4 Aggregation of individual detection in a single probability density map. (**a**) The yeast nucleus is organized around a central axis connecting the nuclear and nucleolar center. (**b**) Alignment of all individual detections. All nuclear centers are translated to the origin (*blue cross*). All nucleolar centers are aligned on *X*-semiaxis (*red* segment). All detected loci (*blue sphere*) are represented in an aggregated 3D map. The median nucleolus (*red shape*) and median nucleus (*yellow circle* with a *dashed line*) are also shown. Rotation around the central axis (*blue arrows*) does not modify distances to nuclear center or nucleolar center. (**c**) Cylindrical projection of genes around the central axis and histogram representation. Gene positions in a 2D map are calculated corresponding to an iso-volume (projected volume per surface unit scale quadratic along the *Y*-axis). A color-coded histogram is determined (*right panel*), in which the colors depict probability density. The kernel distribution does not rely on a histogram, but on kernel density, which allows a smooth representation of the data. The colors indicate the percentage of loci in the enclosing contour

We have suggested that the motion of the locus in the nucleoplasm can be analyzed using the Rouse model (Fig. 2c) [6, 8]. The analysis of MSD is further described in a recent review [7]. Briefly, in a short time interval, the motion of the locus is not restricted by elastic interactions with its neighboring polymer segments, leading to a regime of free diffusion. The second regime corresponds to the Rouse model of polymer dynamics, in which the MSD increases with time with a power-law scaling of 0.54. However, alternative models such as fractional Brownian gene motion in the nucleus have also been proposed [14, 15].

5 Notes

1. The FROS system includes TetR/*tetO* [16], LacI/*lacO* [17], λcl/*λOp* [18]. Genome biology is affected by FROS insertion, and biological consequences should be tested before and after insertion [19]. FROS insertion can affect position of the tagged gene [20], expression of the neighboring gene, and generate artificial tethering between two tagged loci [19]. Due to close proximity of 5′ or 3′ regulatory elements in yeast genome, we insert FROS in both 3′ and 5′ of targeted locus (in 100–800 bp) to explore possible side effect. Nonrepetitive array using ParB-INT appears as an alternative system for gene labeling [21].
2. For fast time-lapse imaging, a single acquisition at each time point (no Z-step) is chosen to shorten time intervals. However, FROS locus can move out of the focal plan. Depth of field is small when using high numerical aperture (NA), typically 1.4. Using variable NA objective (from 1.3 to 0.7), depth of field can be increased. At the cost of a reduced collection of light, single Z-step using NA 1.25 strongly increases trajectory length (with such a setup FROS loci stay in focal plan).
3. Nuclear envelope position is determined using Nup49, an abundant nuclear pore complex (NPC) protein, fused to GFP. Nucleolar volume and position are extracted thanks to the nucleolar protein Nop1, the yeast ortholog of fibrillarin, fused to mCherry. Before tetO insertion, TetR-GFP is distributed throughout the nucleus and appears as a diffuse nuclear staining, which allows (together with GFP-Nup49) a robust determination of the nuclear center. This strain has no loci labeled and must be used as negative control for fluorescent imaging (No-FROS).
4. Methods for tetO insertion including plasmid preparation, yeast transformation, and verification of sequence integration sites have been described previously [18]. We perform an additional pulsed-field gel electrophoresis (PFGE) step to check

possible chromosome abnormalities observed at low frequency (5–10 % of clones) after FROS insertion.

5. Multiple designs exist for live yeast cell imaging. The simplest (agar pad—presented here), concavity slide (Electron Microscopy Science; 1.4–1.6 mm thick), or adhesive gene frame (ABgene; 1.7 × 2.8 cm) allows cells to grow in monolayer for up to 30 min. Longer inspection requires microfluidic device, commercially available (CellASIC™ ONIX Microfluidic Live Cell) or homemade PDMS device, to flow fresh medium in the microfluidic chamber during inspection.
6. Autofluorescence (GFP or mCherry channel) is low in exponentially wild-type yeast cells. Some stress condition (starvation, oxidative stress, aging) can generate autofluorescence and should be carefully investigated. Well-known mutations (*ade1-* or *ade2-*) present in numerous strain backgrounds lead to the accumulation of a red dye in the vacuole generating bright autofluorescence. Such genetic background should be excluded, or large amount of adenine in growth medium should be included to decrease autofluorescence in the vacuole.
7. Chemical fixation (1 % formaldehyde for 15 min, directly in culture medium buffered at 100 mM final concentration with Tris–HCl, pH 8.0 to preserve fluorescence). Glycine is used to neutralize formaldehyde (125 mM final concentration).
8. Preparation of an agar pad was described for DIC observation of *C. elegans* [22]. Place the two taped slides with a clean slide between them on the bench. Place the drop of agar + SC onto the clean slide. Cover the agar with another clean slide placed on top of the three slides. Press gently so that the agar drop is flattened to a circle (the thickness of the tape spacers). Avoid getting bubbles. After the agar solidifies, separate the two slides covering the agar pad by sliding one relative to the other. The agar pad should adhere to one of the slides (usually the bottom one). The agar pad can be kept in a humid chamber for 1–2 h.
9. Automated detection based on Gaussian fitting is typically appropriate for high SNR. Other detection methods (pointpicker, spotdistance, spot tracker, Nemo; see for review [18]) might be more robust and should be explored when SNR cannot be increased.
10. Strong SNR is instrumental to decrease false-detection rate and increase the chance to accurately acquire long trajectories and accurately determine gene territories. Locus motion is analyzed using single particle tracking (SPT) techniques. SPT is based on the ability to accurately identify the center of a fluorescent spot at each time point of time-lapse imaging (2D or 3D) and connect those positions to generate trajectories.

Imaging an isolated fluorescent spot and determining its center is defined as "localization microscopy." Spatial resolution of localization microscopy is not limited by diffraction limit (200–300 nm), but by the signal-to-noise ratio (SNR) which depends on the number of photons detected and the noise generated by microscopic setup and detector (also defined as black noise). Resolution of gene trajectory, when SNR is properly controlled, can make accessible motion below 10 nm (J. Mathon, personal communication). High false-detection rate, followed by automatic reconnection will generate apparent trajectory not related to gene motion. Like the SPT algorithm, 'Nucloc' is based on "localization microscopy" and relies on identifying point-like structures with an estimated resolution of about 30 nm.

11. One important parameter (and source of error) in the detection is that the brightest GFP fluorescent spot is assumed to be the FROS tagged locus. In most of our strains, GFP is used for both TetR-GFP, recognizing tetO at labeled locus and NPC (GFP-Nup49). In normal condition, NPC have the tendency to cluster [23], which can be strongly exacerbated in NPC mutant background (*nup133Δ nup120Δ*). Along the same line, TetR-GFP is homogeneously distributed in the nucleus in most cells, but can form local concentration or aggregates in some cells.
12. Individual transformants should be screened for signal homogeneity of FROS tagged locus. Confocal stacks are processed after maximum intensity projection along *Z*-axis. The tagged gene should be the brightest object of the nucleus (about fivefold over the brightest NPC spot detected). After integration, FROS labeling is stable on petri dishes for months, but might change once propagated from frozen stock. When recovered from frozen stock, individual clones should be rescreened. Very high number of integrated tetO repeats will result in heterogeneous labeling and/or toxicity in the population. When testing novel growth condition (carbon source, different temperature, stresses, etc.), always use No-FROS strain as negative control.
13. SNR is often expressed in decibel (dB). dB is a dimensionless logarithmic unit which express the ratio of two values: $10 \times \log_{10}(P_1/P_0)$. Our calibration showed that SNR > 10 dB is required for accurate detection (precision < 30 nm). SNR > 10 dB requires that the signal-to-noise ratio of genemap means is over 10. In our optical setup (exposure time > 50 ms), the FROS tagged strains used delivered SNR from 20 to 90 dB. We perform accurate locus tracking for SNR 27 dB (a ratio of about 500).

14. For each frame, a detection test is applied first to screen for the presence of Gaussian peaks indicative of FROS tagged genes. This step provides only a binary detection. Next, the identified peaks need to be properly characterized by measuring relevant parameters such as intensity, subpixel position, width, and offset. They are evaluated by a multiparametric Gaussian fit on the signal intensity. Starting from the particles already detected in the current frame, deflation process subtracts their respective estimated Gaussian peaks from the raw image, and then MTT reiterated the detection and estimation processes on the resulting image until it detected only noise. Filtering tests can remove putative aberrant points.
15. For the frame at time t, MTT can iteratively reconstruct trajectories up to time t based on previous detections. Each of the detections (t) is associated with a set of parameters (including position, mean, and standard deviation of intensity). Parameters (t) are used to accurately reconnect trajectories at the next time point, ($t+1$). Connecting individual detection, performed at each time point of the time-lapse acquisition, allows the construction of trajectories of FROS tagged loci (called "reconnection").
16. Extracted trajectories are not corrected for possible motion of the nucleus. Therefore, motion of FROS tagged gene determined in MTT is the sum of locus motion in the nucleus plus the motion of the nucleus in the cell. Ideally, the motion of the nucleus should be subtracted from the measured motion. The nuclear center can be evaluated by measuring the centroid of GFP signal (using ImageJ). When the locus has bright FROS signal, the centroid of the GFP signal might be affected by locus position (FROS tagged gene should contribute to less than 10% of total nuclear fluorescence). For short time-lapse imaging, nuclear center detection is not reliable. Retrieving apparent nuclear motion can only add noise to the experimental data. For long time-lapse imaging (>3 min), motion of the nucleus should be retrieved from the locus motion to exclude infrequent, but significant nuclear motion (>1 μm).
17. When false detections are manually excluded, the accuracy of the detection should be evaluated. Classically, we test the algorithm with simulated images and evaluate the optical setup using fluorescent beads and chemically fixed FROS tagged cells. Simulated images are useful because the absolute positioning is known ("ground truth") and the performance of the algorithm is directly testable. Simulated microscopic images of a time-lapse acquisition are generated using Gaussian approximation of point spread function (PSF) of our microscopic setup [24], with

Poisson noise to approximate photon-counting noise. Known trajectory can then be compared to the measured position. Fluorescent beads provide very high SNR imaging and are required for testing PSF of the optical setup and drift during imaging. Chemical fixation abolishes chromosome motion. Imaging of fixed cells provides an easily accessible control for tracking error, exploring possible cell drift, optical path misalignment, and tracking algorithm imprecision. Other errors, such as dynamic errors due to motion blur (apparent streaking of rapidly moving FROS in a image) during time-lapse imaging can also be directly assessed by data analysis [25].

18. To identify ballistic behavior, the plotting of traveled distance over time can be informative. However, gene motion is typically characterized by random motion and directional motion is rarely observed [26]. In statistical mechanics, the mean square displacement (MSD) is the most common measure of the spatial extent of random motion. In some way, it is often enlightening to think of the MSD as the amount of the system "explored" by the random walker.
19. Nucleus cropping is performed using a Z-projected fluorescent image and a shape criterion is included.
20. This step is very important to evaluate possible errors. Additionally, error-prone detection of nuclear envelope position (estimated by fitting an ellipsoid to the detected NPC) can be automatically discarded by rejecting excessive localization errors. The quality control step can automatically reject also loci with low fluorescent intensity, but this might bias population analysis (G1 or S phase cells have different SNR signal [27]). Therefore, we usually adapt the SNR (select individual clones with higher SNR). Alternatively, one might also omit the NPC labeling for some mutants (nuclear and nucleolar center can be extracted without NPC labeling).
21. We aligned the nuclear landmarks of different nuclei by translations that move the nuclear centers to the origin, followed by rotations around the origin that moved nucleolar centroids onto the half-axis (central axis). To facilitate visualization, we rotated all loci around the central axis and merged the results into a single plane.
22. We have observed that nuclear size and nucleolar size can be reproducibly different between independently generated clones bearing similar FROS tagged locus. Genemap should be performed in at least two independent FROS clones in such cases.

Acknowledgement

This work was supported by ATS-Nudgene and Emergence-CLEMgene of the Toulouse-IDEX. O.G. and C.N. are supported by Agence Nationale de la Recherche (ANDY). We thank I. Léger-Silvestre for thoughtful discussions and technical advices. Julien Mathon wrote the MTT-based executable files.

References

1. van Steensel B, Dekker J (2010) Genomics tools for unraveling chromosome architecture. Nat Biotechnol 28(10):1089–1095
2. Ay F, Noble WS (2015) Analysis methods for studying the 3D architecture of the genome. Genome Biol 16:183
3. Williamson I, Berlivet S, Eskeland R, Boyle S, Illingworth RS, Paquette D, Dostie J, Bickmore WA (2014) Spatial genome organization: contrasting views from chromosome conformation capture and fluorescence in situ hybridization. Genes Dev 28(24):2778–2791
4. Dion V, Gasser SM (2013) Chromatin movement in the maintenance of genome stability. Cell 152(6):1355–1364
5. Huet S, Lavelle C, Ranchon H, Carrivain P, Victor JM, Bancaud A (2014) Relevance and limitations of crowding, fractal, and polymer models to describe nuclear architecture. Int Rev Cell Mol Biol 307:443–479
6. Hajjoul H, Mathon J, Ranchon H, Goiffon I, Mozziconacci J, Albert B, Carrivain P, Victor JM, Gadal O, Bystricky K, Bancaud A (2013) High-throughput chromatin motion tracking in living yeast reveals the flexibility of the fiber throughout the genome. Genome Res 23(11): 1829–1838
7. Wang R, Mozziconacci J, Bancaud A, Gadal O (2015) Principles of chromatin organization in yeast: relevance of polymer models to describe nuclear organization and dynamics. Curr Opin Cell Biol 34:54–60
8. Albert B, Mathon J, Shukla A, Saad H, Normand C, Leger-Silvestre I, Villa D, Kamgoue A, Mozziconacci J, Wong H, Zimmer C, Bhargava P, Bancaud A, Gadal O (2013) Systematic characterization of the conformation and dynamics of budding yeast chromosome XII. J Cell Biol 202(2):201–210
9. Meister P, Gehlen LR, Varela E, Kalck V, Gasser SM (2010) Visualizing yeast chromosomes and nuclear architecture. Methods Enzymol 470:535–567
10. Berger AB, Cabal GG, Fabre E, Duong T, Buc H, Nehrbass U, Olivo-Marin JC, Gadal O, Zimmer C (2008) High-resolution statistical mapping reveals gene territories in live yeast. Nat Methods 5(12):1031–1037
11. Serge A, Bertaux N, Rigneault H, Marguet D (2008) Dynamic multiple-target tracing to probe spatiotemporal cartography of cell membranes. Nat Methods 5(8):687–694
12. Hajjoul HM, Mathon J, Viero Y, Bancaud A (2011) Optimized micromirrors for three-dimensional single-particle tracking in living cells. Appl Phys Lett 98:243701
13. Therizols P, Duong T, Dujon B, Zimmer C, Fabre E (2010) Chromosome arm length and nuclear constraints determine the dynamic relationship of yeast subtelomeres. Proc Natl Acad Sci U S A 107(5):2025–2030
14. Weber SC, Thompson MA, Moerner WE, Spakowitz AJ, Theriot JA (2012) Analytical tools to distinguish the effects of localization error, confinement, and medium elasticity on the velocity autocorrelation function. Biophys J 102(11):2443–2450
15. Backlund MP, Joyner R, Weis K, Moerner WE (2014) Correlations of three-dimensional motion of chromosomal loci in yeast revealed by the double-helix point spread function microscope. Mol Biol Cell 25(22): 3619–3629
16. Michaelis C, Ciosk R, Nasmyth K (1997) Cohesins: chromosomal proteins that prevent premature separation of sister chromatids. Cell 91(1):35–45
17. Robinett CC, Straight A, Li G, Willhelm C, Sudlow G, Murray A, Belmont AS (1996) In vivo localization of DNA sequences and visualization of large-scale chromatin organization using lac operator/repressor recognition. J Cell Biol 135(6 Pt 2):1685–1700
18. Lassadi I, Bystricky K (2011) Tracking of single and multiple genomic loci in living yeast cells. Methods Mol Biol 745:499–522
19. Loiodice I, Dubarry M, Taddei A (2014) Scoring and manipulating gene position and dynamics using FROS in budding yeast. Curr Protoc Cell Biol 62: Unit 22 17 21–14

20. Dubarry M, Loiodice I, Chen CL, Thermes C, Taddei A (2011) Tight protein-DNA interactions favor gene silencing. Genes Dev 25(13): 1365–1370
21. Saad H, Gallardo F, Dalvai M, Tanguy-le-Gac N, Lane D, Bystricky K (2014) DNA dynamics during early double-strand break processing revealed by non-intrusive imaging of living cells. PLoS Genet 10(3):e1004187
22. Shaham S (2006) WormBook: methods in cell biology. The C. elegans Research Community (ed), WormBook
23. Winey M, Yarar D, Giddings TH Jr, Mastronarde DN (1997) Nuclear pore complex number and distribution throughout the Saccharomyces cerevisiae cell cycle by three-dimensional reconstruction from electron micrographs of nuclear envelopes. Mol Biol Cell 8(11):2119–2132
24. Zhang B, Zerubia J, Olivo-Marin J (2007) Gaussian approximations of fluorescence microscope point-spread function models. Appl Opt 46(10):1819
25. Backlund MP, Joyner R, Moerner WE (2015) Chromosomal locus tracking with proper accounting of static and dynamic errors. Phys Rev E Stat Nonlin Soft Matter Phys 91(6):062716
26. Chuang CH, Carpenter AE, Fuchsova B, Johnson T, de Lanerolle P, Belmont AS (2006) Long-range directional movement of an interphase chromosome site. Curr Biol 16(8): 825–831
27. Saner N, Karschau J, Natsume T, Gierlinski M, Retkute R, Hawkins M, Nieduszynski CA, Blow JJ, de Moura AP, Tanaka TU (2013) Stochastic association of neighboring replicons creates replication factories in budding yeast. J Cell Biol 202(7):1001–1012